Suspended Sediment Transport and Fluid Mud Dynamics in Tidal Estuaries

Dissertation zur Erlangung des Doktorgrades der Naturwissenschaften

im Fachbereich Geowissenschaften der Universität Bremen

vorgelegt von

Marius Becker

Bremen, Juli 2011

Tag des Kolloquiums:

19.12.2011

Gutachter:

Prof. Dr. Dierk Hebbeln

Prof. Dr. Tobias Mörz

Prüfer:

Prof. Dr. Tilo von Dobeneck

Dr. Christian Winter

Marius Becker
Sankt-Jürgen-Straße 96
28203 Bremen

06.07.2011

Erklärung

Hiermit versichere ich, dass ich die Arbeit ohne unerlaubte fremde Hilfe angefertigt habe, keine anderen als die von mir angegebenen Quellen und Hilfsmittel benutzt habe und die den benutzten Werken wörtlich oder inhaltlich entnommenen Stellen als solche kenntlich gemacht habe.

Bremen, den 06.07.2011

“During every hour of daylight
and many of darkness
sailing or anchored, aground or afloat
in rain and shine, wind and calm
we studied the bed of the estuaries
and practiced ourselves
in threading their network of channels …
We were creeping gingerly
round the deeper arteries
that surround the sand,
examining their convolutions
as it were the veins of a living tissue
and the circulation of the tide
throbbing through them like blood.”

Erskine Childers, The Riddle of the Sands

Contents

Acknowledgements

This Ph.D. study was carried out in the course of projects, financed by the German Science Foundation as part of MARUM, Center for Marine Environmental Sciences, at the University of Bremen. Supervisor of the Ph.D. study was Prof. Dr. Dierk Hebbeln. In this context, I am indebted to Prof. Dr. Dierk Hebbeln, Prof. Dr. Burkhard Flemming and Dr. Alexander Bartholomä for providing an excellent working environment.

I would also like to express my gratitude to Prof. Dr. Tobias Mörz, the second reviewer.

Dr. Alexander Bartholomä and Prof. Dr. Kerstin Schrottke are thanked for their help and expertise, and for their enduring efforts in terms of data collection and cruise planning. The data set, on which this study is primarily based, was truly challenging and turned out to be exceedingly precious, in many ways.

Dr. Verner Ernstsen and Dr. Christian Winter are thanked for their openness, stimulating discussions, much encouragement, and a pleasant working atmosphere.

The crew of the RV Senckenberg, especially Karl, Rainer, Manni and Detlef, did a marvellous job; and Arne Schwab is thanked for his sacrificial assistance during the cruises. Likewise, thanks to the technicians at the Senckenberg Institute, Marine Science Department, in Wilhelmshaven.

Finally, in any aspect whatsoever, I am indebted to my parents, Hermann and Christa.

Summary

Cohesive sediments transport has been systematically studied for more than a century from field studies, laboratory experiments, and mathematical models. During the past decades, the accumulation of flocculated cohesive sediments and the formation of weakly consolidated mud deposits, including fluid mud, gained increased attention. Despite extensive research efforts, the governing processes of fluid mud formation are far from being fully understood.

The primary objective of this study is to investigate tide-driven dynamics of fluid mud in estuaries. State of the art hydroacoustic subbottom (SES) and current velocity profilers (ADCP) are used, to measure fluid mud dynamics on appropriate temporal and spatial scales. Connected fields of research are to be taken into account, such as bedload transport and the influence of subaqueous dunes on the turbulent flow field. Technical aspects are considered, in particular the detection of suspended cohesive sediments. Measurements are conducted in the Ems and the Weser estuary, located along the North Sea coast of Germany. Other study sites in the North Sea are the Jade Bay in Germany and the Grådyb tidal inlet in Denmark.

Not only the combined deployment of different hydroacoustic profiling devices but also the combined processing of collected data allows fluid mud dynamics to be studied in great detail. Combined processing is implemented in a software tool, programmed in MATLAB™. The software facilitates the acoustic backscatter calibration with respect to suspended sediment concentration (SSC) and thus joins information on hydrodynamic, near-bed density stratification and SSC in the water column.

A large data set is collected in the Weser estuary and analysed regarding tide-driven dynamics of fluid mud. Fluid mud does not appear in the suggested form of a contiguous layer, but is deposited in depressions, in troughs of subaqueous dunes, as well as in the form of mud drapes during slack water. Entrainment is controlled by local production of turbulence, which is, in turn, influenced by local morphology. Fluid mud deposits in dune troughs are rapidly entrained, induced by strong turbulent stresses which are generated at the dune crest and advected in direction of the lutocline, i.e. the density gradient between fluid mud and the water column. Mobile mud layers are significantly resistant to entrainment and partly survive half a tidal cycle. Continuous feeding by slack water deposition induces a positive feedback of in-

creasing concentrations and increased damping of turbulence, which inevitably leads to the formation of erosion-resistant estuarine mud deposits.

A new method for the detection of density stratification is introduced, based on the backscatter gradient of acoustic current profiles. Furthermore, the gradient Richardson stability criterion is also expressed in terms of the backscatter gradient and proved to be applicable in order to assess lutocline stability under intricate hydrodynamic conditions in the Ems estuary. In the heavily engineered Ems estuary, weir closure during flood slack water and the subsequent release of captured water masses induce the flushing of the estuary and catastrophic downstream advection of fluid mud. By the time the estuary returns to flood-dominated conditions, fluid mud is rapidly advected upstream and re-established in the upper part of the estuary.

In the Grådyb tidal inlet channel bedload transport in presence of large dunes is determined on the basis of highly accurate multibeam measurements. Bathymetrical changes are converted into bedload transport rates, which are not predicted by classical bedload transport formulae due to variations in grain-size composition of the mobilised sediment. Results from this study are applied to the Weser estuary to infer that lee-side deposition occurs simultaneously to the entrainment of fluid mud in dune troughs.

An instrumental study conducted in the Jade Bay concerning suspended sediment dynamics reveals that suspended sediment is transported in form of turbidity clouds. Thereby, acoustic methods underestimate SSC when large aggregates are present. Several floc populations coexist in the water column, covering a wide range of sizes from a few microns to millimetre size.

Chapter 1: General introduction

1.1 Fluid mud in tidal estuaries

The past decades saw a significant progress in the understanding of physical and biological processes involved in the transport and deposition of cohesive sediment [*Allen*, 1993; *Winterwerp and Van Kesteren*, 2004]. Beside recent advances in numerical modelling and the development of innovative measuring techniques, Henry Clifton Sorby's statement did by no means lose its relevance, when he, more than a century ago, declared mud deposition to be one of the most challenging topics in sedimentary geology [*Sorby*, 1908].

Whereas low-energy conditions were long thought to be a prerequisite of mud formation, this paradigm has recently been challenged by Schieber et al. [2007], who found evidence of ripples in mudstone beds, ascribed to the impact of considerably strong currents on flocculated cohesive sediments. While this was a new aspect in the palaeoenvironmental interpretation of mud stones, flocculation and its influence on settling were intensively studied in the context of mud deposition in recent domains, such as tidal estuaries [e.g. *Berlamont et al.*, 1993].

Tide-dominated estuaries are governed by both fluvial and marine sediment transport processes, acting on diverse temporal and spatial scales, where the coexistence of cohesive and non-cohesive sediments inherently complicates both the investigation of recent environments as well as the interpretation of estuarine stratigraphical features [*Dalrymple and Choi*, 2007; *Dyer*, 1995; *Uncles*, 2002].

In estuaries, accumulation of mud essentially occurs in the turbidity maximum zone (TMZ) [*Kirby*, 1988; *Wells*, 1995], which forms at the upstream end of the salt intrusion [*Dyer*, 1988; *Postma and Kalle*, 1955]. Different hydrodynamic processes were identified to contribute to TMZ dynamics, controlling position and trapping efficiency of suspended sediments. As reviewed by MacCready and Geyer [2009], these are the baroclinic residual circulation [e.g. *Pritchard*, 1954], the tidal current asymmetry [e.g. *Dronkers*, 1986a] and the tidal mixing asymmetry [e.g. *Simpson et al.*, 1990]. The tidal current asymmetry, inducing strong upstream directed tidal pumping of sediments, was shown to be particularly important for mesotidal and macrotidal coastal plain estuaries with moderate discharge, such as the Weser estuary, debouching into the North Sea [*Burchard and Baumert*, 1998].

From a hydrodynamic point of view, the Weser estuary is ebb-dominated, the ordinate tidal current acting downstream. Together, ebb-dominance and tidal pumping lead to the aforementioned coexistence and interaction of both cohesive and non-cohesive sediments, mainly in the upstream part of the TMZ. Here, the fluvial influence is significant, reflected by an increase of grain size, which effects both bed sediments and the suspended fractions [*Van den Berg et al.*, 2007]. In flood-dominated estuaries like the Ems estuary [*Jensen et al.*, 2003], the TMZ penetrates further upstream and also the fluvial part of the estuary is characterised by fine grained sediments.

In the TMZ, deposition of cohesive sediment is controlled by the formation of mud flocs, inducing an increase of settling velocities and, accordingly, an increase of the mass settling flux [*Eisma*, 1986; *Manning and Dyer*, 2007]. Settling is hindered as near-bed densities increase [*Mehta*, 1984], accounting for distinct vertical density gradients in the water column, i.e. lutoclines [*Kirby and Parker*, 1983; *Vinzon and Mehta*, 2003; *Wolanski et al.*, 1989]. In concentrated near-bed suspensions below the lutocline, an effective strength builds up only when concentrations reach the gelling point and mud flocs form a space-filling network. This state is generally considered as fluid mud [*Inglis and Allen*, 1957; *Winterwerp*, 2002].

1.2 Motivation and objectives

Preserved in the sedimentary record of estuarine and also deltaic deposits, fluid mud accounts for particular types of strata, i.e. thick mud drapes without sand partings [*Hovikoski et al.*, 2008; *Ichaso and Dalrymple*, 2009; *Shanley et al.*, 1992]. From the viewpoint of coastal engineering, accumulation of fluid mud affects the navigability of shipping channels and leads to siltation of harbour basins, thus being of socio-economic relevance [*McAnally et al.*, 2007a; *Wurpts*, 2005a]. The related tasks, namely palaeoenvironmental reconstruction on the basis of sedimentary records and the prediction of mud accumulation in recent environments, rely on the understanding and possible quantification of the preservation potential of fluid mud.

The preservation potential of fluid mud is controlled by the mass settling flux during favourable conditions, e.g. accumulation during slack water, and the interaction with the turbulent flow field during unfavourable conditions, e.g. entrainment during strong tidal currents. Research on the relevant processes of flocculation, settling, consolidation, and turbulent entrainment was substantially forwarded by the development of hydrodynamic numerical mod-

els, serving as a tool of extrapolation of small-scale processes [*Malcherek*, 1995; *Toorman*, 2000; *Winterwerp and Van Kesteren*, 2004].

Here the gap between the scales is obvious. Small-scale processes are sensitive to a number of empirical parameters, which are quantified on the basis of laboratory studies or sparse in-situ point measurements [e.g. *Bruens et al.*, 2002; *de Boer et al.*, 2007]. These processes, extrapolated within the framework of numerical modelling studies, predict highly variable natural phenomena on large spatial but short temporal scales, such as tide-driven dynamics of cohesive sediments in estuaries [*Guan et al.*, 2005; *Vinzon et al.*, 2009].

These models are difficult to validate, since the described combination of scales is difficult to observe. This is reflected by the predominant type of measuring campaigns presented in literature, namely high-frequency profiling and point measurements of limited spatial range [e.g. *Blake et al.*, 2001; *Dyer and Manning*, 1999; *Fettweis et al.*, 2006; *Kineke et al.*, 1996; and many others]. Consequently, field observations on larger spatial scales are related to longer temporal scales, such as seasonal variations of fluid mud deposits [e.g. *Sottolichio and Castaing*, 1999].

Another factor, complicating the observation of short term, large scale fluid mud dynamics, is the hitherto limited availability of measuring techniques concerning the bottom boundary layer. An example is the MASEX (mud and suspended sediment experiment) survey in the Weser between 1983 and 1985 [*Fanger et al.*, 1985]. Surveys were conducted on appropriate spatial and temporal scales in terms of longitudinal transects during the tidal cycle. Adversely, near-bed concentration measurements were obtained from a few locations only, and results were, beside the low resolution, affected by positioning problems.

The primary objective of this study is to investigate tide-driven dynamics of fluid mud in estuaries. State of the art hydroacoustic subbottom and current velocity profilers are used, presenting the opportunity to measure fluid mud and hydrodynamics on the desired spatial and temporal scales with significantly improved resolution, compared to earlier studies. If required, connected fields of research are to be taken into account, such as bedload transport and the influence of subaqueous dunes on the turbulent flow field. Finally, technical aspects are considered to be of importance, in particular the detection of suspended cohesive sediments.

1.3 Study area

Measurements are conducted in both the Ems and the Weser estuary. Fluid mud and mobile mud dynamics are studied in the Weser estuary. The Ems serves as natural laboratory to explore density stratification and fluid mud stability. These investigations are aided by an instrumental study of the detection of turbidity clouds, located in the Jade Bay, and by a measuring campaign concerning bedload transport in a field of subaqueous dunes in the Grådyb tidal inlet channel. These four sites are located along the North Sea coast of Denmark and Germany (Figure 1.1). Subsequently, the estuaries of the Weser and the Ems are introduced. Further information concerning the Grådyb tidal inlet channel and the Jade Bay are found in Chapter 7 and Chapter 8, respectively.

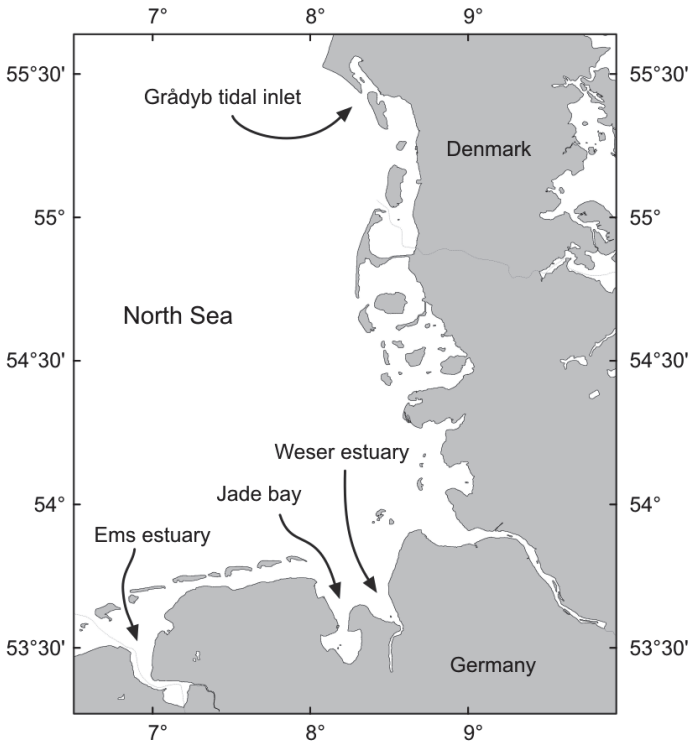

Figure 1.1: Locations of the Weser estuary, the Ems estuary, the Grådyb tidal inlet and the Jade Bay along the German and the Danish coast in the North Sea.

1.3.1 The Weser Estuary

The Weser estuary is located along the southern North Sea coast of Germany. The tidally influenced stretch is about 120 km long, extending from the weir at Bremen to the open North Sea. The estuary is divided into an upper, channel-like section between Bremen and Bremerhaven and a lower, funnel-shaped section between Bremerhaven and the open North Sea, bounded by tidal flats, with navigation depths of 14 m downstream and 9 m upstream of Bremerhaven. The upper mesotidal to lower macrotidal Weser estuary is partially mixed and

ebb-dominated, governed by semidiurnal tides. The long-term mean annual freshwater discharge, referring to the gauge of Intschede, located 30 km upstream from Bremen, amounts to 327 m^3/s with a low mean of 118 m^3/s and a high mean of 1,230 m^3/s [*Deutsches Gewässerkundliches Jahrbuch*, 2005]. The mean tidal range is 3.5 m at Bremerhaven, varying by about 1 m between mean spring and mean neap tide [*Grabemann et al.*, 1997]. Differences in SSC can be rather pronounced between spring and neap tide, with values varying by factors up to two [*Grabemann et al.*, 1997].

The turbidity maximum zone (TMZ), located between Brake and Bremerhaven, coincides with the low-salinity reach and extends over 15-20 km, whereas near-bed suspended sediment concentrations (SSCs) strongly exceed 0.25 g/l [*Fanger et al.*, 1985; *Grabemann and Krause*, 1989; *Riethmüller et al.*, 1988]. Bed sediment consists of fine and medium sand, with low contents of silt, clay, and organic matter. In the range of the centre of the TMZ muddy sediments dominate, containing up to 25% silt and clay and 5% organic matter [*Grabemann and Krause*, 2001]. In general, the TMZ in the Weser estuary forms due to the combined effects of tidal asymmetry [*Grabemann et al.*, 1997; *Lang et al.*, 1989] and non-tidal estuarine gravitational circulation [*Riethmüller et al.*, 1988]. Upstream and downstream of the TMZ SSCs are generally less than 0.05 g/l (Grabemann and Krause, 2001). The longterm mean fluvial input of SSC amounts to 0.04 g/l. [*Deutsches Gewässerkundliches Jahrbuch*, 2005]. According to Irion et al. [1987], most fluvial sediments are trapped in the estuary, whereas the overall budget is dominated by influx of marine sediments.

So far, fluid mud has not been studied in the Weser estuary. Wellershaus [1981] measured near-bed sediment concentrations of 70 g/l during slack water. Besides this observation, fluid mud deposition and consolidation were suggested as potential source for enhanced siltification in deeper parts of the navigation channel close to Bremerhaven and in the mud-reach between river km 57 and km 59 [*Fanger et al.*, 1985; *Riethmüller et al.*, 1988].

1.3.2 The Ems estuary

Such as the Weser, the Ems estuary is located along the southern North Sea coast of Germany. The anthropogenic influence is significant [*de Jonge*, 1988]. The river stretch between Emden and Papenburg was deepened in three steps during the past 20 years, reaching a navigation depth of 7.4 m [*Jensen et al.*, 2003], which resulted in an increase of the tidal range by approximately 1.5 m [*Talke and de Swart*, 2006].

In the TMZ, SSCs increased significantly by as much as two orders of magnitude. A contiguous zone forms downstream of the weir at Herbrum, characterised by high near-bed concentrations and fluid mud layers of about 2 m thickness [*Talke et al.*, 2009]. As a consequence of the deepening of the navigation channel, the TMZ shifted upstream. Hence, today the TMZ reaches into the fluvial freshwater zone [*Wurpts*, 2005b]. The mesotidal Ems estuary is partially mixed and flood-dominated. The long-term mean freshwater runoff amounts to 80.6 m^3/s with low mean value of 15.9 m^3/s and high mean value of 379 m^3/s [*Deutsches Gewässerkundliches Jahrbuch*, 2005]. The maximum tidal range of 3.5 m occurs at Papenburg [*Herrling and Niemeyer*, 2008]; and current velocities do not exceed 1 m/s [*Spingat*, 1997]. The mud content of bed sediments varies between more than 75% on the intertidal flats and the margins of the Dollard bay to less than 2% in the estuarine inlet and the offshore areas [*Herrling and Niemeyer*, 2008]. In the TMZ, bed sediments are composed of 50% clay, 20% sand, and 10% sand of mixed sizes. The organic content amounts to 20% [*Dette et al.*, 1994]. Concentrations may exceed 25 g/l already at a depth of 2 m below the surface [*Talke and de Swart*, 2006].

1.4 Methods

1.4.1 Hydrodynamics

Current velocity data were collected by means of a 1.2 MHz acoustic Doppler current profiler (ADCP, RDI), deployed on a rigid frame, which was attached to the starboard side of the ship. The instrument was located at a depth of 1.35 m below the water surface. Due to the blanking distance, the first measuring point was located 1.8 m below the surface. The vertical resolution of the ADCP was set to 0.25 m. In general, the horizontal resolution depends on ship speed and ping rates; the latter varied between 2.4 s to 3.8 s during the surveys. At present, ADCPs are routinely used to measure current velocities in a variety of fluvial and marine environments, as outlined by Muste et al. [2004a; 2004b].

1.4.2 Subbottom profiling

A parametric sediment echo sounder (SES-2000® Standard, Innomar Technology; hereafter referred to as SES) was deployed to detect vertical near-bed density gradients in the water column with a high vertical resolution (~0.06 m). The SES operates on a primary frequency of 100 kHz. A secondary frequency of 12 kHz was selected for all surveys. Profiles were generated from SES raw data with the ISE acquisition and post-processing software, distrib-

uted by Innomar. A detailed description of the SES is presented by Schrottke et al. [2006, this volume, Chapter 2].

1.4.3 Sampling methods

Bed samples were collected using a Shipek grab sampler [*Murdoch and Azcue*, 1995]. Subsamples were processed by standard laboratory procedures including grain size analysis by means of a settling tube, sedigraph and dry sieving, as well as the determination of organic matter content and dry mass per unit sample volume [*Lewis and McConchie*, 1994]. Water samples were collected using a HYDROBIOS (Kiel, Germany) water sampler. To derive SSC, water samples were filtered, the filters dried and weighed. The water column close to the river bed was sampled using a Rumohr-type gravity coring device [*Meischner and Rumohr*, 1974], equipped with transparent Perspex core barrels of 2 m length. Water samples were extracted in down-core steps of 0.1 m immediately after recovery. A comprehensive description of the sampling extraction procedure is presented by Schrottke et al. [2006, this volume, Chapter 2].

1.5 Processing of hydroacoustic data

1.5.1 Software development: MADCP

In order to process ADCP and SES data, an integrated software tool was programmed in MATLAB™ (The MathWorks). The "MADCP" software implements all common methods to process ADCP data. Beside the projects presented in this volume, MADCP was also used to process data published by Lefebvre et al. [2010], Stark et al. [2011] and Svensson et al. [2009]. The software is optimised to process ship based data collected on longitudinal transects, and handles the much simpler cases of up-looking and down-looking devices, obtained during stationary deployments.

Software development aims for a balance between standardised and customised processing. Standard methods are essential for the comparability and reproducibility of results and limit the presumed technical knowledge of the user. Regarding the required flexibility, customized processing is important for scientific applications. It was thus chosen to use both graphical user interfaces, which implicitly enforce a decent level of standardisation, and to implement an open data interface, to access source data at any time while working with MADCP in the MATLAB programming environment.

The main aim of ADCP data processing is to perform the moving platform correction, i.e. the transformation of raw data into the desired reference coordinate system [*RD Instruments*, 2008]. The coordinate transformation requires reference data concerning the movements of the specific platform, either in terms of bottom track information, recorded by the ADCP, or GPS based navigation data.

Both sources are necessary to compensate for each others deficits. In case of down-looking deployments in sandy, bedload dominated rivers or muddy estuaries, the bottom track system frequently fails, and navigation data may be used for the velocity correction [*Mueller and Wagner*, 2007]. Adversely, since the internal compass is biased in nearly all deployments on moving platforms, the correct reference heading is unknown, navigation not applicable, and bottom track required for the velocity correction [*Trump and Marmorino*, 1997]. Additional errors to be compensated in both bottom track and navigation data are outliers, scatter, and invalid data points.

Commercial ADCP processing tools capable of cleaning reference data for the moving platform correction are not available, at present. MADCP implements the appropriate algorithms in order to correct the named sources of errors. MADCP also enables to mix navigation and bottom track data to optimize the velocity correction. Essentially, the relationship of bottom track and navigation based ship velocity magnitude is used to correct velocity components of the desired reference system.

Further processing methods comprise matching of ADCP and SES files, interpolation in terms of equidistant steps along prescribed navigation lines in meandering channels, vertical interpolation, the application of filters, averaging in both vertical and horizontal direction, and file handling in general. Horizontal averaging is implemented in terms of spatial averaging [*Smith and McLean*, 1977], double averaging [*Nikora et al.*, 2007a; b], and averaging along lines of equal relative height above the bed, normalized by the water depth. Outliers in current velocity data may be removed by the procedure of Dinehart and Burau [2005]. Similarly to the horizontal averaging procedure, the horizontal interpolation may be carried out in terms of interpolation along lines of equal relative height above the bed, again normalized by the water depth.

1.5.2 Backscatter calibration

MADCP implements the acoustic backscatter calibration according to Deines [1999], including an iterative approach to correct for sediment absorption, as described by Thorne et al.

[1994] and Holdaway et al. [1999]. The backscatter calibration requires reference SSC measurements, typically derived from water samples or optical backscatter sensors. Reference SSC data are imported and matched with the ADCP files. ASCII sample data may additionally contain temperature and salinity, in order to calculate water absorption coefficients.

In principle, the acoustic echo intensity depends on the volume backscattering strength BS, subsequently referred to as backscatter, which is expressed in terms of the backscattering cross section σ_{bs} of the particles in suspension:

$$BS = 10\log_{10}\left(\frac{I_{bs}}{I_i}\right)\Bigg|_{r=1m} = 10\log_{10}\left(n_p\sigma_{bs}\right) \quad [dB] \tag{1.1}$$

where I_i is the incident intensity, I_{bs} is the backscattered intensity and n_p is number of particles in the scattering volume. In the Rayleigh scattering regime for particles smaller than the acoustic wavelength the backscattering cross section reads

$$\sigma_{bs} = \xi k^4 a^6 \tag{1.2}$$

where $k = 2\pi/\lambda$ is the wave number depending on the acoustic wave length λ, *a* is the particle radius and ξ describes the scattering properties of particles in suspension [*Medwin*, 2005]. Unless the scattering properties are constant equations 1.1 and 1.2 imply a linear relationship between BS and SSC, given by

$$BS = A\log_{10}\left(SSC\right) + B \tag{1.3}$$

The backscattering properties are implicitly determined during the calibration. To calculate backscatter from echo intensity the sonar equation is adapted to the ADCP configuration and, according to Deines [1999], written as

$$BS = K_c\left(E - E_R\right) + TL + 10\log_{10}\left(T\right) + C \quad [dB] \tag{1.4}$$

where E is the ADCP echo intensity and E_R is the echo reference level, both given in counts, K_c is the scale factor to convert counts to dB, T is the transducer temperature, and C comprises source level, pulse length and physical transducer parameters. For the practical application of the sonar equation it is not necessary to determine C and E_R; they are constant and merged with parameter B during the calibration [*Gartner*, 2004]. The transducer temperature is measured by the ADCP. TL is the two-way transmission loss, given by

$$TL = 20\log_{10}(r) + 2\alpha r \tag{1.5}$$

in which r is the range from the transducer and α is the absorption coefficient, in dB/m. The first term corrects for beam spreading and the second term for absorption effects in the water column. The absorption coefficient α comprises water absorption and sound attenuation due to suspended sediment. The water absorption coefficient may determined using different empirical relationships [e.g. *Ainslie and McColm*, 1998]. The sediment absorption coefficient is calculated according to Urick [1948]. Further details concerning the sediment absorption correction are presented in Chapter 3.3.4.

1.6 Results

1.6.1 The Weser estuary

The main results concerning tide-driven dynamics of fluid mud, as observed in the Weser estuary, are summarised in the following three chapters. Fluid mud does not appear in the suggested form of a contiguous layer, but is deposited in depressions and trenches, as well as in form of mud drapes during slack water, which temporarily cover small bed forms and in general smooth the river bed. This is described in Chapter 2.

Chapter 3 presents a study on fluid mud deposition in troughs of subtidal dunes. Thereby, the local morphology controls the preservation potential of fluid mud after slack water. Fluid mud deposits in dune troughs are rapidly entrained. This is not explained by the break-down of shear instabilities at the lutocline, but by strong turbulent stresses, generated at the dune crest and advected in direction of the lutocline during the onset of flow separation. Referring to results from Chapter 7, bedload transport already occurs at the time of entrainment, which induces mixing of sand and fluid mud in the dune trough and promotes embedding of mud due to lee-side deposition.

In the case that deposition occurs on predominantly flat ground, fluid mud transforms into a mobile mud layer and is dragged by the shear flow, which is introduced in Chapter 4. Mobile mud layers are shown to be significantly more resistant to entrainment, compared to fluid mud deposits in troughs large dunes. It is suggested that turbulence, produced at the lower boundary, leads to partial dewatering and consolidation.

The mobile mud layer may lose sediment to the shear flow by a process more similar to erosion than entrainment. Based on the observation, that mobile mud is partially preserved

until the subsequent slack water, semi-diurnal feeding of the mud layer potentially leads to a positive feedback of turbulence damping and consolidation, which inevitably promotes the formation of erosion-resistant estuarine mud. Semi-diurnal slack water deposition occurs in the centre of the TMZ, which explains the correlation between the centre of the TMZ and estuarine mud deposits.

1.6.2 The Ems estuary

Results related to fluid mud dynamics in the Ems estuary are presented in Chapter 5 and 6. A new method for the detection of density stratification is introduced, based on the backscatter gradient of acoustic current profiles. Furthermore, the gradient Richardson stability criterion is also expressed in terms of the backscatter gradient and proved to be applicable in order to assess lutocline stability under intricate hydrodynamic conditions in the Ems estuary. The lutocline rises and falls in response to the tidal flow, probably because the fluid mud layer becomes turbulent and entrains water from the upper layer during accelerating currents.

In the heavily engineered Ems estuary, weir closure during flood slack water and the subsequent release of captured water masses induce the flushing of the estuary and catastrophic downstream advection of fluid mud. By the time the estuary returns to flood-dominated conditions, fluid mud is rapidly advected upstream and re-established in the upper part of the estuary.

1.6.3 The Grådyb tidal inlet

As described in Chapter 7, bedload transport in presence of large dunes is determined on the basis of highly accurate multibeam measurements. Bathymetrical changes are converted into bedload transport rates, which are not predicted by classical bedload transport formulae due to variations in grain-size composition of the mobilised sediment. Results in terms of bedload transport during decelerating ebb currents are applied to the dunes in the Weser, as described in Chapter 3. It is inferred that lee-side deposition occurs simultaneously to the entrainment of fluid mud in dune troughs.

1.6.4 The Jade Bay

Results of an instrumental study concerning suspended sediment dynamics are presented in Chapter 8. Suspended sediment is transported in form of turbidity clouds, which are measured by different sensors, using both optical and acoustic backscatter. Simultaneous in-situ

measurements of floc sizes show that acoustic methods underestimate SSC when large aggregates are present. Several floc populations coexist in the water column, covering a wide range of sizes from a few microns to millimetre size.

Chapter 2: Paper I

Fluid mud dynamics in the Weser estuary turbidity zone tracked by high-resolution side-scan sonar and parametric sub-bottom profiler

K. Schrottke[1], M. Becker[1], A. Bartholomä[2]
B. W. Flemming[2], D. Hebbeln[1]

[1]MARUM, Center for Marine Environmental Sciences, University of Bremen, Germany
[2]Senckenberg Institute, Wilhelmshaven, Germany

Geo-Marine Letters (published)

Abstract

Fluid mud in estuarine turbidity maximum zones (TMZ) can pose considerable navigation risks due to potentially substantial reductions in nautical depth, coupled with an inherent difficulty of detection by conventional echo-sounders. Despite intensive research efforts, however, our knowledge about the spatial and temporal dynamics of fluid mud is still not sufficient. In this study, the combined use of a side-scan sonar (Sportscan ®, Imagenex) and a parametric sub-bottom profiler (SES-2000®, Innomar Technology GmbH) has proved successful for high-resolution fluid mud detection and volumetric quantification in an estuarine environment. In 2004 and 2005, repeated surveys were conducted in the navigation channel of the upper meso- to lower macrotidal Weser estuary TMZ (German North Sea coast) at different tidal stages and river discharges. Current velocity data were simultaneously collected by 1,200-kHz broadband ADCP (RDInstruments) measurements. Ground-truthing was carried out by means of grab sampling and gravity coring, adapted to fluid mud conditions. It was found that fluid mud occurrence in the Weser estuary is highly variable on time scales of a few hours and spatial scales of several metres. The riverbed is characterised by sand and mud deposits, and a complex morphology including subaqueous dunes and smooth bed deposits intermittently overlain by fluid mud. Thus, a continuous, coherent fluid mud body covering the entire TMZ riverbed was not observed. Rather, spatial distribution was patchy and highly

dependent on suspended particulate matter (SPM) concentrations in the water column, as a result of which local fluid mud deposits varied in thickness from centimetres to metres. The formation of fluid mud was largely restricted to slack water, although slack-water conditions were not necessarily associated with large-scale fluid mud appearance. Advective SPM transport of resuspended fluid mud seems to be the most plausible explanation for the high spatial variability observed, even between two successive tides. The amount of fluid mud deposited and resuspended in the course of a tidal cycle can reach several 10s of tons even in small riverbed depressions.

2.1 Introduction

Tidal estuaries are highly dynamic coastal systems where tide- and wind-induced forces as well as variable river discharge lead to complex interactions between saltwater and freshwater sediment loads. High sediment turnovers, especially of fine-grained cohesive particles, occur in the turbidity maximum zones (TMZ) of estuaries [*Eisma*, 1993; *Woodruff et al.*, 2001], where water masses of different salinities, densities, temperatures and particle concentrations meet. Depending on local circumstances such as tidal flow strength, tidal asymmetry and river discharge, estuarine waters can be well mixed, partially mixed, or stratified. However, density stratification is induced not only by salinity or temperature gradients but also by lutoclines formed by high concentrations of near-bed suspended particulate matter [*Eisma*, 1993; *Wolanski et al.*, 1992b].

In the TMZ, collision processes of suspended particles lead to aggregation and floc formation [*Whitehouse et al.*, 2000; *Winterwerp*, 2002], thereby enhancing settling rates to ultimately result in mud deposition. Such deposits are initially in a weakly consolidated state, showing sediment concentrations of several grams to 100 s of grams per litre [*Eisma*, 1993; *Guan et al.*, 2005; *Kineke et al.*, 1996; *Whitehouse et al.*, 2000], and having highly thixotropic characteristics. Such deposits are generally termed “fluid mud”. Depending on sediment supply and available settling time, they can reach a few metres in thickness [*Spingat*, 1997].

Indications are that the amount of SPM within the TMZ is dependent on the length and tidal flow strength of an estuary [*Uncles*, 2002]. Furthermore, due to tidal pumping, flood-dominated estuaries tend to have higher SPM concentrations than ebb-dominated ones. In general, the retention period of fresh mud deposits is dependent on the duration of slack water, the erosive capacity of the next tide, and the rate of sediment consolidation [*Abril et al.*,

2000; *Whitehouse et al.*, 2000]. The spatial distribution and temporal variability of TMZs are linked to the tidal amplitude, spring-neap cyclicity, the volume of river discharge, and wind-induced water-level fluctuations.

As a consequence, the locations of fine-grained sediment accumulation and erosion can be displaced up- and downstream by considerable distances, even in the course of a single tidal cycle [*Abril et al.*, 2000; *Grabemann and Krause*, 2001; *Uncles et al.*, 2006a]. All these processes, of course, have a direct impact on sediment distribution in an estuary. In estuaries which are used as shipping channels, continuous mud deposition can be a threat to navigability when causing considerable reductions in nautical depth [*Wolanski et al.*, 1992b]. This problem can be exacerbated by the fact that mud, in its unconsolidated and highly dynamic fluid state, can generally not be adequately detected by conventional echo-sounders installed on commercial vessels. This emphasises the need not only for further investigations of the fluid mud issue itself but also for the development of appropriate detection devices.

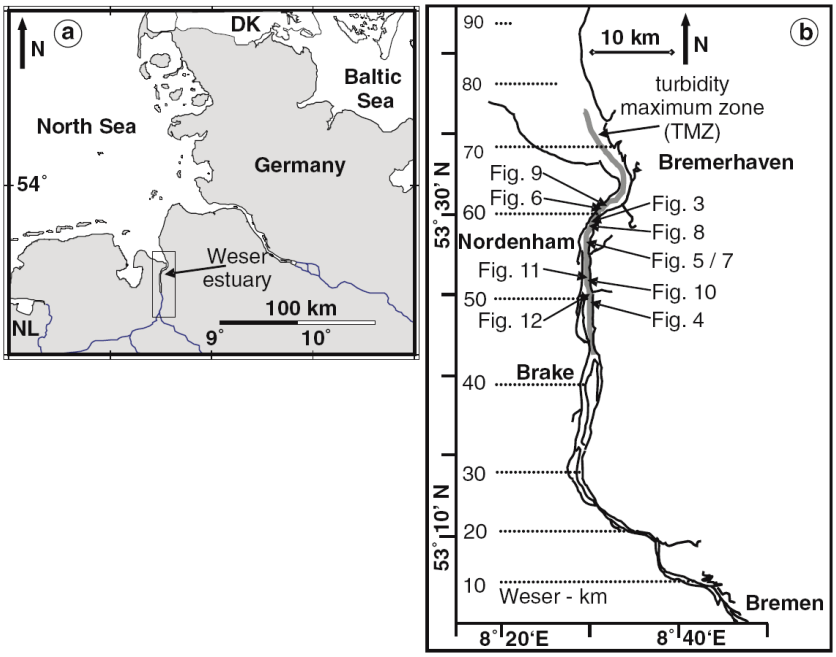

Figure 2.2: a: Location of the study area along the German North Sea coast. b: Position of the turbidity maximum zone (TMZ) in the Weser estuary.

Advances in our knowledge of dynamic processes within the TMZ over the last few decades have been summarised by, amongst others, Uncles [2002]. Emphasis has been given to parameter studies based on laboratory experiments [*Wolanski et al.*, 1992b] and modelling approaches [*Winterwerp*, 2002]. Field studies have generally focused on small-scale processes such as the settling behaviour of different types of particles at various concentration levels

[*Dyer et al.*, 1996; *Fugate and Friedrichs*, 2002]. Apart from extrapolations and modelling based on single-point measurements at fixed stations or along longitudinal profiles [*Grabemann and Krause*, 2001; *Guan et al.*, 1998; *Guan et al.*, 2005; *Riethmüller et al.*, 1988; *Uncles et al.*, 2006a; *Uncles et al.*, 1992], hardly any studies have thus far dealt with the resolution of fluid mud dynamics at larger spatial scales.

The purpose of this paper is to present results of a study in a tidal estuary obtained by the application of new acoustic profiling equipment which facilitates the detection of fluid mud at high vertical resolution and over relatively large areas, at the same time penetrating several metres into the sub-bottom sediments. Although focusing on a better understanding of regional fluid mud dynamics using this new methodology in a specific study area, this paper also contributes to elucidating the spatial and temporal dynamics of estuarine fluid mud in general.

2.2 Regional setting

The upper mesotidal to lower macrotidal Weser estuary is located along the southern North Sea coast of Germany (Figure 2.2). It is a heavily engineered estuary, having been repeatedly deepened and straightened for use as a major navigation channel for large ships up to the city of Bremen [*Franzius*, 1991; *Wienberg*, 2003]. As a consequence, the range of the semidiurnal tide at Bremen has increased from about 0.13 m in 1882 to over 4 m in 1990 [*Bundesanstalt für Gewässerkunde*, 1992]. The tidally influenced stretch of the Weser is about 120 km long, extending from the weir at Bremen to the open North Sea. The seaward limit has been defined as the location where salinity levels are almost constant over individual tidal cycles, irrespective of seasonal fluctuations [*Grabemann and Krause*, 2001]. The estuary can be subdivided into an upper, channel-like section between Bremen and Bremerhaven, with a sustained navigation depth of 9 m at low-water springs, and a lower, funnel-shaped section between Bremerhaven and the open North Sea, bounded by tidal flats and with a navigation depth of 14 m (Figure 2.2).

The long-term mean annual freshwater discharge, which is regularly measured at the village of Intschede about 30 km upstream from Bremen and which is currently based on the dataset covering the period 1941-2002, amounts to 327 m^3/s with a low mean of 118 m^3/s and a high mean of 1,230 m^3/s [*Deutsches Gewässerkundliches Jahrbuch*, 2005]. The mean tidal range of the estuary is 3.5 m at Bremerhaven, varying by about 1 m between mean spring and mean neap tide [*Grabemann et al.*, 1997]. Differences in SPM concentrations can be rather

pronounced between spring and neap tide, with values varying by factors of up to two [*Grabemann et al.*, 1997]. The Weser estuary is partially mixed, exhibiting a well-developed TMZ along the low-salinity reach which extends over 15-20 km and is defined by near-bed SPM concentrations exceeding 0.25 g/l [*Fanger et al.*, 1985; *Grabemann and Krause*, 2001; *Grabemann and Krause*, 1989; *Riethmüller et al.*, 1988]. This zone is located roughly between Brake and Bremerhaven (Figure 2.2, a). The tidal current is ebb-dominated with mean values of about 1 m/s to 1.3 m/s, reaching a maximum value of 2.6 m/s. The flood current is only slightly lower on average, but generally not exceeds 2.0 m/s [*Bundesanstalt für Gewässerkunde*, 1992].

Although the construction of groins, sheet pilings and subaqueous embankments canalises the tidal currents to reduce sediment deposition in the navigation channel, frequent dredging is nevertheless required, especially near Nordenham (Figure 2.2) [*Grabemann et al.*, 1997; *Müller*, 1985; *Riethmüller et al.*, 1988]. This river stretch coincides with the mean central section of the TMZ.

2.3 Materials and methods

2.3.1 General survey procedures

Although side-scan sonars have been in operation since the 1960s [*Blondel and Murton*, 1997], such high-frequency acoustic devices can be rather limited in waters characterised by dense particle suspensions because the emitted sound can be partially dispersed or even reflected before it reaches the solid bottom. As a result, the return signals are often so weak that almost nothing appears to be recorded. In the presence of fluid mud, this detection problem is particularly prominent. Nevertheless, even weak signals can be meaningfully interpreted if additional information from a simultaneously deployed sub-bottom profiler, capable of identifying both the fluid mud surface and the seafloor beneath it, is available. Although the combined use of such systems is common practice in coastal surveys [*Bates and Oakley*, 2004; *Fenster and FitzGerald*, 1996; *Nitsche et al.*, 2004], only a few sub-bottom profilers currently fulfil the requirement of high vertical resolution (≥6 cm) even within weakly consolidated fluid mud deposits. To date, single-beam echo-sounders with different frequencies have been used to monitor nautical depths. Still, results are not sufficient considering representative correlations between remotely monitored depths and actual sediment layers [*Liebetruth and Eißfeldt*, 2003; *Müller*, 1985]. In this study, a digital side-scan sonar was combined with a

novel parametric sub-bottom profiler (cf. below). The current condition was monitored using an acoustic Doppler current profiler (ADCP). Ground-truthing of the side-scan sonar and sub-bottom data was done by grab sampling and gravity coring, respectively, adapted to fluid mud conditions. Geographical positioning was performed by means of a differential global positioning system (DGPS) in WGS84 coordinates.

2.3.2 Data base

The data presented in this study are based on surveys carried out with the RV Senckenberg in the TMZ of the Weser estuary during the periods 6-10 December 2004 (neap tide, 5 December), 4-15 April 2005 (spring tide, 8 April), and 4-8 July 2005 (spring tide, 6 July; Figure 2.2). The measurements were conducted at different tidal phases along longitudinal profiles covering the centre and both sides of the navigation channel. In all, 60 grab samples and 14 gravity cores were taken at selected sites for groundtruthing. The river discharge at Intschede was about 298 m^3/s in December 2004, 347 m^3/s in April 2005, and 145 m^3/s in July 2005 (discharge data provided by the Federal Institute of Hydrology, Koblenz, Germany).

2.3.3 Side-scan sonar

A digital dual-frequency side-scan sonar system of type 881 Sportscan® (Imagenex) was deployed, using the 330 kHz frequency option. The range resolution at this frequency is 45 mm, and the horizontal and vertical beam spread is 1.8° and 60°, respectively. Both transducers were tilted downwards at 20°. The slant range was set at either 30 or 60 m, resulting in pulse rates of 11.2 and 7.8 pulses per second, and repetition rates of 89 and 128 ms, respectively. The pulse length (up to 25 ms) is automatically adjusted to the selected range. The gain control can be set in either automatic or manual mode.

The towfish was deployed over the stern of the vessel at a survey speed of about 4 knots, an automatic speed correction being applied throughout. The sound velocity in water was set at 1,500 m/s. In addition, the towfish layback relative to the GPS antenna was corrected.

2.3.4 Parametric sub-bottom profiler

For sub-bottom profiling, a parametric echo-sounder of type SES-2000® Standard by Innomar Technology GmbH (Rostock, Germany) was used. This instrument is able to detect even weakly consolidated fluid mud at high vertical resolution [*Schrottke et al.*, 2005]. The instrument emits high pressure sound pulses (electrical pulse power >18 kW; acoustic source

level >239 dB μPa^{-1} re 1 m), which results in nonlinear sound propagation. The parametric effect is achieved by simultaneously emitting, from the same transducer, sound pulses at two slightly different frequencies around 100 kHz. In this way, sum and difference frequencies are achieved while interacting in the water column. The repetition rate is set at rates of up to 50 pulses per second, which corresponds to pulse widths of 0.066-0.8 ms, depending on the selected slant range. Secondary low frequencies in the range of 4-15 kHz are used for subbottom profiling. In the present case, the most efficient frequency was found to be 12 kHz with which a subbottom penetration of up to 5 m was achieved.

The advantage of such systems is that the parametric difference frequency forms an exceedingly narrow beam, produces virtually no side lobes, and can be transmitted from a physically small transducer [*Loeser*, 1992]. High and low frequencies have the same footprint. The system enables precise detection of the sediment surface (high frequency: 100 kHz) as well as internal sedimentary structures (low frequency: selectable 4-15 kHz) with a high vertical resolution (≥6 cm) and accuracy, e.g. 100/10 kHz: 2/4 cm+0.02% of the water depth [*Wunderlich and Müller*, 2003].

The SES-2000® device basically consists of a control unit, which includes the power supply and data processing hardware, and a small transducer (active area: 22×22 cm) with a beam width of 3.6°. During the surveys, the transducer was firmly attached to the portside of the vessel at a depth of about 1.8 m below the water surface. Ship movements (heave, roll, pitch and heading) were compensated via a motion sensor (Seatex® MRU-6). CTD measurements were used for the correction of the SES data with respect to the sound velocity propagation.

2.3.5 Acoustic Doppler current profiler

An RD Instruments® 1,200-kHz direct-reading broadband ADCP was used to measure current velocity and direction in a profiling mode. The instrument was deployed in a rigid frame attached to the starboard side of the vessel at a depth of 1.35 m below the water surface. At the selected cell size of 25 cm, the statistical uncertainty of the horizontal, single-ping velocity is 10 cm/s. However, this decreases proportionally with the square root of the number of averaged pings. The long-term accuracy thus amounts to 0.2% of the measured velocity ±0.2 cm/s. The heading values from the internal fluxgate compass have a resolution of 0.2° and an accuracy of ±2°. The data are processed in real time and can thus be used for on-site cruise planning.

2.3.6 Sediment sampling for ground-truthing

An important aspect in such surveys is the calibration of the acoustic data. This is particularly recommended in highly dynamic environments such as tidal estuaries, where water and riverbed conditions change almost continuously. For surface sediments, a Shipek grab sampler was used because it recovers samples with largely undisturbed surfaces. The potential sample area is 20×20 cm (full bucket) and the corresponding sample volume is 3,000 cm^3. Depending on the material strength (e.g. consolidated mud) and grain size (e.g. gravel) of the sediment, actual sample areas and volumes can be smaller due to limited penetration of the bucket into the ground. A detailed description of the sampler is provided in [*Murdoch and Azcue*, 1995]. Small-scale morphological features at the sampled bed surface were noted by visual inspection of the sediment surface in the bucket. Subsamples of the sediment in the grab were processed using standard laboratory procedures including grain size analyses by means of a settling tube, sedigraph and dry sieving, as well as the determination of organic matter content and dry mass per unit sample volume [*Lewis and McConchie*, 1994].

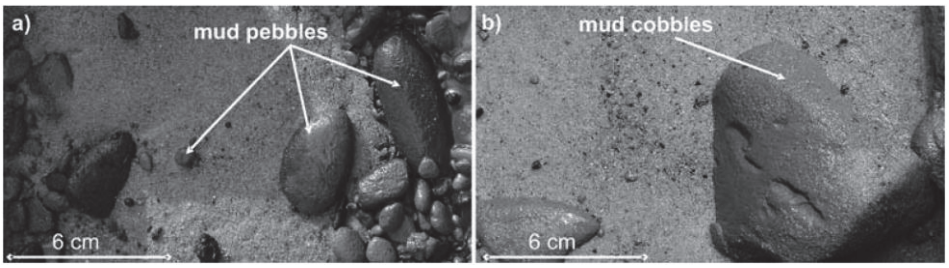

Figure 2.3: Fine to medium sand with some gravel and mud pebbles at the sample locations at a 53°27.912'N/08°29.447'E, and b 53°27.598'N/08°29.471'E on 12 April 2005.

Different techniques, amongst others coring devices have been used for the vertical sampling of highly concentrated near-bed suspensions and underlying stiff mud [*Eißfeldt and Pietsch*, 2001]. In this study, Rumohr-type gravity cores [*Meischner and Rumohr*, 1974], comprising transparent Perspex core barrels 8 cm in diameter and 2 m in length, were taken primarily to validate the sub-bottom profiling data. The corer weighs about 50 kg and, during sampling, care was taken to lower it gently to the riverbed. For subsampling, holes 2 cm in diameter and spaced at 10 cm intervals were drilled along each core barrel [*Schrottke et al.*, 2005]. Before deployment, the holes were taped and then stepwise reopened for quick sampling after recovery, thus minimising sediment settling and consolidation in the case of fluid mud. Depending on particle density and the viscosity of the suspension, the samples were transferred into bottles by means of tubes or syringes. In this way, closely spaced samples of

fluid mud were recovered. Along core sections having low SPM concentrations, several consecutive subsamples were combined into one larger subsample. To ensure complete vertical penetration of the fluid mud, coring stations were selected at which the fluid mud did not exceed thicknesses of 1.5 m. The samples were subsequently analysed for SPM concentration (dry mass per unit sample volume), particulate organic content (POC) and grain size distribution. In cases of low SPM concentrations, the subsamples were processed by vacuum filtration and subsequently analysed with a CIS laser particle sizer [*Schrottke and Abegg*, 2006].

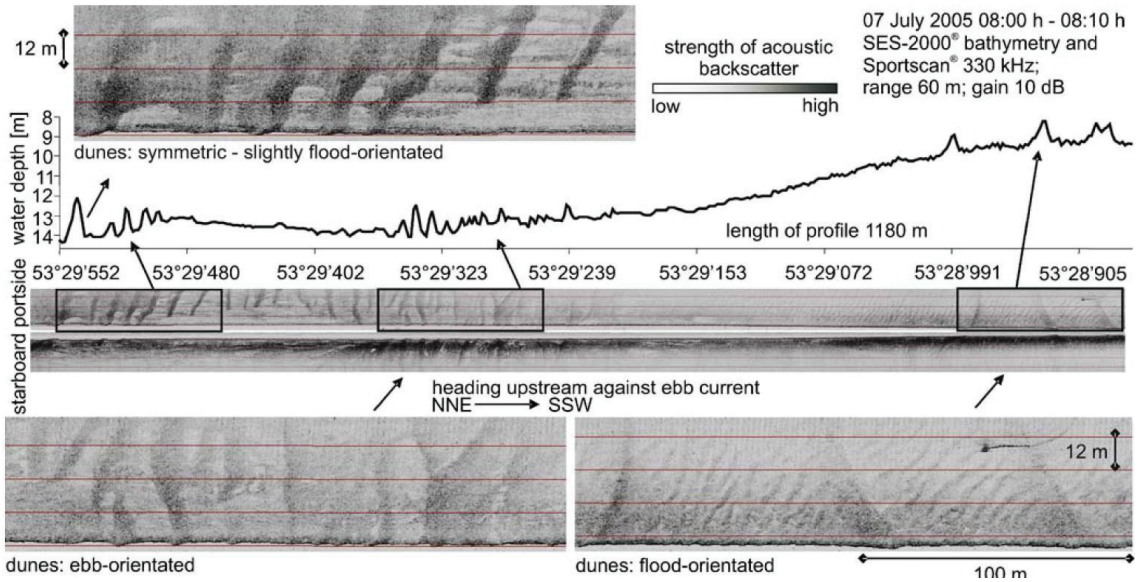

Figure 2.4: Side-scan sonar images and longitudinal bathymetric profile of subaqueous dunes with alternating orientations near Nordenham during ebb tide on 7 July 2005.

2.4 Results

2.4.1 Surface sediments in the Weser TMZ

The riverbed in the turbidity zone of the Weser estuary is characterised by fine- to coarse-grained sand and mud deposits. The mud fraction (<63 µm) can reach 98% of the total sediment and predominantly consists of silts and clays with variable amounts of organic matter and generally low sand contents. Overall, the mud deposits displayed extremely variable states of consolidation, ranging from very fluid to highly compacted. This suggests the side-by-side existence of mud deposits of different ages (hours-years) and of highly variable depositional factors. The erosion of freshly deposited mud is documented by a frequent occurrence of very soft mud pebbles and cobbles having a variety of shapes. These were also found on sandy beds or embedded in sand deposits (Figure 2.3). The occurrence of coarse-grained

sediments is restricted to isolated gravel and pebble patches, sometimes intermixed with sand and mud. Glacial till and peat were found to outcrop at some locations near the riverbanks, sometimes creating a prominent relief.

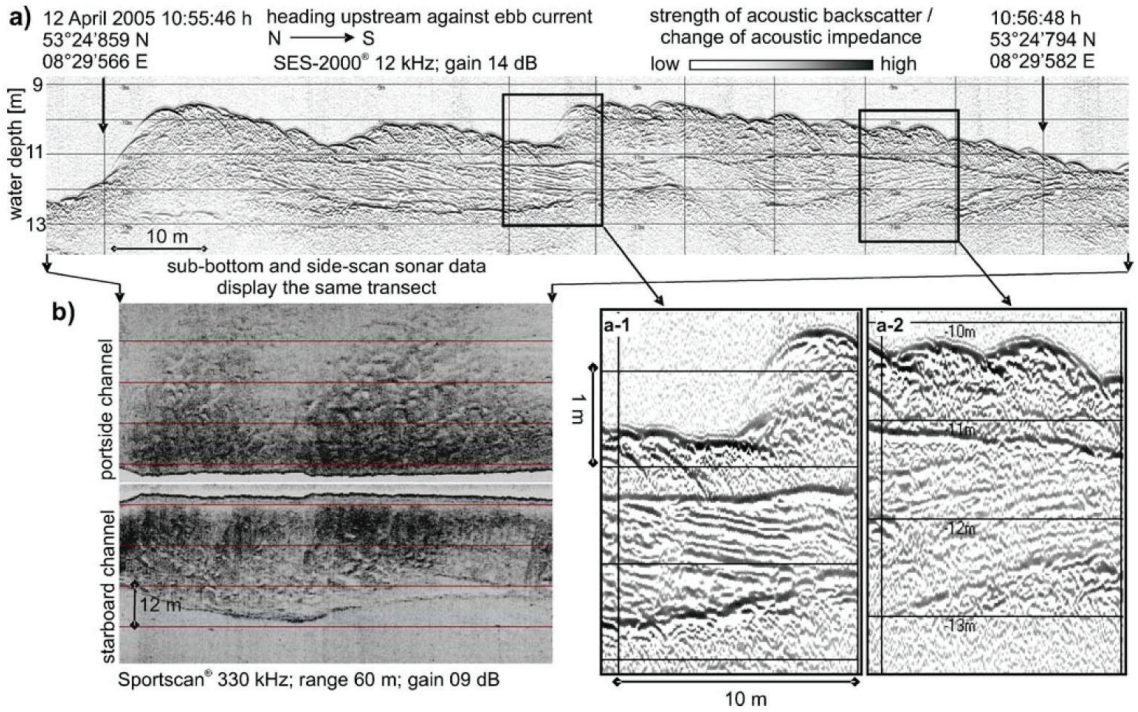

Figure 2.5: Bathymetry and sub-bottom stratification along a longitudinal transect in the Weser estuary on 12 April 2005 during ebb tide. a: SES-2000® sub-bottom profile. b: Side-scan sonar record. The riverbed is dominated by superimposed, ebb-dominated dunes showing complex internal structures (a-1, a-2).

2.4.2 Bed morphology in the Weser TMZ

The riverbed morphology, as revealed by the complex bathymetry, comprises stretches of smooth bed, dredged areas riddled with large dredge scours, and extensive subaqueous dune fields of varying size and shape. Subaqueous dunes, the most prominent bed features, reach heights of up to 6 m and lengths of up to 150 m but, on average, are 2-3 m high and 50 m long. The dune shapes are mostly two- or three-dimensional, the larger dunes being often superimposed by smaller ones. Although the dunes are mainly asymmetrical in the direction of the ebb tide, symmetrical and even flood-dominated forms were found, mainly along the western channel margin, the orientation of the bedforms being evidently controlled by the Coriolis force. More complex is the dune geometry along the channel section near Nordenham where dune orientation alternates within a few hundreds of metres, a good example being shown in Figure 2.4, these data stemming from 7 July 2005 during maximum ebb flow.

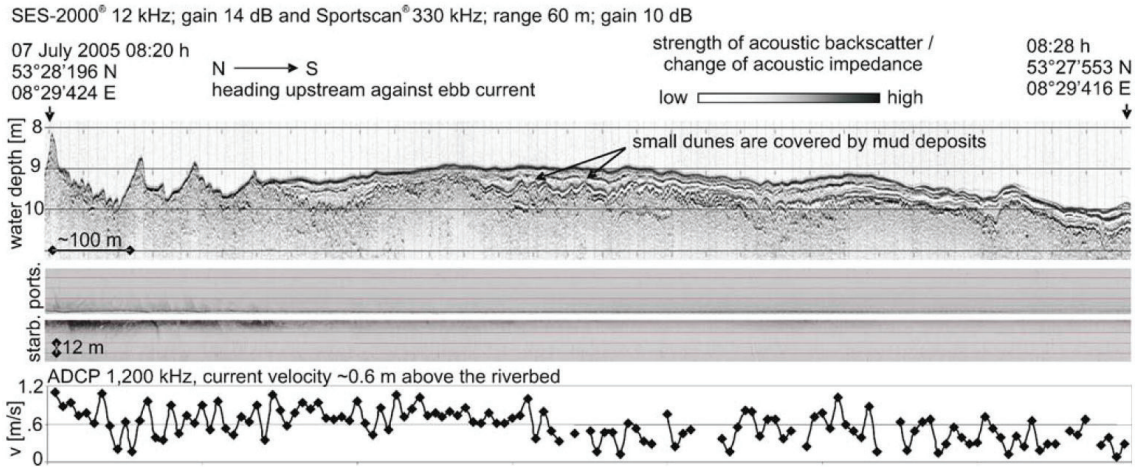

Figure 2.6: Longitudinal sub-bottom profile and the associated riverbed surface (cf. side-scan sonar record) on 7 July 2005 near Nordenham, showing a smooth bed composed of a mud drape covering subaqueous dunes. Mean current velocity at ~0.6 m above the riverbed, based on ADCP measurements, is shown in the lower panel for the same transect.

The sub-bottom displays complex bedding structures, as illustrated in Figure 2.5 (a) and the insets a 1 and a 2 where a modern dune field at the surface is underlain by metre-thick sequences of older cross-bedded sands showing different dip directions. In addition, the older (truncated) dune generations have distinctly different geometries (heights and spacings). The side-scan sonar image in Figure 2.5 (b) reveals that the modern dunes display at least two different size classes, i.e. small and large dunes, according to the classification in Ashley [1990].

Smooth beds were repeatedly observed in the estuary section between Bremerhaven and Nordenham. On side-scan sonar records, these areas are characterised by constant low backscatter (Figure 2.6, middle panel). In the example shown here, the sediment-validated sub-bottom profile (Figure 2.6, upper panel) reveals that the smooth bed surface consists of a mud drape which also covers a series of small dunes. This illustrates the high spatial fluctuation of different sediment facies, both laterally and vertically. To complete the catalogue of bedforms, a number of large, steeply sided and up to ~5 m deep grooves downstream of Nordenham should not be ignored (Figure 2.7). These produce a prominent and, based on repeated surveys, apparently permanent relief, carved into relatively compacted fine-grained sediments.

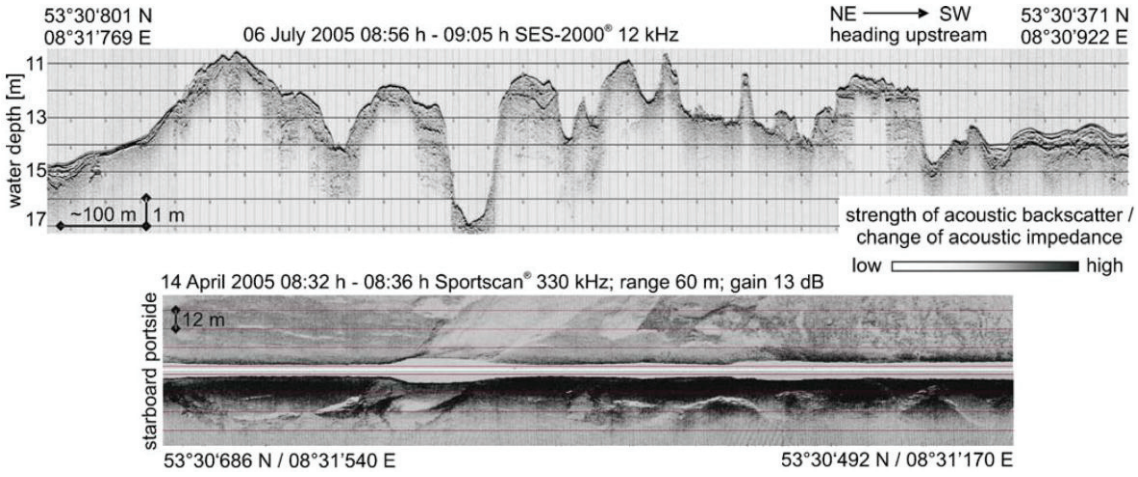

Figure 2.7: Longitudinal sub-bottom profile on 6 July 2005 and the associated riverbed surface (cf. side-scan sonar record) on 14 April 2005 downstream of Nordenham, showing deep and steep-sided grooves in relatively firm, fine-grained deposits.

The origin of these more static features is unclear. That they represent normal dredge marks can be excluded because these, although frequently observed within the TMZ, are generally very much smaller and by far not as deep. On the other hand, the rather frequent dredging operations in the area clearly disturb the sub-bottom stratification and thereby influence sedimentation and erosion processes. In particular, it would seem that dredging may be responsible for the initiation of new bedforms or the modification of existing ones. In addition, shoreline-stabilisation structures such as groins and sheet pilings result in a diversification of local bedforms, e.g. by producing scour holes and local sediment accumulations.

2.4.3 Spatial and temporal distribution of mud deposits in the Weser TMZ

The highest rate of mud deposition was found in the mean central section of the TMZ where extensive areas of smooth bed deposits occur. These are internally stratified and consist of relatively consolidated mud (e.g. Figure 2.6). They appear to be quite resistant to the force of the tidal flow, which is dominated by mean depth-averaged ebb-current velocities of 0.8 m/s and mean velocities of 0.6 m/s at a height of ~0.6 m above the riverbed (min. 0.1 and max. 1.1 m/s; Figure 2.6, lower panel). Despite the generally low backscatter, they are nevertheless firm enough to produce a clear bottom return on the side-scan sonar records (Figure 2.6).

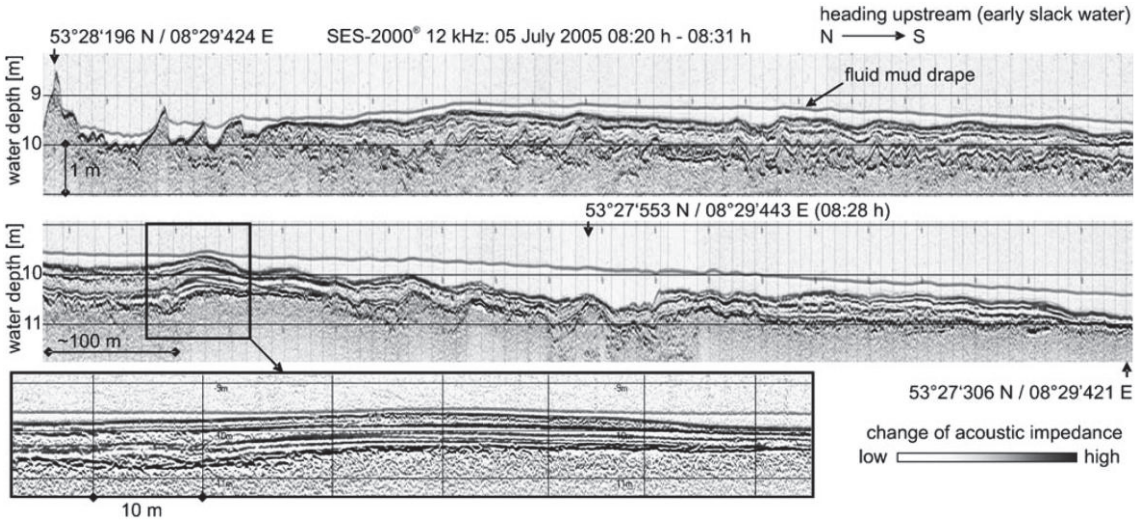

Figure 2.8: Longitudinal sub-bottom profile on 5 July 2005 near Nordenham, showing a smoothed bed produced by a drape of fluid mud. The enlargement shows a sequence of mud layers underneath the fluid mud.

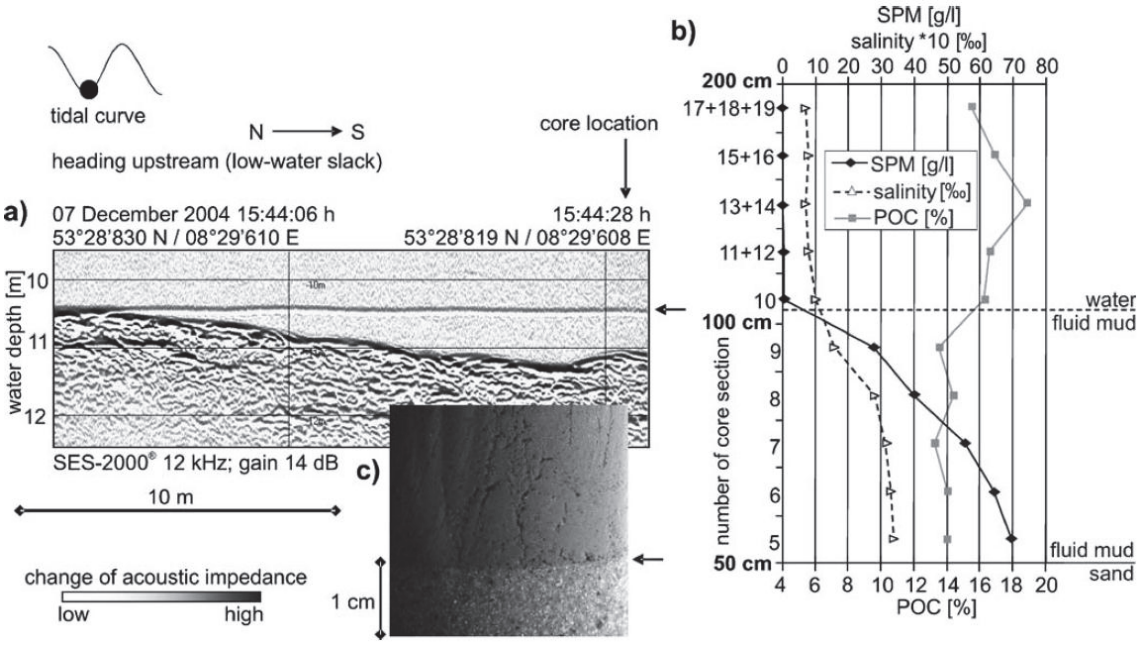

Figure 2.9: a: Longitudinal sub-bottom profile showing the core position on a sandy bed overlain by fluid mud during low water on 7 December 2004. b: Down-core trends in suspended particulate matter (SPM) concentration, salinity, and particulate organic content (POC). c Photograph of the fluid mud – sandy riverbed interface in the core.

When comparing the echo-sounder profiles of Figure 2.6 and Figure 2.8, which display roughly the same section exactly 48 h apart but at different tidal phases, it can be seen that the state of the surface drape changes markedly over time in terms of the acoustic signals. Thus, during early slack water at a mean depth-averaged current velocity of 0.25 m/s, a weak

change in acoustic impedance appeared a few decimetres above the more solid bottom (Figure 2.8), indicating the presence of a fresh fluid mud layer.

Cores recovered during such tidal phases, even along sand-dominated river sections, indeed demonstrate that the faint change in acoustic impedance is related to fluid mud freshly deposited over the more consolidated estuary bed (Figure 2.9, a). As shown in Figure 2.9 (b), SPM concentration increased sharply down-core from the acoustic interface, reaching values of several decigrams per litre. At the same time, the salinity increased threefold and the organic content decreased by 2-3%. The interface between the fluid mud and the sandy riverbed is illustrated in Figure 2.9 (c).

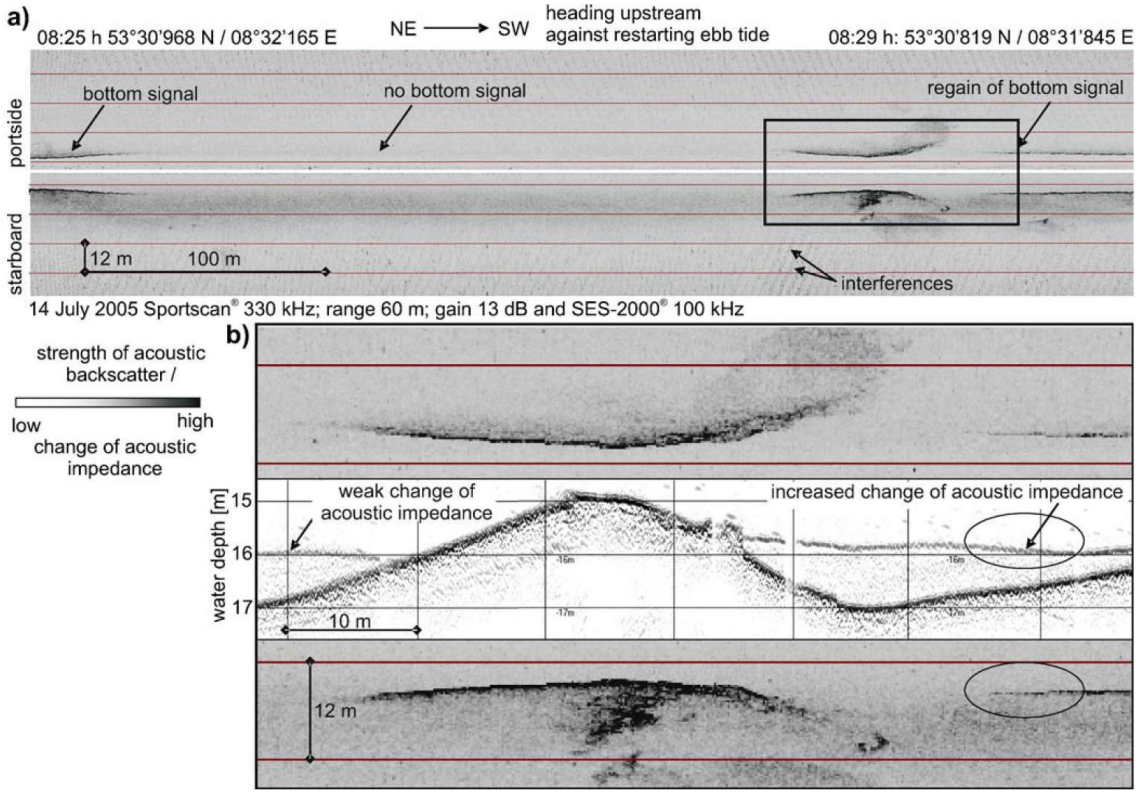

Figure 2.10: a: Example of fluid mud detection by side-scan sonar on 14 July 2005 downstream of Nordenham. b: Enlargement of a profile section with fluid mud, in which the side-scan sonar bottom signal is sporadically lost and regained. For comparison, a sub-bottom profile showing the change in acoustic impedance has been added.

Over time intervals during which a drape of fluid mud covers the more solid riverbed, the overall morphology is strongly smoothed (Figure 2.8). Applying side-scan sonar under such conditions generally results in an almost complete loss of the bottom signal (Figure 2.10). In

the example shown here, the solid bottom is still clearly visible at the beginning of the profile where the riverbed consists of strongly reflecting sediment.

Thereafter, the bottom signal disappears on both channels, as the backscattered signal becomes too weak for recording, only to reappear in places where the solid bottom protrudes through the fluid mud (Figure 2.10). In this case, the slightly stronger backscatter (darker tone) on the starboard channel is ascribed to a steeper incidence angle along the channel margin. In Figure 2.10 (b), the received sound signal of the subbottom profiler reflects an increased change in acoustic impedance on the upstream (right-hand) side of the protruding bedform. This indicates a change in fluid mud characteristics, probably pointing towards higher sediment concentrations. At the same time, the side-scan sonar relocates the bottom.

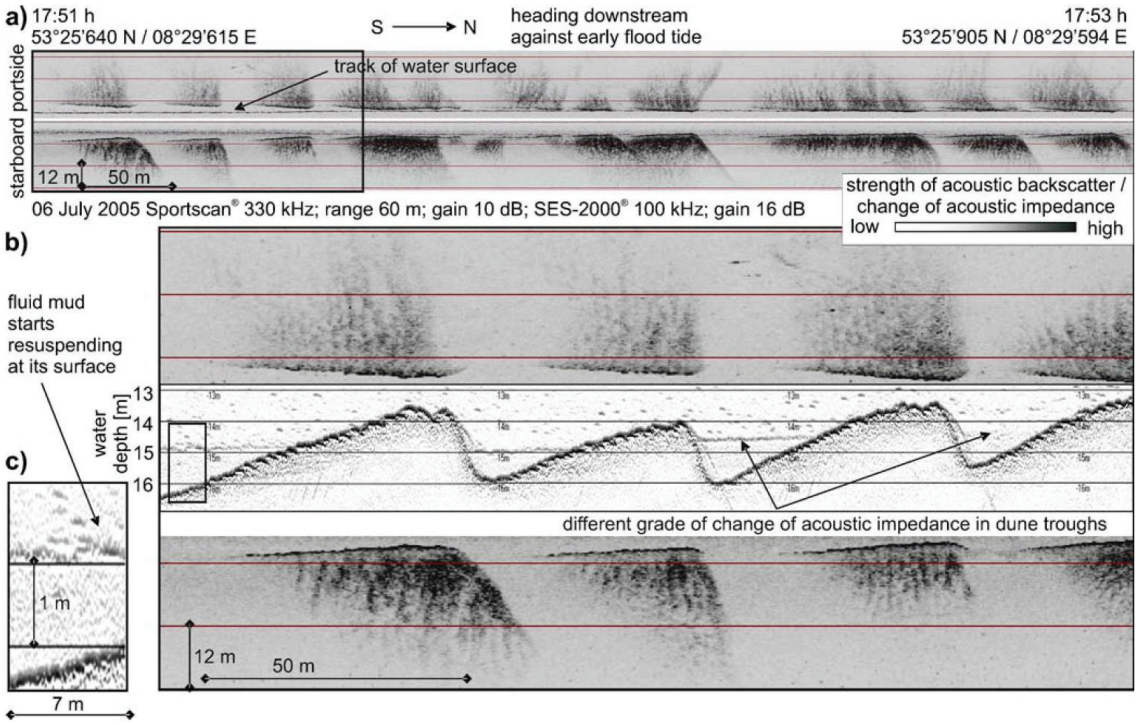

Figure 2.11: a: Longitudinal side-scan sonar profile recorded on 6 July 2005 downstream of Brake, showing fluid mud in the troughs of subaqueous dunes. b: Enlargement of a profile section showing changes in the acoustic characteristics of the side-scan sonar and SES-2000® bottom signals. c SES-2000® record indicating a rough fluid mud surface.

Apart from spatially extensive areas of fluid mud deposition within the mean central section of the TMZ, more patchy distributions were observed throughout the whole TMZ, including areas of large subaqueous dune fields near Brake (Figure 2.11). Here, the dune crests can be seen to protrude at regular intervals through the fluid mud horizon, the side-scan sonar loosing the bottom signal in the same rhythm (Figure 2.11, a). Furthermore, fluid mud does

not form a constant depth level but rather varies in height, thickness, slope and surface roughness from one dune trough to another, as derived from the sound characteristics retrieved by the SES-2000® (Figure 2.11, b). This situation occurs mostly at early slack water when fluid mud formation starts, and at the beginning of the returning tide when resuspension is initiated (Figure 2.11, c). By that time, the forming of the first acoustic reflector is highly variable.

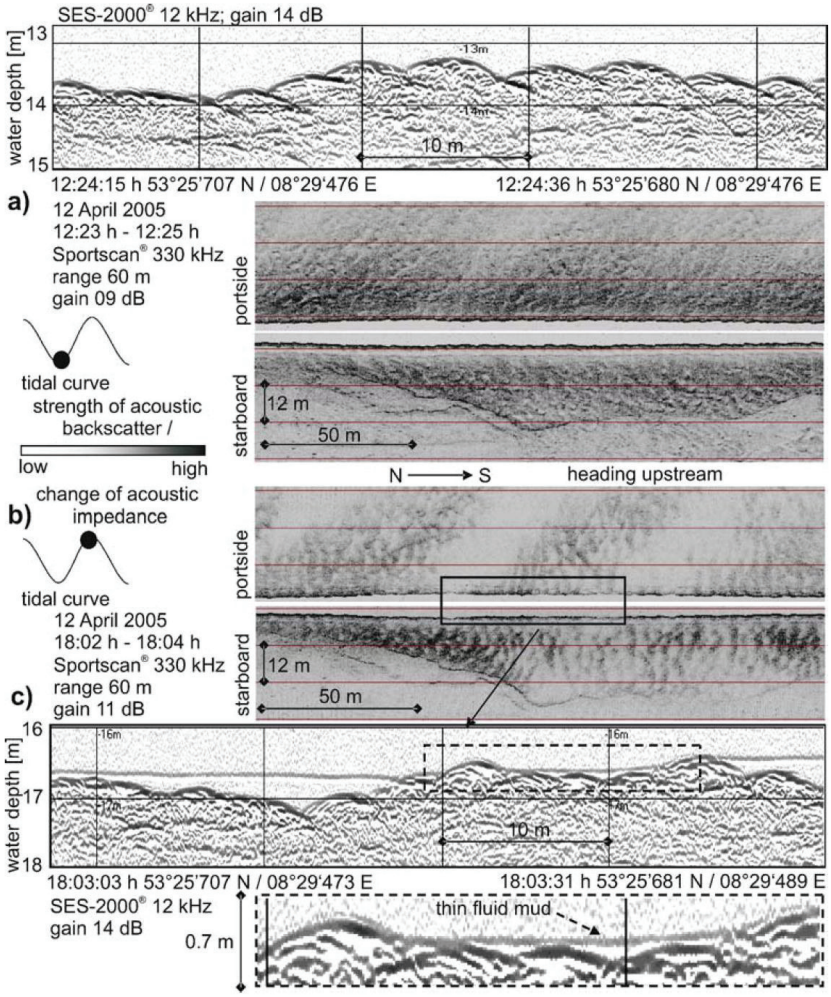

Figure 2.12: a-c: SES-2000® and side-scan sonar images of a river section during low-water (a) and high-water slack tide (b) on 12 April 2005. Note that fluid mud deposition occurs only during the high-water slack tide. c Record showing a very thin, fluid mud drape over a sand bottom.

Another point of interest is that fluid mud does not form at the same locations during all slack-water periods. This is illustrated in Figure 2.12 (a) where no fluid mud was deposited during the low-water phase on 12 April 2005. The bed morphology at this location is characterised by compound dunes. Roughly 6 h later, i.e. during high-water slack tide, fluid mud was once again present (Figure 2.12, b). In this example, the fluid mud layer was rather thin,

reaching thicknesses of only a few centimetres in the troughs of the small superimposed dunes (Figure 2.12, c). At some localities, fluid mud occurs only intermittently in small patches and, when present, accumulates in shallow depressions (Figure 2.13). Thus, no fluid mud was recorded at the depression shown in Figure 2.13 on 12 April 2005 about 20 min before low water. On 6 July 2005, by contrast, fluid mud appeared at the same location some 45 min after high-water slack tide, reaching thicknesses of about 1 m. This river section is situated near the upstream limit of the TMZ.

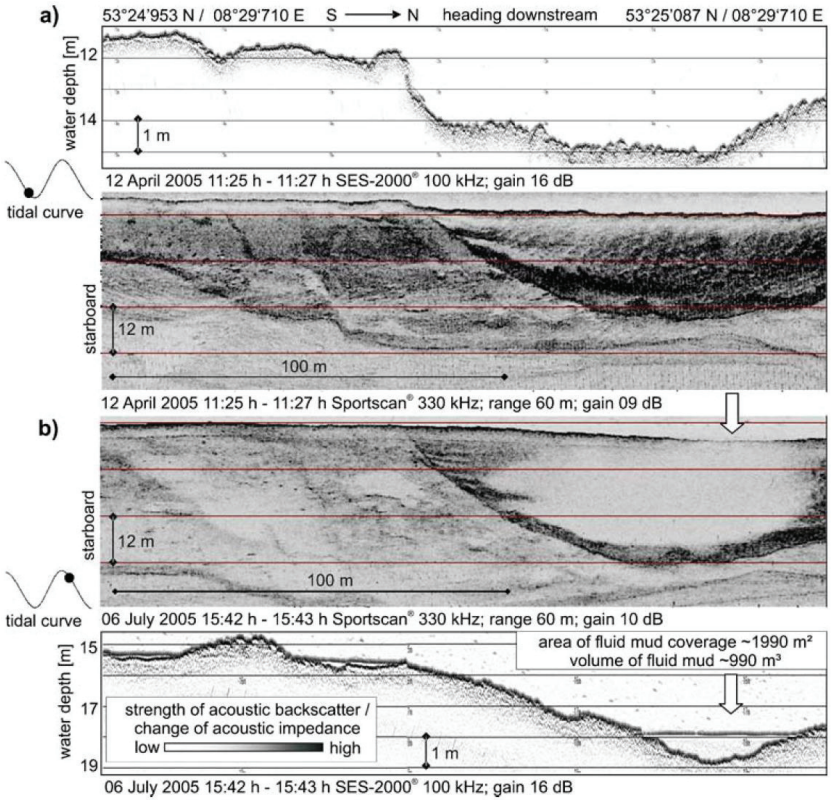

Figure 2.13: a: SES-2000®and sidescan sonar image of a riverbed depression without fluid mud shortly before low-water slack tide on 12 April 2005. b: The same section, displaying fluid mud shortly after high-water slack tide on 6 July 2005, used to quantify the fluid mud in the depression by combining the side-scan sonar and sub-bottom profiling data.

Apart from the fact that fluid mud formation begins only once the current drops below a critical level near slack tide, it does not always form at this location. This occurs more often during low tide and high river discharge, as was observed on 12 April 2005 (daily mean river outflow at Intschede was 354 m^3/s), than during high tide and low river discharge, as observed on 6 July 2005 (daily mean river outflow at Intschede was 154 m^3/s; data provided by the Federal Institute of Hydrology, Koblenz, Germany).

Quantifying fluid mud deposition under conditions as variable as those outlined above (cf. spatial distribution, thickness and particle concentration) would appear a rather daunting undertaking. Nevertheless, by combining the side-scan sonar, sub-bottom and ground-truthing datasets, a first-order volumetric quantification of fluid mud does indeed seem feasible, at least for individual deposits.

Thus, in the case of the depression illustrated in Figure 2.13, the fluid mud had a volume of 990 m^3, covering an area of about 1,990 m^2 on 6 July 2005. Assuming a depth-averaged particle concentration of about 50 g/l (based on extrapolations from vertical core samplings and SPM analyses shown, for example, in Figure 2.9, b), the total mass of fluid mud temporarily deposited in this depression during the associated slack-water period would have amounted to almost 50 t (ton).

2.5 Discussion

Attempts to detect fluid mud or weakly consolidated fine-grained deposits in estuaries have thus far not made systematic use of side-scan sonar recordings [*Madson and Sommerfield*, 2003; *Woodruff et al.*, 2001]. This might be due to the fact that side-scan sonar has inherent difficulties in detecting the bottom in areas of freshly deposited fluid mud. Depending on the physical state of the fluid mud, amongst others, SPM concentration and consolidation level, the sonar can loose the bottom signal (Figure 2.10). However, as demonstrated in this study, even weak acoustic backscatter signals of high-frequency side-scan sonars can be meaningfully interpreted when combined with sub-bottom profiling data. The main advantage of this approach is that side-scan sonars can provide a complete spatial coverage of a study area.

Compared with conventional dual-frequency echo-sounder systems commonly used for fluid mud detection, the SES-2000® sub-bottom profiler not only provides information on the fluid mud surface, internal structures (if present) and the consolidated bed surface but also penetrates into the sub-bottom at very high vertical resolutions. This high resolution of the first few metres of the bed sediments substantially improves the interpretation of the acquired data, as previously emphasised by Nitsche et al. [2004]. This results in a better classification and differentiation of sedimentary facies and expands the information on their dynamics. Common difficulties experienced when attempting to classify bedding sequences from dual-frequency echo-sounder data, reported by Müller [1985] as well as Liebetruth and Eißfeldt

[2003], are thereby minimised. The combined use of side-scan sonar and sub-bottom profiler now enables a rapid, quasi-three-dimensional mapping of spatially extensive fluid mud deposits. The physical nature of the solid riverbed sediments in the navigation channel of the Weser TMZ, essentially comprising relatively compacted sand and mud deposits, had already been reported by Lüneburg [1955; 1975], Wellershaus [1981], Grabemann [1992] and, more recently, also by Schrottke et al. [2005].

Apart from temporal and spatial variations of the solid riverbed (Figure 2.6), there are locations which appear to be relatively stable over many months (Figure 2.13), and this despite strong tidal currents (up to 2.6 m/s) and considerable river discharge. The prominent surface structures observed near Nordenham exist for several years now, suggesting that these deposits comprise erosion-resistant sediments such as stiff muds, till or peat.

Based on repeated surveys with side-scan sonar and subbottom profiler, the mobile riverbed surface in the navigation channel of the Weser TMZ was found to have a complex and highly variable morphology and sediment distribution, at time scales of hours and at spatial scales of metres. This is almost entirely due to the temporary deposition of fluid mud having concentrations of several decigrams per litre (Figure 2.9). Once the suspended matter settles out, it drapes the solid bottom and thereby causes remarkable and rapid changes in the instantaneous constitution of the riverbed surface. It is important to note that the occurrence of fluid mud is not necessarily associated with that of consolidated sub-bottom mud deposits commonly found in the mean central section of the TMZ near Nordenham (Figure 2.6 and Figure 2.8).

On the contrary, fluid mud occurs also where the solid riverbed is composed of sand, gravel and even organic deposits (Figure 2.9 and Figure 2.11). This means that the nature of sedimentary facies characterising the riverbed can change completely within very short time intervals when fluid mud is formed or shifted from one location to another in the system (Figure 2.12). Depending on the thickness of the fluid mud, which can vary from a few centimetres to several metres in the present case, the solid riverbed can be transformed to show a more patchy sediment pattern (Figure 2.12) or even a completely different facies pattern (Figure 2.8). One-off sampling surveys of estuaries characterised by temporary fluid mud deposition may thus yield a totally erroneous picture of the riverbed sediment character and distribution.

Associated with the rapid changes in sediment character, the bathymetry and morphology can undergo similarly abrupt modifications due to fluid mud dynamics. On the one hand, fluid mud deposits exceeding several metres in thickness can reduce the nautical depth to critical levels. On the other hand, morphological features such as subaqueous dune troughs and riverbed depressions can be temporarily levelled by fluid mud infilling (Figure 2.10 and Figure 2.11). Furthermore, the generation of such flat beds strongly affects the bottom roughness.

It has been demonstrated that the deposition of fresh fluid mud is highly dependent on the tidal phase, beginning shortly before slack water. The resuspension process then starts after slack water when the returning tide exceeds a critical velocity, as has recently been reported for the Weser estuary by Schrottke et al. (2005b).

Also, it has been shown that slack-water conditions as such are no guarantee for fluid mud deposition (Figure 2.12). In addition, fluid mud does not always occur at the same locations, rather being highly variable in instantaneous spatial distribution. The reason for this is the almost complete resuspension of fluid mud at most sites, and the subsequent advective SPM transport within the water column in response to changing residual current strengths in the course of spring-neap cycles, the daily inequality of the tide, and changing freshwater discharges. As a result, the distance covered by the resuspended muds can be quite substantial between successive tides, and subsequent redeposition will thus occur at different locations over time.

Furthermore, this differential residual transport causes the fluid mud to migrate up and down the estuary over a distance which defines the TMZ. Such shifts in fluid mud depocentres and, thus, SPM result in periodic displacements of the TMZ. Grabemann and Krause [2001] came to similar conclusions based on stationary measurements of turbidity, salinity, temperature, water level and current velocity at five locations within the TMZ of the Weser estuary. They assumed a periodic exchange of SPM between two temporary and spatially limited deposits in the estuary, located at each end of the TMZ. Comparable findings have recently been reported by Uncles et al. [2006a] for the Humber estuary in England, this TMZ having been subdivided into a core, nose and tail region, and ascribing SPM transport mainly to advection in the course of daily tides and lunar cycles. Small-scale spatial variations of fluid mud distribution were not mentioned in that publication.

The small-scale spatial variability of fluid mud deposits in the Weser estuary observed in the course of this study is probably linked to the complex, highly turbulent and locally chang-

ing current pattern in this TMZ. Strong supporting evidence is the asymmetry of subaqueous dunes which changes direction within a few hundreds of metres (Figure 2.4), a feature reflected also in the complex internal sedimentary structures (Figure 2.5). As a consequence, the spatial distribution of fluid mud within the TMZ differs from one tide to the next, and is therefore not predictable at this point in time. Nevertheless, the volumetric quantification of fluid mud masses deposited during a single slack-water period, as demonstrated in this study for a relatively small depression (~50 t) in the Weser estuary, has taken the fluid mud issue a step further. Extrapolating this value over the area covered with fluid mud within the TMZ would yield an impressive amount of fine-grained sediment in this estuary.

Having documented the high dynamics of fluid mud in the Weser TMZ, the question arises as to why dredging is required to maintain the navigation depth. Although the fluid mud is almost entirely resuspended at the study locations after each slack water, a certain amount of mud is evidently transformed into more consolidated and, hence, more erosion-resistant deposits at some locations. This is illustrated in the enlargement of Figure 2.8, which shows sequences of mud layers being temporarily overlain by fluid mud. With time, cumulative deposition would lead to a gradual reduction in the channel depth, necessitating the frequent dredging activities taking place in the Weser [*Eißfeldt and Pietsch*, 2001; *Müller*, 1985]. The ubiquitous occurrence of mud pebbles consisting of rather weakly consolidated material (Figure 2.3) also strongly supports this postulated accretion process.

2.6 Conclusions

From the results of this study, the following major conclusions can be drawn.

- The problem of tracking the spatial distribution and dynamics of fluid mud with a high temporal and spatial resolution can be solved by combining high-frequency side-scan sonar records with validated sub-bottom profiles using a parametric sound source and groundtruthing. Furthermore, this new approach substantially improves the application potential of side-scan sonars in estuarine waters. It also provides area-wide datasets of, amongst others, bottom roughness, an important parameter in numerical models.
- Fluid mud can now be volumetrically quantified to some extent by the three-dimensional resolution of fluid mud deposits.
- It can now be shown that fluid mud deposits in the navigation channel of the Weser TMZ are patchy and highly variable, both on temporal and spatial scales spanning single tidal

cycles and several 10 s of metres, respectively. Although fluid mud deposition is almost entirely restricted to slack-water periods, neither does it occur at the same locations during every slack tide nor does it cover the entire TMZ at any particular time. These findings need to be considered when interpreting single-point measurements.

- Due to the patchiness and rapid deposition and resuspension of fluid mud, one-off seabed mapping surveys in estuaries with highly dynamic TMZs may record transient facies, rather than solid bed deposits.
- Despite the almost total resuspension of fluid mud observed at the present study locations in the Weser estuary, indications are that a certain amount of fluid mud consolidates to form thin layers of erosion-resistant mud. This leads to gradual bed accretion at some locations, thereby requiring regular dredging of such navigation channels.

Acknowledgements

The authors would like to thank the team members of Innomar Technology GmbH, Germany for the kind provision of the SES-2000®, for their tremendous efforts to support the study and for their sustained cooperation. The captain and crew of the RV Senckenberg made an excellent job of all the cruises. The assistance of A. Raschke, N. Rötzer-Manken, M. Irmer and M. Wilsenack in the sediment laboratories and in the technical preparation of the cruises is also gratefully acknowledged. We are indebted to the Federal Institute of Hydrology, Koblenz, Germany for kindly providing river-discharge data, and to the local Waterways and Shipping office (WSA) in Bremerhaven for helpful discussion on bathymetric data. Constructive review comments made by K. Schwarzer and one anonymous referee are appreciated. This work was funded by the Deutsche Forschungsgemeinschaft as part of the DFG Research Center Ocean Margins of the University of Bremen RCOM no 0404 and the Senckenberg Institute who provided the ship time.

Chapter 3: Paper II

Tide-driven dynamics of ephemeral fluid mud deposits in troughs of large, subaqueous dunes in an estuarine turbidity zone

M. Becker[1], K. Schrottke[2], A. Bartholomä[3], V. B. Ernstsen[4], C. Winter[1], D. Hebbeln[1]

[1]MARUM, Center for Marine Environmental Sciences, University of Bremen, Germany
[2]Institute of Geosciences, Christian-Albrechts University Kiel, Germany
[3]Senckenberg Institute, Wilhelmshaven, Germany
[4]Department of Geography and Geology, University of Copenhagen, Denmark

Abstract

Based on hydroacoustic measurements, the tidal dynamics of ephemeral fluid mud deposits in troughs of subtidal dunes were investigated in the Weser estuary. Fluid mud was found to consist of a dense suspension of large mud flocs of variable concentration, ranging from 25 g/l below the lutocline to 70 g/l at the river bed, whereas the gelling concentration was close to 70 g/l. Fluid mud deposition correlated with the location of the turbidity maximum zone during slack water. Accumulation of suspended sediment was initially observed 1.2 h before slack water. Fluid mud was formed during slack water and remained in dune troughs for approximately 2 h. Subsequently, fluid mud deposits were rapidly entrained. The entrainment is explained to be induced by advection of strong turbulence and the development of the dune specific turbulent flow field, linked to the onset of flow separation during accelerating currents. During the entrainment phase, flow velocities were strong enough to induce bed load transport, leading to mixing of sand and fluid mud in the dune trough. The deposition of fluid mud in dune troughs is discussed in terms of the formation of mud drapes and the composition of sediments in dune troughs.

3.1 Introduction

Tide-dominated estuaries are complex depositional systems, governed by both fluvial and marine sediment transport processes and often characterised by an abundance of suspended cohesive sediments [*Uncles*, 2002]. In particular, the coexistence and interplay of cohesive and non-cohesive sediments pose a challenge to the investigation of recent environments, as well as to the interpretation of estuarine stratigraphical features, preserved in the sedimentary record [*Dalrymple and Choi*, 2007; *Dyer*, 1995]. Thereby, mud drapes constitute a prominent example, delineating tidal couplets in cross-bedded sands, which are interpreted as slack water deposits embedded during the strong tidal currents, as dunes migrate and mud drapes are buried by lee-side deposition [*Allen*, 1982; *Siegenthaler*, 1982; *Visser*, 1980].

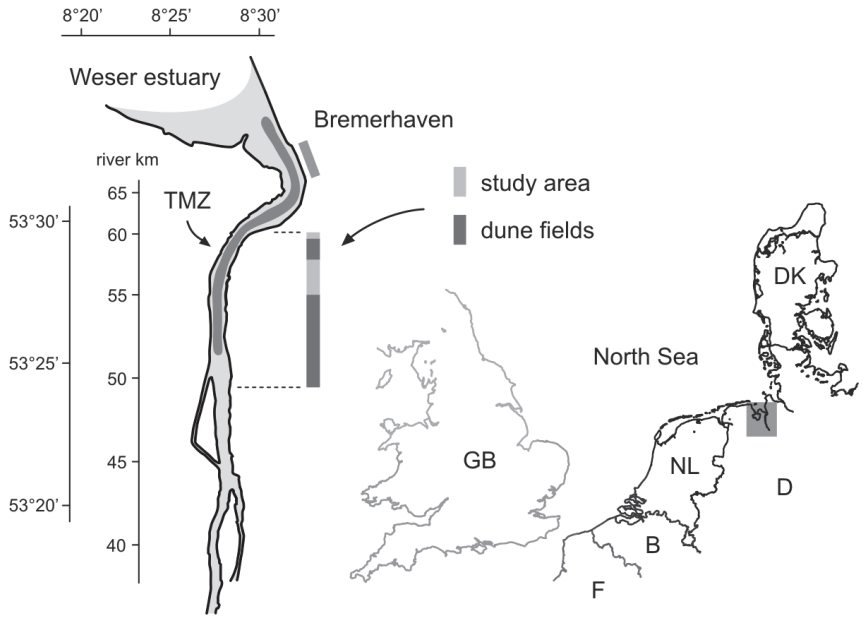

Figure 3.1: Location of the study area along the German North Sea coast. The turbidity maximum zone (TMZ) is shown at its tidally averaged location during conditions of long-term mean freshwater discharge [Grabemann and Krause, 2001]. Longitudinal surveys were conducted between river km 49 and km 61, covering fields of subaqueous dunes. Stationary measurements were located at river km 62.

Slack water deposition of mud in estuaries occurs predominantly in the turbidity maximum zone (TMZ) [*Kirby*, 1988; *Wells*, 1995], which forms at the upstream end of the salt intrusion and is regularly shifted by tidal currents [*Dyer*, 1988; *Prandle*, 2004]. The link between mud drapes and the position of the TMZ was, amongst others, considered by Dalrym-

ple and Choi [2007] and Van den Berg et al. [2007], who discussed thickness and composition of mud drapes in the sedimentary record of estuarine dunes.

Slack water deposition in estuaries is controlled by formation of mud flocs in the water column, resulting in an increase of settling velocities and, accordingly, an increase of the mass settling flux [*Eisma*, 1986; *Manning and Dyer*, 2007]. Settling is substantially hindered as near-bed densities increase [*Mehta*, 1984], accounting for distinct density gradients in the water column [*Kirby and Parker*, 1983; *Vinzon and Mehta*, 2003; *Wolanski et al.*, 1989]. These lutoclines indicate concentrated near-bed suspensions and have been investigated by hydroacoustic methods [*Hamilton et al.*, 1998; *Shi et al.*, 1997].

In concentrated suspensions, an effective strength builds up only as concentrations reach the gelling point and mud flocs form a space-filling network, a state which is generally considered as fluid mud [*Winterwerp*, 2002]. The importance of fluid mud for the estuarine sediment cycle is widely recognized [*Manning et al.*, 2010; *McAnally et al.*, 2007a], whereas fluid mud was studied in recent estuarine environments mainly regarding the formation of estuarine mud deposits [e.g. *Blake et al.*, 2001; *Guan et al.*, 2005; *Sottolichio and Castaing*, 1999; *Uncles et al.*, 2006b]. Fluid mud deposits were also identified as source of particular types of strata, thick mud drapes without sand partings, in sedimentary records of estuarine or deltaic deposits [*Hovikoski et al.*, 2008; *Ichaso and Dalrymple*, 2009; *Shanley et al.*, 1992]. In a recent study, Schrottke et al. [2006, this volume, Chapter 2] documented large, subtidal dunes in the Weser estuary, partly filled with fluid mud during slack water.

In the context of both the formation of mud drapes as well as the interaction with the turbulent flow field in presence of dunes, tide-driven dynamics and formation of fluid mud in dune troughs were rarely investigated. Carling et al. [2006] and Fenies et al. [1999] observed ponds of fluid mud retained in troughs of intertidal dunes in the Severn and the Gironde estuary, respectively, accounting for embedded mud drapes. Based on flume experiments, Sato et al. [2011, hereafter STTM] studied deposition of mud drapes in current ripples, whereas preserved flame structures were ascribed to remnants of fluid mud, buried by sand during accelerating currents. Concerning suspended sediment transport in presence of dunes, investigations focussed on dispersion of non-cohesive sediments [*Kostaschuk*, 2000; *McLean et al.*, 2007], or on the interaction of non-stratified, cohesive sediment suspensions with the dune-specific turbulent flow field [*Baas and Best*, 2008].

On basis of hydroacoustic measurements, the tide-driven dynamics of ephemeral fluid mud deposits in troughs of subtidal dunes in the Weser estuary are investigated (Figure 3.1). Thereby, the term “fluid mud” is used to describe concentrated near-bed suspensions at or beyond the gelling concentration; and the term “SSC” (suspended sediment concentration) solely refers to concentrations in the water column, not in concentrated near-bed suspension layers.

3.2 Study area

The Weser estuary is located at the North Sea coast of Germany between the Jade Bay and the Elbe estuary (Figure 3.1). Tides are semidiurnal with a mean tidal range of 3.5 m at Bremerhaven, varying by about 1 m between spring and neap tides. The hydrodynamic regime is ebb-dominated with mean depth averaged current velocities of 1.3 m/s. The mean annual freshwater discharge amounts to 327 m^3/s [*Deutsches Gewässerkundliches Jahrbuch*, 2005]. The water column is well mixed, whereas slight stratification occurs during flood, neap tides, and times of high river discharge [*Grabemann and Krause*, 1989; *Malcherek*, 1995].

Suspended sediment concentrations (SSC) in the turbidity maximum zone (TMZ) of the Weser vary between 0.1 g/l and 2 g/l [*Lüneburg et al.*, 1974]. The TMZ covers a river stretch of 15 km to 20 km with a tidal displacement of approximately 15 km. Its specific location between Brake (km 41) and Bremerhaven (km 68) depends on river discharge and coincides with the low-salinity reach [*Grabemann and Krause*, 2001].

Sediment trapping in the estuary is caused by the combined effects of tidal asymmetry and residual circulation [*Burchard and Baumert*, 1998; *Malcherek*, 1995]. The vertical distribution of suspended sediments varies during a tidal cycle and is controlled by turbulent mixing during periods of strong tidal currents and settling during slack water [*Lang et al.*, 1989; *Riethmüller et al.*, 1988]. According to Wellershaus [1981], fluid mud layers form during slack water at the river bed with concentrations up to 70 g/l.

The navigation depth below chart datum is 9 m upstream and 14 m downstream of Bremerhaven. Morphology and surface sediments are highly variable [*Schrottke et al.*, 2006], whereas subaqueous dunes are predominantly located upstream of km 55 and form on sandy beds, consisting of fine to medium sand [*Nasner*, 1974]. North of km 55, the bed is mainly flat with surface sediments alternating between clay drapes and sandy areas. Accumulation of

mud occurs south of Bremerhaven in the centre of the TMZ and in deeper parts of the navigation channel along the extent of the TMZ [*Riethmüller et al.*, 1988; *Schrottke et al.*, 2006].

3.3 Methods

3.3.1 Surveys and instruments

Hydroacoustic data were collected in terms of time series of longitudinal transects in the navigation channel during ship-based surveys in the Weser estuary (Table 3.1). Transects were collected on both sides of the river with a mean cross-channel distance between 130 m and 180 m. The study area covered the stretch between river km 49 and km 61 (Figure 3.1). Current velocities were recorded by means of a down-looking 1.2 MHz ADCP (Workhorse, TRDI) with a cell size configuration of 0.25 m and ping rates varying between 2.4 s to 3.8 s. ADCP data were collected in mode 1 without internal averaging. According to deployment depth and blanking distance the first measuring point was located 1.8 m below the surface.

Table 3.1: Survey overview. Freshwater discharge was provided by the Federal Institute of Hydrology (Koblenz, Germany).

survey	*date*	*river km*	*slack water*	*discharge*	*lunar phase*
I-A	*2004 Jun 15*	*50 - 54*	*flood*	*212 m^3/s*	*spring –3d*
I-B	*2004 Jun 16*	*49 - 53*	*flood*		*spring –2d*
II-A	*2004 Dec 07*	*59 - 61*	*ebb*	*298 m^3/s*	*neap +1d*
II-B	*2004 Dec 09*	*50 - 53*	*flood*		*neap +3d*
III-A	*2005 Apr 07*	*48 - 54*	*flood*	*347 m^3/s*	*spring –2d*
III-B	*2005 Apr 12*	*50 - 56*	*flood*		*spring +2d*
IV-A	*2005 Jul 05*	*49 - 54*	*flood*		*spring –2d*
IV-B	*2005 Jul 06*	*49 - 53*	*flood*	*145 m^3/s*	*spring –1d*
IV-C	*2005 Jul 07*	*49 - 53*	*flood*		*spring*

A parametric sediment echo sounder (SES-2000® Standard, Innomar Technology; hereafter referred to as SES) was deployed to detect vertical near-bed density gradients in the water column with a high vertical resolution (~0.06 m). The SES operates on a primary frequency of 100 kHz. A secondary frequency of 12 kHz was selected for all surveys. Profiles were generated from SES raw data with the ISE acquisition and post-processing software, distributed by Innomar. A detailed description of the SES is presented by Schrottke et al. [2006].

Further steps regarding the processing of SES profiles and ADCP data were implemented in MATLAB™ (The MathWorks).

The water column close to the river bed was sampled using a Rumohr-type gravity coring device [*Meischner and Rumohr*, 1974], equipped with transparent Perspex core barrels of 2 m length. Water samples were extracted in down-core steps of 0.1 m immediately after recovery. To determine near-bed profiles of sediment concentration each sample volume was filtered and the filters dried and weighed.

3.3.1.1 Current velocity correction

Challenged by the instrument's specific alignment and variable river bed conditions, raw velocities measured by the ADCP were corrected for ship speed and heading. The internal compass of the ADCP was biased due to its on-board deployment close to the engine. The error was depending on ship speed, precluding correction via a deviation table. In addition, bottom track velocities were partially invalid and obviously influenced by mobile bed sediments, causing a negative bias of corrected current velocities [*Mueller and Wagner*, 2007]. The navigation (GPS) based ship velocity was not directly applicable, as the deviation of heading angles between coordinate systems caused significant errors in corrected current velocities [*Trump and Marmorino*, 1997].

To compensate heading bias and bottom track velocity errors, two correction steps were performed. First, invalid bottom track velocities were linearly interpolated, assuming steady ship velocity for the duration and corresponding number of invalid ensembles. Next, the relationship of navigation to bottom track based ship velocity was used to correct the potentially biased bottom track east and north velocity components, which were then applied during the moving platform correction [*RD Instruments*, 2008]. Whereas current velocity magnitude is thereby correctly determined, velocity vectors are still aligned with respect to the biased compass heading. The analysis was based on velocity magnitude and further corrections concerning velocity direction were not required.

3.3.2 Morphology and density gradients

Distinct vertical density gradients between the upper water column and higher concentrated near-bed suspension layers are clearly visible in SES profiles. Schrottke et al. [2006] correlated a relatively strong acoustic reflector with an increase of concentration from 0.3 g/l to 27 g/l, measured at slack water between two adjacent sampling positions along the core

barrel. Subsequently, density gradients observed in SES profiles are referred to as lutoclines. Focussing on suspension layers in dune troughs, a trough was considered for the analysis if the associated lutocline was located at a height of at least 0.3 m above the bed and spatially covered more than 15 m transect length.

The vertical position of current velocity measurements with respect to the river bed was determined using the ADCP bottom track range. Taking into account that bed form crests were oriented predominantly perpendicular to the main channel, the morphology was governed by small scale surface gradients in longitudinal direction. Consequently, bottom track ranges of transverse directed beams were averaged (beam 1, port side, and beam 2, bow side), and a good correlation was found with the uppermost sediment surface in SES profiles. In presence of near-bed suspensions the bottom track range either indicated the level of the lutocline, or was invalid and manually corrected with respect to corresponding SES profiles (Figure 3.2, a).

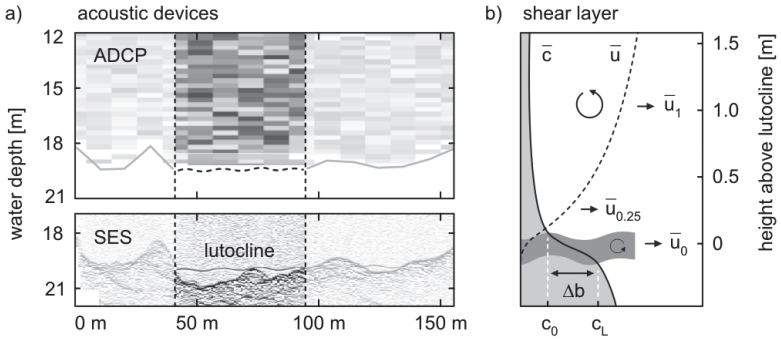

Figure 3.2 a: Configuration of measurements in dune troughs. ADCP and SES profiles are shown in the upper and lower panel, respectively. The dashed part of the bottom line in the ADCP profile indicates bad bottom track range manually adjusted with respect to the SES profile. Hydrodynamic parameters are calculated for the spatial extent of lutoclines, as observed in SES profiles. b: In presence of the density gradient an interfacial shear layer develops under hydrodynamic forcing, whereas the lutocline marks the highest local vertical density gradient. The water column is turbulent; the suspension layer below is stationary. Overlined symbols indicate spatially averaged parameters. Vertical profiles of concentration and velocity are marked by $\bar{c}$ and $\bar{u}$, respectively. Further explanation concerning the parameterisation of the interfacial shear layer is given in the text.

The identification of bedform dimensions from in-situ bed elevation data has been addressed by e.g. van der Mark et al. [2008], van Dijk et al. [2008] and also Ernstsen et al. [2009], who required precise measurements for the analysis of small-scale, short-term mor-

phodynamics. This study is concerned with suspended sediment transport processes; and large dunes, although they are the most prominent features within the study area, are solely regarded as part of the given bathymetry. To obtain characteristic dune dimensions, the bed elevation was manually derived from SES profiles with sufficient accuracy.

Average values were based on the complete SES data base, collected between river km 47 and km 60 during the surveys. Dune length was determined as the distance between the deepest points of two consecutive troughs. Dune height was considered as the vertical distance between the maximum elevation at the dune crest and the deepest point of the lee-side trough. The lee-side angle was measured with respect to the slope of the steepest part of the lee-side. Subsequently, the terms “lee-side” and “stoss-side” are used in a geometrical sense with respect to the main dune direction, also if the tidal flow is oppositely oriented.

3.3.3 Shear stress, stability, and entrainment

Hydrodynamic parameters of each dune trough were based on ADCP ensembles located within the extent of the detected lutocline (Figure 3.2, a). Each trough was represented by a limited number of ADCP ensembles (<10), corresponding to a short duration of measurements that was far below the integral time scale of the flow (~10 min in a tidal environment, e.g. Soulsby [1980]). Values representing a single trough are thus expected to be not only influenced by Doppler noise but also by local turbulence. Measurements from dune troughs were used also in absence of lutoclines. These locations were only considered if lutoclines were observed in the specific dune trough during the time series of transects. Provided that measurements covered the corresponding parts of the tidal cycle, the last empty trough before slack water and, accordingly, the first empty trough after slack water were taken into account. In this case hydrodynamic parameters were calculated with respect to the consolidated river bed.

Following the spatial-averaging approach of Smith and McLean [1977], current velocity measurements were averaged along lines of constant height above the bed. If a lutocline was observed, the corresponding acoustic reflector was used as lower boundary. Starting at a height of 0.25 m above the boundary, individual ADCP ensembles were linearly interpolated in steps of 0.05 m and spatially averaged.

Velocity magnitude was calculated from velocity components that were interpolated and averaged individually. Subsequently, overlined symbols indicate spatially averaged parameter. Shear stress was assumed to be invariant of height close to the boundary and current ve-

locities to be logarithmically distributed. The shear velocity u_* was determined by fitting measured current velocities to logarithmic profiles (least-squares) and applying the von Kármán-Prandtl equation

$$\frac{d\bar{u}}{dz} = \frac{1}{\kappa}\frac{u_*}{z} \tag{3.6}$$

where $\bar{u}$ is the current velocity at height z above the river bed and κ is von Kármán's constant ($\kappa = 0.4$). The shear stress τ was calculated by $\tau = \rho u_*^2$, where ρ is the water density.

If the flow is oriented in dune direction, spatially averaged vertical velocity profiles over bed forms have been found to consist of two or more log-linear segments [*Chriss and Caldwell*, 1982; *Smith and McLean*, 1977], whereas the first segment above the bed is considered to be influenced by grain roughness only. Spatially averaged velocity profiles from several laboratory experiments with fixed dune-shaped roughness elements indicate the first kink in the profile, i.e. the lower boundary of the influence of form drag, at a vertical position comparable to one dune height [*McLean et al.*, 2008].

The extent of the first segment unaffected by form drag was thus confined at a height of 1.5 m, less than the average dune height in the study area and located within the lower 20% of the water column, where the log-law usually applies under zero-pressure-gradient conditions [*Nezu and Nakagawa*, 1993]. However, due to the specific position of lutoclines in dune troughs, shear stress and shear velocity may be influenced by local pressure gradients, which is discussed in Section 3.5. As exposed to velocity shear, lutoclines represent stratified interfacial shear layers, governed by vertical differences of velocity and buoyancy. The stability of associated density gradients is assessed by the gradient Richardson number Ri_g, relating the buoyancy gradient to the velocity shear (Figure 3.2, b). Shear induced disturbances are dampened for values of $Ri_g \geq 0.25$ and the density gradient is considered stable [*Fernando*, 1991; *Miles*, 1961]. Gradient Richardson numbers were frequently used to analyse the stability of lutoclines [*Jiang and Mehta*, 2002; *Wolanski et al.*, 1989]. In case of stationary near-bed suspension layers, trapped between two adjacent dunes, the time averaged velocity below the lutocline is zero.

Using the lowest available spatially averaged current velocity at the height h of 0.25 m above the lutocline ($\bar{u}_{0.25}$), the average gradient Richardson number ($\overline{Ri}_g$) reads

$$\overline{Ri}_g = -h\,\Delta b / \bar{u}_h^2 = -(0.25\,m)\,\Delta b / \bar{u}_{0.25}^2 \tag{3.7}$$

where Δb is the buoyancy difference. The buoyancy difference is calculated by

$$\Delta b = g\left(\rho_0 - \rho_L\right)/\rho_0 \tag{3.8}$$

in which g is the acceleration due to gravity and ρ_0 and ρ_L are densities above and below the lutocline, respectively, depending on sediment concentrations c_0 and c_L (Figure 3.2, b).

Entrainment rates were calculated according to Kranenburg and Winterwerp [1997], who derived an entrainment function for fluid mud from the vertical balance of turbulent kinetic energy, whereas the entrainment rate u_e is expressed in terms of the shear velocity. Neglecting viscous effects ($\overline{u}_0 = 0$), the entrainment function reads

$$u_e/u_* = \left(0.5/\left(5.6 + Ri_b\right)\right)^{0.5} \tag{3.9}$$

with the bulk Richardson number

$$Ri_b = H\,\Delta b/u_* \tag{3.10}$$

where H is the water depth.

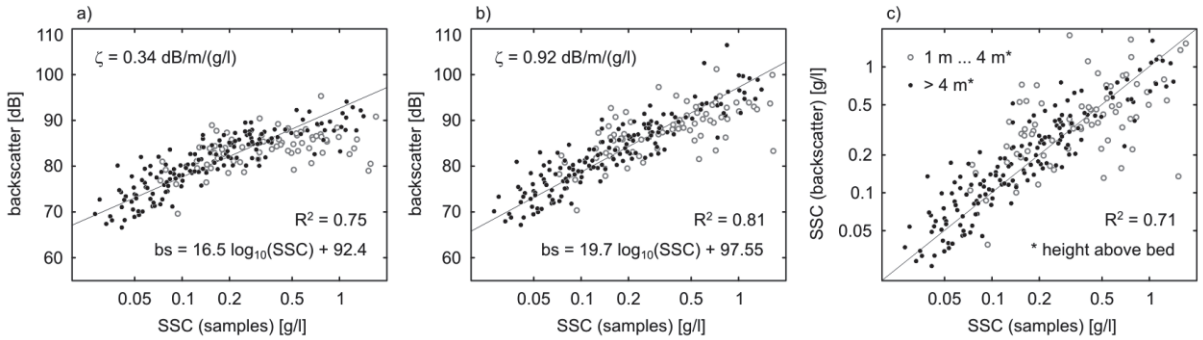

Figure 3.3: Calibration of backscatter with respect to SSC. Black dots indicate samples collected between the surface and 4 m above the river bed. Grey circles indicate samples collected between 1 m and 4 m above the river bed. a: Calibration using the presumed particle diameter of 15 µm. b: Improved calibration with increased sediment attenuation. c: Backscatter based SSC compared to SSC derived from water samples.

3.3.4 Suspended sediment concentration

ADCP backscatter was calibrated with respect to suspended sediment concentration (SSC). Water samples were collected during stationary measurements at river km 62. The mean water depth was 11.5 m. As a result of the tidal TMZ displacement, SSCs were relatively low during flood and high during ebb, accounting for a significant range of SSCs (Figure 3.3). Backscatter calibration facilitates the extrapolation of SSC point measurements to the temporal and spatial range of profiling devices, and was applied frequently during the past years [*Gartner*, 2004; *Hill et al.*, 2003; *Hoitink and Hoekstra*, 2005; *Kostaschuk et al.*,

2005]. Thereby, the quality of the calibration depends predominantly on the compensation of absorption effects in the water column. The water absorption coefficient was determined using the empirical relationship of Ainslie and McColm [1998]. Attenuation due to suspended sediment was calculated by

$$\alpha_s = \int_0^R \varsigma \, SSC(r)\, dr \tag{3.11}$$

in which r is the distance from the transducer and ζ is the sediment attenuation coefficient.

In general, the calibration is performed in order to calculate SSC profiles, which are, in turn, necessary to correct backscatter for sediment attenuation. This is solved by an iterative procedure described by Thorne et al. [1994] and applied by Holdaway et al. [1999] to single-frequency hydroacoustic data.

Accordingly, in the first step backscatter was corrected for sediment attenuation, which was estimated by the average concentration derived from water samples. Based on the resulting calibration, SSC profiles were determined in order to calculate sediment attenuation, which were applied in the next iterative step. The iteration was continued until the correlation, with respect to R^2, did not further improve. Depending on the sediment attenuation coefficient, convergent solutions were obtained after 6 to 12 steps, which is in accordance with Holdaway et al. [1999]. Following Urick [1948], the sediment attenuation coefficient ζ depends on the particle size. Suspended particles in the Weser TMZ consist of clay, silt, and a small fraction of fine sand [*Wellershaus*, 1981]. A representative particle diameter of 15 µm was presumed. Taking into account the theoretical linear relationship between backscatter and logarithm of SSC, results indicate that high backscatter values were underestimated (Figure 3.3, a). The corresponding samples were predominantly collected in the lower part of the water column. Since the influence of sediment attenuation on backscatter increases with distance from the transducer, the underestimation was ascribed to an insufficient correction of sediment attenuation. Therefore, the attenuation coefficient was successively increased, optimizing the correlation between sampled SSC and calibrated backscatter (Figure 3.3, b).

Exceptionally high SSCs were measured close to the bed, which is attributed to effects of bedload and changes in particle size. At an acoustic frequency of 1.2 MHz the sensitivity of backscatter increases with particle size for grains up to 400 µm in diameter and the acoustic signal was potentially biased near the river bed by suspended sand particles. Depth averaged SSCs for each dune trough were determined by averaging corresponding SSC profiles,

whereas data located below 1.5 m above the bed was omitted to eliminate the influence of near-bed particle size variations.

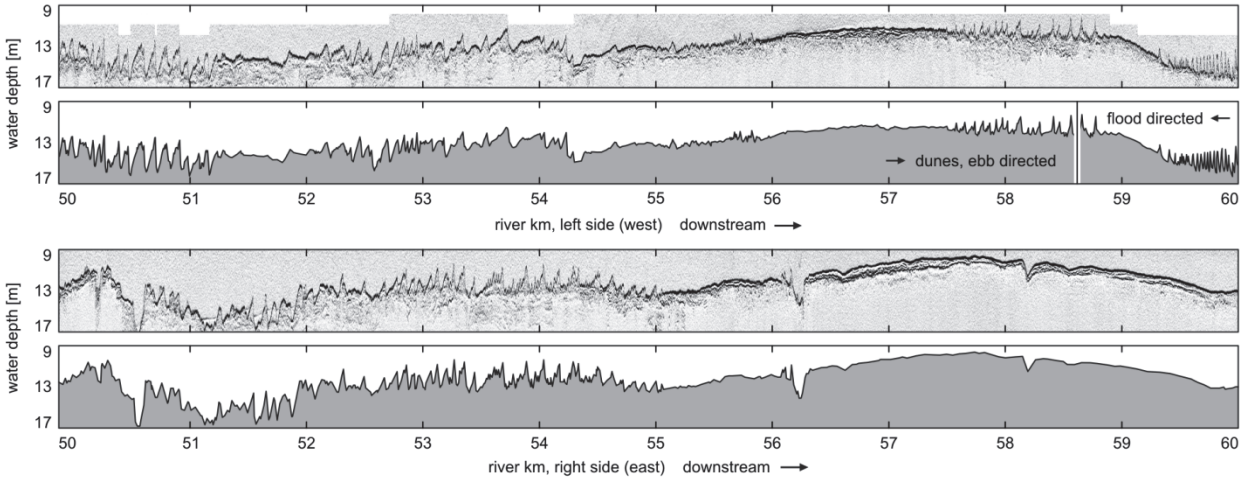

Figure 3.4: Morphology and bed elevation profiles obtained from SES images. Data was collected during survey I-B. The distribution of subaqueous dunes is shown between river km 50 and km 60. Dunes are predominantly ebb-directed. Flood-directed dunes are observed on the left channel side, as indicated in the bed elevation profile.

3.4 Observations

3.4.1 Dune dimensions

Dune dimensions were obtained from bed elevation profiles, based on SES images (Figure 3.4). The river bed upstream of river km 55 was covered by large, asymmetric, ebb-directed dunes. An average dune length of 58 m was determined. The average dune height was 2.4 m, and the lee-side angle was 18°. Flood-directed dunes were found only on the left side of the navigation channel downstream of km 58. Average dune length, dune height and lee-side angle were 38 m, 1.7 m, and 19°, respectively. The distribution of dunes varied between the left and the right side of the channel, whereas individual dunes are hardly recognized on both channel sides. It is noted that sharp and round crests were observed, as well as partly dredged dunes, contributing to the overall variability of dune shapes.

3.4.2 Suspension layers in dune troughs

Corresponding to sites at which lutoclines were observed in dune fields, three cores were collected during survey II-A and II-B (Figure 3.5, core locations are indicated in Figure 3.7). Concentrations above the lutocline ranged from 0.3 g/l to 0.5 g/l. All cores showed a trend of

concentrations to increase down-core with maximum values of 27 g/l below the lutocline and 70 g/l at the consolidated bed, measured in core R2. R1 and R2 were taken during slack water. R3 was taken 1.3 h after slack water.

As observed in the transparent core barrels of all cores, the upper part of the suspension layer below the lutocline consisted of a suspension of mud flocs, which formed a dense network in the lower part of the core near the river bed. The maximum floc size was approximately 2.5 mm. The transition from floc suspension to floc network was smooth and a specific boundary was not determined. The first significant down-core increase of sediment concentration was found to correspond to the lutocline, as observed in SES profiles.

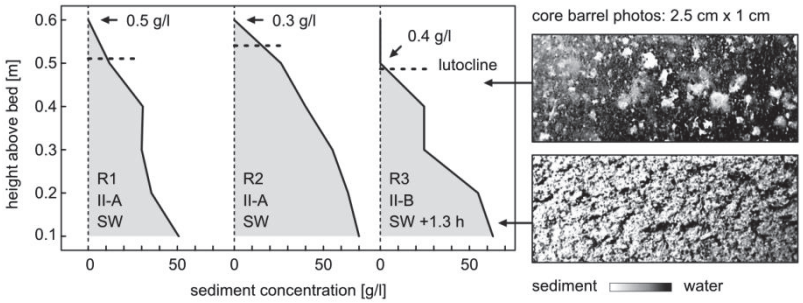

Figure 3.5: Vertical distribution of sediment concentration below the lutocline with respect to height above the bed. Core numbers and survey numbers refer to Figure 3.7. Note that all cores were taken at different locations. Vertical dashed lines indicate lutoclines observed in SES profiles. Photos of the transparent core barrels show the consistency of the mud-water-mixture, namely a suspension of mud flocs below the lutocline and a dense network of flocs close to the river bed. The gray scale of the photo below the lutocline was inverted for better visibility; the photo was taken without flash and mud flocs appeared dark, originally.

Lutoclines were identified by the respective acoustic reflector in SES profiles. During the tidal cycle different appearances of lutoclines were observed (Figure 3.6). Before slack water lutoclines were flat or inclined with positive slope in current direction (Plot 1). The corresponding acoustic reflector was relatively weak.

Flat lutoclines were recorded during slack water, indicated by a relatively strong reflector (Plot 2a). Lutoclines of inclined shape were observed after slack water, reaching a maximum vertical offset of 0.4 m (Plot 2b and 2c). After slack water lutoclines appeared perturbed or interrupted, associated with relatively weak reflectors (Plot 3b, 4, and 5).

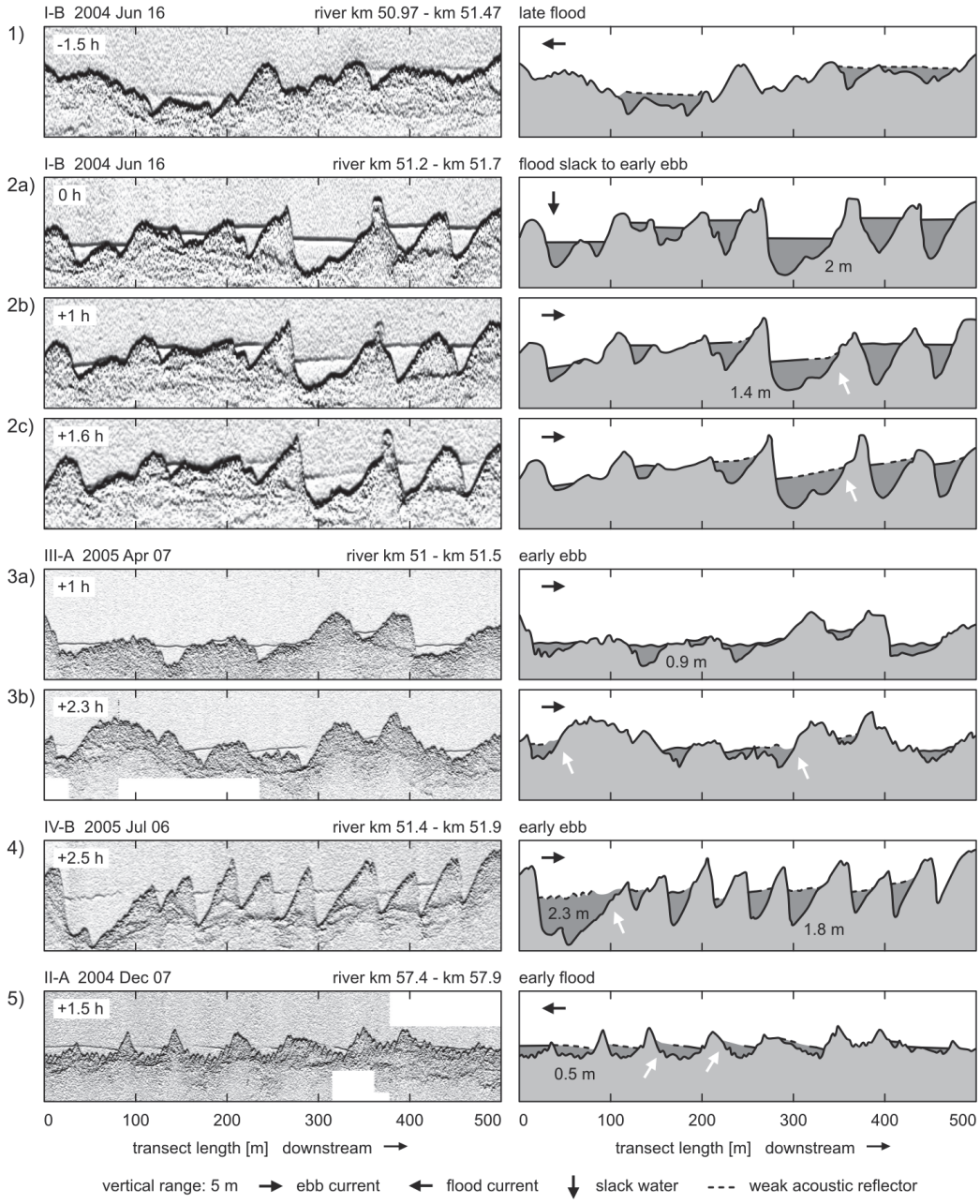

Figure 3.6: Different shapes of lutoclines, observed during the tidal cycle. SES profiles are shown with a vertical range of 5 m and a length of 500 m, directed downstream. The aspect ratio is 1:25. Weak acoustic reflectors are indicated by dashed lines. Time is given in terms of hours after slack water. Black arrows indicate tidal currents. Numbers at dune troughs denote the maximum lutocline distance from the bed. All plots depict ebb-directed dunes, except for Plot 5, showing flood-directed dunes. Plot 2a, 2b and 2c present a time series of consecutive transects collected during survey I-B, such as Plot 3a and 3b, collected during survey III-A. White arrows in Plot 2b and 2c indicate lutoclines with an upward slope in current direction. White arrows in Plot 3b, 4 and 5 indicate gaps and perturbations.

In case of interrupted lutoclines, the reflector strength decreased downstream and gaps were observed close to the stoss-side of the adjacent dune. The same shape was also observed in troughs of flood-directed dunes (Plot 5). Whereas flat, inclined, and interrupted or perturbed shapes occurred frequently, symmetrical internal waves were observed only during survey III-A, 1 h after slack water (Plot 3a). In general lutoclines spatially covered 50% to 75% of the dune length. The relative vertical position of lutoclines and the layer thickness varied significantly between adjacent troughs (e.g. Plot 2a). By contrast, the layer thickness of individual deposits did not vary significantly with time between consecutive transects (Plot 2a, 2b, and 2c; Plot 3a and 3b).

All lutoclines observed in dune troughs were classified on the basis of SES images. Their shape was described as flat, inclined or perturbed, whereas inclinations were considered if respective offsets exceeded a vertical distance of 0.15 m. Straight and inclined reflectors with significant gaps were regarded as a kind of perturbed shape.

Lutoclines were further differentiated by the strength of the reflector as a relative measure between consecutive transects of a time series. Six different combinations of lutocline shape and reflector strength were identified, hereafter referred to as lutocline state (Figure 3.7).

Lutoclines, and thus near-bed suspension layers, were observed in troughs of ebb-directed dunes at the end of the flood phase, except for survey II-A, where lutoclines appeared in a field of flood-directed dunes after the ebb phase (see also Figure 3.6, Plot 5). Accordingly, currents were oriented against the dune direction as lutoclines emerged and along the dune direction when lutoclines disappeared. During high water lutoclines were located in an average depth of 16 m. Those observed during survey II-A during low water were located in a depth of 12.5 m. During survey II-A lutoclines were observed between river km 59 and km 61 whereas all other observations of lutoclines were located further upstream between river km 49 and km 54.

3.4.3 Suspended sediment and hydrodynamics

To relate different lutocline states to tidal variations of SSC and shear stress, all parameters were plotted with respect to current velocity ($\overline{u}_1$) measured 1 m above the lower boundary (Figure 3.8, left side). Each data point refers to one dune trough. Irrespective of sediment supply and the position of the TMZ, results from all surveys were combined since the emergence and subsequent disappearance of lutoclines was captured only during two surveys, I-B

and IV-B, and since surveys such as II-A and IV-A exhibited considerable gaps in the time series. Another reason for the combined treatment is, as already described, the large scatter due to Doppler noise and local turbulence.

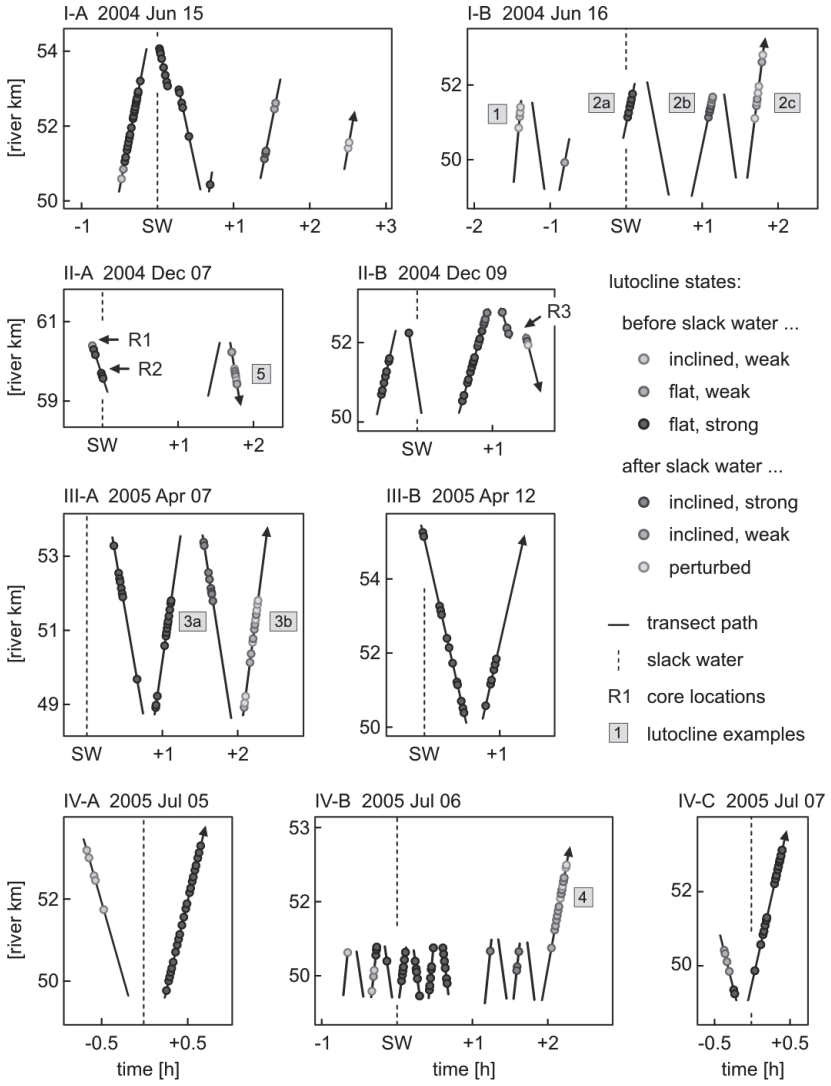

Figure 3.7: Temporal and spatial distribution of lutoclines in dune troughs. Transects are shown with respect to location (river km) and time in terms of hours after slack water (SW). Slack water was defined for each survey according to minimum near-bed current velocity. Each plot refers to one survey. Each row of plots presents surveys conducted during one weak of measurements. Transects are only shown for the time frame between the first and last observation of lutoclines. Transects with a negative slope in the graph are directed upstream, recorded on the left side of the navigation channel. Transects with a positive slope are directed downstream, located on the right channel side. Numbers in boxes refer to plots in Figure 3.6, indicating the location of SES profiles.

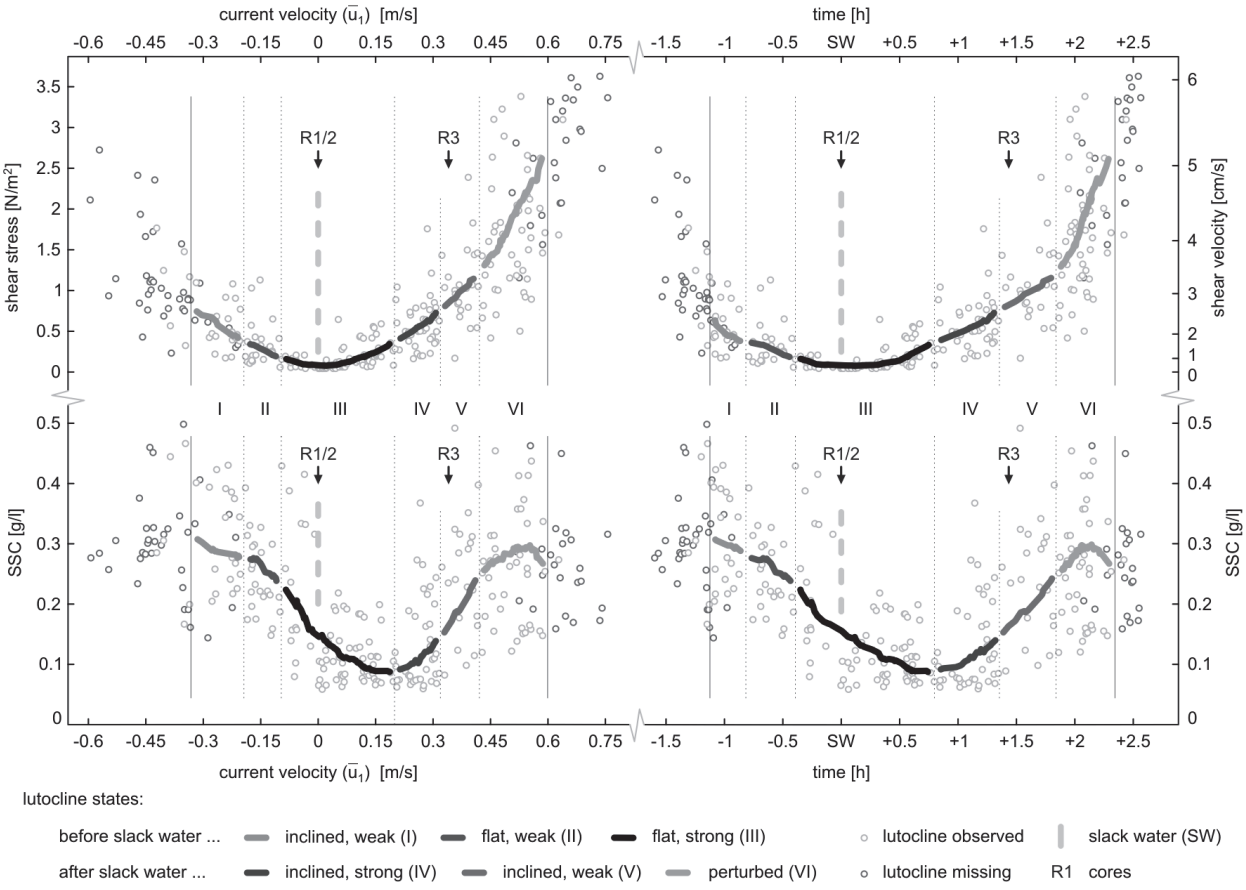

Figure 3.8: Shear stress, shear velocity, and SSC related to current velocity and time in terms of hours after slack water. Velocity is positive after slack water and was measured 1 m above the boundary, i.e. lutocline or river bed. SSC is depth averaged, whereas data below 1.5 m above the boundary was omitted. Gaps in the trend line are introduced to better differentiate between lutocline states, emphasized also by vertical lines. Core numbers are placed according to the near-bed current velocity measured at the sampling location. Further explanation concerning the trend line and the time axis is given in the text.

The main trend was derived by applying a moving average filter with a window size of 0.15 m/s. The resulting trend line shows the distribution of lutocline states, which was defined for each position along the line as the lutocline state encountered most frequently in the velocity range of the corresponding filter window (Figure 3.8, thick line). The same filter was also applied to current velocities close to the bed ($\bar{u}_{0.25}$), which were required to calculate $\overline{Ri}_g$ and referred to in section 3.5. Data was collected during neap as well as spring tide and during both low and mean discharge conditions (Table 3.1). Hydrodynamic parameters and suspended sediment concentrations derived by the aforementioned procedure thus present an average of various environmental conditions.

Measurements were also related to time after slack water. Previously, one specific slack water time was determined for each survey (see Figure 3.7), whereas, from a hydrodynamic point of view, measurements taken in considerable distance along the channel do not match, since the precise time of slack water varies with tidal wave propagation, while its shape and celerity are further influenced by along-channel variations of morphology and cross-section.

Tidal wave propagation also depends on discharge and lunar phase and certainly varied between the weeks of measurements, precluding the direct comparison of different surveys. Therefore, an average relation between near-bed velocity and time after slack water was derived, again based on the complete data set. The relation yields a characteristic time after slack water for each location along the channel according to the specific near-bed velocity (Figure 3.8, right side). Subsequently, results are described on the basis of the filtered data set, referring to the trend line.

Table 3.2: Physical parameters at the beginning of each stage of fluid mud development. C_L is the concentration below the lutocline; values in brackets are estimated. At the beginning of stage II and III C_L is unknown; $\overline{Ri}_g$, Ri_b, and u_e are not calculated. C_L assigned to stage III was obtained from core R2, taken at slack water.

stage	$\overline{u}_{0.25}$ *[m/s]*	$\overline{u}_1$ *[m/s]*	u_* *[cm/s]*	τ *[N/m²]*	*SSC [g/l]*	C_L *[g/l]*	$\overline{Ri}_g$	Ri_b	u_e *[mm/s]*	*lutocline state*
I	*0.15*	*0.33*	*2.5*	*0.75*	*~0.31*	*(>5.3)*	*0.25*	*750*	*0.64*	*inclined, weak*
II	*0.09*	*0.2*	*1.6*	*0.4*	*0.28*					*flat, weak*
III	*0.05*	*0.1*	*1*	*0.2*	*0.23*	*27*				*flat, strong*
IV	*0.09*	*0.2*	*1.6*	*0.4*	*0.08*	*(27)*	*4.6*	*10100*	*0.11*	*inclined, strong*
V	*0.13*	*0.32*	*2.7*	*0.74*	*0.14*	*24*	*2.2*	*3280*	*0.33*	*inclined, weak*
VI	*0.17*	*0.42*	*3.5*	*1.25*	*0.25*	*(24)*	*1.3*	*1950*	*0.56*	*perturbed*
VII	*0.25*	*0.6*	*5.4*	*2.8*	*~0.28*					

Lutoclines were observed during a time period of 3.5 h. On average lutoclines appeared 1.2 h before slack water and disappeared 2.3 h after slack water. The corresponding current velocity threshold ($\overline{u}_1$) of 0.33 m/s before slack water was significantly lower, compared to 0.6 m/s after slack water. This difference was also reflected by thresholds of shear stress, i.e. 0.75 N/m^2 before and 2.8 N/m^2 after slack water.

The emergence of lutoclines correlated with SSCs around 0.31 g/l in the water column, which is comparable to values measured during the last observations of lutoclines, namely 0.28 g/l. The decrease of SSC demonstrated a significant lag, reaching a minimum of 0.08 g/l

only 0.75 h after slack water. It is noted that no considerable decrease of SSC preceded the emergence of lutoclines. Concerning the situation during rising current, the rate of increase of SSC was relatively constant until 1.8 h after slack water, whereas a stagnation of SSCs was observed as lutoclines disappeared.

Observed lutocline shapes correlated with hydrodynamic conditions. The shift from inclined to flat lutoclines and vice versa occurred at current velocities of 0.2 m/s and shear stresses of 0.4 N/m^2, both before and after slack water. The last observation of flat lutoclines, 0.8 h after slack water, concurred with the aforementioned minimum of SSC. Perturbed or interrupted lutoclines were observed not earlier than 1.8 h after slack water at current velocities exceeding 0.42 m/s.

The observed reflector strength exhibited a lag similar to the lag of SSC. Before slack water the reflector strength increased at lower velocities compared to those measured after slack water, as the reflector strength decreased. Threshold velocities were 0.1 m/s before and 0.32 m/s after slack water. Overall, strong reflectors were observed during a considerably long period of time of 1.7 h, between 0.4 h before slack water and 1.3 h after slack water.

3.5 Dynamics of ephemeral fluid mud deposits

Formation and entrainment of ephemeral fluid mud deposits in dune troughs are described in terms of observed lutocline states, current velocity, depth averaged SSC, and vertical concentration profiles obtained from core samples. Each lutocline state is considered as one stage of the development of fluid mud deposits, which are sketched in Figure 3.9. All environmental parameters used are summarised in Table 3.2.

The observed acoustic reflector strength is interpreted to reflect the density gradient between the near-bed suspension and the water column. The density gradient at the lutocline depends both on the overall difference of sediment concentration and on the thickness of the interfacial shear layer, which is controlled by settling properties of particles and small scale mixing due to local turbulence [*Noh and Fernando*, 1991; *Winterwerp et al.*, 2002]. Since concentrations in the water column are relatively low, the density gradient is fully represented by the concentration below the lutocline and was estimated on the basis of core samples, using the first significant down-core increase of sediment concentration (Figure 3.2, b; for concentrations, see also Figure 3.5). Richardson numbers were calculated assuming a concentra-

tion of 0.5 g/l above the lutocline. Furthermore, Richardson numbers are based on filtered current velocities and shear velocities, as presented in the preceding section (3.4.3).

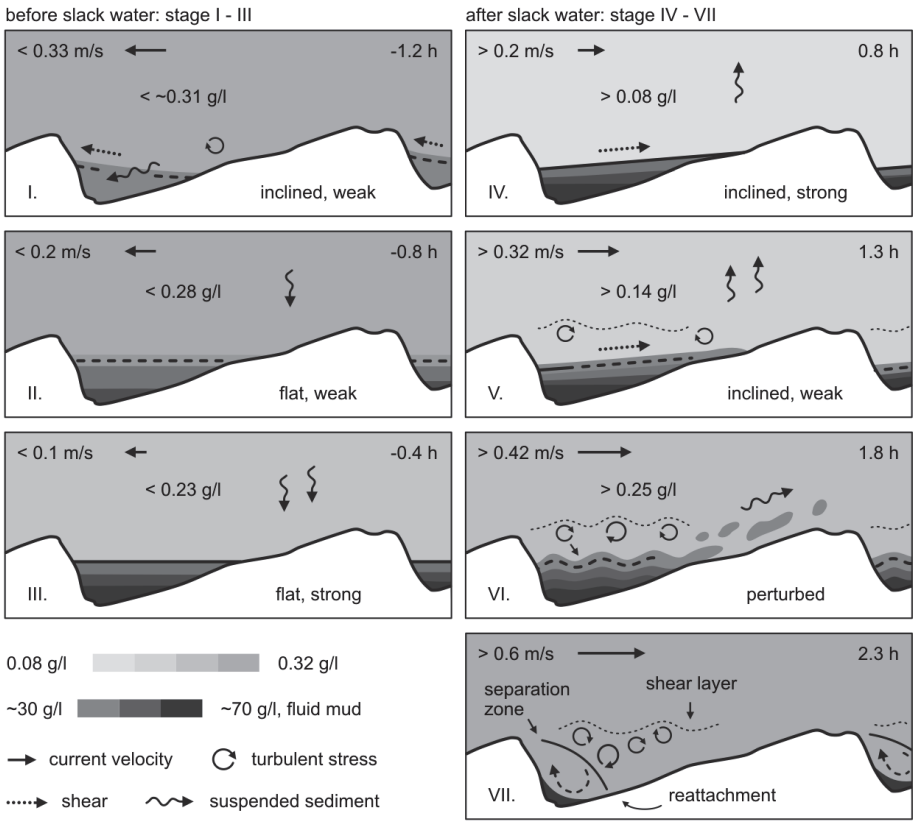

Figure 3.9: Different stages of the development of fluid mud deposits in dune troughs. Dune shape and suspension layer thickness of the example correspond to dunes depicted in Figure 3.6, Plot 4. All stages, except for stage VII, refer to the different lutocline states as observed in SES profiles. Values of current velocity ($\overline{u}_1$) and SSC correspond to the beginning of each stage. Time is given in terms of hours after slack water. Stage I, II, and III show the accumulation of suspended sediment and fluid mud formation during slack water. Stage IV is governed by velocity shear. Stage V depicts the transition from the influence of shear to turbulent entrainment, which occurs during stage VI. The dune specific distribution of currents and turbulence in the lee-side is sketched in the plot of stage VII, with flow oriented in dune direction.

3.5.1 Formation of fluid mud

Stage I of the development of fluid mud deposits was characterised by the initial observation of lutoclines, indicating that suspended sediments accumulated in front of the lee-side of dunes near the river bed during decelerating currents before slack water (Figure 3.9, Stage I). Thereby, the flow was oriented against the dune direction. Near-bed sediment concentrations were not measured and the minimum density gradient to be detected by the SES is unknown.

Irrespective of the actual process of sediment accumulation, a lutocline develops due to the effect of hindered settling, provided that local turbulence is sufficiently reduced. According to the average gradient Richardson number ($\overline{Ri}_g$), an initial sediment concentration of 5.3 g/l was required for stable conditions below the lutocline (see Table 3.2). However, this solely indicates that in presence of lower concentrations a lutocline does not develop under the given forcing.

During stage I lutoclines appeared inclined. Results show that lutocline shapes correlated with shear stress, which indicates that the inclination was caused by shear, acting on the lutocline and forcing the suspension layer up the lee-side of the adjacent dune. According to the observed reflector strength and estimated initial concentration, the overall density gradient was comparatively weak. It is believed that the interfacial shear layer practically reached down to the bed and that the suspension layer was initially turbulent, i.e. flocs were subject to small-scale movements not only at the lutocline, but within the entire suspension layer.

During stage II and III sediment concentrations in the suspension layer increased, taking into account the estimation of the initial concentration of 5.3 g/l and layer averaged sediment concentrations of 27 g/l and 48 g/l below the lutocline, measured in core R1 and R2 at slack water. The transition from stage II to stage III during decelerating currents was marked by a significant increase of reflector strength, indicating an increase of the density gradient and a decrease of the height of the interfacial shear layer. The corresponding decline of turbulence and densification up to the gelling concentration inevitably lead to the formation of fluid mud, as it was observed in core R1 and core R2, where concentrations reached 70 g/l and flocs formed a dense network near the river bed (Figure 3.9, Stage III, see also Figure 3.5).

It is noted that SSCs decreased during stage I, II, and III, and, assuming spatial homogeneity, settling of particles in the water column contributed to the aforementioned increase of sediment concentrations in suspension layers. Adversely, no significant decrease of SSC preceded the initial observation of lutoclines in dune troughs at the beginning of stage I.

3.5.2 Entrainment of fluid mud

After slack water, at the beginning of stage IV, lutoclines appeared inclined (Figure 3.9, stage IV). During accelerating currents the inclination was induced by shear, comparable to stage I, while during stage IV the observed lutocline strength was considerably higher, indicating a relatively strong and steady density gradient. This is confirmed by a comparison of core R2 and R3, where concentrations below the lutocline did not change significantly, vary-

ing between 27 g/l before stage IV and 24 g/l afterwards. During stage IV $\overline{Ri}_g$ decreased from 4.6 to 2.2, suggesting that instabilities were dampened at the lutocline and that fluid mud in the lower part of the deposit remained undisturbed.

Between stage IV and stage V the lutocline strength decreased, indicating a reduced density gradient and an increase of the interfacial shear layer (Figure 3.9, Stage V). This is ascribed to a further increase of velocity shear. Comparing stage IV and stage V, a reduction of the layer thickness was not observed. This is shown by a time series of transects presented in Figure 3.6, where lutoclines in Plots 2a to 2c represent stages III to V and the layer thickness was, besides the increasing inclination, quasi constant. Likewise, $\overline{Ri}_g$ decreased from 2.2 to 1.3, pointing to an overall stable density gradient, and, together with the stable layer thickness, indicates that no entrainment occurred.

$\overline{Ri}_g$ is, however, based on current velocities spatially averaged for the extent of lutoclines and a concentration of 24 g/l, measured in core R3 early during stage V. Regarding the observed inclination, lutoclines most likely protruded into the region of higher velocity shear and increased turbulence, inducing interfacial mixing and an increase of the shear layer at the stoss side of the adjacent dune. This explains variations of reflector strength, which, already low, decreased further in current direction along the fluid mud deposit.

The stability of fluid mud deposits is further shown by a comparison of entrainment rates, determined for the beginning of stage I and the end of stage V. At the beginning of stage I, the entrainment rate was 0.64 mm/s, based on the initial sediment concentration of 5.3 g/l. Stage I was characterised by accumulation of sediments, and any entrainment induced by the turbulent flow field was compensated by settling. Therefore, entrainment is expected to occur if entrainment rates exceed the value determined for the beginning of stage I. At the end of stage V the entrainment rate was still lower, namely 0.56 mm/s, and, provided that settling velocities of flocs at the lutocline did not change, no entrainment occurred during stage V. According to the stability of fluid mud deposits, entrained fluid mud does not contribute to the observed increase of SSC during stage IV and V.

During stage VI perturbations and gaps were observed, not only at the adjacent stoss-side but also along the entire lutocline (Figure 3.9, stage VI). Perturbations resemble interfacial instabilities and gaps show that the local density gradient was too low to be detected by the SES. Since no lutoclines were found at a later point in time, fluid mud deposits were entrained and sediments resuspended. By contrast, based on a concentration of 24 g/l below the luto-

cline, $\overline{Ri}_g$ indicates stable conditions at the beginning of stage VI, which means that local production of turbulence due to shear instabilities alone was insufficient and turbulence of another source was required to induce the observed entrainment. It is suggested that strong turbulence, generated at the dune crest, is advected in direction of the lutocline under the influence of the adverse pressure gradient, which is potentially related to the onset of flow separation. Remarkably, no significant increase of SSC was measured as fluid mud deposits were entrained.

Stage VI covers a time frame of 0.5 h, which means that lutoclines showed signs of entrainment such as gaps or perturbations during this part of the tidal cycle. Depending on layer thickness and the individual shape of dunes, fluid mud deposits are considered to be rapidly entrained at different points in time during stage VI, which is confirmed by the fact that, as already mentioned, along the time series of transects a gradual reduction of layer thickness was not observed. It is further noted that the entrainment of fluid mud concurred with depth averaged current velocities exceeding 0.8 m/s. Taking into account that in the Weser estuary dunes consists of fine to medium sand, it is highly probable that bedload transport already occurred at dune crests at the beginning of stage VI.

3.6 Discussion

3.6.1 Lutocline stability

At the beginning of stage I, lutocline stability is used to estimate the initial concentration below the lutocline on the basis of the local gradient Richardson number. Concerning the transition from unstable to stable conditions, the validity of $Ri_g \geq 0.25$ has been questioned, and local production of turbulence due to shear instabilities was found to occur up to $Ri_g \sim 1$ [*Balsley et al.*, 2008; *Stull*, 1993]. Also, since turbulence was not only locally produced but also advected, the initial concentration was most probably higher than 5.3 g/l, in order to resist the erosion potential of the turbulent flow.

Winterwerp [2002] expressed the settling velocity in terms of the gelling concentration and showed that settling velocities decreased for concentrations exceeding 3 g/l for a range of gelling concentrations between 40 g/l and 120 g/l. In the core barrels mud flocs formed a dense network close to the bed, indicating that the gelling concentration was close to 70 g/l, and that the threshold concentration of the hindered settling regime applies to cohesive sediments of the Weser estuary. This confirms the estimation of the initial concentration of 5.3 g/l

at the beginning of stage I, in the sense that settling velocities are reduced, which promotes the formation of a lutocline. Regarding gelling point and fluid mud concentrations, also Wellershaus [1981] states 70 g/l as a typical concentration of near-bed suspensions deposited during slack water in the Weser estuary.

It was argued that no entrainment occurred during stage IV and V, based on a comparison of entrainment rates, scaling with the bulk Richardson number. This comparison is influenced by the initial concentration below the lutocline. It is noted that the entrainment rate at the end of stage V was still lower than the corresponding entrainment rate at the beginning of stage I for initial concentrations up to 7.2 g/l.

At the end of stage V, the adverse pressure gradient in the lee-side of the dune crest has so far been neglected. Dunes were filled only partly by fluid mud and a negative step between 0.5 m and 1 m was present. Taking into account the specific position of vertical velocity profiles behind the dune crest, namely the region between 0.25 m and 1.5 m above the lutocline, local pressure gradients probably had a strong influence on vertical velocity profiles at higher current velocities. In case of local deceleration of flow behind the crest, the logarithmic velocity profile is shaped convex upward, and shear velocity and entrainment rates are considerably overestimated [*Dyer*, 1986]. This, in turn, indicates that the actual entrainment rate at the end of stage V was smaller than 0.56 mm/s, which, compared to stage I, confirms that in deed no entrainment occurred during stage V.

Calculating shear velocity, any influence due to suspended sediment stratification was also neglected, which potentially leads to an overestimation of shear velocity [*Dyer*, 1986]. To ignore stratification may be justified as similar SSCs were measured in the water column at the beginning of stage I and the end of stage V (~0.3 g/l), which caused equivalent bias in both situations. Admittedly, SSC was determined omitting the lowest 1.5 m above the boundary and the influence of suspended sediment stratification in this region is unknown.

The lack of entrainment during stage IV and V was further shown by the constant layer thickness. According to Kranenburg and Winterwerp [1997] and Bruens et al. [2002], the layer thickness is reduced during entrainment if the ambient flow is significantly more turbulent than the stationary lower layer, where concentrations are then constant. This is also seen in results from flume experiments, presented by Sato et al. [2011, hereafter STTM], who physically modelled the formation of mud drapes in current ripples. During the entrainment phase, the

thickness of a layer of fluid mud, deposited in the ripple trough, gradually decreased during entrainment. Conclusively, no entrainment occurred during stage IV and stage V.

3.6.2 Turbulence and entrainment

As reviewed by Best et al. [2005a], the turbulent flow field in the lee-side of dunes is governed by the adverse pressure gradient, inducing flow separation, recirculation and the development of a shear layer [*Baas and Best*, 2008; *McLean and Smith*, 1979]. Flow separation depends on the lee-side angle. Best and Kostaschuk [2002] found intermittent flow separation for lee-side angles up to 14°, suggesting permanent flow separation at higher angles. Paarlberg et al. [2009] used 10° as critical minimum lee-side angle for flow separation in their dune evolution model [see also *Wilbers*, 2004]. Both thresholds are exceeded by the measured lee-side angle of 18° in the study area, and the named characteristics of dune related turbulence are expected to control the flow after slack water, when currents are oriented in dune direction.

The position of the shear layer, extending from the crest to the stoss-side of the adjacent dune, is not constant but subject to low-frequency vertical "flapping" motions, induced by large-scale turbulent structures, which are generated at the dune crest and advected downstream [*Nelson et al.*, 1993; *Simpson*, 1989]. This periodic vertical displacement of the shear layer is regarded as one possible mechanism to transport high turbulent kinetic energy towards the lutocline (Figure 3.9, Stage VII).

The generation of large-scale turbulent structures at the dune crest is, in turn, linked to flow separation [*Nelson et al.*, 1993]. Flow separation was, referring to the average lee-side angle of dunes in the study area, shown to occur most likely under present conditions. It is unknown when flow separation starts during accelerating tidal currents and to which degree this may be influenced by the fluid mud deposit.

In general, flow separation is considered to be independent of flow conditions. Paarlberg et al. [2007] parameterised the separation stream line using data from several flume experiments, whereas the lowest Froude number related to flow separation was 0.1, corresponding to an experiment by McLean et al. [1999]. During stage VI, Froude numbers ranged from 0.81 to 1.05, depending on depth averaged current velocities and water depths associated with lutoclines.

This shows that, at least without fluid mud in dune troughs, flow separation occurred most probably under hydrodynamic conditions during stage VI. In case of flow separation in presence of fluid mud, a recirculation cell would be located between the separation point and the lutocline and turbulence advected along the separation stream line towards the lutocline, inducing maximum turbulent bed stresses at or slightly downstream of the reattachment point [*Bennett and Best*, 1995].

Independent of the actual process of advection of turbulence, either advection along a separation stream line or advection due to wake flapping, it is hypothesised that, once that large-scale turbulent structures are generated at the dune crest, each fluid mud deposit is rapidly entrained during accelerating currents. This is further supported by STTM, who found the onset of entrainment of fluid mud in troughs to be related to vortices, shed from the ripple crests during their already mentioned flume experiments.

In fluvial environments in presence of dunes, boils are frequently observed to erupt at the water surface. Boils are related to the advection of large-scale turbulent structures and may carry significant loads of suspended sediments [e.g. *Best*, 2005b]. During accelerating currents in tidal estuaries with sufficient supply of cohesive sediment, entrained fluid mud is suggested as a potential source of the sediment observed within the boil structure.

3.6.3 Suspended sediment dynamics

It was shown that no entrainment occurred until the end of stage V, in turn indicating that concentrations below the lutocline were constant during stage IV and V, whereas an increase of SSC was observed. This could be related to the dispersion of suspended sediment, located within the vertical range of 1.5 m above the lutocline or the river bed, which was omitted calculating depth averaged SSC. Other deposits of fluid mud in locations less sheltered than dune troughs and entrained at an earlier time after slack water potentially contribute to the increase of SSC. Due to lateral dispersion, although less probable, other sources aside from the main channel may play a role, such as adjacent muddy areas located closer to the river banks.

SSC measurements conducted in the TMZ, presented by Riethmüller et al. [1988] and Grabemann and Krause [2001], show that depth averaged values between 0.8 g/l and 0.3 g/l are characteristic not for the centre of the TMZ, but for the upstream end, which is, with respect to the position of the TMZ, in accordance with the observed position of fluid mud deposits (see Figure 3.1 and Figure 3.7).

This inhomogeneity of SSC in the TMZ, together with effects of advection, may further account for measured SSCs before stage I and during stage VI, whereas no significant decrease of SSC preceded the accumulation and no increase of SSC followed the entrainment of fluid mud. Most of the fluid mud deposits were observed after the flood phase between river km 49 and km 54. While the TMZ is shifted upstream during flood, the decrease of SSC due to settling before stage I is potentially compensated by advection of higher concentrated estuarine waters. The opposite effect may occur after slack water during stage VI, where fluid mud is entrained and the increase of SSC due to resuspension of sediments is compensated by downstream advection of lower concentrated riverine waters.

Upstream of river km 54, no fluid mud deposits were observed in dune fields during and after ebb slack water, which is also ascribed to the tidal displacement of the TMZ, namely the downstream shift during the ebb phase and the occurrence of relatively low SSCs upstream of km 54. This supports the general assumption that fluid mud formation, depending on sufficient supply of suspended cohesive sediments, is linked to the slack water position of the TMZ.

3.6.4 Implications for embedding of mud

In a tidal inlet channel, Ernstsen et al. [2007] measured lee-side deposition during the tidal cycle in a field of large, ebb-directed dunes. Dune dimensions and water depth were comparable to the Weser dunes, the only notable difference being the grain size, which was larger than 0.3 mm, compared to circa 0.25 mm in the Weser estuary. During accelerating currents, lee-side deposition initially occurred approximately 2 h after flood slack water at a depth averaged current velocity of 0.7 m/s, coinciding with highest bedload transport rates. In the Weser estuary, depth averaged current velocities exceeded 0.8 m/s at the beginning of stage VI, which indicates, also regarding the smaller grain size, that sand was already eroded at the dune crest and transported as bedload simultaneously to the entrainment of fluid mud. In the aforementioned flume experiments of Sato et al. [2011, hereafter STTM], sand of a grain size of 0.23 mm was eroded from ripple crests and mixed with fluid mud prior to entrainment.

In case of the Weser dunes, sand eroded from the crests would also mix with fluid mud in the dune trough. In the ripple troughs, STTM found a mud layer deposited between bed and fluid mud during the simulated slack water, to which an unspecified grain size distribution was ascribed, reportedly typical for mud drapes as pictured in literature. This layer was pre-

served, accounting for typical flaser bedding structures, whereas fluid mud was, if at all, preserved only in terms of flame structures, embedded by ripple migration during the following tidal phase.

The aforementioned intermediate layer was deposited earlier than fluid mud, indicating higher settling velocities of the corresponding type of suspended cohesive sediment. In the TMZ, mud flocs settle with a velocity in the range of several millimetres per second [e.g. *Van Leussen*, 1988], which was shown for the Weser by Puls et al. [1988]; and it is unlikely that any other fraction of cohesive sediments settles significantly faster. These mud flocs were certainly not present in the STTM experiment. As sediments accumulate in dune troughs, the presence of large estuarine mud flocs is considered to prevent any stratification, since unflocculated silt and probably even very fine sand are potentially incorporated in the floc structure during settling. They do not reach the bed, and thus do not build a separate layer. Therefore, fluid mud induced mud drapes in cross-strata may show a signature differing from mud drapes that were created outside the influence of the TMZ, where flocculation is important.

Fluid mud formed during stage III at slack water and remained undisturbed for at least 2 h, whereas turbulence was dampened at the lutocline. The onset of entrainment at the beginning of stage VI thus confined the time period of consolidation. Concerning self-weight consolidation of flocculated mud, Been and Sills [1981] conducted a settling column experiment under conditions comparable to fluid mud in dune troughs. Starting with a concentration of approximately 100 g/l and height of 1.75 m, after 2 h a layer of 0.1 m in thickness formed at the bed with a concentration exceeding 280 g/l. Accordingly, the formation of a thin, higher concentrated mud layer at the river bed is considered to be highly probable.

This layer may be sufficiently resistant to erosion to survive the initial part of the entrainment phase, and covered by sand as a result of bedload transport and lee-side deposition. If this is not the case, and the fluid mud layer is entirely entrained, the embedding of an intermediate layer is implicitly prevented, in contrast to the results of STTM, since unflocculated silt and very fine sand, as already suggested, were probably incorporated in the floc structure during settling.

Concerning the lower part of the lee-side, Kleinhans [2004] discussed the enrichment by fine sediment due to slack water deposition, depending on SSC in the water column. In the case that sediments form a fluid mud layer during settling, it is evident that the sediment

composition in the trough region is also controlled by the time frame of consolidation, which determines the preservation potential of any higher concentrated layer at the bed.

Not only the time frame of consolidation, but also the embedding of mud due to dune migration depends on local hydrodynamics, which is controlled by the strength of the ordinate tide. To complete the tidal cycle, further mud layers may be formed by slack water deposition after the ordinate tide and further erosion may occur in the trough region during the subordinate tidal current. In the upstream part of the estuary, slack water deposition increases downstream towards the centre of the TMZ, as well as the possibility that deposition occurs during both slack waters.

Adversely, as the fluvial influence is decreased, the tidal current asymmetry changes in favour of the subordinate tide, the influence of which being purely erosive. Inevitably, these counteracting influences lead to a local optimum of the preservation potential of fluid mud induced mud drapes in the cross-strata. The maximum preservation potential of this type of mud drapes is expected to occur somewhere upstream of the centre of the TMZ. As already suggested, fluid mud induced mud drapes may show a different signature compared to mud drapes created outside the TMZ. This is in accordance with Van den Berg et al. [2007], who found mud drapes in the fluvial-tidal transition zone further upstream to "be of a more silty nature as compared with estuarine slack water deposits".

3.7 Conclusions

The dynamics of ephemeral fluid mud deposits in troughs of subtidal dunes were analysed on the basis of a hydroacoustic measurements, collected in the range of the TMZ of the Weser estuary. Different stages of the development of fluid mud were related to environmental parameters, derived from a comprehensive data set, which covered various flow conditions with respect to discharge and lunar phase. The picture of fluid mud dynamics in dune troughs is regarded to be applicable not only to the Weser, but in general to large dunes in the upstream part of estuaries with a pronounced TMZ.

From the results of this study, the following conclusions are drawn:

- In the Weser estuary, fluid mud deposits in dune troughs consist of a dense suspension of large mud flocs of variable concentration, ranging from 25 g/l below the lutocline to 70 g/l at the river bed, where the gelling concentration is reached and mud flocs form a space-filling network.

- Regarding the extent of dune fields considered in this study, sites of fluid mud deposition correlate with the location of the TMZ during slack water. Thereby, fluid mud formation and entrainment is only partly reflected by the distribution of SSCs in the water column.
- Including accumulation and entrainment, the overall maximum residence time of concentrated near-bed suspensions in dune troughs is 3.5 h, which is considerably long, compared to the commonly stated slack water duration of 15 to 30 minutes.
- As fluid mud forms close to slack water, the time frame of consolidation is approximately 2 h, limited by the onset of entrainment. Consolidation of 2 h may lead to the formation of a thin layer of higher concentrated fluid mud, potentially embedded by sand due to lee-side deposition.
- Rapid entrainment correlates with flow separation and the development of the dune-specific turbulent flow field. Entrainment is not induced by break-down of shear instabilities, but by strong turbulent stresses, linked to large-scale turbulent structures, which are produced at the dune crest and advected in direction of the lutocline. Entrainment coincides with bedload transport, which leads to mixing of sand and fluid mud in the dune trough.
- The accumulation of a dense suspension of mud flocs in dune troughs is considered to influence the stratification of sediments deposited before slack water, which in turn effects the composition of sediments potentially embedded after slack water. Fluid mud induced mud drapes in cross-strata may show a signature differing from mud drapes deposited outside the influence of the TMZ.

Acknowledgements

The authors would like to thank the Innomar Technology GmbH, Germany for the kind provision of the SES-2000®. The captain and crew of the RV Senckenberg made an excellent job during the cruises. The Federal Institute of Hydrology, Koblenz, Germany is thanked for providing river-discharge data. This work was funded by the Deutsche Forschungsgemeinschaft as part of the MARUM, Center for Marine Environmental Research. The Senckenberg Institute is thanked for providing the ship time.

Chapter 4: Paper III

Effects of small scale morphology on tide-driven mobile mud dynamics

M. Becker[1], K. Schrottke[2], A. Bartholomä[3], V. B. Ernstsen[4], C. Winter[1], D. Hebbeln[1]

[1]MARUM, Center for Marine Environmental Sciences, University of Bremen, Germany

[2]Institute of Geosciences, Christian-Albrechts University Kiel, Germany

[3]Senckenberg Institute, Wilhelmshaven, Germany

[4]Department of Geography and Geology, University of Copenhagen, Denmark

Abstract

Based of hydroacoustic measurements, the tide-driven dynamics of extended fluid mud layers were investigated in the Weser estuary, North Sea, Germany. In the case that deposition occurs in smooth areas, fluid mud transforms into a mobile mud layer and is dragged by the shear flow. Mobile mud layers are shown to be significantly more resistant to entrainment, compared to fluid mud deposits in troughs large dunes. It is suggested that turbulence, produced at the lower boundary, leads to partial dewatering and consolidation. The mobile mud layer are partly entrained, whereas the entrainment process does not follow the entrainment model of Kranenburg and Winterwerp [1997]. Based on the observation, that mobile mud is partially preserved until the subsequent slack water, semi-diurnal feeding of the mud layer potentially leads to a positive feedback of turbulence damping and consolidation, which inevitably promotes the formation of erosion-resistant estuarine mud. Semi-diurnal slack water deposition occurs in the centre of the TMZ, which explains the correlation between the centre of the TMZ and estuarine mud deposits.

4.1 Introduction

Near-bed accumulations of cohesive particulate matter in the form of high concentrated suspension layers play an important role in estuarine sedimentation processes. The formation

of these layers, generally referred to as “fluid mud”, requires a significant supply of suspended matter; fluid mud is thus found in tidal estuaries in the reach of the estuarine turbidity maxi-mum, the turbidity maximum zone (TMZ).

Fluid mud layers can lead to an apparent reduction of the nautical depth in navigation channels with an impact to ship navigation issues thus being of socio-economic relevance. Fluid mud layers may consolidate under favourable hydrodynamic conditions and form stable deposits of estuarine mud, resulting in enormous expenses for maintenance and dredging.

Based on decade-long measurements in the Severn Estuary and inner Bristol Channel, Kirby and Parker [1983] identified muds as forming settled deposits, stationary suspensions, and mobile suspensions, in accordance with their behavioural characteristics. Thereby, formation of fluid mud is coupled to the spring-neap cycle. Longer slack water and reduced current velocities increase the amount of sediments which settles during slack water and also increase the time frame of consolidation [*Wells*, 1995]. Agitation of stationary mud by waves or excess shear stress may result in a thick, near-bed layer which never consolidates [*Manning et al.*, 2010].

Hydroacoustic measurements were conducted in the TMZ of the Weser estuary in order to analyse fluid mud deposition and the preservation potential of fluid mud layers.

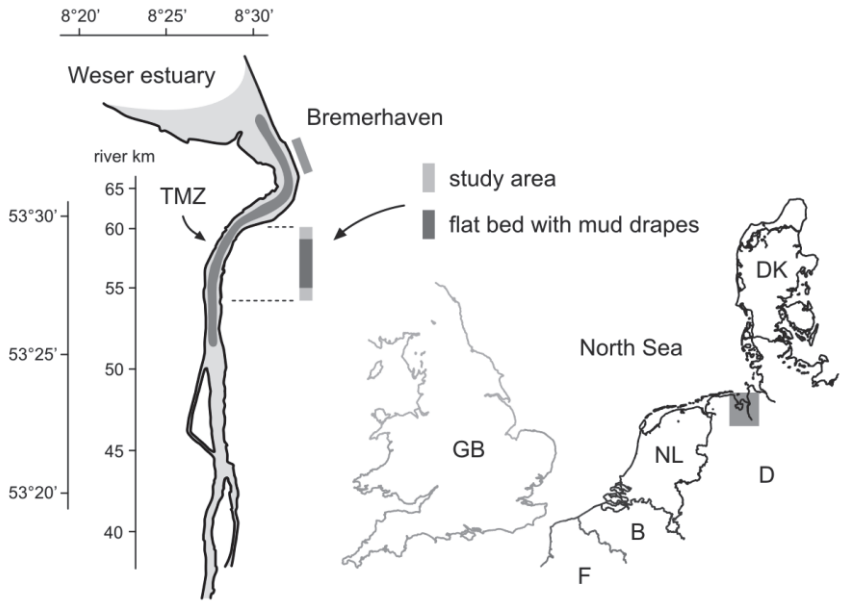

Figure 3.1: Location of the study area along the German North Sea coast. The turbidity maximum zone (TMZ) is shown at its tidally averaged location during conditions of long-term mean freshwater discharge [Grabemann and Krause, 2001]. Longitudinal surveys were conducted between river km 54 and km 60, in predominantly smooth areas.

4.2 Study area

The Weser estuary is located at the North Sea coast of Germany between the Jade Bay and the Elbe estuary (Figure 3.1). Tides are semidiurnal with a mean tidal range of 3.5 m at Bremerhaven, varying by about 1 m between spring and neap tides. The hydrodynamic regime is ebb-dominated with mean depth averaged current velocities of 1.3 m/s. The mean annual freshwater discharge amounts to 327 m^3/s [*Deutsches Gewässerkundliches Jahrbuch*, 2005]. The water column is well mixed, whereas slight stratification occurs during flood, neap tides, and times of high river discharge [*Grabemann and Krause*, 1989; *Malcherek*, 1995].

Suspended sediment concentrations (SSC) in the turbidity maximum zone (TMZ) of the Weser vary between 0.1 g/l and 2 g/l [*Lüneburg et al.*, 1974]. The TMZ covers a river stretch of 15 km to 20 km with a tidal displacement of approximately 15 km. Its specific location between Brake (km 41) and Bremerhaven (km 68) depends on river discharge and coincides with the low-salinity reach [*Grabemann and Krause*, 2001].

Sediment trapping in the estuary is caused by the combined effects of tidal asymmetry and residual circulation [*Burchard and Baumert*, 1998; *Malcherek*, 1995]. The vertical distribution of suspended sediments varies during a tidal cycle and is controlled by turbulent mixing during periods of strong tidal currents and settling during slack water [*Lang et al.*, 1989; *Riethmüller et al.*, 1988]. According to Wellershaus [1981], fluid mud layers form during slack water at the river bed with concentrations up to 70 g/l.

The navigation depth below chart datum is 9 m upstream and 14 m downstream of Bremerhaven. Morphology and surface sediments are highly variable [*Schrottke et al.*, 2006], whereas subaqueous dunes are predominantly located upstream of km 55 and form on sandy beds, consisting of fine to medium sand [*Nasner*, 1974]. North of km 55, the bed is mainly flat with surface sediments alternating between clay drapes and sandy areas. Accumulation of mud occurs south of Bremerhaven in the centre of the TMZ and in deeper parts of the navigation channel along the extent of the TMZ [*Riethmüller et al.*, 1988; *Schrottke et al.*, 2006].

4.3 Methods

4.3.1 Surveys and instruments

Hydroacoustic data were collected in terms of time series of longitudinal transects in the navigation channel during two ship-based surveys in the Weser estuary. Transects were col-

lected on the left channel side on 07 December 2004 and on the right channel side on 05 April 2005. The study area covered the stretch between river km 54 and km 60 (Figure 3.1Figure 3.1). Current velocities were recorded by means of a down-looking 1.2 MHz ADCP (Workhorse, TRDI) with a cell size configuration of 0.25 m and ping rates varying between 2.4 s to 3.8 s. ADCP data were collected in mode 1 without internal averaging. According to deployment depth and blanking distance the first measuring point was located 1.8 m below the surface. Details concerning velocity correction methods are presented in Chapter 3. Current velocity profiles were averaged along lines of constant relative height above the river bed, normalised by the water depth. A characteristic near-bed current velocity was extracted at a height of 1 m above the river bed or the fluid mud surface.

A parametric sediment echo sounder (SES-2000® Standard, Innomar Technology; hereafter referred to as SES) was deployed to detect vertical near-bed density gradients in the water column with a high vertical resolution (~0.06 m). The SES operates on a primary frequency of 100 kHz. A secondary frequency of 12 kHz was selected for all surveys. Profiles were generated from SES raw data with the ISE acquisition and post-processing software, distributed by Innomar. A detailed description of the SES is presented by Schrottke et al. [2006]. Further steps regarding the processing of SES profiles and ADCP data were implemented in MATLAB™ (The MathWorks).

The water column close to the river bed was sampled using a Rumohr-type gravity coring device [*Meischner and Rumohr*, 1974], equipped with transparent Perspex core barrels of 2 m length. Water samples were extracted in down-core steps of 0.1 m immediately after recovery. To determine near-bed profiles of sediment concentration each sample volume was filtered and the filters dried and weighed.

4.3.2 Fluid mud detection

Distinct vertical density gradients between the upper water column and higher concentrated near-bed suspension layers are clearly visible in SES profiles. Schrottke et al. [2006] correlated a relatively strong acoustic reflector with an increase of concentration from 0.3 g/l to 27 g/l, measured at slack water between two adjacent sampling positions along the core barrel. Subsequently, density gradients observed in SES profiles are referred to as lutoclines. Focussing on suspension layers in dune troughs, a trough was considered for the analysis if the associated lutocline was located at a height of at least 0.3 m above the bed and spatially covered more than 15 m transect length.

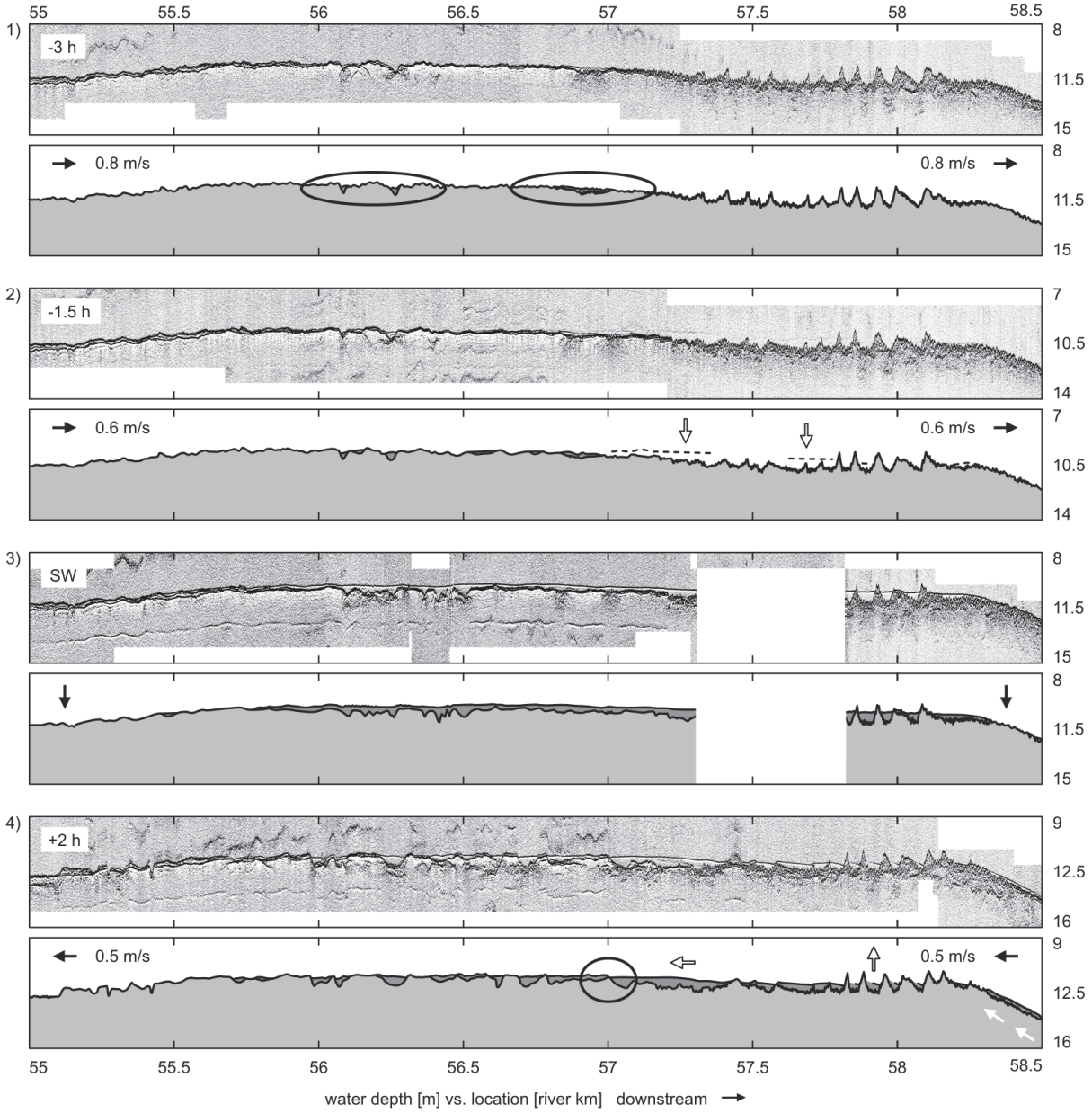

Figure 3.2: SES data and bed elevation profile measured on 07 December 2004; one day after neap tide. The time series depicts slack water deposition both in smooth areas and in a dune field. 2 h after slack water the lutocline in dune troughs shows signs of entrainment, whereas on smooth ground this is not observed.

The vertical position of current velocity measurements with respect to the river bed was determined using the ADCP bottom track range. Taking into account that bed form crests were oriented predominantly perpendicular to the main channel, the morphology was governed by small scale surface gradients in longitudinal direction. Consequently, bottom track ranges of transverse directed beams were averaged (beam 1, port side, and beam 2, bow side), and a good correlation was found with the uppermost sediment surface in SES profiles. In

presence of near-bed suspensions the bottom track range either indicated the level of the lutocline, or was invalid and manually corrected with respect to corresponding SES profiles.

4.4 Observations

Figure 3.2 presents bed elevation profile obtained from SES data on 07 December 2004, measured one day after neap tide. During flood, the time series started 3 h before the ebb slack. Initially, remnants of fluid mud were observed (encircled in Plot 1). A weak reflector indicates deposition of fluid mud 1.5 h before slack water, pointed out by vertical arrows above the river bed (Plot 2). Fluid mud was deposited during slack water both in the dune field and in adjacent smooth areas (Plot 3). Hereafter, the term "smooth" is used to indicate the height of roughness elements in relation to the mud layer thickness. 2 h after slack water the thickness of the fluid mud layer was slightly reduced (Plot 4). The lutocline in dune troughs showed a different appearance compared to the rest of the profile. The reflector strength is reduced, the layer inclined and gaps occur at the stoss-side of the adjacent dune. At km 57 the fluid mud surface meets a local elevation and its height increases slightly in current direction. At km 58.5 a layer emerges at the upstream end, which was absent during slack water.

Figure 3.3 presents bed elevation profile obtained from SES data on 18 April 2005, measured one day after neap tide. During the flood slack water a fluid mud layer was present (Plot 1). 1.5 h after slack water the distribution of fluid mud changed and the layer thickness was reduced (Plot 2). As encircled, a local depression of the river bed is also reflected in the shape of the lutocline (Plot 2 and Plot 3). 2.5 h after slack water the layer thickness was further reduced (Plot 3). 1 h later, only a small part of the bed profile was covered by fluid mud (Plot 4). During the ebb slack water this part was still covered with fluid mud, whereas new deposition was not observed (Plot 5).

4.5 Discussion

Kirby and Parker [1983] found fluid mud formation to be linked to the spring-neap cycle in the Severn Estuary, the formation of fluid mud being enhanced due to longer slack water duration, increased settling of suspended sediments, and overall lower current velocities. The herein presented results were obtained from surveys conducted one and two days after neap tide, respectively.

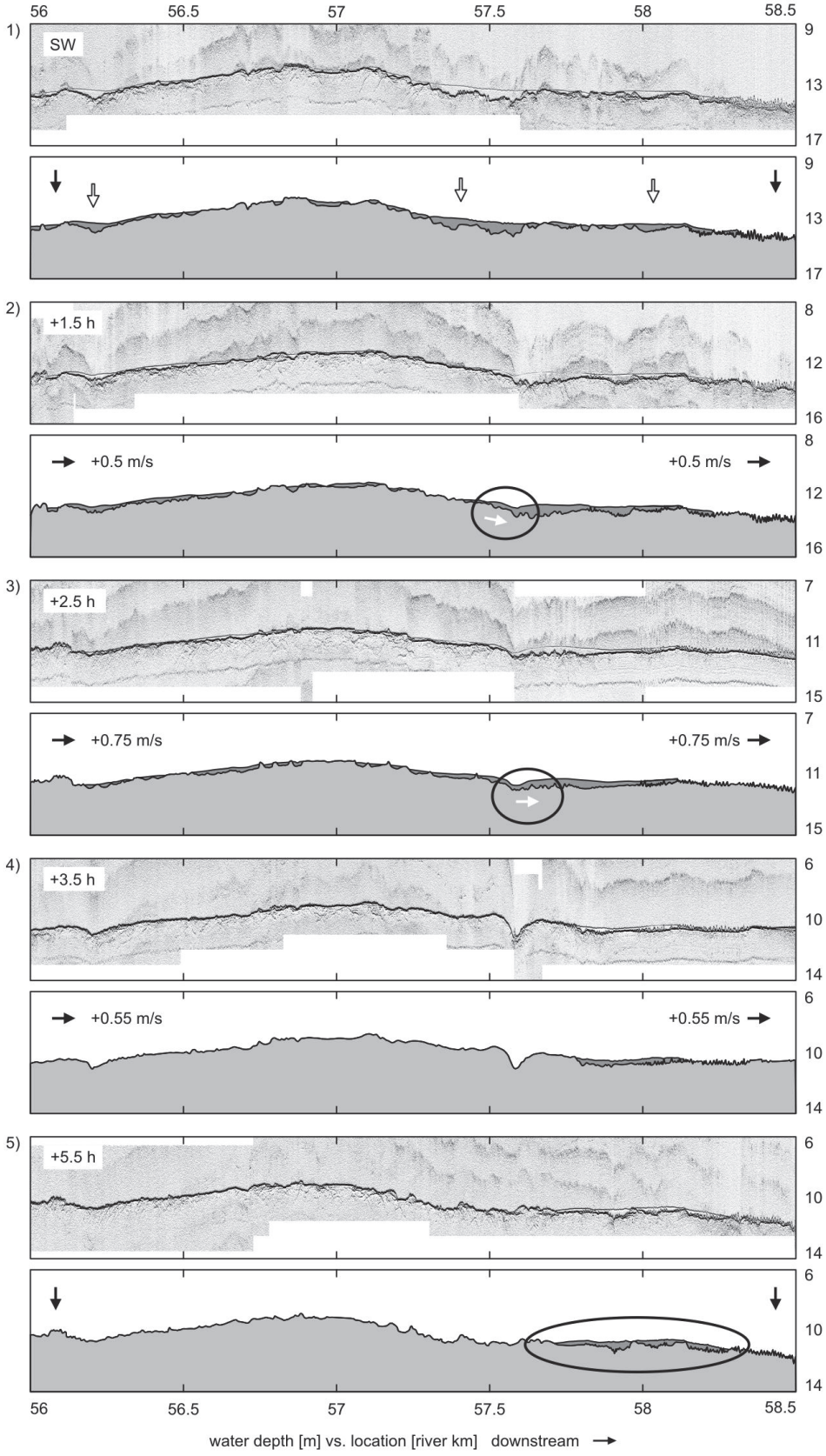

Figure 3.3: SES data and bed elevation profile measured on 18 April 2005; two day after neap tide. During flood slack water a fluid mud layer is present (1). 1.5 h the distribution of fluid mud has changed. As encircled, a local depression of the river bed is also seen in the lutocline

(2). 2.5 h after slack water the layer thickness is slightly reduced (3). Only a small part of the bed profile is covered by fluid mud (4). During the ebb slack water this part is still covered with fluid mud (5). New deposition is not observed.

However, dune troughs were found to be filled with fluid mud also during spring tide (Chapter 3). Obviously, much less suspended sediment is necessary to form an observable fluid mud deposit in a dune trough, compared to deposition in smooth areas. Thus, the observed mud layers are also considered to be linked to hydrodynamic conditions typical for the neap tide, which is supported by Grabemann and Krause [1989], who found SSC increased during spring tide due to higher current velocities.

Furthermore, the increased deposition of suspended matter and thus the formation of fluid mud layers at the particular location is in accordance with results from a numerical modelling study conducted by Malcherek [1995]. Significantly reduced shear velocities were found at river km 58 and ascribed to a local increase of the cross-section in the range of the harbour at Nordenham. Consequently, the model predicted an increase of accumulation of sediments at the corresponding location.

It was suggested in Chapter 3, that fluid mud deposits in dune troughs are rapidly entrained. This was explained by strong turbulent stresses, generated at the dune crest and advected in direction of the lutocline during the onset of flow separation. In the comparison with fluid mud deposited in smooth areas, it is obvious that entrainment in dune troughs occurs much earlier according to higher levels of turbulence.

In smooth areas, fluid mud is potentially dragged by velocity shear and becomes mobile. Encircled parts in Figure 3.2, Plot 4, as well as Figure 3.3, Plot 2 and 3, point to specific shapes of the mud layer, which may reflect the reaction of a creeping or flowing mass to local irregularities. Figure 3.2, Plot 4, shows a thin deposit emerging at the upstream end during flood, indicated by white arrows. As deposition is unlikely at this stage of the tide, this layer might have been moved by tidal currents.

The mobility could contribute to the observed stability of the mud layer in two ways. According to Winterwerp [1999] a moderate level of turbulence leads to dewatering and consolidation. This turbulence may be generated at the lower boundary with the consolidated river bed, which leads to dewatering and consolidation. Increased concentrations, in turn, promote damping of turbulence at the lutocline and increase the stability of the mud layer. The consolidation may explain the observed reduction of layer thickness, whereas the disappearance of

large parts of the fluid mud deposits is ascribed to entrainment, which takes place simultaneously. The shape of the lutocline does, however, not show signs of entrainment. Also, according to the entrainment model of Kranenburg and Winterwerp [1997], in case of a turbulent mud layer, the water column is entrained, the concentration reduced and the layer thickness increased. This means, if the mud layer is mobile, it is certainly not more turbulent than the water column. The obvious loss of sediment and partial disappearance of the mud layer is thus explained by erosion at the lutocline.

Based on the observation, that mobile mud is partially preserved until the subsequent slack water, semi-diurnal feeding of the mud layer potentially leads to a positive feedback of turbulence damping and consolidation, which inevitably promotes the formation of erosion-resistant estuarine mud. Semi-diurnal slack water deposition occurs in the centre of the TMZ, which explains the correlation between the centre of the TMZ and estuarine mud deposits.

4.6 Conclusions

The dynamics of fluid mud layers in the form of mobile mud were analysed on the basis of a hydroacoustic measurements, collected in the range of the TMZ of the Weser estuary. From the results of this study, the following conclusions are drawn:

- The general assumption that fluid mud accumulation is related favourable hydrodynamic conditions, which predominantly occur during neap tide, is confirmed.
- Mobile mud layers are significantly more resistant to entrainment, compared to fluid mud deposits in troughs large dunes. It is suggested that turbulence, produced at the lower boundary, leads to partial dewatering and consolidation.
- Consolidation may explain a reduction of layer thickness but does not explain the partial disappearance of fluid mud. The observed disappearance can only be explained by an largely unresolved erosion process.
- As the mud layer is partially preserved until the subsequent slack water, semi-diurnal feeding of the mud layer potentially leads to formation of erosion-resistant estuarine mud. Semi-diurnal slack water deposition occurs in the centre of the TMZ, which explains the correlation between the centre of the TMZ and estuarine mud deposits.

Chapter 5: Paper IV

Tide driven dynamics of a fluid mud lutocline

L. Wang[1], M. Becker[1], D. Hebbeln[1], C. Winter[1]

[1]MARUM, Center for Marine Environmental Sciences, University of Bremen, Germany

Continental Shelf Research (under revision)

Abstract

In the turbidity maximum zone of the Ems estuary, Germany, cohesive sediments can form thick fluid mud bodies, up to a few metres. Sediment concentrations vary from several g/l in the upper layer up to over a hundred g/l above the consolidated bed. An abrupt change of suspended sediment concentration at the upper boundary of the fluid mud layer is called a lutocline, and is of prime importance in the effects of sediment-induced stratification in turbid estuaries. Here an examination of the position, strength and dynamics of the lutocline is presented based on acoustic backscatter measurements by three standard acoustic Doppler current profilers (ADCP). The position and strength of the lutocline can be described by the peak acoustic backscatter gradient (PABG) derived from the ADCPs. Although three ADCPs exhibited different backscatter intensity in terms of magnitude, the PABG was highly consistent for the three ADCPs in terms of its strength and position. The intratidal variability of lutocline characteristics and its dependency on forcing hydrodynamics are demonstrated.

5.1 Introduction

Fluid mud can be formed in estuaries with sufficient fine-sediment supply and periods of low intensity hydrodynamics due to the fact that the flux of settling particles towards the bed exceeds the consolidation rate of the bed and a gradual build-up of unconsolidated sediment takes place [*McAnally et al.*, 2007b]. It is a high concentration aqueous suspension of fine-grained sediment with concentrations of tens to hundreds of grams per litre, in which settling of particles and flocs are substantially hindered [*Kineke et al.*, 1996; *Kirby and Parker*, 1977].

Kirby and Parker [1983] firstly used the term “lutocline” to describe the sudden increase of suspended sediment concentration (SSC) at some depth in the water column. As a transition zone between the dilute upper suspension layer with relatively low concentrations and the lower dense fluid mud layer with much higher concentrations, the lutocline is governed by the flow-sediment interaction [*Mehta*, 1989]. Lutocline characteristics play an important role regarding the fate of estuarine turbulent kinetic energy (TKE). On one hand, it is widely recognised that the lutocline has a virtual effect on damping of TKE diffusion and extent of the damping was investigated by parameterisation [*Trowbridge and Kineke*, 1994; *Winterwerp*, 2002]. On the other hand, internal waves riding on the lutocline enhance turbulence [*Jiang and Mehta*, 2002; *Uittenbogaard*, 1995].

In turbid water, as a significant marker in the vertical SSC profile, the prediction of the position and strength of the lutocline is of considerable importance to properly estimate the total sediment transport over the vertical, but presently hindered by a lack of adequate understanding of lutocline-associated processes. Although many efforts have been devoted to study the lutocline behaviour in laboratory experiments [*Kranenburg and Winterwerp*, 1997; *Wolanski et al.*, 1989] as well as field measurements [*Dong et al.*, 1997; *Dyer et al.*, 2004; *Vinzon and Mehta*, 2003], there are few in situ observations of lutocline dynamics of high temporal and spatial resolution in tidal estuaries.

Acoustic Doppler Current Profilers (ADCPs) are common instruments to measure current velocity profiles in marine environments [*Dinehart and Burau*, 2005; *Lueck and Lu*, 1997; *Simpson and Oltmann*, 1993]. In the past decades, ADCPs have also been employed to measure suspended sediment characteristics in that the acoustic backscatter intensity was calibrated to measured values of SSC [*Holdaway et al.*, 1999; *Kim and Voulgaris*, 2003; *Merckelbach and Ridderinkhof*, 2006]. In addition, based on the same principle, there are several other specialised devices of using acoustic backscatter to acquire information only with regard to SSC [*Shi et al.*, 1996; *Shi et al.*, 1999; *Thorne et al.*, 1993; *Villard et al.*, 2000] and the investigation of lutoclines [*Shi et al.*, 1997]. These latter devices are favourably used in the measurement due to their non-intrusive remote monitoring capabilities with high spatial and temporal resolution but are not capable of measuring flow velocity.

In this study the temporal evolution of the lutocline in the turbidity maximum zone of the Ems estuary (Germany) has been observed throughout several tidal cycles. Standard commercial ADCPs have been applied to investigate the hydrodynamic environment and the formation and disintegration of the lutocline in the tidal currents. The performance of three

ADCPs with different operating frequencies was inter-compared. Flow velocities measured by the ADCP were compared to those measured by an electromagnetic current meter (ECM). It is shown that the lutocline can be characterised by the gradient of ADCP acoustic backscatter. This was confirmed by SSC profiles derived from a calibrated optical backscatter sensor (OBS).

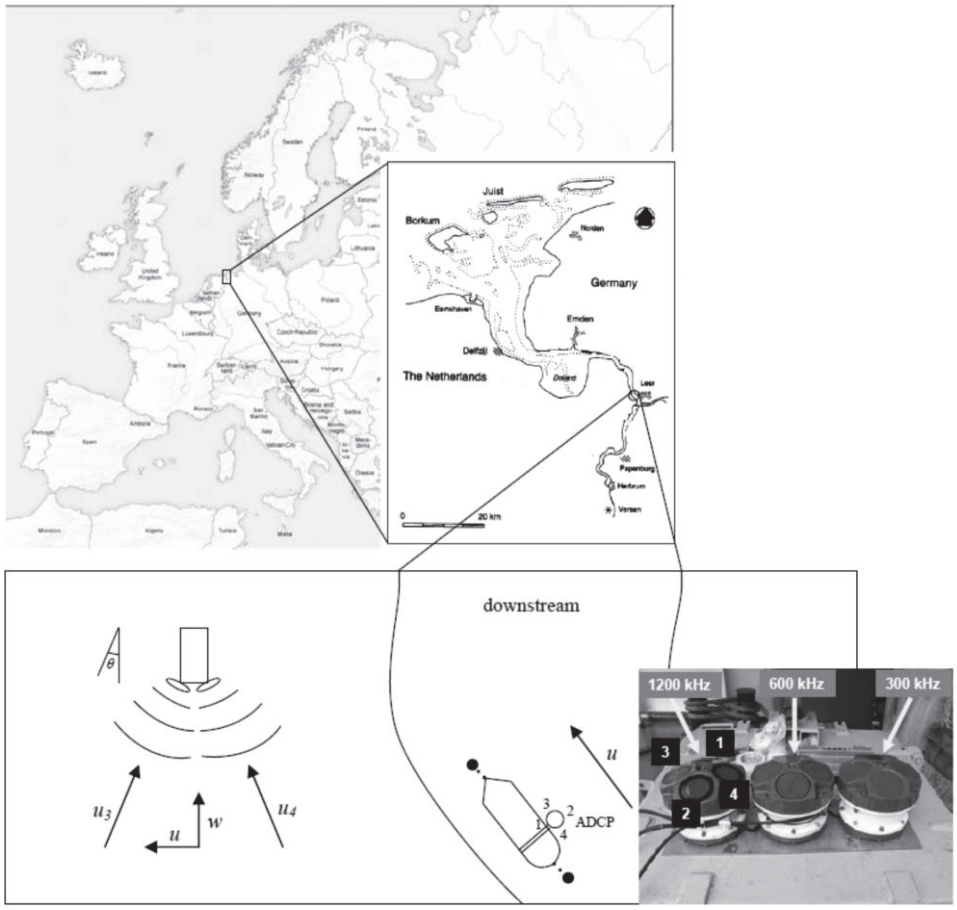

Figure 5.1: Location of the stationary measuring point, arrangement of the ship and ADCP at the measuring point and layout of the three ADCPs with different operating frequencies. 1, 2, 3, 4 denote 1, 2, 3 and 4, respectively, for all ADCPs on the frame. u is the longitudinal current velocity along the channel, w is the vertical velocity, u_3, u_4 are the measured along beam velocities of beam 3 and beam 4, θ is the angle of the beam to the vertical.

5.2 Regional setting

The Ems estuary is a partially mixed, mesotidal estuary defined from the upstream end of tidal influence of the weir in Herbrum (0 km), passing by Papenburg (12 km) and Emden (50 km), down towards the island of Borkum (100 km) in the Wadden Sea (Figure 5.1). The estuary was formed by rising sea levels after the last ice age ended 10,000 years ago [*Streif*

and Köster, 1978]. The sea level rise is continuing, remaining a constant rate at about 10-12 cm per 100 years since 1901 [*Jensen and Mudersbach*, 2006]. The anthropogenic effects on the estuary are significant. From the 16th century to middle of the 20th century, diking, land reclamation and polderisation were being conducted, resulting in a profound change of the form and functioning of the Ems estuary [*Dinehart and Burau*, 2005; *Gienapp*, 1983].

After the Second World War, in order to satisfy the increasing demand of shipping transport, dredging activity and construction measures in harbours and navigational channels have been being maintained, greatly altering the physical processes including hydrodynamics and sedimentological dynamics in the Ems estuary [*Steen*, 2003]. The estuary hydrodynamics have been changed significantly mainly due to a decrease in hydraulic roughness [*de Jonge*, 1983], further leading to an increase as much as 1.5 m on tidal range [*Jensen et al.*, 2003] and pronounced flood dominance [*Van de Kreeke et al.*, 1997; *Van Leussen*, 1995].

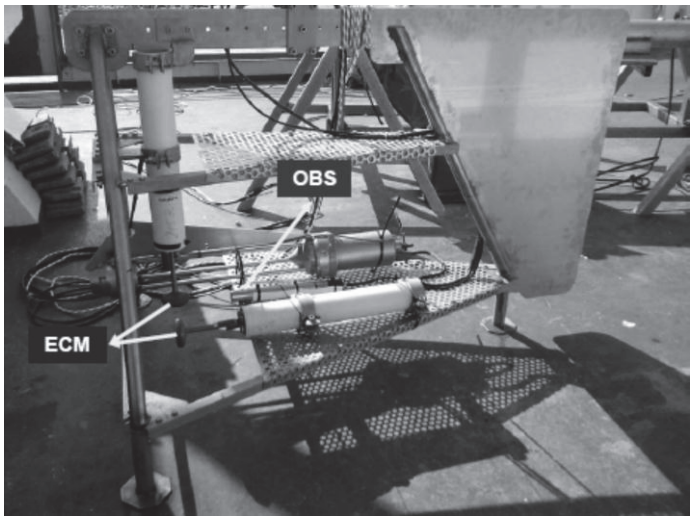

Figure 5.2: Structure of the frame employed in this measurement and measuring devices mounted on the frame. (ECM: electromagnetic current meter, OBS: optical backscatter sensor)

The change on hydrodynamics inevitably has influenced the sediment transport in the estuary. In the turbidity maximum zone of the estuary, the SSC is currently between 1-2 orders of magnitude larger than in the 1950's. Surface water concentrations have reached nearly 5 g/l during the summer months and data from fixed measuring points between 1-2 m above the bed suggest that concentrations sometimes exceed 25 g/l during late summer [*Talke and de Swart*, 2006].

5.3 Methods

The here presented data on local hydro- and sediment dynamics were measured from a moored ship at the western bank of the Ems estuary (53°14'11.51"N, 7°23'48.63"E, approximately 22 km upstream of Emden, see Figure 5.2) during a period of 26 hours from 15:33 on the 9th to 17:51 on the 10th September 2008.

The water level is recorded by the tidal gauge at Leerort approximately 3.5 km upstream from the measuring point, which is operated by the local Water and Shipping authority (WSA Emden). Three downward-looking ADCPs with different operating frequencies were mounted on the starboard side of the ship (Figure 5.2). Additionally, a sensor carrier equipped with two electromagnetic current metres and an optical backscatter sensor (OBS) was deployed in a profiling mode (Figure 5.3). All sensor data were corrected for tidal elevation.

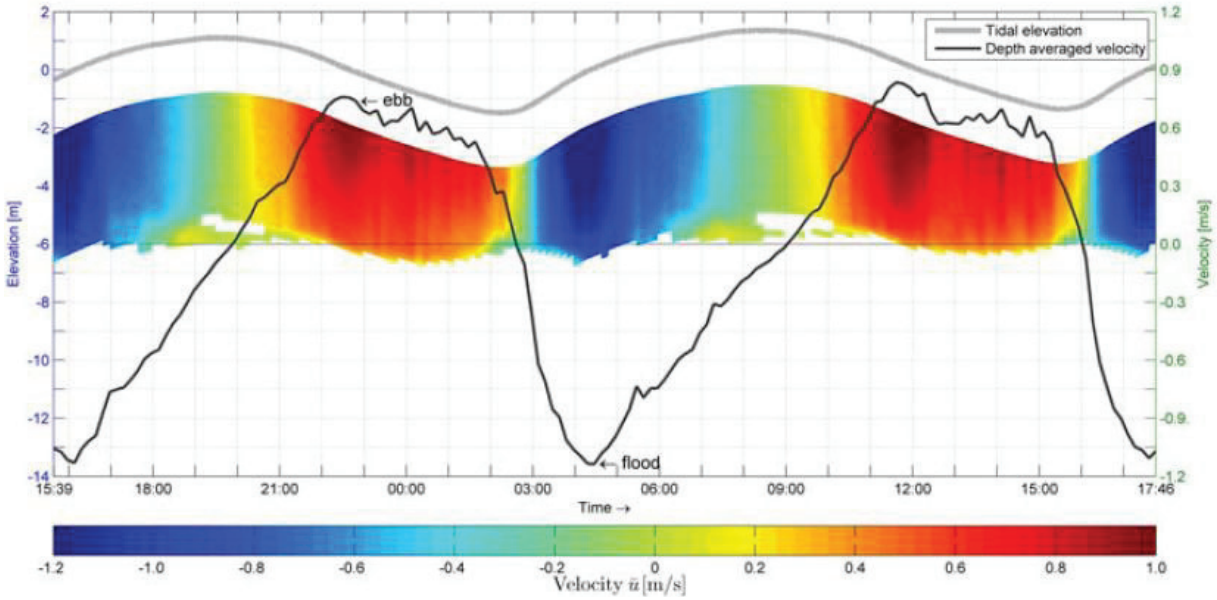

Figure 5.3: Contour of time averaged longitudinal velocity u over the measurable range and depth averaged velocity from the 120 kHz ADCP. For the depth averaged velocity, "+" represents the direction of ebb current; "–" represents the direction of flood current.

5.3.1 Acoustic Doppler Current Profiler

Three standard RD Instruments Rio Grande ADCPs of operating acoustic frequencies of 300, 600 and 1200 kHz with a vertical resolution (bin size) of 20 cm and 40 bins over the vertical (RD Instruments 1996) were used at a stationary measuring point during the campaign. Sampling frequencies were slightly different, 0.6 Hz for the 300 kHz ADCP and 0.9 Hz for the 600 and 1200 kHz ADCP respectively. The ADCPs were mounted with Beam 3 pointing

towards the bow of the ship which is marked by number "3" in Figure 5.2. Due to the location of the ADCPs at 1.35 m below the water surface and the device specific blanking distance below the acoustic transducers, data available appeared 1.88, 2.03 and 2.77 m below the water surface for the 1200, 600, 300 kHz ADCPs respectively. Invalid bins recorded by ADCPs were identified and removed prior to analysis. The chosen bin size for the 300 kHz ADCP is too small for reliable velocity measurements, but was used for the analysis of acoustic backscatter only. As shown in Figure 5.2, the ship was aligned parallel to the channel. Therefore a longitudinal velocity u along the channel can be calculated from ADCP beam velocities u_3 and u_4 by

$$u = \frac{(u_4 - u_3)}{2\sin\theta} \tag{5.1}$$

in which *u3*, *u4* are the measured along-beam velocities of beam 3 and beam 4, and θ=20° is the angle of the beam to the vertical (Figure 5.2). In the post-processing of ADCP data, a 10-minute averaging period was used to calculate mean velocities [*Soulsby*, 1980]. If the number of valid velocity data was less than 80% of the total number, the averaged velocity was treated as invalid. Apart from the Doppler shift derived current velocities, also the acoustic echo intensity can be used to provide information on the type and quantity of particulate matter in the water column. The echo intensity as recorded by each device was corrected for beam spreading and water absorption in order to determine the acoustic backscatter intensity in the water column [*Deines*, 1999]. The absorption due to sediment in the water column is not taken into account in this study. The mean of the four beams backscatter data was calculated and filtered by blockwise ensemble average for 10-minute windows. A backscatter gradient *SVgrd* [dB/m] is defined as:

$$\mathrm{SV}_{grd} = \frac{\mathrm{SV}_{upper} - \mathrm{SV}_{lower}}{\Delta z} \tag{5.2}$$

where *SVupper* represents the backscatter intensity in the upper bin and *SVlower* the backscatter intensity in the adjacent lower bin, z is positive upwards, and Δz is 0.2 m of the bin (one depth cell) size.

5.3.2 Electromagnetic current metres

From the anchored ship an instrument carrier was deployed in profiling mode. A fin at the rear of the device keeps it in a streamwise direction towards the tidal currents (Figure 5.3) [*Trevethan et al.*, 2009]. Two electromagnetic current metres (ECMs) (HS Engineers Series

2001) were used to derive velocity data even in highly concentrated suspension, where hydro-acoustic devices are not applicable. One was placed horizontally to measure vertical velocities, the other vertically to measure horizontal velocities. Their sampling frequencies were both 0.5 Hz. Vertical profiles of ECM current velocity were derived by averaging 100 samples at 1 m depth intervals. The instantaneous depth was recorded by a piezo-resistive pressure sensor (KELLER AG, Switzerland) attached to the ECM and also averaged by 10 minutes.

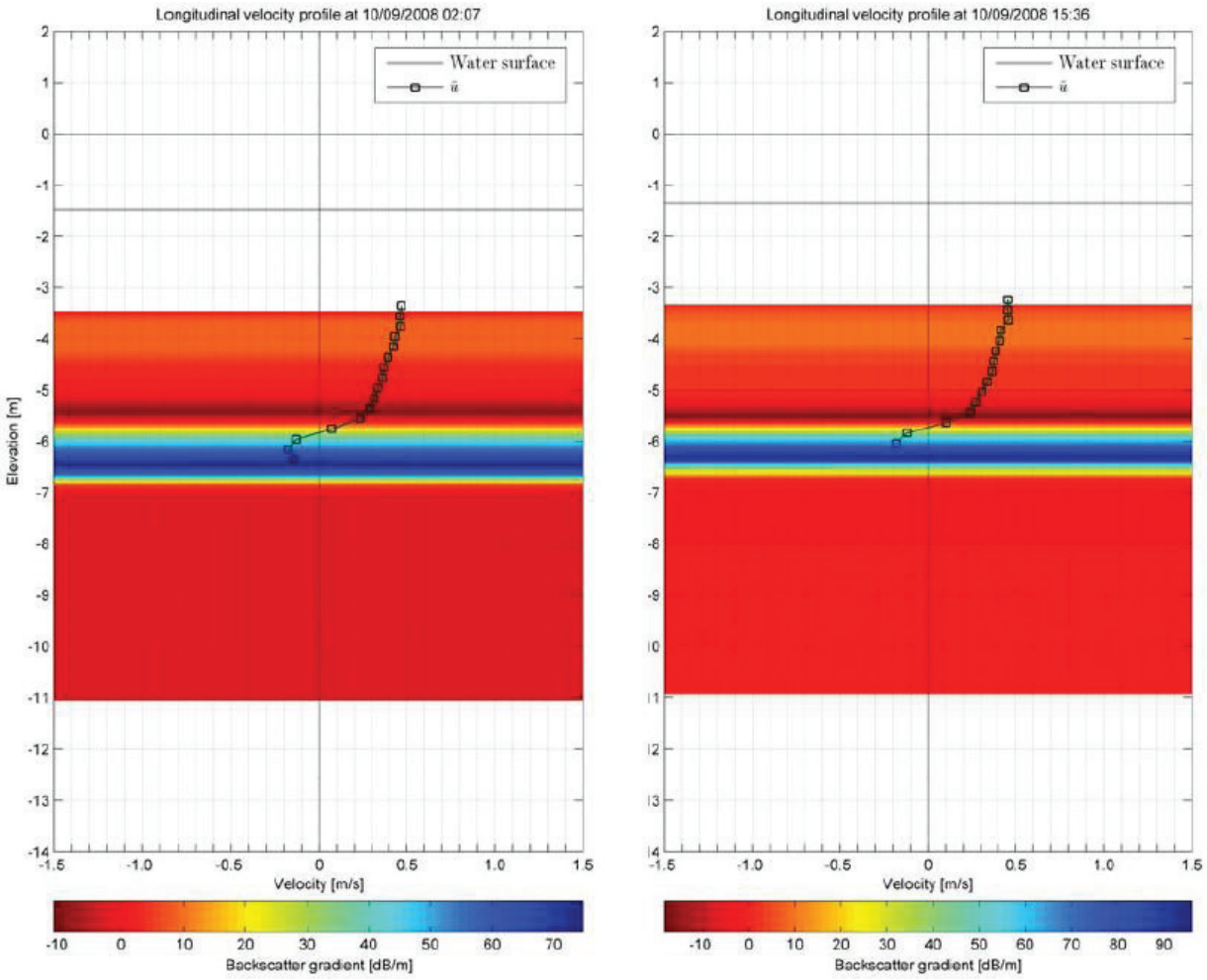

Figure 5.4: Velocity profiles from the 1200 kHz ADCP in the transition from ebb to flood and contour plot with regard to backscatter gradient SV_{grd} from the 1200 kHz ADCP.

5.3.3 Optical backscatter sensor

Additionally an optical backscatter sensor (OBS) ViSolid® 700 IQ (Wissenschaftlich-Technische Werkstätten GmbH) was mounted on the same frame. The OBS was used to estimate SSC in the water column by the light scattered and reflected by the total suspended particulate matter. It recorded the data with the same sampling frequency and at the same sam-

pling positions as the ECM to derive SSC depth profiles. SSC was quantified by a calibration of the OBS data to filtered and weighted suspended sediment samples. Due to technical limitations of the OBS sensor the valid range of conditions does not exceed SSC magnitudes of 22 g/l.

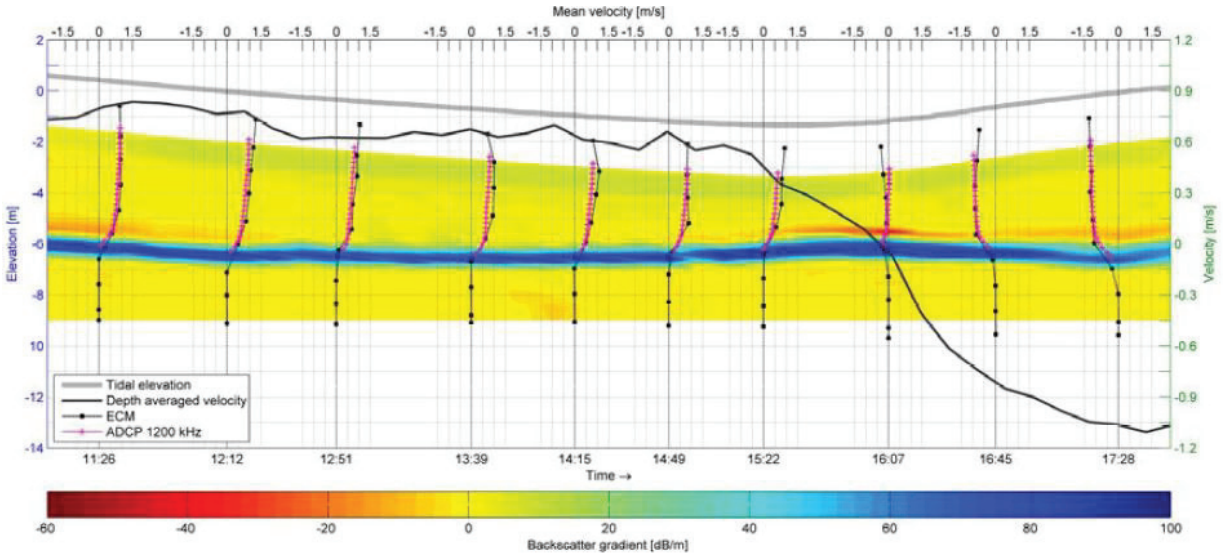

Figure 5.5: Streamwise velocity profiles measured by the ECM, longitudinal velocity profiles measured by the 1200 kHz ADCP and contour plot with regard to backscatter gradient SV_{grd} from the 1200 kHz ADCP.

5.4 Results

5.4.1 Current velocities

In contrast to other typical marine environments at the measuring position in the Ems estuary a layer of fluid mud bed obscures the detection of a rigid bed. After correction for the tidal elevation, from now on the depth refers to mean sea level. The measured raw velocity data by the three ADCPs, gave valid numbers down to about -6 m, all bins below -7 m are not valid. The consolidated bed was touched by the instrument frame at an approximate depth of -9 m. For a period of 26 hours all ADCPs measured current velocity profiles from the level of their individual blanking distance down to a depth of approximately -7 m. As expected the measured velocities of the 300 kHz ADCP were not reliable (>20% invalid data) because of the small bin size. The 600 and 1200 kHz ADCPs measured with better reliability (invalid data 5.2% and 1.2% respectively). The depth averaged velocities of the 600 and 1200 kHz ADCP are similar with a root mean square deviation of 0.03 m/s. Only velocity profiles measured by the 1200 kHz ADCP have been taken into account in this study. After averaging

ADCP velocities over 10 minute intervals, it was found that the averaged longitudinal velocity is close to averaged velocity magnitude with a root mean square deviation of 0.02 m/s. Thus the effect of lateral flow was ignored further on.

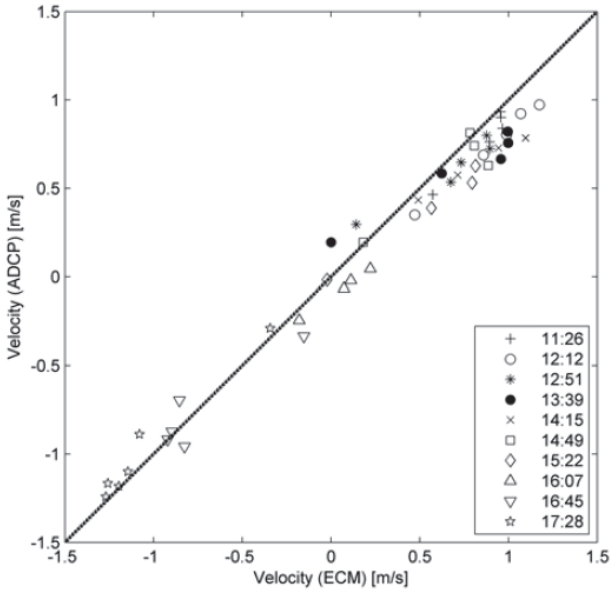

Figure 5.6: Velocities measured by the 1200 kHz ADCP vs. ECM at different time points.

As shown in Figure 5.4, most cells below -6 m contain invalid values and are removed from further analysis. The 1200 kHz ADCP was able to penetrate to below -6 m during strong currents. The black solid line representing the depth averaged velocity shows the significantly larger flood current compared to the ebb, implying a local flood dominance of the system. During the two tidal cycles, the depth averaged velocity ranged from 1.1 m/s at flood to 0.8 m/s at ebb current. The flood current quickly peaked at 1.1 m/s from zero within a short accelerating period less than 2 hours and then gradually weakened until slack water within a decelerating period around 4.5 hours after a typical short duration of one distinct flood peak (1.1 m/s). The ebb current increased to the maximum 2.5 hours later since the high slack water and continued for a longer ebb phase with several current peaks at around 0.7 m/s. The ebb current persisted for longer time in particular with more oscillations during the maximum. The duration time of high slack water is much longer than the low slack water.

In transitions from ebb to flood around 02:40 and 16:00, it is observed that the flow firstly changed direction starting from the bottom with the coming of flood current (Figure 5.5). The maximum flow reached nearly 0.2 m/s in flood direction and nearly 0.5 m/s in ebb direction.

Electromagnetic current metres were used for 6 hours from ebb peak (11:07) to flood peak current (17:47) on September 10th to compare with the ADCP readings close to the fluid mud layer where the ADCP was expected not to be able to collect reliable data with regard to velocity. The instrument frame was lowered throughout the whole water column and fluid mud layer down to the consolidated bed at approximately -9 m. The averaged velocity calculated from 100 samples at each depth is called mean velocity in Figure 5.6. To get a complete profile of velocity using ECM required around 40-50 minutes, also depending on the temporal water depth determined by tidal elevation. For comparison with ADCP data the ECM profile data was plotted for a time point midway during the time period required to measure each velocity profile.

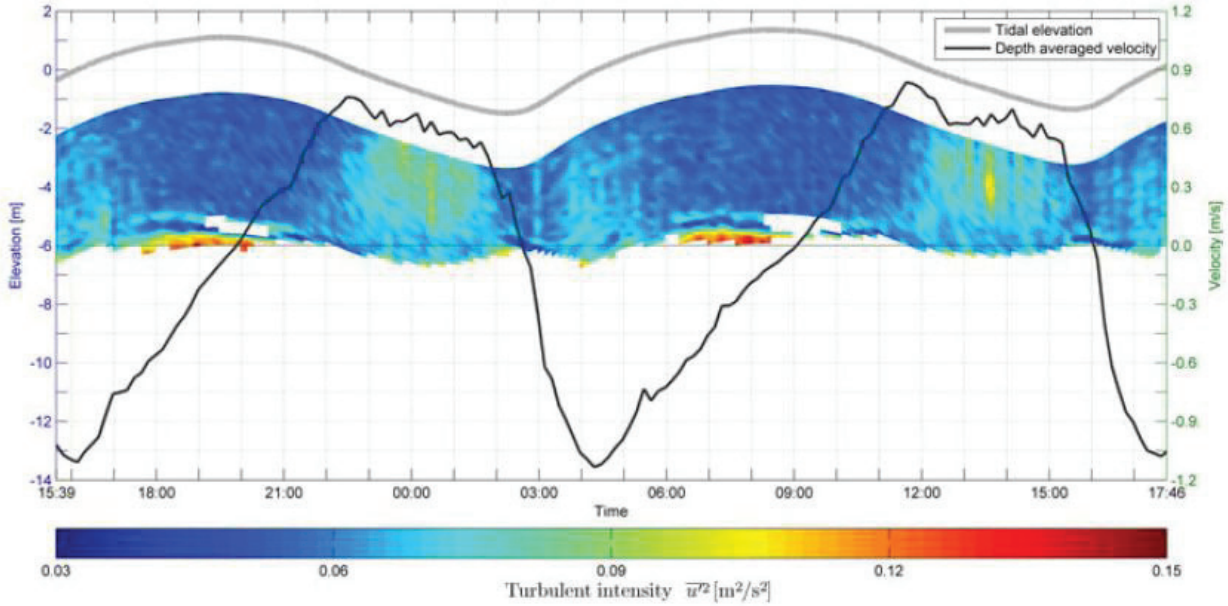

Figure 5.7: Contour of turbulent intensity u'² over the range from the 1200 kHz ADCP.

Seven ADCP profiles during ebb and two during flood currents show logarithmic shape approaching zero velocity at a depth of about -6.5 m. One profile taken during slack water shows an indifferent profile. In comparison to the ECM profiles, that measured down to the consolidated bed at about -9 m, they generally show an acceptable agreement (overall correlation coefficient R = 0.917~0.997) in the part of the profile covered by the ADCP velocity data. However, ECM velocities are somewhat higher.

At some profiles the lowermost part of the ADCP velocity profile appears not to match the numbers given by ECM. However, further analysis is not possible due to the rather distant 1 m intervals of ECM profile data. Although the ECM could be lowered down to the consoli-

dated bed, the velocity measured by ECM in the range of about 2 m upwards from the bed was zero for most of the measuring time. It shall be noted that some movement was activated to a deeper position driven by the strong flood current at 17:28, which can be also seen from the velocity profile measured by the ADCP.

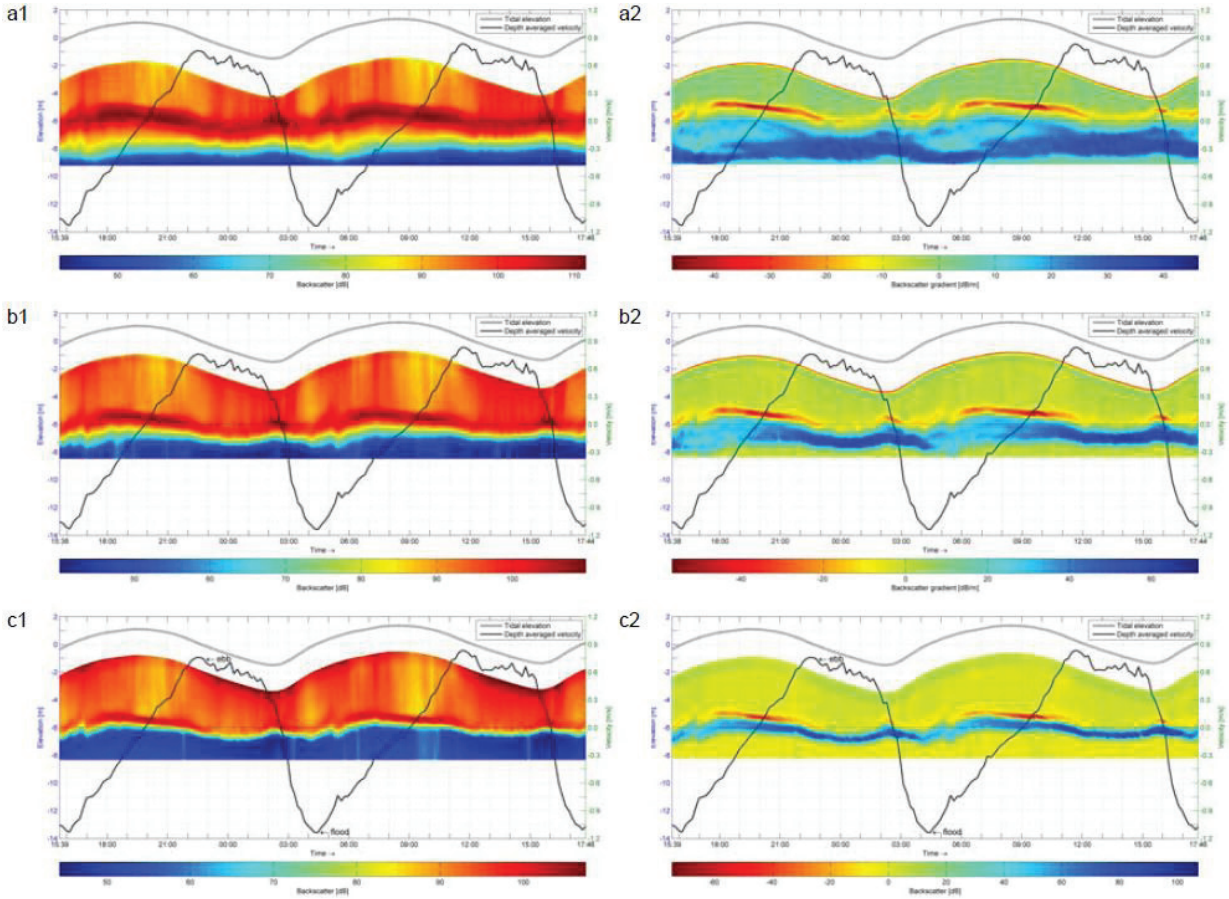

Figure 5.8: Contour plots with regard to backscatter SV and backscatter gradient SV_{grd} from the three ADCPs and the tidal elevation (thick grey line) from the tidal gauge at Leerort; a1, b1, and c1 show backscatter from the 300 kHz, 600 kHz, 1200 kHz ADCP; a1, b1, and c1 show the backscatter gradient.

5.4.2 Acoustic backscatter

Acoustic echo intensities as recorded by the three ADCPs and corrected for beam spreading and water adsorption for two tidal cycles are shown in Figure 5.7 a1, b1, c1. Depending on their acoustic frequency absolute values differ, but general patterns are similar: at all times the acoustic backscatter increases from the upper water column to about -5 m water depth, depending on the tidal stage. Below this follows a pronounced increase of acoustic backscatter to maximum values at about -6 m. Below this peak, echo intensities drop rapidly to a sys-

tem noise level of below 60 dB. Intensities change along the tidal cycle with a repeated general pattern of lower intensities at high water slack; and maximum values at the low water. The significant increase of acoustic backscatter in a depth of about -6 m is highlighted in Figure 5.7 a2, b2, c2 as a pronounced peak of the gradient of acoustic backscatter (PABG).

This PABG is stronger at slack waters, around 20:00 and 09:00 at high water slack, around 02:30 and 16:00 at the much shorter low water slack time, but weak at full tidal currents. In particular seen for the PABG of the 1200 kHz ADCP decayed when the depth averaged velocity reached around 0.7 m/s. The vertical position of the PABG gradually changes with the tidal currents.

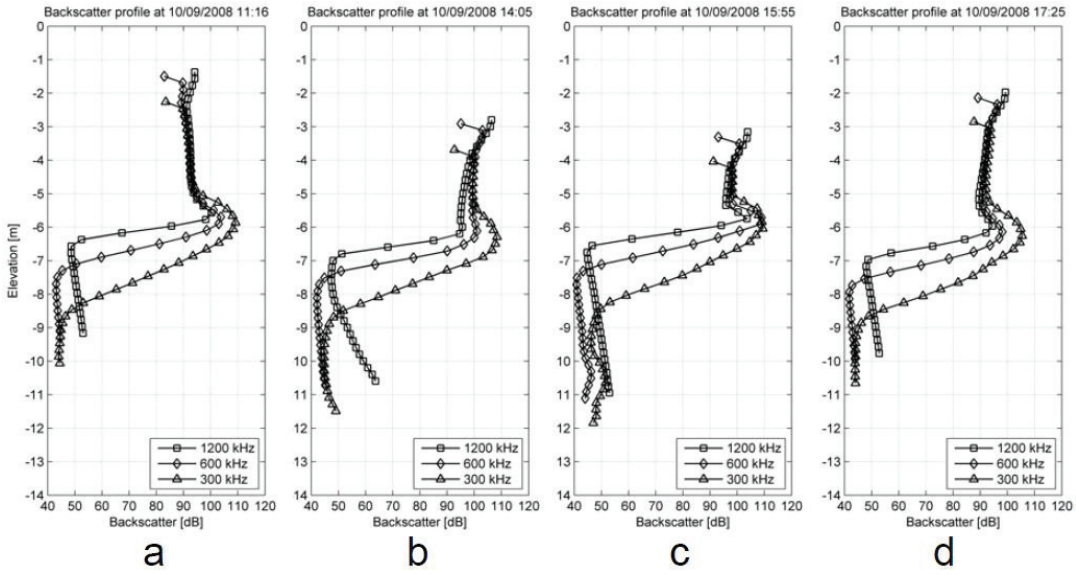

Figure 5.9: Backscatter profiles measured by the three ADCPs at the time points nearest to those denoted by the downward arrows in Figure 5.10.

Exemplarily for some time points marked in Figure 5.9, the backscatter profiles over the depth from the three ADCPs are presented in Figure 5.8. At the first time point (11:16), the ebb current just reached the maximum velocity and all three ADCPs showed a significant PABG (quantify 300/600/1200) in the zone between -5 and -6 m on the backscatter profile (Figure 5.8, a).

At the second time point (14:05), with continuation of the ebb maximum current, the PABG almost vanishes (quantify) especially for the 1200 kHz ADCP (Figure 5.7, a2; Figure 5.8, b). At low water slack (15:55), the PABG recovered to one of its maxima (quantify) throughout the tidal cycle (Figure 5.8, c). With rising flood currents the PABG weakened again (Figure 5.8, d).

5.4.3 Suspended sediment concentration

Suspended sediment concentration (SSC) profiles were obtained from OBS at ten times from maximum ebb flow over low water slack to maximum flood flow. SSC values in the upper water column range from 1 g/l after slack waters to about 2 g/l at high currents (Figure 5.9, upper panel). It shall be noted that due to technical limitations, SSC magnitudes exceeding 22 g/l could not be quantified. Thus no valid information with regard to SSC could be obtained near the bottom.

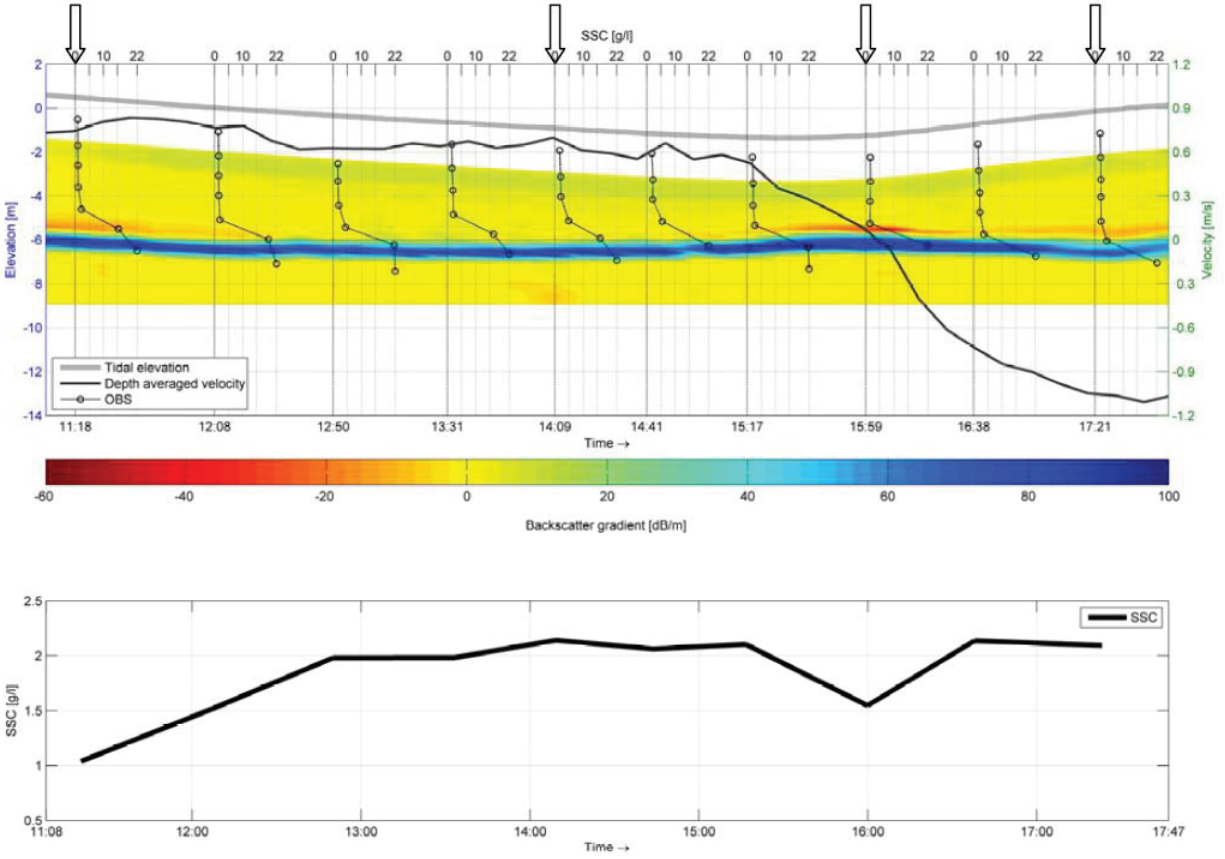

Figure 5.10: Upper panel: SSC profiles from the calibrated OBS and contour plot with regard to backscatter gradient SV_{grd} from the 1200 kHz ADCP. The upper arrows denote the time points nearest to which backscatter profiles are plotted at the corresponding time points in Figure 5.9; Lower panel: SSC from the calibrated OBS at points nearest to -4 m at elevation.

All the SSC profiles showed significant gradients at depths around -6 m. On the first profile at 11:18, the SSC increased from 2.2 to 15.3 g/l between the depths of -4.6 and -5.5 m across the PABG. In the following ebb current more sediment was suspended into the upper water column, which can be observed from the profiles of SSC. More explicitly, it can be seen from the lower panel of Figure 5.9 that the variation of SSC sampled at the points near-

est -4 m of elevation during the ebb maximum current from 12:50 to 15:17. At slack water (15:59), the SSC in the upper water column decreased.

The maximum gradients of the SSC profiles were fairly consistent with the position of PABG which was reformed with the decay of the currents. Following the slack water, the flood current acceleration (0.011 m/min) forced an increase in the SSC in upper water column.

5.5 Discussion

The comparison between the 1200 kHz ADCP and ECM current velocities suggested a good agreement. However, the time required to measure a profile of velocity by the ECM was too long to meet the stationary condition within which the flow can be thought of as quasi-stationary in a tidal estuary [*Soulsby*, 1980], even though the single velocity measured at a point would meet the stationary condition. The vertical resolution of 1 m turned out to be too large to truly reflect the values between the neighbouring points by a linear interpolation between them.

The ADCP exhibited an obvious advantage of measuring the velocity fast and non-intrusively with much higher spatial resolution (20 cm), however only down to a level where the attenuation of the acoustic backscatter signal travelling does not hinder ADCP processing. ECM data of this tidal cycle shows that there is no movement in the fluid mud layer below the lutocline zone most of the time. Only at maximum flood currents the fluid mud layer is moved with a velocity around 0.25 m/s accompanied by entrainment of suspended matter into the upper water body. The observation of the flow changing direction firstly from the bottom at 16:07 with more significant velocity magnitude compared to that occurring during the high water slack indicates an effect of density induced baroclinic pressure gradients resulting from extremely high SSC near the bottom [*Winterwerp and van Kessel*, 2003].

The acoustic backscatter intensity is assumed to be an indicator of the SSC. The absolute values are dependent on instrument specifications [*Deines*, 1999; *Gartner*, 2004; *Kostaschuk et al.*, 2005] and the three ADCPs recorded different absolute intensity magnitudes. However similar patterns were observed: The peak of acoustic backscatter between -5 m and -6 m was obvious in all ADCP readings and implied the presence of very high SSC, which is known to be the upper boundary of the fluid mud layer. Compared to the OBS, the backscatter from the ADCP may give quantitative information on SSC if accounting for the effect of sediment at-

tenuation [*Flammer*, 1962; *Gray and Gartner*, 2009; *Thorne et al.*, 1991] and sufficient calibration. However in this context only a qualitative analysis was envisaged.

Despite their different energy dissipation rates, all three ADCPs readings featured the significant peak of acoustic backscatter gradient (PABG) at the interface between the upper water column and the fluid mud layer. Here a significant increase in OBS derived SSC indicates the presence of the lutocline. Thus the PAGB could be related to the position and strength of the fluid mud lutocline throughout the measured tidal cycles.

Generally the lutocline is expected to become more pronounced with the gradual decrease of currents as the sediment suspended in the water column then settles down. At higher flow stages sediment is brought into suspension again and the lutocline becomes less pronounced (Figure. 9) [*Ross and Mehta*, 1989; *Wolanski et al.*, 1992a]. This periodic pattern could also be observed in the PAGB signal during the measurements (Figure 5.7, a2, b2, c2). Depending on the type of ADCP, PAGB signals showed different magnitudes.

In the transition from ebb to flood during which the changing rate (deceleration and acceleration) of current velocity is quite large, the time of slack water was quite short and the flood current came quite rapidly with higher peak velocity, hence the time for the sediment to settle down was not sufficient and the lutocline was not as strong as the one during slack water in the transition from flood to ebb with apparently smaller deceleration and acceleration.

During stronger currents, the sediment was mixed upward, leading to the strong backscatter concentrated in the upper water column as shown in Plot a1 of Figure 5.7. Accordingly the lutocline was obscured in view of the backscatter gradient processed from the 600 and 1200 kHz ADCP as shown in the right panel of Figure 5.7. However, the lutocline was still present, which can be confirmed by the continuous distinct layer of representing strong backscatter intensity around -6 m in c1 of Figure 5.7 and the prominent jumps of SSC profiles measured by the OBS (Figure 5.9).

Moreover, the lutocline underwent a vertical displacement during the high and low slack waters. Due to the settling of sediment from the upper water column, the lutocline firstly rose up for a while at the beginning of the slack water. Then as a result of dewatering, the lutocline settled down.

During the deceleration of flood currents from 17:00 to 20:00, at the first stage the rise of lutocline can be attributed to the effect of hindered settling, which can be identified by an increase of PABG in magnitude from -10 to -30 dB/m in view of the data measured by the

600 kHz ADCP (Figure 5.7, c2). At the second stage, after 19:00 the lutocline moves down and the PABG continues to increase to -50 dB/m, indicating that the settling still prevails along with dewatering. The same variation pattern can be also observed during the second deceleration of flood currents from 06:00 to 09:00. With the gradual increase of the current velocity, the entrainment on lutocline started to play a dominant role under the impact of the strong current, which is suggested by the fact that the colour of PABG started to become lighter and its position continued to drop down.

The position of the lutocline can be confirmed by the prominent gradients of SSC profiles derived from OBS. The SSC in the lutocline zone is around 15 g/l, and even higher during the slack water due to the settling of sediment from the upper part of water column. On the two SSC profiles during the acceleration of flood current, the most pronounced increase seems to be not consistent with the lutocline stated by the PABG (Figure 5.9). In fact, the measuring point next to the lowest point on which the SSC is 22 g/l should be a little higher than its position in the plot because the time required to measure a complete profile was quite long relative to the rapid variation of tidal elevation during the acceleration of flood currents and the tidal elevation had increased a lot since the data was sampled at the first point near the surface. In addition, the variation of fluid density over the depth also introduced an error in deriving the depth from pressure sensor and made the derived depth larger than the real value in the lower part due to the increase of fluid density resulting from the increase of SSC.

Summarizing all the measured results, the system may be described by the scheme proposed by Figure 5.10. In the study presented in this paper, the lutocline layer occurred between -5 m and -6 m at elevation according to the acoustic backscatter gradient sampled in the field, where the effect of hindered settling was remarkable during the deceleration of currents and the entrainment took place at strong currents. The PAGB from the three ADCPs suggests that the lutocline at the same position which is stated by the distinct dark layers (Figure 5.8, a2, b2, c2) changes its strength and position due to hindered settling, dewatering and entrainment which are affected by the tidal current.

Above the lutocline, a layer defined as mobile suspension the SSC may reach several g/l in the measuring period. In this layer, SSC is governed by the current. When the current is strong, there is more sediment mixed upwards from the lutocline zone and even the lower fluid mud layer, and the SSC gradient in the lutocline zone becomes smaller. But when the current is weak, sediment freely falls and the settling is aggravated due to flocculation. In the lutocline zone, the SSC gradient is largely enhanced again due to hindered settling effect and

decline of mixing. Below the lutocline zone, a fluid mud layer is present with much higher SSC over a hundred g/l derived from sediment samples.

The instruments could be lowered down to around -9 m where the consolidated bed is expected. Therefore, the fluid mud layer between the lutocline zone and consolidated bed was more than 2 m thick, in which there was no movement most of the time.

5.6 Conclusions

Standard acoustic Doppler current profiler (ADCP) can be used to examine local current profiles, qualitative SSC in upper water column and dynamic properties of a fluid mud lutocline at the same time. Based on data collected by a field campaign in the Ems estuary in September of 2008, ADCP derived velocities were compared to electromagnetic current metres and showed to be reliable down to the lutocline layer below which the velocities approach zero. It was shown that the gradient of acoustic echo intensity can be used to qualitatively describe the position and strength of the lutocline without an extended calibration of the acoustic backscatter to suspended sediment concentration being necessary.

The magnitude of acoustic backscatter gradients can be used to qualitatively demonstrate the strength of the lutocline. Its evolution under tidal forcing is governed by several processes like entrainment, hindered settling and dewatering.

At slack water times a strong lutocline is formed due to less mixing and hindered settling, which is reflected by increasing ADCP backscatter gradients; whereas at hydrodynamic forcing the lutocline is weakened because of intensive mixing and entrainment, reflected by decreasing of ADCP backscatter gradients. Compared to the short period for the deceleration of ebb current, the period for deceleration of flood is quite long, which is favourable for continuous increase of the strength of the lutocline with effect of hindered settling and even dewatering.

It is recognized that under the upper strong flow sediment is entrained from the fluid mud layer into the lutocline zone firstly and further mixed up to the mobile suspension layer. Nevertheless, the sediment exchange between the fluid mud layer and the consolidated bed is still poorly understood. Hence, detailed description of this sediment exchange through laboratory experiments and field measurements are required to gain better understanding of this process.

Acknowledgements

The work is funded trough DFG-Research Center/Excellent Cluster “The Ocean in the Earth System”. The authors thank Dr. Mark Trevethan for sharing data and also thank captain and crew of the RV Senckenberg. Bundesanstalt für Wasserbau (Federal Waterways Engineering and Research Institute) is gratefully acknowledged for providing technical support. The authors thank Dr. Andreas Wurpts from Franzius-Institut für Wasserbau und Küsteningenieurwesen (Franzius Institute of Hydraulics, Waterways and Coastal Engineering) for cooperation in this campaign.

Chapter 6: Paper V

The stability of a mobile fluid mud lutocline under tidal currents measured by standard ADCP

L. Wang[1, 2], M. Becker[1], C. Winter[1]

[1]MARUM, Center for Marine Environmental Sciences, University of Bremen, Germany
[2]GLOMAR, Bremen International Graduate School for Marine Sciences, University of Bremen, Germany

Journal of Geophysical Research (Submitted)

Abstract

Fluid mud is observed in estuaries and lakes throughout the world. Despite the common interest in a fundamental understanding of the formation and dynamics of fluid mud layers, detailed data on the occurrence and stability of fluid mud is scarce. Here the (re-) formation of a fluid mud body by tidal pumping was observed in the German Ems estuary. Detailed measurements of the hydrodynamics and sediment dynamics are presented. Standard commercial acoustic Doppler current profilers (ADCPs) could be used to derive continuous observation of the lutocline dynamics and quantitative measures of the fluid mud lutocline stability. The observed suspended sediment dynamics follow a repeated cycle of rapid settling of flocculated sediment and immediate formation of a stable lutocline at slack high water, characterised by a rapid increase in gradient Richardson numbers. Subsequent self-weight consolidation (dewatering) is reflected by a constant decrease of the level of maximum backscatter gradient (0.056 mm/s). Increasing ebb currents completely remove the fluid mud body out of the domain of observation or break up the lutocline by enhanced turbulence which is reflected by low gradient Richardson numbers (<0.25). The very short low slack water (less than 2 hours from the high ebb current to the flood peak current) features a temporary formation of a stable lutocline, which however is immediately destroyed by pronounced flood currents acceleration, and high turbulence intensity. Time scales for the formation of a stable lutocline at slack water are in the order of 4 hours.

6.1 Introduction

A turbidity maximum zone (TMZ) may form in estuaries if sediments originating from marine and/or terrestrial sources converge to form locally increased turbidity with suspended sediment concentration (SSC) 10 to 100 times greater than those upstream or seaward [*Nichols and Biggs*, 1985]. The TMZ plays an important role in estuarine sedimentary and ecological processes: Settling rates are enhanced by flocculation of sediment grains in saline environments [*Gibbs et al.*, 1989; *Kranck*, 1984; *Winterwerp*, 2002], while primary production is influenced by impairment of light penetration [*Colijn*, 1982; *Joint and Pomroy*, 1981; *Malone*, 1976; *Pennock and Sharp*, 1986] and pathogenic bacteria is protected from UV light in turbid environments [*Alkan et al.*, 1995; *Pommepuy et al.*, 1992; *Rozen and Belkin*, 2001] thus suspended sediment is a governing parameter for water quality. The causative mechanisms for TMZ formation vary depending on factors like channel morphology, tide-driven dynamics, sediment availability and characteristics and riverine influence [*Dronkers*, 1986b; *Nichols and Poor*, 1976; *Sanford et al.*, 2001; *Schoellhamer et al.*, 2000; *Schubel and Carter*, 1984; *Talke et al.*, 2009].

High contents of suspended matter in the TMZ may lead to highly variable density stratifications [*Dyer et al.*, 2004; *Uncles et al.*, 2006b] from concentrated benthic suspension (CBS) to highly concentrated benthic suspension (HCBS) [*Whitehouse et al.*, 2000; *Winterwerp and Van Kesteren*, 2004] up to fluid mud layers with high concentrations of tens to hundreds of grams per litre, in which settling of particles and flocs are substantially hindered [*Kineke et al.*, 1996; *Kirby and Parker*, 1977; *Uncles et al.*, 2006a]. Kirby and Parker [1983] coined the term “lutocline” to describe discontinuities in the vertical suspended sediment concentration (SSC) profile.

Observations of critical states and the dynamics are crucial for the understanding of formation processes, dynamics of fluid mud bodies, and the development, calibration, validation of numerical models [*Guan et al.*, 2005; *Hsu et al.*, 2009; *Hsu et al.*, 2007; *Li Hir et al.*, 2001; *Nguyen et al.*, 2009; *Watanabe et al.*, 2000; *Winterwerp*, 2002]. The stability (or instability) of density stratifications is commonly expressed by the dimensionless gradient Richardson number which is a convenient and frequently used measure of vertical stability of flows [*Shi*, 1998] based on the ratio between the potential energy required for vertical mixing and the turbulent kinetic energy available in the flow for mixing. According to the definition arising

from the balance equation for turbulent energy [*Tennekes and Lumley*, 1972], the gradient Richardson number is calculated as:

$$Ri = -\frac{\frac{g}{\rho}\frac{d\rho}{dz}}{\left(\frac{dU}{dz}\right)^2} = \frac{-((\rho_s - \rho_w)/\rho_s)g\partial c/\partial z}{\overline{\rho}(\partial u/\partial z)^2} \tag{6.1}$$

where $\frac{d\rho}{dz}$ states the term for potential energy due to density gradient, whereas $\left(\frac{dU}{dz}\right)^2$ the term for kinetic energy due to velocity gradient, ρ_s is the density of the sediment and ρ_w density of the water, $\overline{\rho}$ is the mean density of sediment-water mixture and can be approximately replaced by ρ_w, g is the gravity constant;.

The dependence of SSC stratification effects on the gradient Richardson number was indicated in studies by Wolanski et al. [1988] and Sheng and Villaret [1989]. West and Oduyeme [1989] found a reduction in vertical sediment flux up to 90% at gradient Richardson numbers exceeding 0.25. Van der Ham et al. [2001] carried out detailed turbulence measurements by high-frequency flow metres and fibre optical turbidity sensors at three fixed levels close to the bed in the tidal channel of the Dollard estuary. The gradient Richardson number was calculated based on the data sampled by two neighbouring sensors at fixed position and effects of SSC induced density stratification on turbulence structure were analysed. A similar measurement was also carried out by West and Oduyeme [1989] using sensors at fixed heights above the bed to investigate the dependence of relative velocities upon the gradient Richardson number. However, fixed sensors are limited to environments where the position of the lutocline does not change in time.

Although the vertical adjustment of sensors in a vertical profiling mode appears to be an alternative, it is an intensive work and suffers from a constraint on temporal resolution at each sampling depth point. Acoustic backscatter profiling devices instantaneously offer a good estimation of SSC distribution in the whole water column [*Gartner*, 2004; *Merckelbach and Ridderinkhof*, 2006; *Thorne et al.*, 1993; *Topping et al.*, 2007; *Vincent*, 2007]. However, in a highly turbid environment with extremely high SSC and irregular geometry of particles due to flocculation, uncertainties in the acoustic absorption character of suspended matter make the quantification of SSC, a very complex, yet not fully resolvable task [*Gray and Gartner*, 2009; *Thorne and Hanes*, 2002].

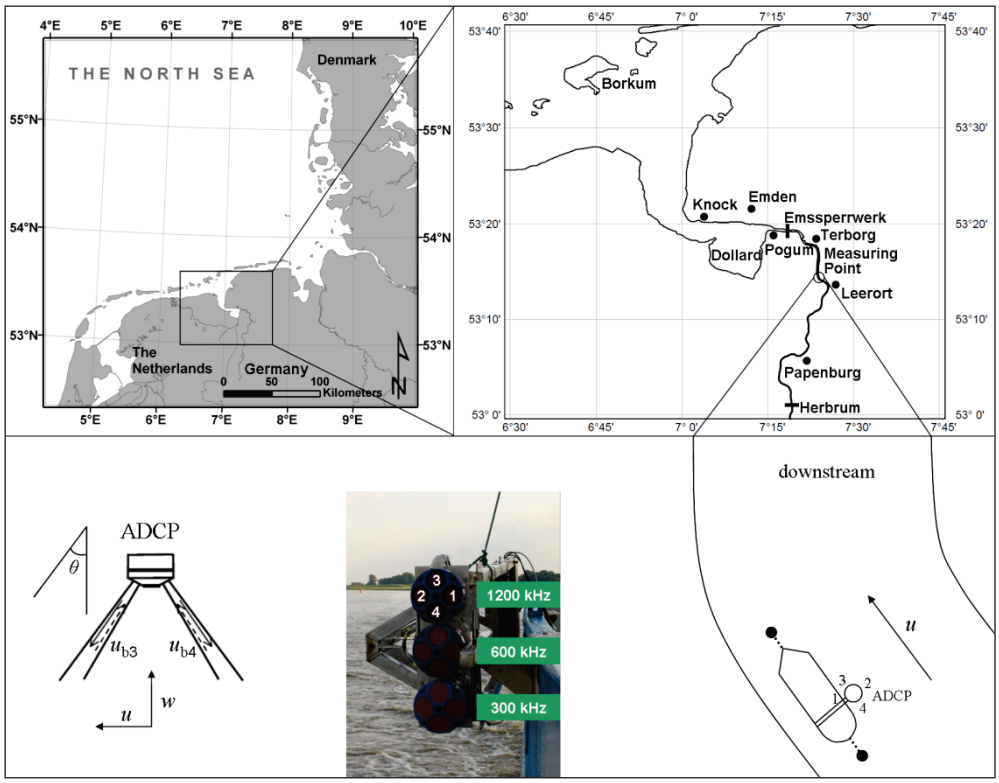

Figure 6.1: Location of the fixed measuring point, arrangement of the ship and ADCP at the measuring point and layout of the three ADCPs with different operational frequencies. 1, 2, 3, 4 denote beam 1, 2, 3 and 4, respectively, for all ADCPs on the frame.

In this paper we demonstrate a characterisation of lutoclines in estuarine high suspension load layers and mobile fluid mud by conventional Acoustic Doppler Current Profilers (ADCPs). The gradients in acoustic backscatter of 300 and 600 kHz ADCP were used to specifically derive the SSC gradient at the lutocline without the need for a calibration of the acoustic backscatter to SSC.

By combination with the velocity gradient measured simultaneously by a 1200 kHz ADCP, the gradient Richardson number was calculated. This procedure is shown on a data-set from River Ems in Germany, which was acquired during the sediment and hydrodynamic response of the estuarine system to weir closure, opening and subsequent flushing. Local tidal asymmetry induces strong near bed transport of significant layers of high concentrated mud suspensions, which are advected upstream and finally form a stable fluid mud.

6.2 Regional setting and background

The Ems estuary is a partially mixed, mesotidal estuary, which is located at the border of the Netherlands and Germany (Figure 6.1). The estuary connects the north-eastern part of the

Netherlands and the north-western part of Germany with the North Sea and forms an important navigation route for sea-going and river ships. Between the North Sea barrier islands and the harbour town of Emden the water depth averages between 10 and 20 m, while much of the remaining 53 km to the tidal weir in Herbrum is maintained at a navigable depth around 7 m [*Talke et al.*, 2009]. In the estuary the actual mean tidal range increases upstream from 2.4 m at the island of Borkum to its maximum of 3.5 m at Papenburg and then decreases upstream to 2.7 m at the tidal border at Herbrum [*Herrling and Niemeyer*, 2008]. Approximately 90% of the freshwater input into the estuary comes from the Ems River with an average fresh discharge of 100 m^3/s [*de Jonge*, 1992]. In addition, the Ems estuary is characterised by a large gradient in salinity. A maximum gradient is found in the vicinity of Emden under a mean freshwater discharge. For mean conditions of freshwater discharge and tidal current, a salt level of less than 0.5 PSU can be found near Papenburg, less than 3 PSU at Terborg and 7 PSU at Emssperrwerk [*Krebs and Weilbeer*, 2008].

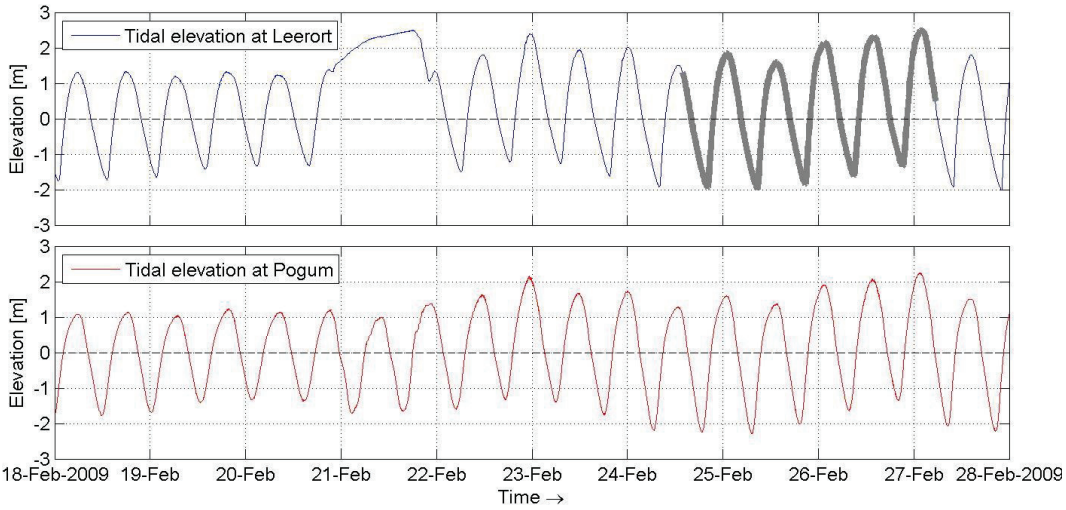

Figure 6.2: Tidal elevation at the tidal gauges at Leerort and Pogum. The thick grey line denotes the measuring period.

The Ems estuary is a relatively young hydro-morphological system with an age of just a few thousand years and hence has a highly dynamic character [*Krebs and Weilbeer*, 2008]. The morphology in the estuary is characterised by highly dynamic tidal channels and flats [*Van de Kreeke et al.*, 1997]. Natural and anthropogenic processes induce continuous sedimentation and erosion or the migration of tidal channels and gullies. The bed sediment composition in the estuary varies from very high mud contents (>75%) on the intertidal flats and

the margins of the Dollard Bay to very low cohesive sediment contents (<2%) in the estuarine inlet and the offshore areas [*Herrling and Niemeyer*, 2008].

The content of cohesive sediment is strongly dependent on the degree of exposure to currents and waves. The remaining sediment percentage mainly consists of fine to coarse sands, while larger grain sizes are found in the tidal channels and the estuarine inlet. Significant layers of fluid mud are common in the reach between Knock and Leerort [*Herrling and Niemeyer*, 2008] and even were recently found in the reach upwards to the weir at Herbrum [*Talke et al.*, 2009], which cause pronounced changes on the density and viscosity over the vertical.

In the Ems River the barrier work "Emssperrwerk", is situated about 3.5 km upstream from Pogum (Figure 6.1). This barrier functions to protect upstream country from storm surges and regulate the water level for shipping. The measurement campaign presented in this paper was undertaken some days after a temporary closure of the barrier to allow for a large ship passage from a shipyard in Papenburg to the North Sea. As a result of the closure of the barrier work and prominent river runoff, in the upper estuary the tidal elevation at gauge Leerort was continuously rising after February 21, while in the same period the change of the tidal elevation at Pogum downstream from the barrier work seems to be not affected by the closure of the barrier work (Figure 6.2).

6.3 Methods

The presented data on the local hydro- and sediment dynamics were collected from 18:48 on the 24th to 05:32 on the 27th February 2009. The collection was started three days prior to the spring tide on the 27th. During these almost 55 hours the research vessel "FK Senckenberg" was moored between two dolphins close to the main navigation channel near the western bank of the Ems estuary (53°14'11.51"N, 7°23'48.63"E, approximately 22 km upstream of Emden, see Figure 6.1).

Three RDI ADCPs with different operational frequencies were mounted on the starboard side of the ship (Figure 6.1). Additionally, an optical backscatter sensor (OBS) was used to profile the water column for almost one tidal cycle. The elevation of all data at sampling points was tidally corrected. The water level was recorded at the tidal gauge of "Leerort" approximately 3.5 km away from the measuring position.

6.3.1 Acoustic Doppler Current Profilers

Three standard RD Instruments Rio Grande ADCPTM with operational frequencies of 300, 600 and 1200 kHz were deployed (RD Instruments, 1996). All ADCPs utilised a same vertical resolution (bin size) of 25 cm. Their sampling frequencies were 0.67 Hz for the 300 kHz ADCP, 3.57 Hz for the 600 kHz ADCP, and 0.92 Hz for the 1200 kHz ADCP respectively. The three ADCPs were mounted with Beam 3 facing the bow of the ship (NW direction) as marked in Figure 6.1.

Due to the location of the ADCPs at 1.35 m below the water surface and the specific blanking distance below the acoustic transducers for each device, data available appeared 2.8, 2.08 and 1.9 m below the water surface for the 300, 600, 1200 kHz ADCP respectively. Invalid bins were identified by outliers and removed prior to analysis. Due to the fact that the bin size (a depth cell) of 25 cm is too small for the 300 and 600 kHz to sample reliable information with regard to current velocity, the information with regard to current velocity was taken from the 1200 kHz ADCP.

As shown as Figure 6.1, the ship was aligned parallel to the channel. Therefore a longitudinal streamwise velocity u along the channel could be calculated:

$$u = \frac{u_{b4} - u_{b3}}{2\sin\theta} \tag{6.2}$$

In which u_{b3}, u_{b4} are the measured along beam velocities of beam 3 and beam 4 of the 1200 kHz ADCP, and $\theta = 20°$ is the angle of the beam to the perpendicular direction (Figure 6.1). In the post-processing of ADCP data a 10-minute averaging period was used to calculate mean velocities and turbulence statistics. If the number of valid velocity data was less than 80% of the total number in the averaging period of 10 minutes, the mean velocity was treated as an invalid value in the cell at corresponding depth and time points. The velocity gradient U_{grd} is defined as:

$$U_{grd} = \frac{\partial \bar{u}}{\partial z} = \frac{\bar{u}_{upper} - \bar{u}_{lower}}{\Delta z} \tag{6.3}$$

where $\bar{u}$ is the mean longitudinal velocity based on the 10-minute averaging period, $\bar{u}_{upper}$ and $\bar{u}_{lower}$ represent the mean longitudinal velocity in the upper bin and neighbouring lower bin respectively, z is positive upwards, and Δz is the bin size of 0.25 m. A turbulent intensity $\overline{u'^2}$ was calculated:

$$\overline{u'^2} = \frac{1}{n}\sum_{i=n}\left(u_i - \bar{u}\right)^2 \tag{6.4}$$

In which *n* is the number of samples in an averaging period of 10 minutes; *ui* is the instantaneous longitudinal velocity *u* for each sample.

The ADCP acoustic backscatter intensities of the 300 and 600 kHz ADCPs were used to provide qualitative information on suspended matter in the water column. A conversion from received device specific echo intensity [counts] to acoustic backscatter [dB] took into consideration device specific variables, effects of beam spreading, and sound adsorption due to water [*Deines*, 1999].

Sound absorption due to suspended matter in the water column was not taken into account due to the unknown particle size distribution and real suspended matter concentration. The mean acoustic backscatter of beam 3 and beam 4 was calculated for each vertical bin and averaged for 10-minute windows. Similar to definition of the velocity gradient, the backscatter gradient SV_{grd} [dB/m] is defined as:

$$\mathrm{SV}_{grd} = \frac{\overline{\mathrm{SV}}_{upper} - \overline{\mathrm{SV}}_{lower}}{\Delta z} \tag{6.5}$$

where $\overline{\mathrm{SV}}_{upper}$ and $\overline{\mathrm{SV}}_{lower}$ represent the mean backscatter intensity in the upper bin and neighbouring lower one respectively, and Δz the bin size equal to 0.25 m.

6.3.2 Optical backscatter sensor

An optical backscatter sensor (OBS) ViSolid® 700 IQ (Wissenschaftlich-Technische Werkstätten GmbH) was used to infer the mass concentration (or dry density) in the water column by the light scattered and reflected by the total suspended particulate matter. OBS data was calibrated for suspended sediment concentration (SSC) on filtered and dry weighted water samples of suspended sediment [*Trevethan et al.*, 2009].

For technical reasons the OBS could not sample exactly at the measuring volume of the ADCPs but some metres towards the channel centre. The SSC was profiled at roughly 1 m intervals over the depth by a crane on the starboard side of the ship. It recorded the data with a sampling frequency of 1 Hz. The vertical profile of mean SSC was derived by averaging 50 samples at each depth. The SSC gradient was calculated as:

$$C_{grd} = \frac{\partial \bar{c}}{\partial z} = \frac{\bar{c}_{upper} - \bar{c}_{lower}}{\Delta z} \tag{6.6}$$

where $\bar{c}$ is the mean SSC based on the 50-second averaging period, $\bar{c}_{upper}$ and $\bar{c}_{lower}$ represent the mean SSC at the upper sampling point and neighbouring lower one respectively, and Δz is the interval distance between two neighbouring sampling points, which is roughly equal to 1 m.

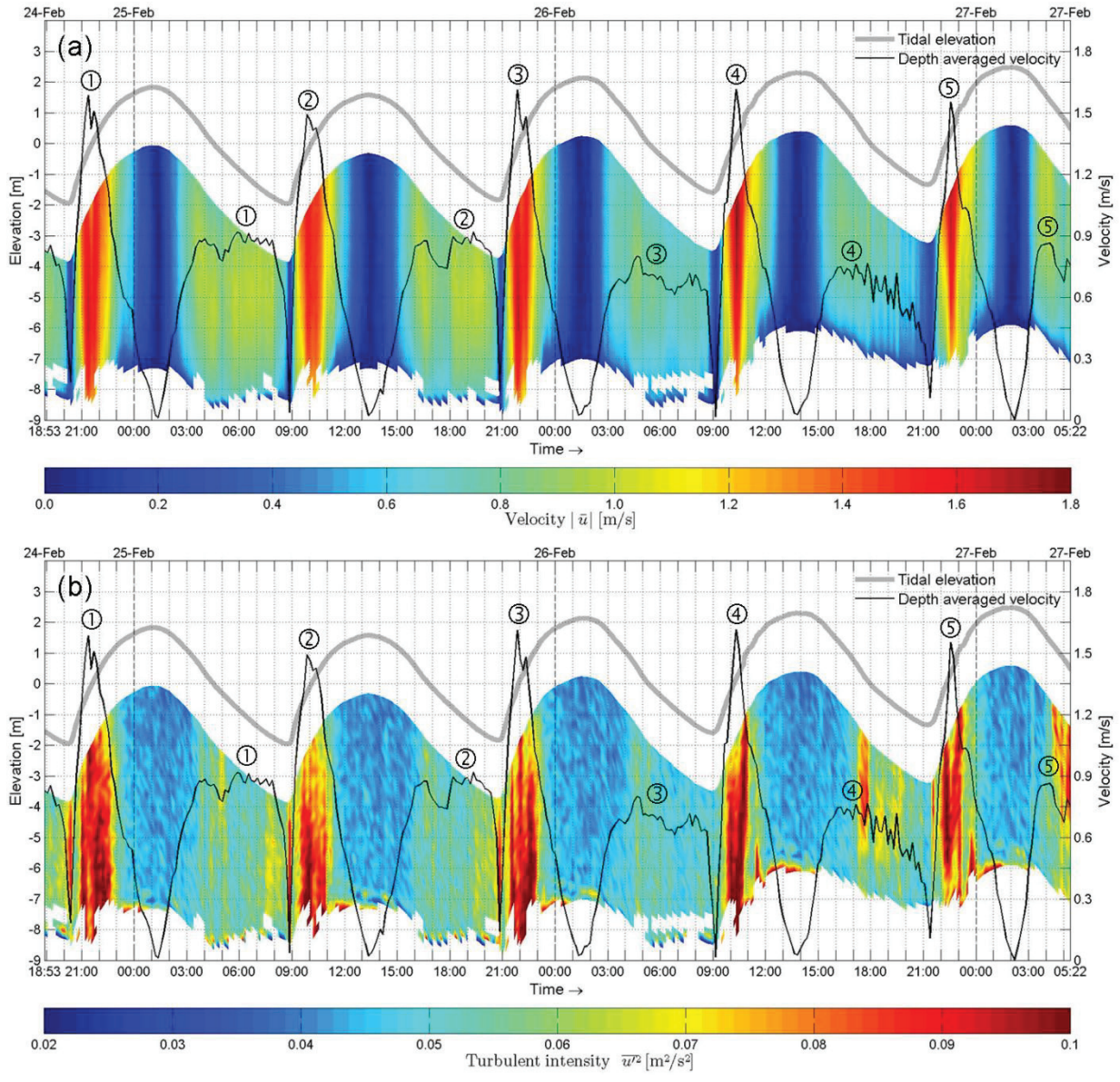

Figure 6.3: Time averaged longitudinal velocity (a) and turbulent intensity (b) over the measurable range and depth averaged velocity from the 1200 kHz ADCP. The numbers in circle denote floods and ebbs in sequence.

6.4 Results

6.4.1 Acoustic Doppler Current Profiler

6.4.2 Hydrodynamics

Streamwise velocity magnitude profiles, depth averaged velocity and the tidal elevation as calculated from the 1200 kHz ADCP data are shown in Figure 6.3 (a) for five complete tidal cycles. The tidal flow was asymmetric with higher velocities during a short flood period compared to the longer ebb. The depth averaged velocity of the flood current exceeded 1.5 m/s at peak with a pronounced acceleration around 4.17×10^{-4} m/s^2 from a low slack water and then gradually decreased to high slack water. Depth averaged velocity of the ebb current only reached 0.9 m/s at peak and the peak currents remained almost constant for about 4 hours in terms of the two ebb periods on February 25.

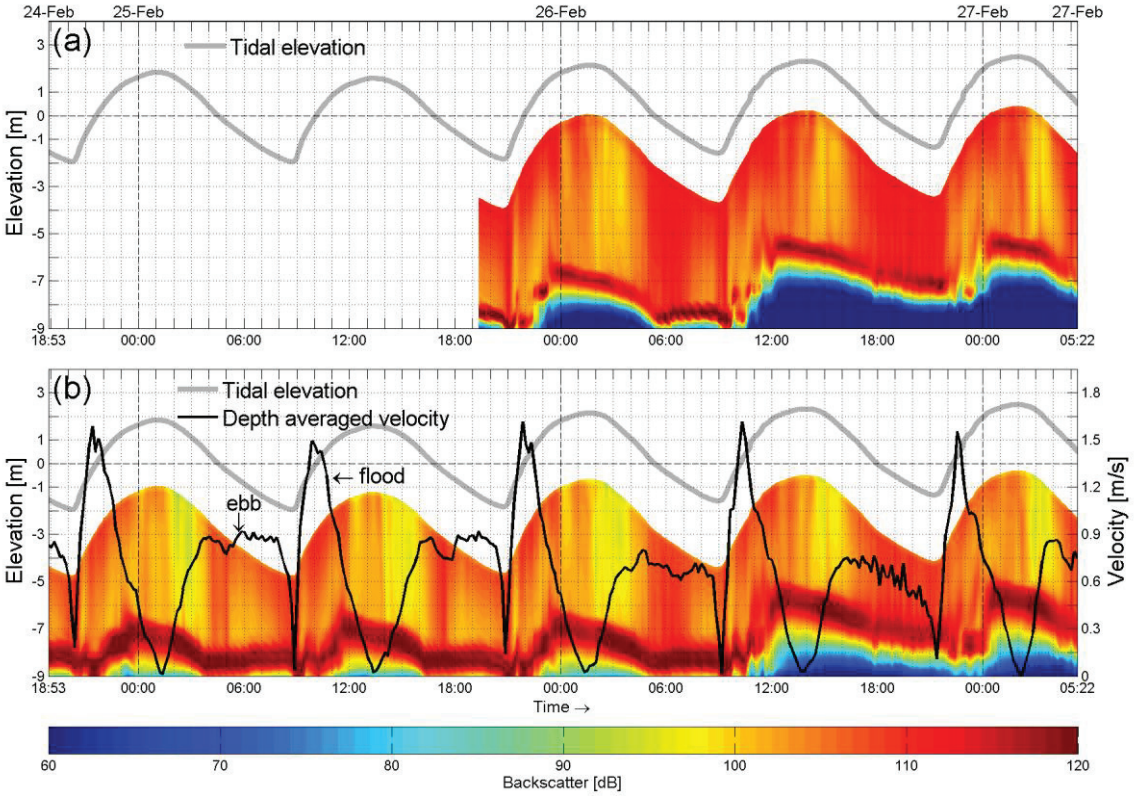

Figure 6.4: Backscatter intensity of two ADCPs and the tidal elevation (thick grey line) of the tidal gauge at Leerort. a: Backscatter intensity of the 600 kHz ADCP. The information before 19:21 on the 25th was missing, which can be also seen in Figure 6.5. b: Backscatter intensity of the 300 kHz ADCP.

During the two following ebb periods on February 26, the peak current was reduced to 0.75 m/s and the second ebb currents occurring in the period from 14:00 to 21:00 decreased more gently with remarkable oscillations towards the low slack water. Turbulent intensity was very high during flood phases, throughout low water slack and the ebb periods, compared to very low values around high water (Figure 6.3, b).

High turbulent intensity values at the lowermost part of the water column are not taken into account in the analysis as they are most probably biased by technical constraints of the ADCP. Note the change in detectable depth over time. The duration of high slack water is much longer (more than 5 hours from the flood peak current to the high ebb current) than the low slack water (less than 2 hours from the high ebb current to the flood peak current).

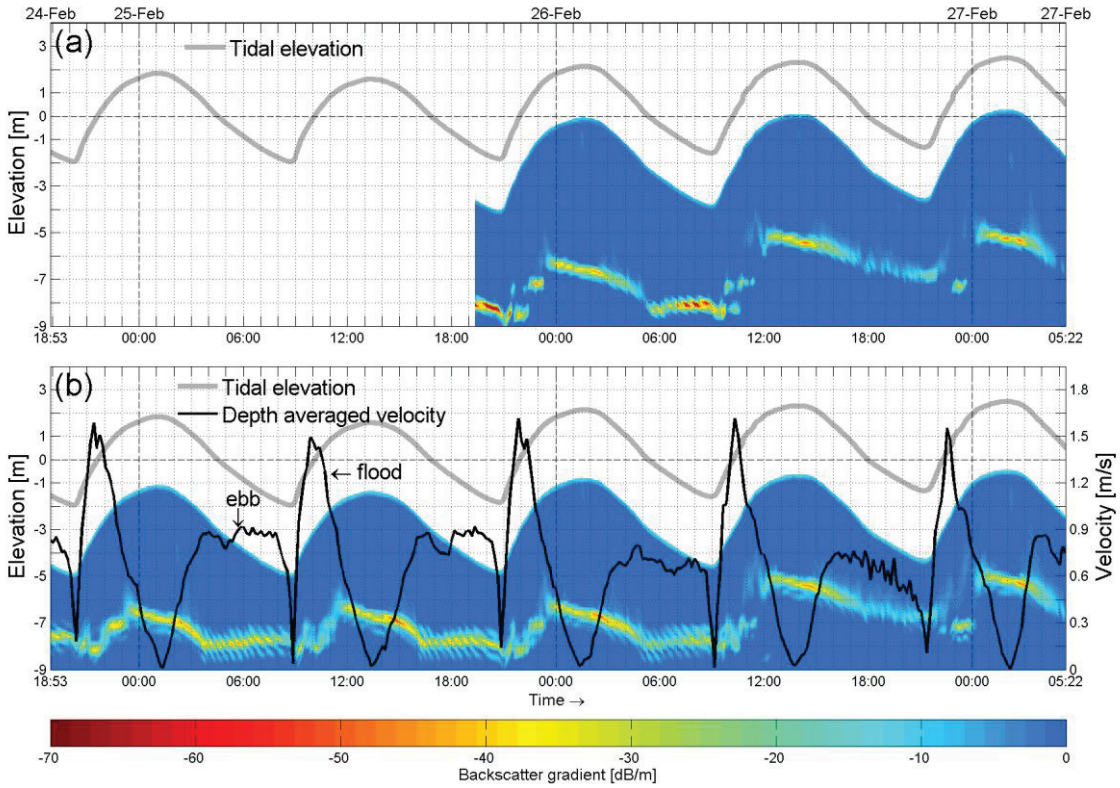

Figure 6.5: Backscatter gradient SV_{grd} of two ADCPs and the tidal elevation (thick grey line) of the tidal gauge at Leerort. a: Backscatter gradient of the 600 kHz ADCP. b: Backscatter gradient of the 300 kHz ADCP.

6.4.3 Acoustic backscatter

The evolution of acoustic backscatter profiles in time is shown in Figure 6.4 for the 300 kHz and 600 kHz ADCPs. Absolute values differ, but the variation of patterns has great similarity in the two ADCP signals. During ebb currents strong backscatter intensity takes

place in almost whole water column, whereas during flood current the strong backscatter intensity takes place only in the upper part of water column and decays quite fast downwards to the lower part.

Both ADCPs indicate a distinct peak in acoustic backscatter below a level of about -5 m almost throughout the whole measuring period. The elevation of this peak changes significantly during each tidal cycle and even more for the fourth one. During the periods of high ebb flow velocities, the backscatter peak appears at nearly constant elevation of around -8m except for the fourth ebb period during which the backscatter peak appears at around -7 m. In the fourth flood period backscatter peak has been elevated to reach the highest point at the elevation of around -6 m after the flood current decay. During the long high water slack phase the position of the backscatter peak drops with a constant rate of about 0.2 m/h (0.056 mm/s).

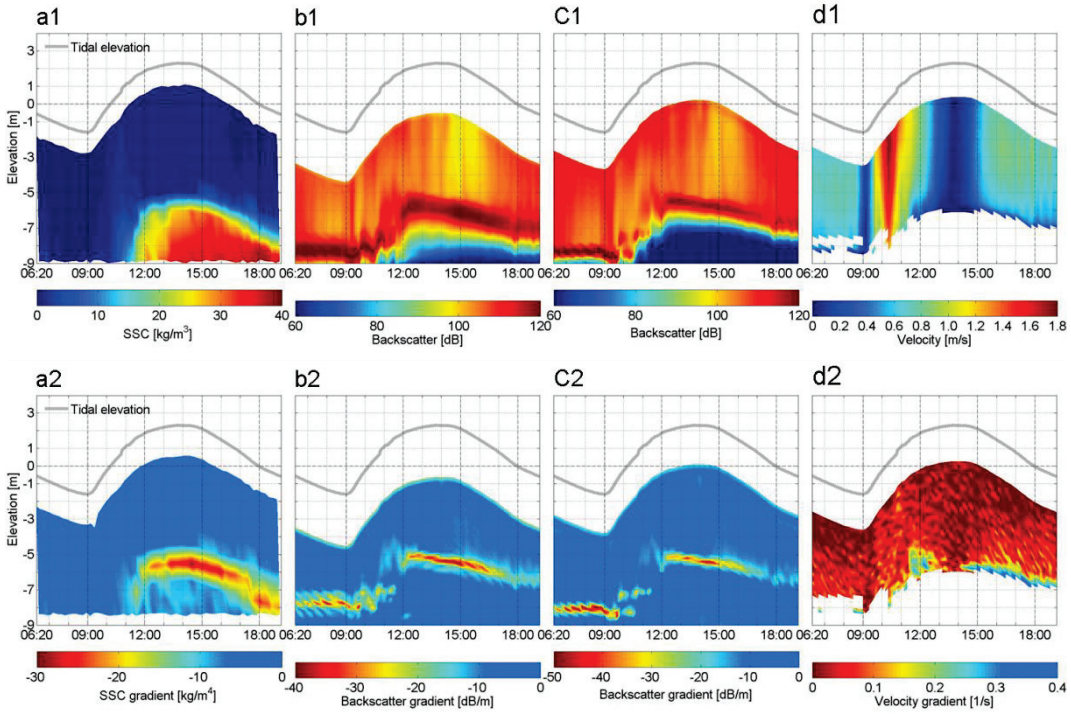

Figure 6.6: Suspended sediment concentration (SSC), backscatter intensity and longitudinal velocity and their gradients C_{grd}, SV_{grd}, and U_{grd} for a complete tidal cycle from 06:20 to 19:04 on February 26. a1: SSC by OBS, a2: SSC gradient derived from a1; b1 and c1: backscatter intensity from the 300 and 600 kHz ADCP, respectively; b2 and c2: backscatter gradient derived from b1 and c1, respectively; d1: longitudinal velocity sampled by the 1200 kHz ADCP; d2: velocity gradient derived from d1.

The characteristics of the acoustic backscatter over time are further described by its gradient as shown in Figure 6.5. It shall be noted that only the (negative) gradient down to the

level of maximum backscatter intensity is shown for a better visualisation of patterns. The two ADCPs show a similar variation pattern with respect to the backscatter gradient. Absolute values are different, but the above description of the time variation in the ebb and flood periods is similar. The position of the peak in backscatter gradient changes over time with a typical pattern in the first three tidal cycles: After the ebb current reaches its maximum value, the elevation remains at about -8 m throughout the whole ebb current. After low water slack the elevation of the backscatter gradient peak increases by about 1 metre (to about -7 m), with a concurrent decrease in intensity.

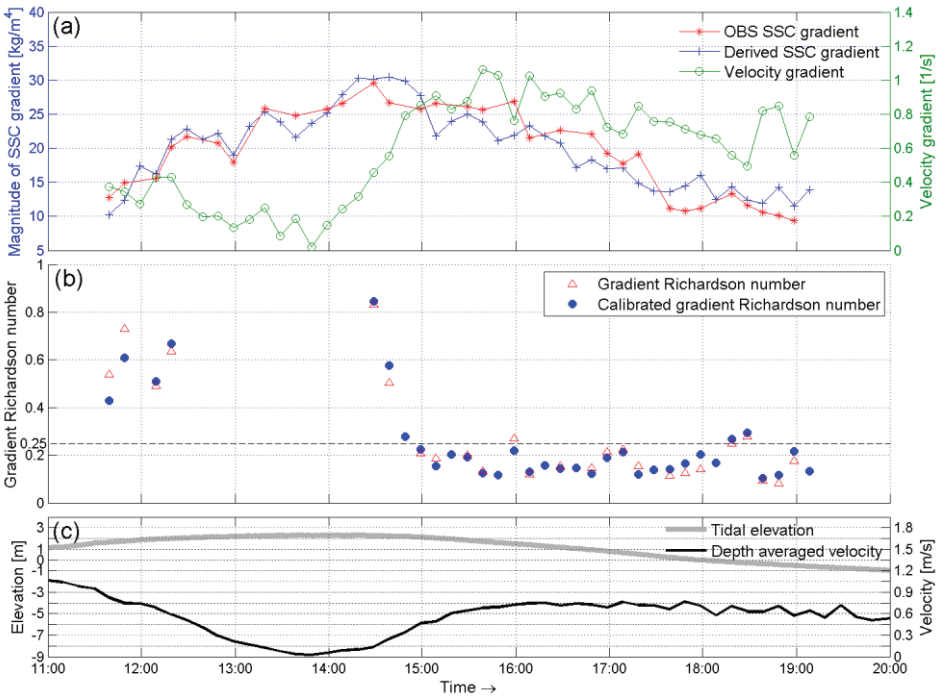

Figure 6.7: a: SSC gradient measured by OBS, SSC gradient derived from the backscatter gradient from the 300 kHz ADCP by linear fitted function (see Figure 6.8), and the velocity gradient from the 1200 kHz ADCP. b: Gradient Richardson number Ri calculated based on the directly measured SSC gradient by OBS and velocity gradient as shown as in (a), and the calibrated gradient Richardson number Ri_{cbs} calculated based on the derived SSC gradient and directly measured velocity gradient as shown as in (a). c: Depth averaged velocity measured by 1200 kHz ADCP and the tidal elevation.

After the flood peak and a decay of the mean current velocity below about 0.6 m/s the highest elevation was observed. During high water slack the peak in backscatter gradient is lowered at an approximate rate of 0.2 m/h with a pronounced increase in intensity. With the increase in ebb current velocities the signal decays and drops at a higher rate to the -8 m level. This pattern is different in the last two tidal cycles, where highest elevation of the signal peak

reaches the nearly -5 m level with the decaying flood current. Subsequently its elevation is reduced (about 2 m in the following 10 hours). During high water slack the signal gains intensity until it decays throughout the ebb period. This pattern is repeated at the very last observed tidal cycle.

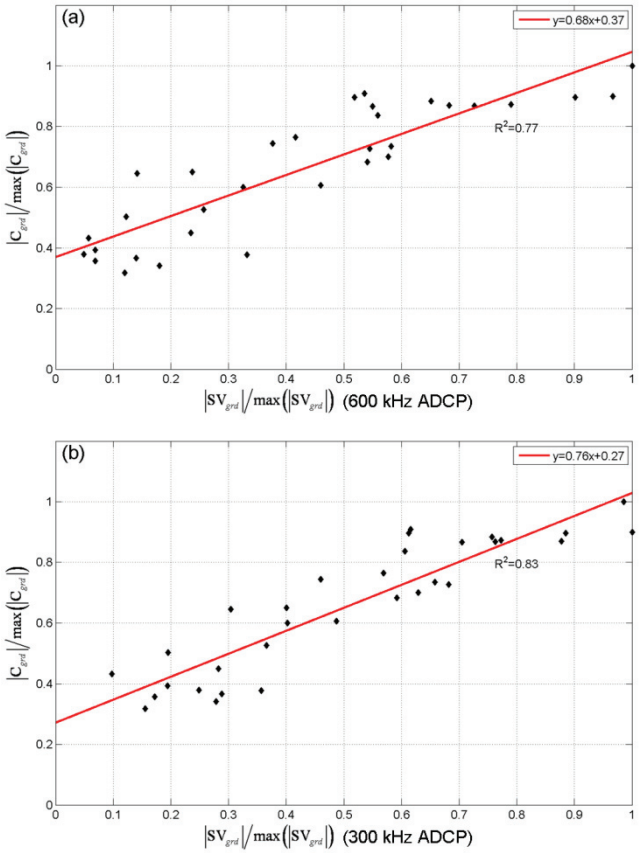

Figure 6.8: Linear fitted regression based on the correlation between backscatter and SSC gradients for the 600 kHz ADCP (a) and the 300 kHz ADCP (b).

6.4.4 Suspended sediment concentration

OBS profiling was carried out for a single tidal cycle the period from 06:20 to 19:04 on February 26. The evolution of the distribution of suspended sediment concentration (SSC) is visualised by temporal interpolation of the calibrated optical backscatter profiles which were taken at discrete sampling points spaced by around 1 metre. Each profile was completed within 10-15 minutes, which was depending on the temporal tidal elevation (Figure 6.6, a1). During the initial time of the ebb phase (06:20 to 09:00) a low SSC (less than 1 g/l) was observed in the water column. After the short low slack water around 09:00, the SSC showed a slight increase (over than 1 g/l) in the entire water column. The increase was even visually found

near the water surface at the peak flood current around 10:30 and concurrently the SSC reached over 10 g/l at the bottom.

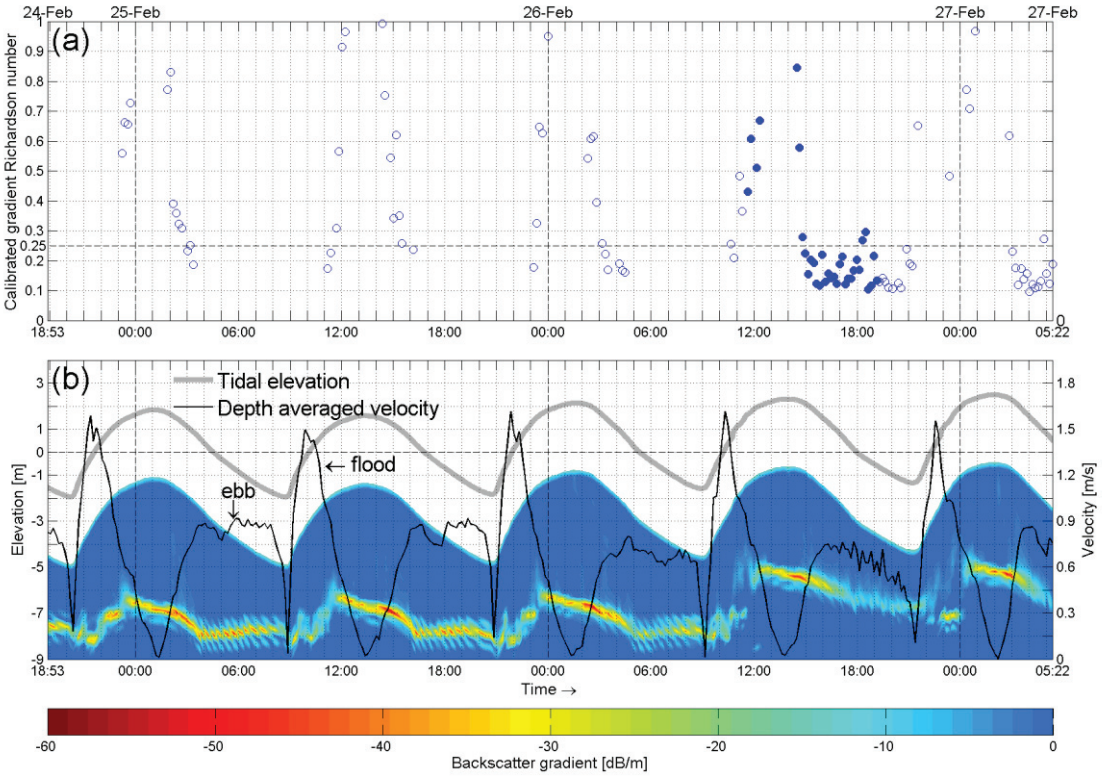

Figure 6.9: a: Gradient Richardson numbers calculated for the whole measuring period based on the SSC gradient derived from the linear fit function (300 kHz ADCP) in Figure 6.8 and directly measured velocity gradient by the 1200 kHz ADCP. The solid circles are the points used for getting the linear fit function between the backscatter and SSC gradients in Figure 6.8. b: Backscatter gradient of the 300 kHz ADCP and the tidal elevation, which is as same as Figure 6.5 (b) and used to concurrently see the evolution of lutocline and exposure of consolidated bed during ebb currents.

Subsequently around 11:30 a thick (3 m) layer of high SSC (>30 g/l) at the bottom appeared. During the period of high slack water from about 13:00 to 15:00 this layer occupied a large part of the entire water column from the bottom upwards to the elevation around -5.5 m and the SSC at the bottom even exceeds 35 g/l. After the high slack water the height of the described layer decreases to the elevation of around -6.5 m while the SSC at the bottom increases to 40 g/l. The position and intensity of the peak in SSC gradient (Figure 6.6, a2) is reflected by the distinct signals occurring respectively in backscatter intensity for the 300 and 600 kHz ADCPs (Figure 6.6 b1 and c1) as well as the peak backscatter gradients in Figure 6.6 (b2 and 6c2).

6.5 Discussion

The Ems environment is known for featuring pronounced layers of fluid mud. However relevant field and modelling studies for the fluid mud in the estuary are few [*Habermann and Wurpts*, 2008; *Trevethan et al.*, 2009; *Wurpts*, 2005a]. Our observations were made after a flushing of the system, probably an effect of enhanced ebb currents by an abrupt opening of the barrier some days before the measurements.

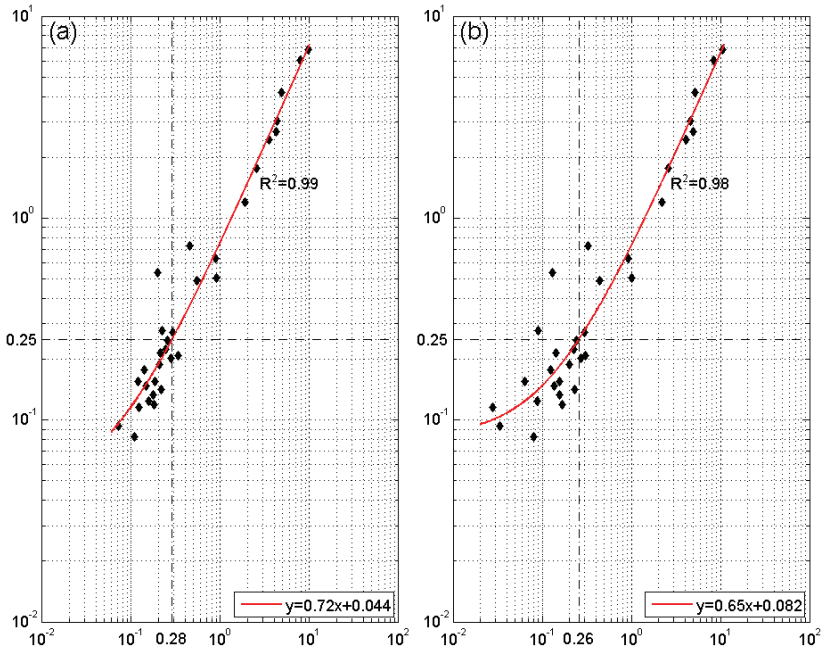

Figure 6.10: The linear fitted regression for two variables backscatter gradient Richardson number Ribs and gradient Richardson number Ri. a: The linear fit function gives a squared correlation coefficient equal to 0.99 for the regression based on the backscatter gradient from the 300 kHz ADCP. b: The linear fit function gives a squared correlation coefficient equal to 0.98 for the regression based on the backscatter gradient from the 600 kHz ADCP.

The data presented above indicates the oscillatory movement of a bed layer of mud suspension into and out of the measuring position. Observed concentrations suggest a classification of the mud suspension as "High concentrated mud suspension" [*Winterwerp*, 1999] or "fluid mud" [*Whitehouse et al.*, 2000]. Without the requirement of a quantitative calibration the gradient of ADCP acoustic backscatter was found to describe the position and some indication of strength of the fluid mud lutocline.

Thus a continuous monitoring of fluid mud dynamics was achieved for five tidal cycles. The flood currents obviously move the fluid mud body upstream, and the ebb currents downstream. In the first three observed tidal cycles the fluid mud is transported out of the point of observation by the ebb currents. This is seen in the rather continuous reflector at -8 m in the ADCP signals, which is interpreted as the rigid, consolidated bed. However, as an effect of the flood dominance, a resulting built-up can be observed, resulting in a persistent fluid mud layer at the bed in the last day of measurements. As shown for the standard 300 and 600 kHz ADCP data it can be observed that also some characteristics of the lutocline can be described: In times of a decay of hydrodynamic energy, the backscatter gradient intensity is enhanced. This is the case especially during the long high water slack time. This is interpreted as a formation of a pronounced lutocline (steep gradient in mass concentration over the vertical) by the rapid settling of mud flocs and subsequently hindered settling effect. Based on the measured data the stability of the lutocline can be quantified by calculation of gradient Richardson numbers.

6.5.1 Gradient Richardson number at the lutocline

To quantify the stability of the interface between low and high SSC as seen in the gradient of OBS data, gradient Richardson numbers were calculated using the observed velocity gradients (1200 kHz ADCP) and OBS SSC gradients (Figure 6.7). The *Ri* on ADCP derived velocities and SSC (by calibrated OBS) is shown for about 8 hours. The lutocline stability changes throughout the formation of a lutocline after decelerating flood currents, reaching a maximum (*Ri*) at high water slack. Subsequently *Ri* decreases to a full break down of the lutocline ($Ri<0.25$) with increasing ebb currents.

6.5.2 Calibrated gradient Richardson number at the lutocline

To allow for longer time series on lutocline stability the use of acoustic backscatter gradient of two ADCPs is tested. Without the need to calibrate from absolute values in terms of SSC, the gradient of backscatter intensity is directly calibrated to derive SSC gradient in the formulation of *Ri*. The observed similarity in SSC gradient (C_{grd}) and ADCP backscatter gradient (SV_{grd}) can be quantified by a linear regression of a normalised backscatter gradient $\left|SV_{grd}\right| \Big/ \max\left(\left|SV_{grd}\right|\right)$ derived from the 300 (600) kHz ADCP and the SSC gradient $\left|C_{grd}\right| \Big/ \max\left(\left|C_{grd}\right|\right)$. This results in coefficients of determination (R^2) of 0.83 (0.77) as shown

in Figure 6.8. The derived linear functions can be used to calibrate the acoustic signals forming a calibrated backscatter gradient SV_{grd}^{cbs} to represent the SSC gradient in *Ri*:

$$SV_{grd}^{cbs} = -\max\left(\left|C_{grd}\right|\right) \cdot F\left(\left|SV_{grd}\right| \Big/ \max\left(\left|SV_{grd}\right|\right)\right) \tag{6.7}$$

in which *F* represents the linear fit function shown in Figure 6.8.

Based on the measured velocity gradient from the 1200 kHz ADCP and backscatter gradient from the 300 kHz ADCP, a calibrated gradient Richardson number Ri_{cbs} was calculated at the position of the maximum backscatter gradient (Figure 6.7), which is assumed to locate the fluid mud lutocline:

$$Ri_{cbs} = \frac{-((\rho_s - \rho_w)/\rho_s) g SV_{grd}^{cbs}}{\overline{\rho} U_{grd}^2} \tag{6.8}$$

The dynamics of this lutocline as observed in 5 tidal cycles in the Ems estuary then can be quantified in terms of Ri_{cbs} (Figure 6.9). In times when no fluid mud was existing at the measuring position (ebb phases of first 3 tidal cycles), and at times of very low current velocities (very high velocity gradient) no significant Ri_{cbs} can be calculated.

A significant amount of mud (height O(~1 m)) is transported upstream into the point of observation with the high energetic flood currents. The suspended material then settles towards slack water. Ri_{cbs} shows a stabilisation ($Ri_{cbs} > 0.25$) and the formation of a distinct lutocline which is existent for several hours over high water slack. The rising ebb currents then break down the stratification, and remove the fluid mud layer down to a depth which is considered as being the consolidated bed. In the subsequent tidal cycles the lutocline appears higher (O(decimetres)) at each high water and the ebb currents need longer (2, 2.5, and 3 h after slack water) to erode and move it out the observation point. Finally at the last observed tidal cycle, not the entire fluid mud layer is eroded during ebb current and a consistent layer, known from other studies at this location is formed. In this period even at the very short low water slack a stable lutocline ($Ri_{cbs} > 0.6$) was observed.

The importance of the gradient Richardson number for internal waves and turbulent diffusion was introduced in studies by Shi et al. [1996] for the Yangtze estuary and Shi [1998] for the Hangzhou bay. However, quantitative calculations for the gradient Richardson number were not performed in their studies. Shi et al. [2006] presented a stable and pronounced lutocline formed with a concentrated benthic sediment plume during flood decay as they observed in the Yangtze estuary. The concentrated sediment plume occupied nearly half of the total wa-

ter column and to a large extent was produced by the horizontal advection of flood current. No sediment entrainment by bottom shear stress was observed in the decaying flood currents. The observed concentrated sediment plume during the flood decay is very similar to our findings in that the concentrated benthic suspension layer returned to our measuring position during flood in each tidal cycle and the lutocline increased in strength with the current deceleration. However Shi et al. [2006] did not calculate gradient Richardson numbers to quantitatively measure the stability (or instability) of the lutocline and the effect of hindered settling was not examined due to the relatively lower SSC less than 10 g/l.

The calculation of the gradient Richardson number during in situ measurements of fluid mud was carried out in other studies [*Adams et al.*, 1990; *Van der Ham et al.*, 2001; *Wu et al.*, 2006]. In a channel that acts as drainage and sediment dispersal routes on a mudflat situated at the Yellow Sea coast of South Korea, Adams et al. [1990] found that lutocline development occurred only during ebbing tide and stratification intensity was indicated by calculations that yield Ri=0.33. In contrast to our measuring site, their measuring site is ebb dominant.

Van der Ham et al.[2001] deployed fixed sensors to investigate turbulent exchange of fine sediments in a tidal channel in the Dollard bay and showed that the measured gradient Richardson number behaved similar to our findings: the gradient Richardson number decreased with acceleration of currents and increased with deceleration of currents, and became indeterminable during periods of slack water. In the study focused on dispersion of disposed dredged slurry in the Yangtze estuary, Wu et al. [2006] used the critical value 0.25 to measure the stability of sediment plume and found that the lutocline was prone to develop with decay of currents from intermediate to neap tide. However, their studies were all carried out in the environment where the fluid mud layer was not present, the SSC was much lower than our findings and hence the hindered settling did not play an important role on the formation of lutocline.

Whereas in laboratory, studies on entrainment with regard to fluid mud layers were carried out by Kranenburg and Winterwerp [1997] and Bruens [2003]. They differentiate two modes for entrainment, which are comparable to our in situ observation. Mode I in which the fluid mud layer is entrained by the upper turbulent water layer, the position of fluid mud lutocline is lowered and the lutocline strength is reduced, is very similar to the destruction of the lutocline as we observed in ebb phases. While mode II in which a turbulent HCMS is able to entrain the upper water layer, the lutocline is elevated and its strength is also reduced, is simi-

lar to the return of the concentrated sediment plume as we observed at acceleration of flood currents.

6.5.3 Calculation of backscatter gradient Richardson number

A further analysis of the derived quantities has shown that also an uncalibrated backscatter gradient (after correction for beam spreading and sound absorption in water) can be used to assess the lutocline stability.

$$Ri_{\mathrm{bs}} = \frac{-((\rho_s - \rho_w)/\rho_s)\mathrm{g}\mathrm{SV}_{grd}}{\overline{\rho}U_{grd}^2} \tag{6.9}$$

As shown in Figure 6.10 for the 600 and 300 kHz ADCP reasonable agreements ($R^2 = 0.98$ and 0.99) between calculated backscatter Richardson number Ri_{bs} and the common gradient Richardson number Ri for which the SSC gradient (C_{grd}) directly derived from the OBS is used were found. However, the direct use of Ri_{bs} for the characterisation of the lutocline stability must consider the slight variation of critical threshold values, which depend on ADCP acoustic frequency (Figure 6.10).

6.6 Conclusions

The re-formation and dynamics of a mobile fluid mud layer as observed in five tidal cycles in the Ems estuary in Germany were described and quantified based on a new simple method of using standard commercial ADCPs (1200, 600 and 300 kHz). It was shown that for the quantification of the lutocline stability and the calculation of the gradient Richardson number at the fluid mud lutocline the SSC gradient could be replaced by the gradient of acoustic backscatter intensity.

The data shows the rapid re-establishment of a fluid mud layer after engineered flushing. The strong tidal asymmetry (tidal pumping) leads to a compensation within timescales of some days. A significant concentrated sediment plume (height O(~1 m)) was transported upstream into the point of observation with the high energetic flood currents.

The observed dynamics of the suspended matter follow a repeated cycle of settling and resuspension throughout the tidal cycles. After slack high water rapid settling of flocculated sediment and immediate formation of a stable lutocline is characterised by a rapid increase in gradient Richardson numbers. Subsequently the lutocline lowers at celerity of 0.056 mm/s for about 4 hours which is related to the self-weight consolidation (dewatering). Increasing ebb

currents completely remove the fluid mud body out of the domain of observation or break up the lutocline by enhanced turbulence which is reflected by low gradient Richardson numbers, below a critical value of about 0.25. In the subsequent tidal cycles the lutocline appears higher (O(decimetres)) at each high water and the ebb currents need longer (2, 2.5, 3 h after slack water) to erode and move it out the observation point. Finally at the last observed tidal cycle, not the entire fluid mud layer is eroded during ebb current and a consistent layer, known from other studies at this location is formed. The very short low slack water (less than 2 hours from the high ebb current to the flood peak current) features a temporary formation of a stable lutocline, which however is immediately destroyed by pronounced flood currents acceleration, and high turbulence intensity. Time scales for the formation of a stable lutocline at slack water are in the order of 4 hours. After the fluid mud layer which survived in the whole ebb period formed, even at the very short low water slack a stable lutocline ($Ri_{cbs} > 0.6$) was observed.

Acknowledgements

This study was funded through DFG-Research Center/Excellence Cluster “The Ocean in the Earth System”. We thank C. Maushake (Federal Waterways Engineering and Research Institute, Hamburg, Germany) for technical support, M. Trevethan (MARUM) for organising the field survey, A. Wurpts (Franzius Institute, Hanover, Germany) for assisting in the field measurements, the Federal Water and Shipping Administration Emden for tidal gauge information, and the captain and crew of FK Senckenberg.

Chapter 7: Paper VI

Bedload transport in an inlet channel during a tidal cycle

V. B. Ernstsen[1], M. Becker[1], C. Winter[1], A. Bartholomä[2], B. Flemming[2], J. Bartholdy[3]

[1]MARUM, Center for Marine Environmental Sciences, University of Bremen, Germany
[2]Senckenberg Institute, Department of Marine Science,Wilhelmshaven, Germany
[3]Department of Geography, University of Copenhagen, Denmark

River, Coastal and Estuarine Morphodynamics: RCEM 2007 (published)

Abstract

Based on high-resolution swath bathymetry measurements at centimetre-scale precision conducted during a tidal cycle in a dune field in the Grådyb tidal inlet channel in the Danish Wadden Sea, a simple tool to calculate bedload transport is presented. Bedload transport was related to simultaneous flow measurements using an acoustic Doppler current profiler. Spatially, bedload transport was higher on the dune crests than in the dune troughs of the large ebb-directed compound dunes, due to higher flow velocities at the crests than in the troughs. Temporally, bedload transport was higher in the troughs of the large ebb-directed compound dunes during the flood tide than during the ebb tide, due to higher near-bed flow velocities in the troughs of the compound dunes during the flood tide as compared to the ebb tide, resulting from flow exposure, i.e. the trough-sheltering effect of the compound dunes being active during the ebb tide, but negligible during the flood tide. Bedload transport was also predicted using five classical and widely used formulae. These predictors were all unable to depict the temporal variation in bedload transport during the tidal cycle. It is suggested that temporal variations in grain-size composition of the mobilised sediment should be taken into account by sediment transport formulae.

7.1 Introduction

Tidal inlet channels play an important role in the exchange of water and sediment between the open ocean and tidal basins. They are characterised by high flow velocities and, ac-

cordingly, the channel beds are typically sandy and covered with dunes. The sandy bed material is transported as bedload or as suspended load.

The classical way to directly measure bedload transport is by using conventional sand traps placed on the channel bed; however, when fine sands predominate such measurements are not reliable because unknown amounts of suspended material will also be trapped [c.f. *Van Den Berg*, 1987]. If the channel bed is covered with dunes, bedload transport can also be measured indirectly by calculating the sediment volume involved in dune migration, using sequential bed profiles from bathymetric measurements obtained by e.g. echo-sounding. The advantage of calculating bedload transport from remote bathymetric measurements is that the seabed remains undisturbed. This latter method of calculating bedload transport from dune celerity (migration rate) and dune dimensions (height and shape) was originally suggested and tested by Simons et al. [1965] on the basis of extensive flume experiments. The applicability of this method to quantify bedload transport has been discussed repeatedly in subsequent studies [e.g. *Engel and Lau*, 1980; *Hoekstra et al.*, 2004; *Van Den Berg*, 1987; *Wilbers and ten Brinke*, 2003], the general consensus being that the method is adequate to determine bedload transport. Recently, Ernstsen et al. [2005] applied the method in a tidal inlet channel on bed profiles extracted from bathymetric grids attained from recordings with a high-resolution, high-precision multibeam echo sounder (MBES) system. Furthermore, Duffy and Hughes-Clarke [2005], Knaapen [2005], and Knaapen et al. [2005] have recently developed new methods to determine dune migration from MBES images.

The introduction of high-resolution, high-precision MBES systems has also led to the development of new approaches to calculate bedload transport. Based on sequential MBES surveys in a dune field Abraham and Pratt [2002] proposed the Integrated Surface Difference Over Time (ISDOT) technique. They argue that bedload transport is equal to the change in volume over time for any incremental area (e.g. square foot) whether the area undergoes net deposition or erosion. Abraham and Pratt [2002] noted that the ISDOT technique apparently underestimated the bedload transport. This is not surprising, as the ISDOT technique is merely a difference plot between the channel bed at two different times, and does therefore not strictly determine the actually transported sediment volume.

The main aim of this paper is to present a simple method of calculating volumetric bedload transport based on sequential bed profiles of dunes attained from e.g. MBES surveys. Further aims are to present and explain the distribution of bedload transport across dunes;

and, finally, to evaluate how some classical and widely used bedload transport formulae perform when applied to a tidal inlet channel.

7.2 Study Area

Surveys were carried out along a 900 m long transect in the Grådyb tidal inlet channel which is located along the Danish west coast between the barrier spit of Skallingen to the northwest and the barrier island of Fanø to the southeast. This inlet connects the northernmost tidal basin of the Wadden Sea with the adjacent North Sea and also forms the navigation channel to Esbjerg (Figure 7.1Figure 7.1).

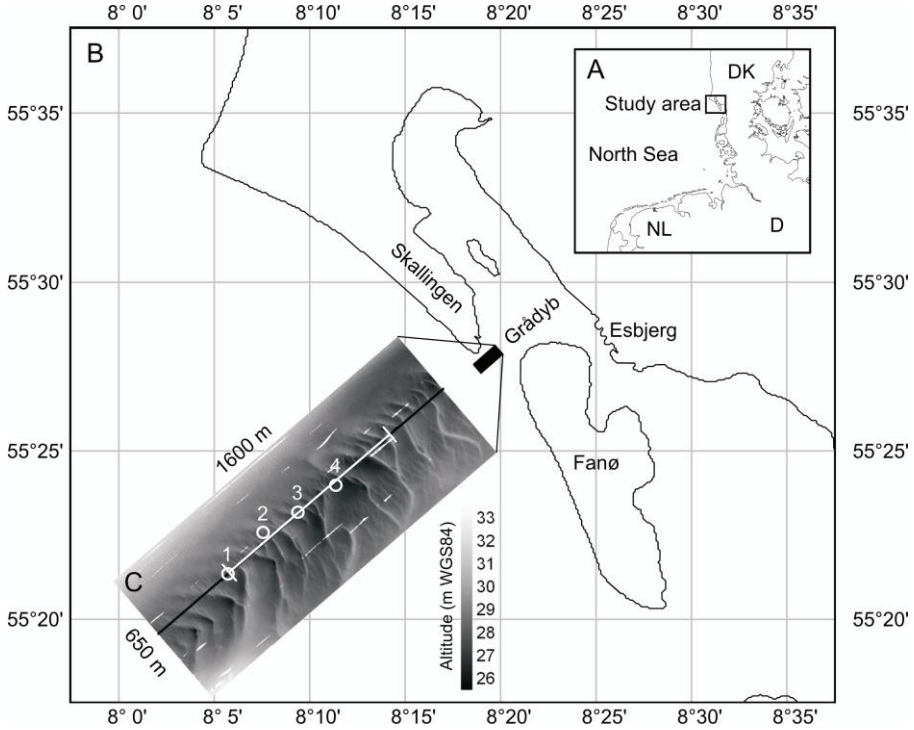

Figure 7.1: (A) Locality map of the study area. (B) Location of the survey area. (C) Bathymetry in the survey area as measured on 10 September 2002. In addition, the location of the 900 m long transect (part of the line between the two hatches) and the four bed sample sites (circles) labelled 1-4 are shown.

The tides are semidiurnal, with a mean tidal range of about 1.5 m and a tidal prism in the order of 150×106 m^3 [*Bartholdy and Anthony*, 1998]. The channel width is roughly 1 km and mean depths range from 10-13 m. The channel is ebb-dominated with maximum ebb and flood current velocities around 1.50 m/s and 1.25 m/s, respectively [*Bartholdy*, 2006]. The sandy channel bed (mean grain sizes of 0.3-0.7 mm) is covered with large to very large, ebb-directed, saddle-shaped compound dunes which are superimposed by small to medium

dunes that reverse direction according to the tide [*Bartholdy et al.*, 2002; *Ernstsen et al.*, 2006b; *Ernstsen et al.*, 2005].

7.3 Methods

7.3.1 Surveys and instruments

In total, 18 surveys were conducted along the transect (Figure 7.1) in the course of 9 h and 15 min during a tidal cycle on 11 September 2002 (Figure 7.2). The first survey was done around 07h15, i.e. ~1¾ h after high water and ~4¼ h before low water, and the last survey ended around 16h30, i.e. about ~5 h after low water and ~1 h before high water. In the following, the survey period is referred to as a tidal cycle, despite the fact that only 80% of the full tidal cycle was covered in this case.

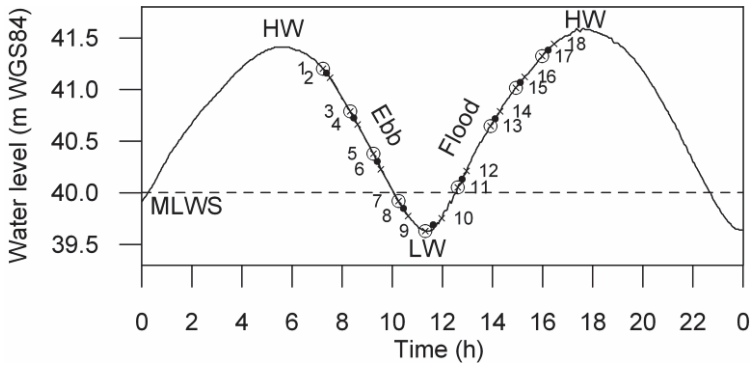

Figure 7.2: Water level curve on 11 September 2002 (Esbjerg Harbour). HW: High water. LW: Low water. MLWS: Mean low water springs. Crosses: The 18 MBES and ADCP surveys during the tidal cycle. Encircled crosses (odd numbers): The 9 MBES surveys analysed in this paper. Dots: The ADCP measurements compensated for over- and underestimation of flow velocities due to bottom-tracking (see text for further explanation).

Bed material was collected at four locations along the transect (Figure 7.1) on 9 September 2002, using a Shipek™ grab sampler.

Flow velocities were measured using a BroadBand™ (RDI) acoustic Doppler current profiler (ADCP) operating at 1,200 kHz, and the WinRiver™ (RDI) software package. The vertical resolution of the ADCP was set to 0.25 m. Lateral resolution was ~10 m at a ping rate of 0.25 Hz and a vessel speed of 2.6 m/s (5kn). The ADCP measurements were conducted parallel to the main current direction using bottom-tracking. The fact that the channel bed moved in the direction of the flow resulted in an underestimation of flow velocities when moving with the flow and an overestimation when moving against the flow. In order to com-

pensate for this over- and underestimation of flow velocities, the average values between two measurements run in opposite direction were used (marked by dots in Figure 7.2).

Bathymetry was recorded by means of a SeaBat™ 8125 (RESON) multibeam echo sounder (MBES) system operating at 455 kHz, and the 6042™ version 7 (QINSY/RESON) data collecting and processing software package. Vertical resolution of the MBES system is at a sub-centimetre scale (www.reson.com), while lateral resolution is a function of water depth and vessel speed. For instance, a water depth of 15 m results in an across-track resolution of 0.13-0.51 m, due to beam spreading at an angle of 0.5°; at a vessel speed of 2.6 m/s (5kn), the along-track resolution is 0.10 m. As the outermost beams were not used in the present analysis, a cell size of 0.2×0.2 m was chosen for the gridding of the bathymetric data. The MBES system was coupled with an AQUARIUS™ 5002MK/SK (THALES) dual-frequency (L1/L2) long-range kinematic (LRK™) global positioning system (GPS). The horizontal and vertical precision of the MBES system during single surveys, conducted at vessel speeds similar to that chosen in this study (cf. above), is ±20 cm and ±2 cm, respectively, at a 95% confidence level [*Ernstsen et al.*, 2006a]. It should be noted that the above horizontal precision does not represent the full potential of the MBES system [*Ernstsen et al.*, 2006a], it probably being of the same order as the vertical precision.

7.3.2 Grain-size analysis

In the laboratory, the bed samples were initially rinsed to remove the salt. The desalted sediments were then washed through a 4 phi (0.063 mm) sieve to separate sand from mud (silt + clay), before being dried over-night in an oven at 70°C. Subsequently, splits of the dried sand fractions were analyzed in a MacroGranometer™ settling tube [*Brezina*, 1979]. Mean grain size, standard deviation, skewness, and kurtosis of the grain-size distributions were determined on the basis of the percentile statistics of Folk and Ward [1957].

7.3.3 Water depth and flow velocity calculation

During the tidal cycle, average water depth along the transect was determined by subtracting the average bed level along the transect derived from the bathymetric grids, from the tidal curve (Figure 7.2). Flow velocities were measured along the transect. At each measuring point, mean flow velocity (depth-averaged) was determined as the average of the flow velocities of all the depth cells of a single ensemble. These single-point mean flow velocities were then used to calculate average mean flow velocity along the transect as well as over the

troughs and crests of the 12 large compound dunes (for location of the large compound dunes see Figure 7.6). Average near-bed flow velocities u_{1m} (0.5-1.5 m above the bed) were calculated in a similar way.

7.3.4 Bedload transport calculation

Dunes migrate by stoss-side erosion and lee-side deposition (Figure 7.3). Assuming that no sediment settles from the water column and no bedload by-passing takes place, the total bedload transport across one dune is equal to the sediment deposited on the lee-side of the dune. The volumetric lee-side deposition, and thereby the bedload transport across one dune, can hence be determined on the basis of sequential flow-parallel bed profiles. This approach can be applied as long as the dune does not travel more than one wavelength between each time step. Lee-side deposition is determined by adding the grey area marked 'Deposition' in Figure 7.3 to the black area marked 'Deposition (and erosion)' in Figure 7.3. In practice, the area 'Deposition' was approximated by step-wise integration of the difference between the dune surface at time 1 and 2. In the present analysis, a step-size of 0.05 m was used. The area 'Deposition (and erosion)' was approximated by calculating the area of the triangle defined by the lee-side trough points of the dune at time 1 and 2, and the intersection point of the dune at time 1 and 2 in-between. The calculations were automated using MATLAB™ (The MathWorks). The identification of the individual dunes was also part of this automation. In order to enable automatic identification of the superimposed dunes, the bed profiles were smoothed using a running average of 21 consecutive points, i.e. a window size of 1 m.

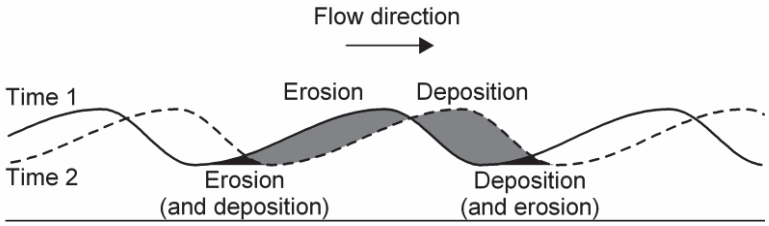

Figure 7.3: Schematic illustration of dune migration in the direction of flow by stoss-side erosion and lee-side deposition used for the determination of bedload transport.

Throughout the eight time steps (surveys 1-3, 3-5, 5-7 etc., see Figure 7.2), the number of dunes along the transect containing all four erosion and deposition units, visualized schematically in Figure 7.3, ranged from 6 to 64 (Table 7.1). These low numbers of identified "complete" dunes are explained by the fact that the triangular units in the trough regions of the dunes were not always developed. This is a result of a combination of the troughs of the dunes

being considerably less mobile than the crests [*Ernstsen et al.*, 2006b] and the time steps being too short to allow the troughs to move sufficiently far to develop the triangular units. On the other hand, due to the higher mobility of the crests, the pure erosion and deposition units were usually well developed in all cases. The number of dunes displaying these units along the transect in the eight time steps hence ranged from 76 to 226 (Table 7.1). To compensate for the missing triangular units, multiplication factors were determined by relating values of volumetric lee-side deposition based on the two units of deposition with values based on only the major unit of deposition. This yielded an average multiplication factor of 1.2 (Table 7.1). Subsequently, values of volumetric lee-side deposition were corrected by multiplying the values based on pure deposition with a compensation factor of 1.2.

Table 7.2: Number of dunes along the transect containing all four erosion and deposition units (n_4 units) as well as those containing at least the two pure erosion and deposition units (n_2 units) (see text and Figure 7.3 for further explanation). In addition, the ratios between values of volumetric lee-side deposition based on the two units of deposition (V_2 units) and values based on the unit of pure deposition (V_1 unit) are shown. See text and Figure 7.3 for further explanation.

Surveys	$n_{4\ units}$	$n_{2\ units}$	$V_{2\ units}/V_{1\ unit}$
1–3	64	195	1.2
3–5	30	186	1.2
5–7	11	76	1.2
7–9	22	200	1.1
9–11	6	124	1.3
11–13	59	216	1.2
13–15	16	190	1.1
15–17	39	226	1.2
Average			1.2

Finally, the calculated values of volumetric lee-side deposition were corrected for porosity assuming a bulk density of newly transported sand of 1700 kg/m^3 [e.g. *Bartholdy et al.*, 1991]. Comparing this to the particle density of quartz (2650 kg/m^3) corresponds to a porosity of 36%.

7.3.5 Bedload transport prediction

In the presence of dunes, the bed shear stress can be divided into a grain-related bed shear stress due to skin friction and a form-related bed shear stress due to form friction [e.g. *Fredsøe and Deigaard*, 1992]. The grain-related bed shear stress is the effective shear stress acting on the bed, whereas the form-related bed shear stress originates from the normal stress

associated with the fluid pressure distribution upstream and downstream of the bedform crest [*Van Rijn*, 1993]. Since sediment is moved by the effective shear stress and is unaffected by the normal stress, only the skin friction component of the total bed shear stress should be used [*Soulsby*, 1997]. Four bedload transport formulae developed during the last four decades were employed to predict volumetric bedload transport: [*Engelund and Fredsoe*, 1976; *Nielsen*, 1992; *Soulsby and Damgaard*, 2005; *Van Rijn*, 1984]. In this paper, the typical version of the formula suggested by Soulsby and Damgaard [2005] was applied which happens to be identical to the one suggested by Nielsen [1992], although it was derived by a different approach. According to the four formulae, the dimensionless bedload transport Φ_b is given by:

$$\Phi_{b,\,Engelund\ and\ Fredsøe\,(1976)} = \frac{5}{\left[1+\frac{0.005}{\left(\theta' - \theta_{cr}\right)^4}\right]^{0.25}}\left(\sqrt{\theta'} - 0.7\sqrt{\theta_{cr}}\right) \tag{7.1}$$

$$\Phi_{b,\,Van\ Rijn\,(1984)} = 0.053\frac{T^{2.1}}{D_*^{0.3}} \quad , \quad T < 3 \tag{7.2}$$

$$\Phi_{b,\,Van\ Rijn\,(1993)} = 0.1\frac{T^{1.5}}{D_*^{0.3}} \quad , \quad T \geq 3 \tag{7.3}$$

$$\Phi_{b,\,Nielsen\,(1992)/\,Soulsby\ and\ Damgaard\,(2005)} = 12\sqrt{\theta'}\left(\theta' - \theta_{cr}\right) \tag{7.4}$$

where θ' = grain-related Shield's parameter; θ_{cr} = threshold Shield's parameter; T = excess bed shear stress parameter equal to $(\theta'-\theta_{cr})/\ \theta_{cr}$; D* = particle parameter, defined as:

$$D_* = \left[\frac{(s-1)\,g}{\nu^2}\right]^{\frac{1}{3}} d_{50} \tag{7.5}$$

where s = relative sediment density equal to ρ_s/ρ; ρ_s = sediment density corresponding to that of quartz particles (2650 kg/m^3); ρ = water density (1021 kg/m^3 at a temperature of 19°C and a salinity of 30 ppt as measured on the 11 September 2002); g = acceleration due to gravity (9.81 m/s^2); ν = kinematic viscosity ($1.03\text{x}10^{-6}$ m^2/s at the temperature and salinity mentioned above); d_{50} = median grain size. The threshold Shield's parameter is calculated by the formula suggested by [*Soulsby and Whitehouse*, 1997]:

$$\theta_{cr} = \frac{0.30}{1+1.2D_*} + 0.055\left[1-\exp\left(-0.020D_*\right)\right] \tag{7.6}$$

The grain-related Shield's parameter is calculated by:

$$\theta' = \frac{u_f'^2}{(s-1)\, g\, d_{50}} \tag{7.7}$$

where u_f' = friction velocity. For turbulent flow the friction velocity can be calculated from the Chézy equation:

$$u_f' = \sqrt{g}\,\frac{U}{C'} \tag{7.8}$$

where U = mean flow velocity (depth averaged); C' = grain related Chézy roughness coefficient which for rough flow is given by:

$$C' = 18\log\left(\frac{12D}{k_s'}\right) \tag{7.9}$$

where D = water depth; k_s' = grain roughness. Van Rijn [1984] relate the grain roughness to the coarse 90th percentile (d_{90}) of the grain-size distribution, i.e. $k_s' = 3d_{90}$. By contrast, Engelund and Fredsøe [1976], Nielsen [1992] and Soulsby and Damgaard [2005] relate the grain roughness to the median grain size (d_{50}), i.e. $k_s' = 2.5d_{50}$. Finally, dimensionless bedload transport is transformed to volumetric bedload transport according to:

$$\Phi = \frac{q_b}{\sqrt{(s-1)\, g\, d_{50}^3}} \tag{7.10}$$

Just as the magnitude of the flow varies during a tidal cycle, the direction of the flow changes with ebb and flood. In this study, flow velocities are considered positive during flood and negative during ebb. Consequently, bedload transport is also positive during flood while negative during ebb.

7.4 Grain Size Distributions

The mean grain size of the bed material along the transect was 0.37 mm on average (Figure 7.4), i.e. medium sand. In the following, median grain size is set equal to mean grain size, i.e. d_{50} = 0.37 mm. On average, the coarse 90th percentile (d_{90}) of the grain size distributions was 0.59 mm along the profile, the sediment being mostly well sorted with an average phi standard deviation of 0.42; only sample 2 was very well sorted. The average skewness was -0.13, i.e. the sediment is near-symmetrical to slightly negatively (coarse) skewed, samples 2 and 3 being near symmetrical, and 1 and 4 negatively (coarse) skewed. The average kurtosis was 1.15 (slightly leptokurtic).

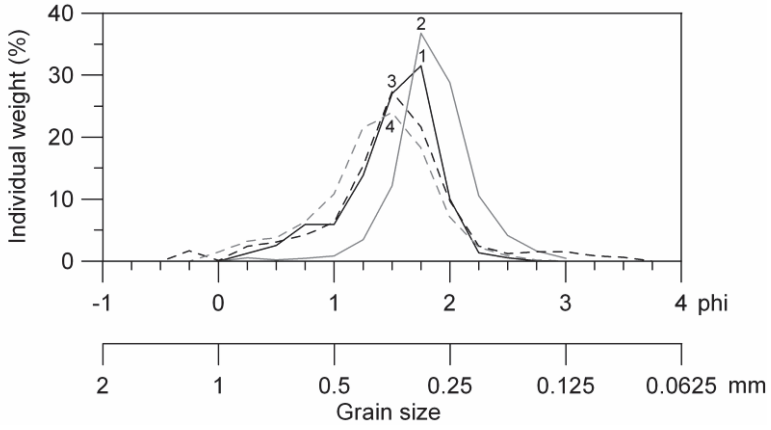

Figure 7.4: Grain-size distributions of the bed material in the area of the transect (for location of the bed material samples see Figure 7.1).

7.5 Water Depth and Flow Velocity

Over the tidal cycle, the average water depth along the transect initially decreased during the ebb tide and subsequently increased during the flood tide (Figure 7.2).

The maximum mean flow velocity was considerably higher during the flood tide than during the ebb tide when integrating over the entire transect (15% higher), as well as the troughs (21% higher) and the crests (14% higher) of the large compound dunes (Figure 7.5). This was also the case for the maximum near-bed flow velocity (1 m above the bed) over the troughs (14% higher) of the large compound dunes. On the other hand, when considering the entire transect as well as the crests of the large compound dunes, the maximum near-bed flow velocity was practically the same during the ebb and the flood tide.

The flow velocity along the transect varied not only temporally but also spatially. On average, the maximum mean flow velocity over the crests of the 12 large compound dunes was 0.97 m/s compared to 0.83 m/s over the troughs during the ebb tide (Figure 7.5). During the flood tide, the maximum mean flow velocity over the crests reached 1.11 m/s compared to 1.00 m/s over the troughs (Figure 7.5). This yields a crest-trough difference of 0.14 m/s and 0.11 m/s during the ebb and flood tide, respectively. This spatial variation in flow velocity was even more pronounced when considering the near-bed flow velocity (1 m above the bed). On average, the maximum near-bed flow velocity over the crests was 0.99 m/s compared to 0.66 m/s over the troughs during the ebb tide (Figure 7.5B). During the flood tide, the maximum near-bed flow velocity over the crests reached 0.98 m/s compared to 0.75 m/s over the troughs (Figure 7.5B). This is equal to a crest-trough difference of 0.33 m/s during the ebb

tide and 0.23 m/s during the flood tide, i.e. more than a factor two larger than in the case of the mean flow velocity.

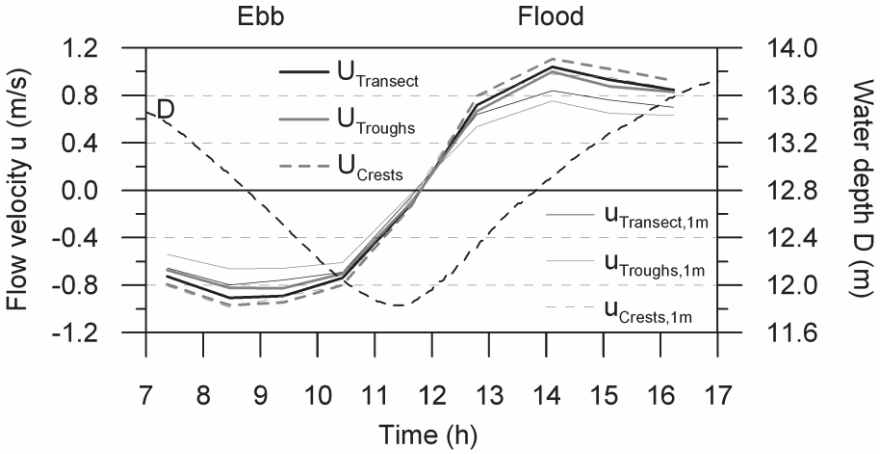

Figure 7.5: Average water depth in addition to mean (depth-averaged) flow velocity and near-bed (1 m above the bed) flow velocity along the transect, as well as over the troughs and crests of the 12 large compound dunes during the tidal cycle (for location of the large compound dunes see Figure 7.6).

7.6 Bedload Transport

Bed profiles were extracted from the bathymetric grids along the transect perpendicular to the crest of the dunes (see Figure 7.1). As an example, the bed profile of survey 9 close to low water is shown in Figure 7.6. The average length and height of the large compound dunes along the survey line was ~70 m and ~2 m, respectively. The superimposed small to medium dunes had lengths and heights of ~5.1 m and ~0.25 m, respectively.

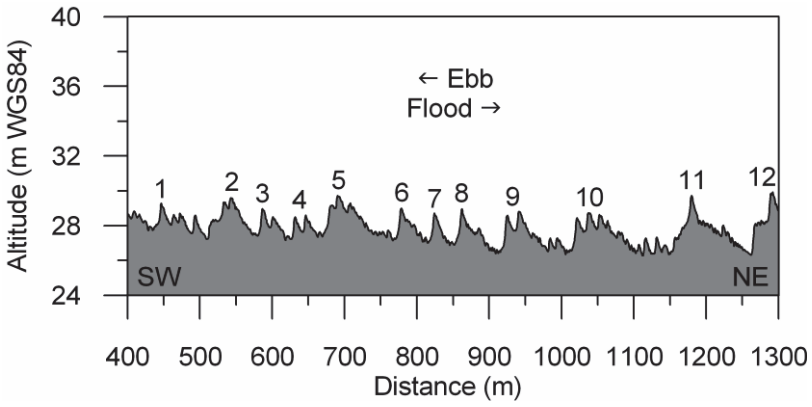

Figure 7.6: Bed profile along the transect close to low water (survey 9, see Figure 7.2; for location see Figure 7.1). The large compound dunes are numbered 1-12.

Stoss-side erosion and lee-side deposition of the superimposed dunes were determined from the extracted bed profiles. Average lee-side deposition during the ebb tide (time steps 1-3, 3-5, 5-7 and 7-9) and the flood tide (time steps 9-11, 11-13, 13-15 and 15-17) along the transect, as well as in the troughs and on the crests of the large compound dunes is shown in Figure 7.7.

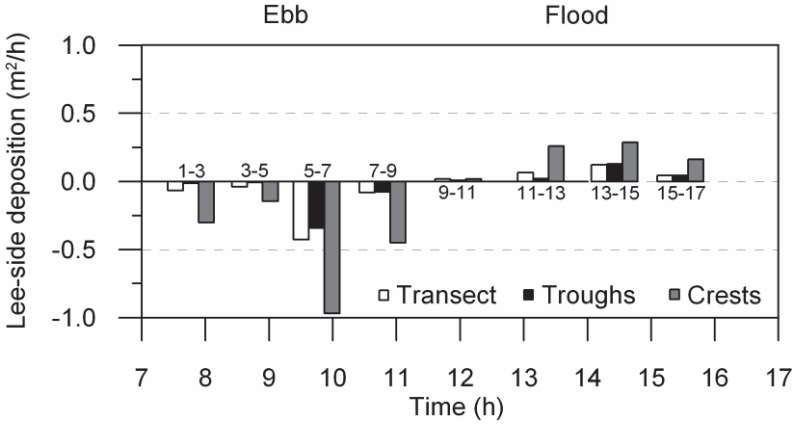

Figure 7.7: Average volumetric lee-side deposition of the superimposed dunes during the tidal cycle along the transect, as well as in the troughs and on the crests of the large compound dunes. For locations of the large compound dunes see Figure 7.6.

Assuming that no sediment eroded from the lee-sides or settled from the water column during the accelerating flow (time steps 1-3, 9-11 and 11-13) or the steady flow (time step 3-5), then the total sediment deposited on the lee-sides was transported as bedload. With decelerating flow, sediment settled from the water column, and it is most conceivable that during these periods, sediment deposited both on stoss-sides and lee-sides. Hence, it is not possible to estimate bedload transport during time steps 5-7, 7-9, 13-15 and 15-17.

Temporally, the highest bedload transport rates along the transect as well as in case of the troughs and crests of the large compound dunes were reached in the last part of the accelerating flow during both the ebb tide (time steps 1-3) and the flood tide (time steps 11-13) (Table 7.2). The lowest values occurred during the initial accelerating flow (time step 9-11); and average values were reached at steady flow (time step 3-5) (Table 7.2).

As in case of flow velocity, bedload transport along the transect varied not only temporally but also spatially. Bedload transport was highest on the crests and lowest in the troughs of the large compound dunes (Table 2). This effect was larger during the ebb tide (factor of 17-21) compared to the flood tide (factor of 2-13) (Table 2).

Table 7.2: Average volumetric bedload transport q_b (m^2/h) along the transect, as well as in the troughs and on the crests of the large compound dunes (same values as shown in Figure 7.7). For locations of the large compound dunes see Figure 7.6.

Tide Time step	Ebb		Flood	
	1–3	3–5	9–11	11–13
$q_{b,Transect}$	−0.067	−0.038	0.017	0.066
$q_{b,Troughs}$	−0.014	−0.008	0.008	0.020
$q_{b,Crests}$	−0.300	−0.145	0.017	0.259

Bedload transport was predicted along the transect at discrete time steps (1 min) by insertion and substitution in Equations (1) - (9) using the mean flow velocities and water depths shown in Figure 7.5 together with the grain size values presented earlier, i.e. d_{50} = 0.37 mm and d_{90} = 0.59 mm. Integrating over the duration of the time steps 1-3, 3-5, 9-11 and 11-13, predicted bedload transport can be compared to the measured bedload transport determined from lee-side deposition (shown in Figure 7.7 and Table 7.2 in m^2/h). This comparison is shown in Figure 8 (in m^2/time step). Bedload transport was also predicted in the troughs and on the crests of the large compound dunes using a similar procedure, but since the patterns were identical to the transect case (merely the magnitude being lower and higher, respectively), they are not shown here.

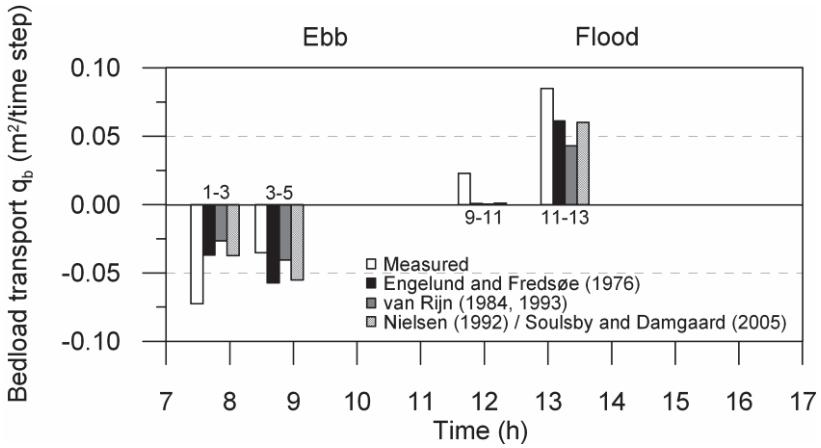

Figure 7.8: Measured and predicted volumetric bedload transport q_b along the transect.

All the evaluated predictors were unable to depict the temporal variation in bedload transport during the tidal cycle. During time step 9-11, the measured bedload transport was underestimated considerably by factors of 20-66. Bedload transport measured during time steps 1-3 and 11-13, where the highest rates were measured, were also underestimated by factors of 1.4-2.7. During time step 3-5, the measured bedload transport rate was only slightly

overestimated by the formula of van Rijn [*Van Rijn*, 1984], a factor of 1.2. The formulae of Engelund and Fredsøe [1976] and Nielsen [1992]/Soulsby and Damgaard [2005] all overestimated the measured bedload transport by ~50%.

7.7 Discussion

A major advantage of calculating bedload transport from lee-side deposition is that it is independent of changes in bedform shape, which makes it applicable also in tidal environments which are characterised by bi-directional flow where small dunes may, for example, change shape during the ebb phase of a tidal cycle from initially asymmetric flood-directed, to symmetric, and finally to asymmetric ebb-directed and, of course, vice versa during the flood phase [*Ernstsen et al.*, 2006b].

The spatial variation in bedload transport with higher rates on the crests than in the troughs of the large compound dunes is a result of the higher flow velocities recorded at the crests relative to the troughs due to flow continuity [c.f. *Ernstsen et al.*, 2006b].

During the last part of accelerating flow in both the ebb tide (time step 1-3) and the flood tide (time step 11-13), the bedload transport rates are practically equal. This is also the case for the maximum near-bed flow velocities (except in case of the near-bed trough flow velocities which are controlled by the exposure to the flow, see below). In the case of maximum mean flow velocity, the magnitude was considerably higher during the flood tide than during the ebb tide. This clearly demonstrates that bedload transport is related to the near-bed flow velocities rather than to the mean flow velocities.

The temporal variation in bedload transport, with low rates in the initial phase of accelerating flow and high rates in the last part, is coherent with the increase in flow velocity. However, the fact that bedload transport occurred at all during the initial phase of accelerating flow (time step 9-11) is probably due to remobilization of the finer fractions of the grain size distribution which had settled around slack water. The prevailing hydrodynamic conditions were hence only sufficient to mobilize the finer fractions in bedload, but were unable to bring these fractions into suspension.

The high bedload transport rates attained during the last part of accelerating flow (time steps 1-3 and 11-13) are probably related to an accompanied mobilisation of coarser fractions with increasing flow velocity. In other words, fractions eroded on the stoss-sides and transported in bedload, to be deposited on the lee-sides in the beginning of the last part of acceler-

ating flow, would at a later point in time have been brought directly into suspension without being deposited until the flow started decelerating, i.e. the high bedload transport during the last part of accelerating flow is due to an increase in flow competence. Average transport rates were attained during the period of steady flow (time step 3-5). Despite the relatively high flow velocity during this period, e.g. compared to the preceding time step 1-3, the bedload transport rate was a factor two smaller than during the preceding period (Table 2). The reason for this is probably that during this period of steady flow the bedload transport is capacity-limited. Hence, part of the temporal variation in bedload transport can be explained by the unsteady tidal flow in combination with the characteristics of the bed material.

In addition, part of the temporal variation in bedload transport can be explained by exposure to the flow. The best example is the higher bedload transport rate in the troughs of the large compound dunes during the flood tide as compared to the ebb tide, when comparing the last part of accelerating flow (time steps 1-3 and 11-13). This is due to considerably higher maximum near-bed trough flow velocities during the flood tide as compared to the ebb tide, a result of the lee effect of the compound dunes during the ebb tide.

Since the bedload transport predictions primarily were a function of mean flow velocity they were unable to capture the bedload transport during the initial phase of accelerating flow (time step 9-11) where the grain-related Shield's parameter in the majority of the time was subordinate to the threshold Shield's parameter, which is related to the mean grain size. Likewise, the formulae were also unable to depict the bedload transport in the last part of accelerating flow (time steps 1-3 and 11-13). Thus, the predictors could not depict bedload transport during accelerating flow where, presumably, the finer fractions of the grain size distribution constituted a major part of the material transported as bedload.

Consequently, the performance of the predictors can strictly only be evaluated during the period with steady flow (time step 3-5). In this period, bedload transport was relatively well predicted using the formula of van Rijn [1984].

7.8 Conclusions

- A simple tool to calculate bedload transport has been presented. Assuming that no sediment settles from the water column with accelerating or steady flow, bedload transport is equal to lee-side deposition of the dunes. Lee-side deposition can be calculated from sequential measurements of migrating bedforms.

- Spatial variation in bedload transport, with higher rates on the crests than in the troughs, is due to higher flow velocities at the crests than in the troughs resulting from flow continuity.
- Temporal variation in bedload transport, e.g. with higher rates in the troughs of the large compound dunes during the flood tide than during the ebb tide, is due to higher near-bed flow velocities in the troughs of the compound dunes during the flood as compared to the ebb tide. This can be explained by flow exposure, i.e. the trough-sheltering effect of the compound dunes being active during the ebb tide, but being negligible during the flood tide.
- All the evaluated bedload transport predictors were unable to depict the temporal variation in bedload transport during a tidal cycle, specifically the bedload transport during accelerating flow where finer fractions of the grain-size distribution presumably constituted a major part of the material transported as bedload. However, during steady flow, bedload transport was relatively well predicted using the formula of van Rijn [1984]. Finally, it is suggested that the temporal variation in grain-size distribution of the mobilised sediment should be taken into account by sediment transport formulae.

Acknowledgements

This study was supported by the German Science Foundation (DFG) as part of the DFG – Research Center Ocean Margins (RCOM) at the University of Bremen, Germany and the Senckenberg Institute who provided the ship time.

Chapter 8: Paper VII

In-situ observation of aggregate dynamics in a tidal channel using acoustics, laser diffraction and optics

C. Winter[1], M. Becker[1], V. B. Ernstsen[1], D. Hebbeln[1]
A. Port[2], A. Bartholomä[3], B. Flemming[3], M. Lunau[4]

[1]MARUM, Center for Marine Environmental Sciences, University of Bremen, Germany
[2]ICBM, University of Oldenburg, Oldenburg, Germany
[3]Senckenberg Institute, Wilhelmshaven, Germany
[4]Alfred Wegener Institute, Bremerhaven, Germany

Journal of Coastal Research (published)

Abstract

To describe the dynamics of aggregates in a tidal channel, in situ measurements of current velocity, turbulence, backscatter intensity, and particle size distribution have been carried out throughout a tidal cycle. The dynamics of suspended particle matter are shown: Distinct turbidity clouds due to temporal increases in total concentration are detected by all sensors, but acoustic methods seem to underestimate the amount of suspended particulate matter (SPM) when large aggregates are present. We compare two different approaches for the in-situ analysis of particle size distributions: A laser diffraction method (Sequoia LISST 100) and image analysis of in-situ photography. Both instruments are limited due to their resolution and technical properties. Applied in combination, the two methods reveal the broad range of particle sizes ranging from a few microns to millimetre size.

8.1 Introduction

The understanding of suspended particle matter (SPM) dynamics in the marine environment such as coastal seas, estuaries and rivers, has been greatly enhanced by the application of modern measuring techniques. The shortcomings of the laborious procedure of repeated mechanical collection of water samples and their subsequent analysis for the description of

suspended matter transport processes have in recent years been largely overcome by in situ optical and acoustic methods, which allow quasi-continuous, autonomous, and less intrusive measurements of SPM and the transporting hydrodynamic environment [*Thorne and Hanes*, 2002].

Optical methods include transmission or backscatter sensors, the signals of which can be calibrated to reflect the concentration of suspended matter in the water. Acoustic methods, on the other hand, are non-intrusive, highly resolving and much less susceptible to biological fouling compared to optical methods [*Bunt et al.*, 1999; *Downing*, 2006]. Acoustic devices, e.g., acoustic Doppler current profiles (ADCP), derive properties of suspended matter based on the echo intensity of high-frequency sound pulses. However, these narrow-band frequency devices are not capable of differentiating between changes in concentration and changes in particle-size distribution [*Deines*, 1999]. Their application thus requires thorough and repeated calibration with water samples, particularly in environments with fluctuating grain-size distributions or unstable aggregates (flocs).

In tidal environments, a high variability in the dimensions of particle aggregates is observed. Thus, in shallow and turbid aquatic systems, aggregates composed of inorganic and organic particles between 5 and 1500 µm in size are the main component of SPM [*Crump and Barross*, 2000; *Simon et al.*, 2002; *Zimmerman and Kausch*, 1996].

Although the composition, aggregation and disaggregation processes, and the role of the hydrodynamic environment and microbial colonisation have been studied in fair detail [*Fugate and Friedrichs*, 2003; *Lunau et al.*, 2004; *Manning and Dyer*, 2002], the fate of aggregates in the cycling of matter as well as decomposition processes are far from being understood, let alone from being predictable. Since the methods mentioned above describe the bulk characteristics rather than the dynamics of individual aggregates, other methods have been developed to allow a more quantitative description of SPM dynamics. Besides the shortcomings already mentioned, mechanical sampling or continuous pumping of water is not advisable for the purpose of subsequent particle-size analysis because aggregates are inevitably broken down in the course of the sampling procedure.

Recently, laser in-situ scattering and transmissiometry (LISST) was introduced as a promising means to assess dynamics and size structure of particles directly in the water. To date, a number of LISST studies have been carried out in a variety of environments, but com-

parisons between different systems have yielded ambiguous results [*Fugate and Friedrichs*, 2002; *Mikkelsen and Pejrup*, 2001]. The performance of LISST thus needs further attention.

Other optical systems commonly used in the open sea, e.g., in-situ video observation or high-resolution photography [*Asper*, 1987; *Costello et al.*, 1989; *Lampitt et al.*, 1993], are limited by high turbidity and current velocities. To overcome this, a number of advanced optical systems for the specific application in turbid environments have been developed [*Eisma et al.*, 1996; *Lunau et al.*, 2004; *Milligan*, 1995; *Van Leussen and Cornelisse*, 1993]. In this paper we introduce a newly developed optical system for the in-situ photography of aggregates and their subsequent image analysis. The data were collected in a tidal channel of the German Wadden Sea and the study incorporates a comprehensive description of SPM dynamics based on two acoustic sensors, in-situ particle size analysis, and in-situ photography. We compare the performance of the devices in terms of bulk SPM characteristics and particle-size distribution.

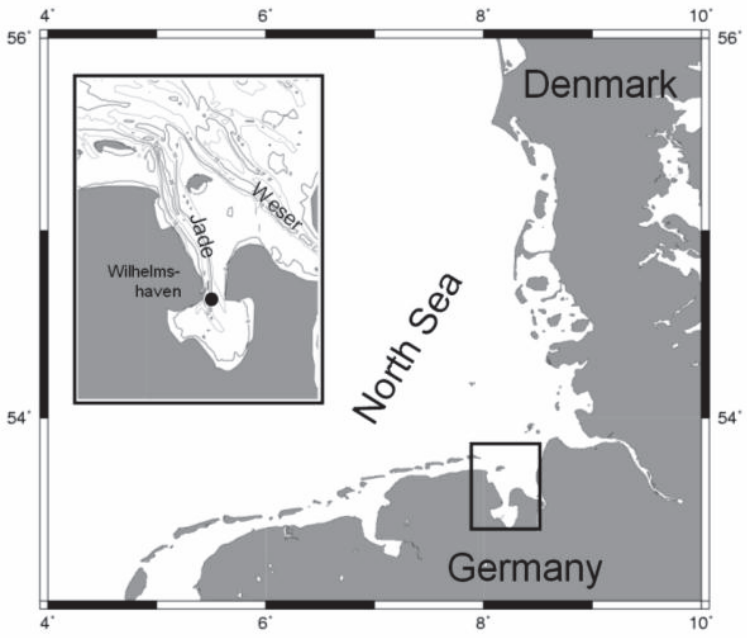

Figure 8.1: Study area: Jade tidal channel in the German Bight

8.2 Study area

The study was carried out from aboard FK Senckenberg at an anchoring position in the inner Jade estuary near Wilhelmshaven, Germany (Figure 8.1). The area is characterised by semidiurnal upper meso- to lower macrotidal conditions with a tidal range of 3.8 m during

spring and 2.6 m during neap tides. The data were gathered during a measuring campaign from low water slack to high water slack on 10 April 2006, between 16h00 and 22h00 MEST. The wind was 10 to 15 knots from N-NW but due to the sheltered location, surface waves were below 1 metre in height with a mean period of 4 seconds.

8.3 Methods

8.3.1 Acoustic Doppler Current Profiler

Today ADCPs are commonly deployed for measuring vertical current velocity profiles. By making use of the Doppler effect, ADCPs derive horizontal (x- and y-axes) and vertical (z-axis) current velocities as a function of depth in a defined number of depth cells. This acoustic method is based on the proportionality between the frequency shift of outgoing and reflected pulses and the celerity of the ensonified scatterers. Besides current velocity, the instrument also provides information on the corresponding acoustic intensity of the backscattered signal. For this study, a direct reading 1200 kHz RDI Rio Grande Workhorse ADCP was mounted downward looking along the side of the anchored vessel. The vertical resolution was set to 0.25 m depth cells (bins) with an average sampling frequency of 0.5 Hz. In this case, only the data of the acoustic beam directed towards the other instruments was taken into consideration.

8.3.2 Acoustic Doppler Velocimeter

At a position approximately 1.5 m below the head of the ADCP, a 16 MHz Sontek MicroADV was mounted in order to measure high-frequency velocity oscillations. The ADV determines acoustic backscatter intensity and the instantaneous three-dimensional velocity for a very small sampling volume (0.09 cm^3) five centimetres below the sensor. In this study, the device was set to sample at 20 Hz. From this, one-minute running averages were calculated to distinguish between local turbulence and mean velocities.

8.3.3 Laser In-Situ Scattering and Transmissiometry

A Sequoia LISST-100 type C instrument was deployed from the anchored vessel at a fixed depth. The device measures the size distribution of SPM in the range of 2.5 to 500 µm. The measuring principle is based on small-angle forward scattering of laser light. The light scattering is detected by 32 logarithmically-scaled ring detectors, the spacing of which determine the size ranges of the scatterers [*Agrawal and Pottsmith*, 2000]. Thus, within the meas-

uring range, light scattered at angles larger or smaller than the angles covered by the ring detectors is not recorded. However, particles smaller than 2.5 µm or larger than 500 µm can still scatter light onto the ring detectors, as each particle creates its own diffraction pattern. Therefore, if smaller or larger particles are present, excess scatter will occur on the first and last rings. Upon inversion of the diffraction pattern, this results in an overestimation of particle volume in the smallest and/or largest size bins [*Agrawal and Pottsmith*, 2000]. This is typically seen as a rising head/tail in the size spectrum [*Mikkelsen*, 2002]. The SPM volume concentration is calculated by adding up the volumetric concentrations of all size classes. In addition, the percent optical transmission of the laser beam is recorded as an indicator of water turbidity. In our case, the instrument was set to output-averaged values of three samples at 0.1 Hz.

8.3.4 Digital In-Situ Documentation of Suspended Aggregates

The newly developed photographic device, designed and constructed by the workshop engineers at the University of Oldenburg, was deployed to take in-situ digital photographs of suspended aggregates which were subsequently analysed by means of image processing. The problem of three-dimensional effects was overcome by using planar laser illumination. Digital In-Situ Documentation of Suspended Aggregates by Laser illumination (DISDAL) is composed of a digital camera (Sony DSC F 828), a red diode laser ($\lambda = 658$ nm, 50 mW, HB-Laser Components, Schwaebisch-Gmuend, Germany) and an autonomous controller for both instruments, all fitted into a water-proof PE-housing. The laser beam is expanded to 1 x 60 mm by a semiplanar lens (Schott, Mainz, Germany). The beam is deflected by a prism and illuminates a defined area of water (48.9 x 36.7 mm) continuously flowing through a 150 x 150 mm PE-tube. The channel is always oriented towards the current by a fin.

In this study, one photograph per minute was taken at a resolution of 15 µm per pixel. For subsequent image analyses, only the red channel of each image was extracted and the resulting 8-bit single-channel images were cropped on all sides to a size of 28.0 x 15.7 mm to exclude out-of-focus rim areas. Segmentation was achieved by applying a global threshold. Image processing and analysis was implemented in MATLAB (The MathWorks, Natick, Massachusetts, USA). Due to the diffuse structure of marine aggregates, it is not possible to assure accurate edge detection. Thus, the derived size distributions must be interpreted with some care, particularly in the small particle-size ranges. Relative SPM concentrations were calculated by the summation of the total area of all detected aggregates at particular points in time.

8.3.5 Direct water sampling

Bulk water samples were taken at 15 minute intervals using a HYDROBIOS (Kiel, Germany) water sampler. On each occasion, two litres of water were taken close to the LISST and the DISDAL devices. The samples were filtered, the filters dried and weighed to derive the bulk SPM concentration for each sample after subtraction of the filter weight.

8.4 Results

8.4.1 Sediment concentration

Time series of current velocity and backscatter intensity as measured by ADV, ADCP acoustic backscatter, the total particle volume concentration as measured by the LISST, and the total area of aggregates detected by DISDAL are plotted in Figure 8.2 along with SPM concentration derived from water samples.

The survey covered a six-hour flood tidal period. The depth-averaged current velocities during that time interval slowly accelerated after low-water slack, to oscillate around a mean value of approximately 0.75 m/s for three hours. The total SPM concentration, as derived by direct samples at 15 minute intervals, shows a fluctuating signal rising from about 40 mg/l to 90 mg/l at the highest current velocities. Two samples, one at 20h45 and the other at 21h00, yielded very high concentration values of around 200 mg/l. Higher-frequency SPM dynamics was approximated on the basis of other measured parameters: Thus, the acoustic backscatter intensity obtained for a depth profile by the ADCP and for a small sampling volume by the ADV can be related to the concentration of suspended particles. However, the problem of absolute conversion is far from trivial and involves frequent calibration with water samples, but is usually still only valid for the specific campaign [*Deines*, 1999; *Lee and Hanes*, 1995].

As the focus of this study was not set to absolute quantities, further conversion was omitted. Relative SPM concentrations were also calculated from LISST and DISDAL data as the total sum of all observed particle volumes, or rather all areas for each point in time. As a matter of course, the different sensors detected different magnitudes and characteristics of SPM dynamics, in spite of the fact that they monitored the same environment. However, all the devices show a similar large-scale tidal signal of SPM, i.e. the SPM concentration increased with a time lag of more than two hours after the accelerating tidal currents. Velocity oscillations of higher frequency show similar patterns as the SPM concentration signals, but no statistically significant correlation could be identified.

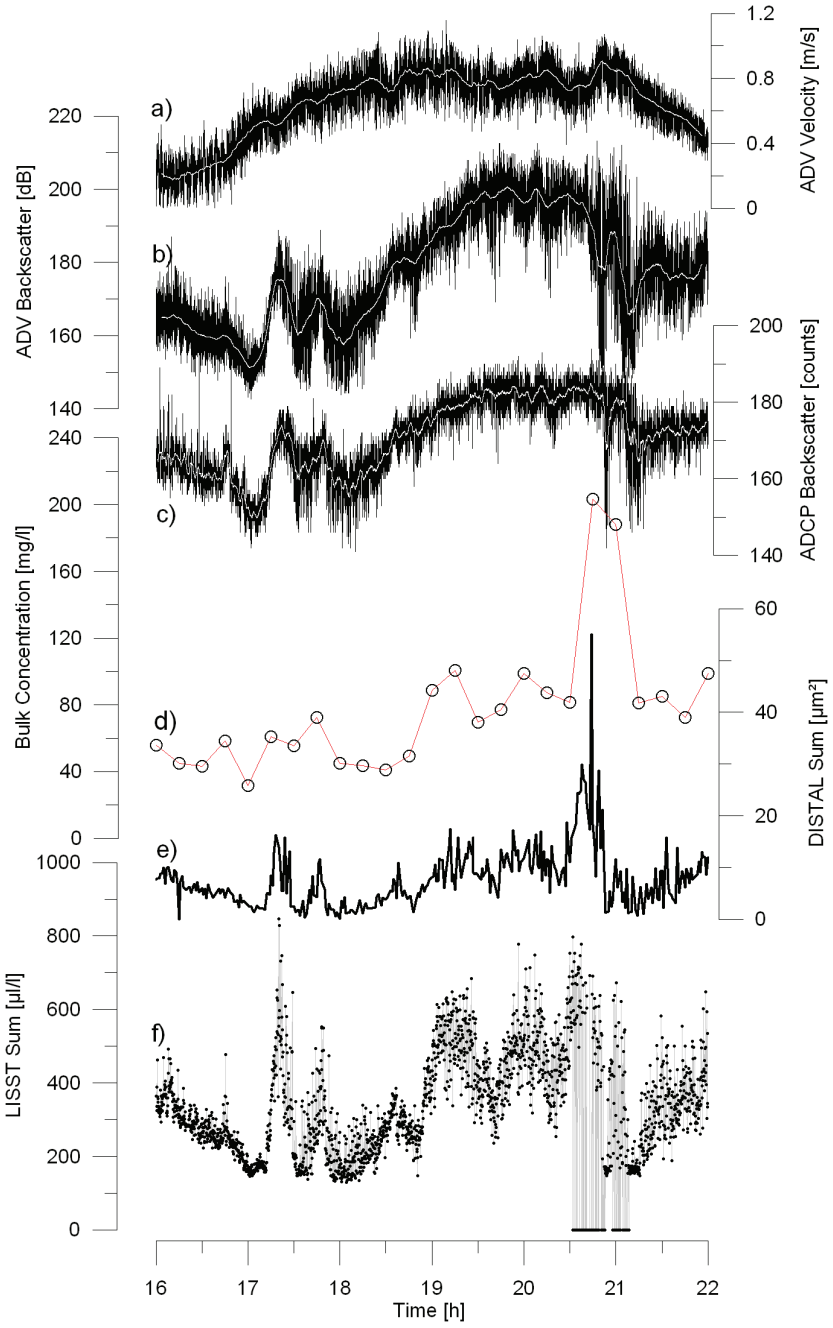

Figure 8.2: Time series of a) ADV current velocities, b) ADV backscatter intensity, c) ADCP backscatter intensity, d) Bulk concentration, e) LISST total particle volume, and f) DISDAL total particle area. The white lines show one minute running averages.

Turbidity clouds appear as distinct SPM concentration maxima during the rising tide. They stand out in the time-series of all four instruments, e.g., at 17h25 and 17h25. Later peaks, appearing at 19h15 and 20h00 in the LISST and the DISTAL time-series, are less pronounced in the acoustic data. The major event, as already seen in the direct samples and in the DISDAL series (20h45), also stands out in the LISST measurements, but is accompanied by a temporal instrument failure due to the exceedance of the transmissivity threshold. These

events are recorded as zero values in the LISST time-series. Note that the DISTAL total particle area values go back to almost zero at times of low acoustic backscatter intensity. By contrast, the total volumetric concentration observed by LISST does not drop below a background concentration of about 150 µl/l, corresponding to a measured concentration value of 35 mg/l.

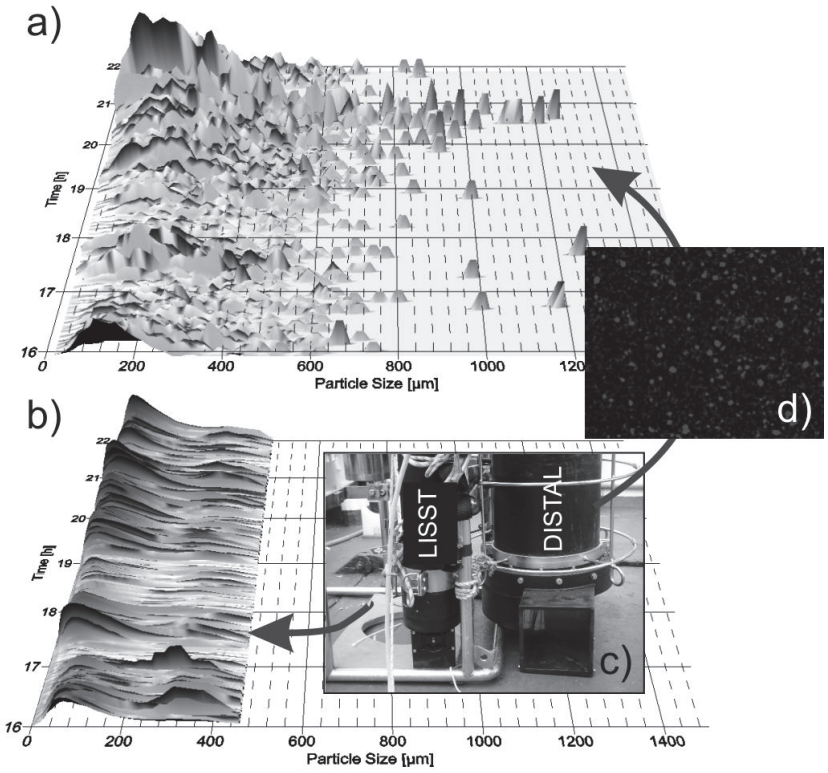

Figure 8.3: Temporal variation in absolute particle size distributions as derived from (a) DISDAL in-situ photographs and image processing and (b) LISST. The photos show (c) LISST and DISTAL mounted into an instrument frame and (d) a DISTAL image of SPM.

8.4.2 Particle-size distributions

Whereas the time-series of acoustic backscatter, total particle volumes and particle areas describe bulk characteristics of SPM as recorded in the sample volume of the respective sensors, further differentiation into particle-size classes is illustrated in Figure 8.3. It should be noted that, due to the complex shape of the aggregates, a conversion from particle areas (as derived from DISTAL) to volumes (as derived from LISST) - or vice versa - was not attempted.

Figure 8.3 (a) shows the variation of particle-size distribution over time as obtained from DISTAL digital image analysis of in-situ photos. The total particle area has been sorted into size classes of 15 µm width. The detected particle equivalent diameters range from the lower limit of resolution (15 µm) to 1300 µm. Due to the narrow size classes, and the inhomogeneous distribution of the particles, the distributions are very incoherent. Nevertheless, a main mode below 200 µm is present over the whole measuring period. The largest particles are generally smaller than 700-800 µm, but larger isolated ones of up to 1300 µm also occur. Whereas most of the peaks in the SPM concentration can be related to variations in the total amount of suspended matter (not changing the distribution), the major event at 20h45 is clearly associated with an accumulation of larger particles.

LISST particle-size distributions, which are based on volumetric concentrations, are plotted in Figure 8.2 (b). Here, the size range of 2.5 - 462 µm is covered in logarithmically scaled classes. This implies that particle sizes smaller than 100 µm are better resolved than those measured by DISTAL, but larger particles are grouped into larger classes. LISST particle-size distributions are less variable in time. The main mode of the distributions is at about 100 µm during the first hour of measurement, and then drops to around 60 to 80 µm for the remaining time. This main mode is frequently accompanied by a second mode at about 350 µm which appears every few minutes. Also, the peaks in SPM concentration can be related to variations in the total amount of suspended matter without changing the shape of the distribution.

8.5 Discussion

A broad range of size classes is present in the water column. Particles of a few microns and up to 1.3 mm in size were detected by in-situ observation. Careful interpretation has allowed the identification of grains belonging to the very fine sand fraction, which appears as an almost constant mode around 80 µm throughout the measuring period in the LISST signal. This material is evidently kept in suspension by local turbulence. This mode, however, does not appear in the DISTAL series, a feature which can be explained by the under-estimation of small particles due to the physical limit of resolution and uncertainties in edge detection: Small particles as observed at times of low turbidity are not at all detected by DISTAL, which then gives almost zero total aggregate areas.

Larger particles, as observed by both LISST and DISTAL, are interpreted here as flocs, i.e. marine aggregates composed of small mineral grains and organic components. These ag-

gregates frequently appear as a secondary mode of approximately 350 µm in the LISST data. The performance of LISST with respect to the correct detection of aggregate dimensions cannot be assessed because the instrument is internally calibrated to express size in terms of a spherical standard which is more appropriate for the detection of sand grains. As a consequence, the LISST tends to over-estimate detected aggregate sizes. On the other hand, the observed mode at around 200 µm in the DISTAL data might be an underestimation. Bearing in mind the effects of population statistics on modes when taking into account particle areas or volumes, we interpret the secondary mode in the LISST and the first main mode in the DISTAL data as the size signal of micro-aggregates somewhere in the range of 200 to 350 µm.

Further inspection of the DISTAL data reveals a substantial scatter in aggregate sizes. Largest flocs of 700 - 800 µm are frequently observed, while occasionally - e.g., during the 20h45 event - aggregates of up to 1300 µm may occur. It is important to note that aggregates larger than 350 µm seem not to by seen by the LISST as discrete objects. This causes the particle distribution to show a rising tail. Since these contribute to the general turbidity of the water, the instrument fails during events with large particle concentrations.

8.6 Conclusions

Suspended Particulate matter (SPM) is highly variable in marine waters, as shown here by the data from a tidal channel of Jade Bay, along the North Sea coast of Germany. In addition to an overall tidal signal, which also is resolved by repetitive mechanical sampling, modern technology allows the description of higher frequency dynamics in terms of concentration and size distribution. Although none of the approaches can be expected to measure true quantities, as various methodical shortcomings must be taken into account, the combination of different instruments reveals different aspects of SPM dynamics.

This study has shown that ADVs and ADCPs detect similar characteristics of SPM dynamics, a feature which has also been demonstrated by previous studies. It has also been shown that the acoustic signals are similar to the patterns observed in the measured SPM concentration, although pronounced turbidity clouds were not detected by these instruments.

The in-situ laser scatterometer LISST used in this study was able to resolve suspended particle sizes from 2.6 µm up to 460 µm. Here the data have been interpreted to show that a fraction of very fine sand (mode around 80 µm) remained in suspension throughout the meas-

uring period. Larger mineral particles were not expected to occur. Thus, the interpretation of larger aggregates as detected by LISST must take into account that these do not correspond to spheres in terms of laser scattering. The newly developed in-situ photographic device DISTAL has proven its applicability in tidal environments. Although the resolution is limited for the time being, the free definition of size classes allows the distinction of aggregates. Thus, the simultaneous deployment of a number of different in-situ devices has revealed the existence of particles ranging from grains a few microns in size to aggregates exceeding 1 mm in diameter.

Pronounced lag effects, single peaks in the SPM time-series unrelated to local velocities, and a vertical distribution of suspended matter as observed in the ADCP acoustic backscatter profiles not shown here, indicate that the recorded suspended material was not brought into suspension at the measuring station but was transported there by the flood current.

It could also be shown that turbidity clouds can be caused by the temporal increase of all size classes, but also by sporadic accumulations of larger aggregates. Whereas the former events are detected by all sensors, acoustic methods seem to underestimate the amount of SPM when large aggregates are present.

Acknowledgements

We thank the Senckenberg Institute in Wilhelmshaven, Germany, for providing ship time of FK Senckenberg, the Sequoia LISST 100, and the ADV. Captain and crew of FK Senckenberg are thanked for their good spirits. The study was funded by the Deutsche Forschungsgemeinschaft as part of the DFG-Research Center ‘Ocean Margins’ at the University of Bremen.

Chapter 9: Concluding remarks and perspectives

Fluid mud is efficiently detected by state of the art hydroacoustic instruments (Chapter 2). It is shown that the volume of isolated fluid mud deposits can be estimated by the combined use of sediment echo sounders and side-scan sonars. This constitutes a significant progress compared to earlier studies. In general, the vertical mass exchange of sediments between the bottom boundary layer and the water column is of particular importance for the estuarine sediment transport cycle. Therefore, the joint application of multibeam and sediment echo sounder is the next logical step in order to precisely determine volumes of fluid mud deposits on the basis of bathymetrical measurements, to be conducted prior to the deposition of fluid mud.

In the Weser estuary, fluid mud deposits are highly variable and do not appear in the suggested form of a contiguous layer. During slack water fluid mud is deposited in depressions, in troughs of subaqueous dunes, and in flat bed areas, where mud drapes are formed. Ephemeral fluid mud deposits, especially mud drapes, smooth small-scale irregularities. Rather than solid bed deposits, one-off seabed mapping surveys may record transient facies, which can be prevented by the deployment of parametric echo sounders.

Deposition of fluid mud depends on the supply of cohesive suspended sediments, whereas the entrainment of fluid mud is controlled by the local production of turbulence, which is, in turn, influenced by local morphology.

This is most apparent in the case of subaqueous dunes, inducing strong turbulent stresses, associated with large-scale turbulent structures, which lead to rapid entrainment of fluid mud (Chapter 3). Fluid mud, being exposed to the dune specific turbulent flow field, brings together two most intricate phenomena of cohesive and non-cohesive sediment transport. In this context entrainment rates need to be treated with care, as turbulence statistics do not necessarily scale with the local shear velocity in the dune trough. Further investigations should aim for the in-situ determination of turbulence in dune troughs in the presence of fluid mud, which is, at any rate, a technical challenge.

If the river bed is flat, i.e. roughness elements do not protrude further than the lutocline, mobile mud forms from the weakly consolidated suspension of mud flocs, deposited during one slack water (Chapter 4). Mobile mud is to some degree resistant to erosion, which is explained by efficient damping of turbulence at the lutocline. A part of the mud layer survives

the following tidal phase, though its thickness is significantly reduced. The latter process is unexpected according to earlier studies, which predicted a reduction of concentration and an increase of layer thickness for mobile mud. The reduction of layer thickness is partly explained by enhanced consolidation, which is induced by moderate levels of turbulence.

If mobile mud was formed and is still present during the next slack water, the layer is enriched by sediments. A positive feedback between the increase in concentration and the damping of turbulence is proposed, which inevitable promotes the formation of erosion-resistant, stationary mud deposits. Semi-diurnal slack water deposition occurs in the centre of the maximum turbidity zone (TMZ), which explains the correlation between the centre of the TMZ and estuarine mud deposits.

Tide-driven dynamics of fluid mud have not been studied in such detail before. As of today, this is possible by the combined use of an acoustic Doppler current profiler (ADCP) and a sediment echo sounder (SES). However, it is essential to conduct measurements on a large spatial scale, e.g. to cover extended dune fields, and to measure on a short temporal scale, e.g. to collect a significant number of transects during the tidal cycle. In this study it was possible to meet both requirements. The presented results substantially contribute to the phenomenological description of fluid mud and the understanding of fluid mud dynamics in the field.

A prerequisite is not only the combined deployment of ADCP and SES but also the combined processing of the acquired data. This is implemented in the MADCP software, which was developed during this study. MADCP implements cleaning methods for the moving platform correction and the acoustic backscatter calibration with respect to suspended sediment concentration (SSC). Near-bed density stratification, SSC in the water column and hydrodynamics are thus combined in one tool.

The stability of fluid mud layers is also studied in the TMZ of the Ems estuary (Chapter 5 and 6). The lutocline rises and falls in response to the tidal flow, probably because the fluid mud layer becomes turbulent and entrains water from the upper layer during accelerating currents. Thereby, the stability of the lutocline is determined by a new method, based on acoustic backscatter measurements. In the heavily engineered Ems estuary, weir closure during flood slack water and the subsequent release of captured water masses induce the flushing of the estuary and catastrophic downstream advection of fluid mud. By the time the estuary returns to flood-dominated conditions, fluid mud is rapidly advected upstream and re-established in the upper part of the estuary.

In the Grådyb tidal inlet channel bedload transport in presence of large dunes is determined on the basis of highly accurate multibeam measurements (Chapter 7). Bathymetrical changes are converted into bedload transport rates, which are not predicted by classical bedload transport formulae due to variations in grain-size composition of the mobilised sediment. To close the loop, results are applied to the Weser estuary and show that lee-side deposition occurs simultaneously to the entrainment of fluid mud in dune troughs.

Concerning flocculation and the formation of turbidity clouds in the water column, an instrumental study reveals that acoustic methods underestimate SSC when large aggregates are present (Chapter 8). In the Jade Bay, several floc populations coexist in the water column, covering a wide range of sizes from a few microns to millimetre size. Such investigations are essential to determine tidal dynamics of cohesive suspended sediments. Additionally, knowledge of the preferences of different measuring techniques is highly valuable, from a practical point of view.

In many aspects, this is a phenomenological study. Processes, already known to govern the behaviour of cohesive sediment, are used to describe observations in the field. In turn, phenomena observed for the first time could only be party explained by the suggested mechanisms. Mobile mud did not behave as predicted, and small scale morphology was shown to have a significant influence on turbulent entrainment.

It remains to test the proposed concepts. They may be substantiated either by further measurements in the laboratory, in different natural environments, or even on different time scales. An elegant way is the incorporation of the underlying physical processes in the framework of numerical models, which, as far as cohesive sediments are concerned, lags behind the research already conducted in terms of individual processes, such as flocculation, hindered settling, or turbulence damping.

This, however, is hoped to happen in the near future.

References

Abraham, D. D., and T. Pratt (2002), Quantification of bed-load transport on the Mississippi River using multibeam survey data and traditional methods, *ERDC/CHL CHETN-VII-4, US Army Corps of Engineers*.

Abril, G., et al. (2000), Transient, Tidal Time-scale, Nitrogen Transformations in an Estuarine Turbidity Maximum - Fluid Mud System (The Gironde, South-west France), *Estuarine, Coastal and Shelf Science*, *50*(5), 703-715.

Adams, C. E., et al. (1990), Internal hydraulics of a sediment-stratified channel flow, *Marine Geology*, *95*, 131-145.

Agrawal, Y. C., and H. C. Pottsmith (2000), Instruments for particle size and settling velocity observations in sediment transport, *Marine Geology*, *168*(1-4), 89-114.

Ainslie, M. A., and J. G. McColm (1998), A simplified formula for viscous and chemical absorption in sea water, *The Journal of the Acoustical Society of America*, *103*(3), 1671-1672.

Alkan, U., et al. (1995), Survival of enteric bacteria in relation to simulated solar radiation and other environmental factors in marine waters, *Water Research*, *29*, 2071-2080.

Allen, J. R. L. (1982), Mud Drapes in Sand-Wave Deposits: A Physical Model with Application to the Folkestone Beds (Early Cretaceous, Southeast England), *Philosophical Transactions of the Royal Society of London. Series A, Mathematical and Physical Sciences*, *306*(1493), 291-345.

Allen, J. R. L. (1993), Sedimentary structures: Sorby and the last decade, *Journal of the Geological Society, London*, *150*(3), 417-425.

Ashley, G. M. (1990), Classification of large-scale subaqueous bedforms; a new look at an old problem, *Journal of Sedimentary Research*, *60*(1), 161.

Asper, V. L. (1987), Measuring the flux and sinking speed of marine snow aggregates, *Deep-Sea Research*, *34*, 1-17.

Baas, J. H., and J. L. Best (2008), The dynamics of turbulent, transitional and laminar clay-laden flow over a fixed current ripple, *Sedimentology*, *55*(3), 635-666.

Balsley, B., et al. (2008), On the Scale-dependence of the Gradient Richardson Number in the Residual Layer, *Boundary-Layer Meteorology*, *127*(1), 57-72.

Bartholdy, J., et al. (1991), Sediment transport within the drainage area of River Ribe Å, *Danish Journal of Geography*, *91*, 1-10.

Bartholdy, J., and D. Anthony (1998), Tidal dynamics and seasonal dependent import and export of fine-grained sediment through a backbarrier tidal channel of the Danish Wadden Sea, in *Tidalites: processes and products*, edited by C. Alexander, et al., pp. 43-52, SEPM Publications.

Bartholdy, J., et al. (2002), Grain-size control of large compound flow-transverse bedforms in a tidal inlet of the Danish Wadden Sea, *Marine Geology*, *188*(3-4), 391-413.

Bartholdy, J. (2006), A simple model for estimating current velocity in tidal inlets: example from Grådyb in the Danish Wadden Sea, *Geo-Marine Letters*, *26*(3), 133-140.

Bates, C. R., and D. J. Oakley (2004), Bathymetric sidescan investigation of sedimentary features in the Tay Estuary, Scotland, *International Journal of Remote Sensing*, *25*(22), 5089-5104.

Been, K., and G. C. Sills (1981), Self-weight consolidation of soft soils: an experimental and theoretical study, *Géotechnique*, *31*(4), 519-535.

Bennett, S. J., and J. L. Best (1995), Mean flow and turbulence structure over fixed, two-dimensional dunes: implications for sediment transport and bedform stability, *Sedimentology*, *42*(3), 491-513.

Berlamont, J., et al. (1993), The characterisation of cohesive sediment properties, *Coastal Engineering*, *21*(1-3), 105-128.

Best, J., and R. Kostaschuk (2002), An experimental study of turbulent flow over a low-angle dune, *Journal of Geophysical Research*, *107*(C9), 3135.

Best, J. (2005a), The fluid dynamics of river dunes: A review and some future research directions, *Journal of Geophysical Research*, *110*(F4), F04S02.

Best, J. (2005b), Kinematics, Topology and Significance of Dune-Related Macroturbulence: Some Observations from the Laboratory and Field, in *Fluvial Sedimentology VII*, edited by M. D. Blum, et al., pp. 41-60, Blackwell Publishing Ltd., Oxford, UK.

Blake, A. C., et al. (2001), Sediment trapping and transport in the ACE Basin, South Carolina, *Estuaries and Coasts*, *24*(5), 721-733.

Blondel, P., and B. J. Murton (1997), *Handbook of seafloor sonar imagery*, 425 pp., Wiley, Chichester.

Brezina, J. (1979), Particle size and settling rate distributions of sand-sized materials, in *Proceedings of 2nd European Symposium on Particle Characterisation, Nürnberg, Germany*, edited.

Bruens, A. W., et al. (2002), Physical modelling of entrainment by a Concentrated Benthic Suspension, in *Fine Sediment Dynamics in the Marine Environment - Intercoh 2000*, edited by J. C. Winterwerp and C. Kranenburg, pp. 109-124, Elsevier.

Bruens, A. W. (2003), Entraining mud suspensions, PhD thesis, 139 pp, Technical University Delft, Delft, The Netherlands.

Bundesanstalt für Gewässerkunde (1992), Anpassung der Fahrrinne der Außenweser an die künftig weltweit gültigen Anforderungen der Containerschifffahrt, SKN-14 m-Ausbau, Umweltverträglichkeitsuntersuchung BFG-0664, Bundesanstalt für Gewässerkunde, Koblenz.

Bunt, J. A. C., et al. (1999), Quantifying the response of optical backscatter devices and transmissometers to variations in suspended particulate matter, *Continental Shelf Research*, *19*, 1199-1220.

Burchard, H., and H. Baumert (1998), The Formation of Estuarine Turbidity Maxima Due to Density Effects in the Salt Wedge. A Hydrodynamic Process Study, *Journal of Physical Oceanography*, *28*(2), 309-321.

Carling, P. A., et al. (2006), The morphodynamics and internal structure of intertidal fine-gravel dunes: Hills Flats, Severn Estuary, UK, *Sedimentary Geology*, *183*(3-4), 159-179.

Chriss, T. M., and D. R. Caldwell (1982), Evidence for the Influence of Form Drag on Bottom Boundary Layer Flow, *Journal of Geophysical Research*, *87*(C6), 4148-4154.

Colijn, F. (1982), Light absorption in the waters of the Ems-Dollard Estuary and its consequences for the growth of phytoplankton and microphytobenthos, *Netherlands Journal of Sea Research*, *15*, 196-216.

Costello, D. K., et al. (1989), In situ holographic imaging of settling particles: applications for individual particle dynamics and ocean flux measurements, *Deep-Sea Research*, *36*, 1595-1605.

Crump, B. C., and J. A. Barross (2000), Characterisation of the bacterially-active particle fraction in the Columbia River estuary, *Marine Ecology Progress Series*, *206*, 13-22.

Dalrymple, R. W., and K. Choi (2007), Morphologic and facies trends through the fluvial-marine transition in tide-dominated depositional systems: A schematic framework for environmental and sequence-stratigraphic interpretation, *Earth-Science Reviews*, *81*(3-4), 135-174.

de Boer, G. J., et al. (2007), A parameterised consolidation model for cohesive sediments, in *Estuarine and Coastal Fine Sediments Dynamics - Intercoh 2003*, edited by J. P. Y. Maa, et al., pp. 243-262, Elsevier.

de Jonge, V. N. (1983), Relation between annual dredging activities, suspended matter concentrations, and the development of the tidal regime in the Ems estuary, *Canadian Journal of Fisheries and Aquatic Sciences*, *40*, 289-300.

de Jonge, V. N. (1988), The abiotic environment, in *Tidal flat estuaries; simulation and analysis of the Ems Estuary*, edited by J. Baretta and P. Ruardij, pp. 14-27, Springer Verlag, Heidelberg.

de Jonge, V. N. (1992), Tidal flow and residual flow in the Ems estuary, *Estuarine, Coastal and Shelf Science*, *34*(1), 1-22.

Deines, K. L. (1999), Backscatter Estimation Using Broadband Acoustic Doppler Current Profilers, *Oceans 99 MTS\IEEE Conference Proceedings, San Diego*.

Dette, H., et al. (1994), Anpassung des Ems-Fahrwassers an ein 7.30 m tiefgehendes Schiff - Beurteilung der Auswirkungen aus Sicht der Hydrologie, *Leichtweiss-Institut für Wasserbau, Bericht Nr. 770, Braunschweig, Germany*.

Deutsches Gewässerkundliches Jahrbuch (2005), *Weser- und Emsgebiet 2002*, Niedersächsischer Landesbetrieb für Wasserwirtschaft, Küsten- und Naturschutz, Norden.

Dinehart, R. L., and J. R. Burau (2005), Repeated surveys by acoustic Doppler current profiler for flow and sediment dynamics in a tidal river, *Journal of Hydrology*, *314*(1-4), 1-21.

Dong, L., et al. (1997), Field and Modeling Studies of Fine Sediment Dynamics in the Extremely Turbid Jiaojiang River Estuary, China, *Journal of Coastal Research*, *13*(4), 995-1003.

Downing, J. (2006), Twenty-five years with OBS sensors: The good, the bad, and the ugly, *Continental Shelf Research*, *26*(17-18), 2299-2318.

Dronkers, J. (1986a), Tidal asymmetry and estuarine morphology, *Netherlands Journal of Sea Research*, *20*(2-3), 117-131.

Dronkers, J. (1986b), Tide-induced Residual Transport of Fine Sediment, in *Physics of Shallow Estuaries and Bays*, edited by J. Van de Kreeke, pp. 228-244, Springer, Berlin.

Duffy, G. P., and J. E. Hughes-Clarke (2005), Application of spatial cross correlation to detection of migration of submarine dunes, *Journal of Geophysical Research*, *110*, F04S12.

Dyer, K. R. (1986), *Coastal and Estuarine Sediment Dynamics*, 337 pp., Wiley-Interscience.

Dyer, K. R. (1988), Fine Sediment Particle Transport in Estuaries, in *Physical processes in estuaries*, edited by J. Dronkers and W. Van Leussen, pp. 295-310, Springer, Berlin

Dyer, K. R. (1995), Sediment Transport Processes in Estuaries, in *Geomorphology and Sedimentology of Estuaries*, edited by G. M. E. Perillo, pp. 423-449, Elsevier.

Dyer, K. R., et al. (1996), A comparison of in situ techniques for estuarine floc settling velocity measurements, *Journal of Sea Research*, *36*(1-2), 15-29.

Dyer, K. R., and A. J. Manning (1999), Observation of the size, settling velocity and effective density of flocs, and their fractal dimensions, *Journal of Sea Research*, *41*(1-2), 87-95.

Dyer, K. R., et al. (2004), The effects of suspended sediment on turbulence within an estuarine turbidity maximum, *Estuarine, Coastal and Shelf Science*, *59*(2), 237-248.

Eisma, D. (1986), Flocculation and de-flocculation of suspended matter in estuaries, *Netherlands Journal of Sea Research*, *20*(2-3), 183-199.

Eisma, D. (1993), *Suspended matter in the aquatic environment*, 327 pp., Springer, Berlin Heidelberg New York.

Eisma, D., et al. (1996), Intercomparison of in situ suspended matter (floc) size measurements, *Journal of Sea Research*, *36*(1-2), 3-14.

Eißfeldt, F. P., and M. Pietsch (2001), Geotechnische und rheologische Untersuchungen zur Nautischen Sohle im Revier der Außenweser, *HANSA*, *138*(6), 89-93.

Engel, P., and Y. L. Lau (1980), Computation of bedload using bathymetric data, *Journal of the Hydraulics Division*, *106*, 369-380.

Engelund, F., and J. Fredsoe (1976), A sediment transport model for straight alluvial channels, *Nordic Hydrology*, *7*(5), 293-306.

Ernstsen, V., et al. (2006a), Precision of high-resolution multibeam echo sounding coupled with high-accuracy positioning in a shallow water coastal environment, *Geo-Marine Letters*, *26*(3), 141-149.

Ernstsen, V., et al. (2006b), Quantification of dune dynamics during a tidal cycle in an inlet channel of the Danish Wadden Sea, *Geo-Marine Letters*, *26*(3), 151-163.

Ernstsen, V. B., et al. (2005), Development of subaqueous barchanoid-shaped dunes due to lateral grain size variability in a tidal inlet channel of the Danish Wadden Sea, *Journal of Geophysical Research*, *110*(F4), F04S08.

Ernstsen, V. B., et al. (2007), Bedload transport in an inlet channel during a tidal cycle, paper presented at River, Coastal and Estuarine Morphodynamics: RCEM 2007, Tayler & Francis: London, Enschede, The Netherlands.

Ernstsen, V. B., et al. (2009), Tide-controlled variations of primary- and secondary-bedform height: Innenjade tidal channel (Jade Bay, German Bight), paper presented at River, Coastal and Estuarine Morphodynamics: RCEM 2009, Tayler & Francis: London, Santa Fe, Argentina.

Fanger, H.-U., et al. (1985), MASEX '83, eine Untersuchung über die Trübungszone der Unterweser, *Die Küste*, *42*, 171-187.

Fenies, H., et al. (1999), Intertidal clay-drape couplets (Gironde estuary, France), *Sedimentology*, *46*(1), 1-15.

Fenster, M. S., and D. M. FitzGerald (1996), Morphodynamics, stratigraphy, and sediment transport patterns of the Kennebec River estuary, Maine, USA, *Sedimentary Geology*, *107*(1-2), 99-120.

Fernando, H. J. S. (1991), Turbulent Mixing in Stratified Fluids, *Annual Review of Fluid Mechanics*, *23*(1), 455-493.

Fettweis, M., et al. (2006), Suspended particulate matter dynamics and aggregate sizes in a high turbidity area, *Marine Geology*, *235*(1-4), 63-74.

Flammer, G. H. (1962), Ultrasonic measurement of suspended sediment, *U.S. Geological Survey Bulletin*, *1141-A*, 48.

Folk, R. L., and W. C. Ward (1957), Brazos riverbar: a study in the significance of grain size parameters, *Journal of Sedimentary Petrology*, *27*(1), 3-26.

Franzius, L. (1991), Die Korrektion der Unterweser (Bremen, Nachdruck von 1888 mit ergänzenden Anmerkungen von Dipl.-Ing. Jan Dierksen), *Die Küste*, *51*, 39-74.

Fredsøe, J., and R. Deigaard (1992), *Mechanics of Coastal Sediment Transport.*, World Scientific Publishing.

Fugate, D. C., and C. T. Friedrichs (2002), Determining concentration and fall velocity of estuarine particle populations using ADV, OBS and LISST, *Continental Shelf Research*, *22*(11-13), 1867-1886.

Fugate, D. C., and C. T. Friedrichs (2003), Controls on suspended aggregate size in partially mixed estuaries, *Estuarine, Coastal and Shelf Science*, *58*(2), 389-404.

Gartner, J. W. (2004), Estimating suspended solids concentrations from backscatter intensity measured by acoustic Doppler current profiler in San Francisco Bay, California, *Marine Geology*, *211*(3-4), 169-187.

Gibbs, R. J., et al. (1989), Coagulation and transport of sediments in the Gironde Estuary, *Sedimentology*, *36*(6), 987-999.

Gienapp, H. (1983), Marine optical investigations in the Ems estuary, *Ocean Dynamics*, *36*(4), 157-165.

Grabemann, I. (1992), Die Trübungszone im Weser-Ästuar: Messungen und Interpretation, *GKSS-Forschungszentrum Geesthacht GmbH, Dissertation Rep 92 E15*.

Grabemann, I., et al. (1997), Behaviour of Turbidity Maxima in the Tamar (U.K.) and Weser (F.R.G.) Estuaries, *Estuarine, Coastal and Shelf Science*, *45*(2), 235-246.

Grabemann, I., and G. Krause (2001), On different time scales of suspended matter dynamics in the Weser estuary, *Estuaries and Coasts*, *24*(5), 688-698.

Grabemann, L., and G. Krause (1989), Transport Processes of Suspended Matter Derived From Time Series in a Tidal Estuary, *Journal of Geophysical Research*, *94*(C10), 14373-14379.

Gray, J. R., and J. W. Gartner (2009), Technological advances in suspended-sediment surrogate monitoring, *Water Resources Research*, *45*, W00D29.

Guan, W. B., et al. (1998), Cohesive Sediment Transport in the Jiaojiang River Estuary, China, *Estuarine, Coastal and Shelf Science*, *46*(6), 861-871.

Guan, W. B., et al. (2005), 3D fluid-mud dynamics in the Jiaojiang Estuary, China, *Estuarine, Coastal and Shelf Science*, *65*(4), 747-762.

Habermann, C., and A. Wurpts (2008), Occurrence, behaviour and physical properties of fluid mud, in *Proceedings of the Chinese-German Joint Symposium on Hydraulic and Ocean Engineering*, edited by U. Zanke, et al., Institute of Hydraulic and Water Resource Engineering, Technische Universität Darmstadt, Darmstadt.

Hamilton, L. J., et al. (1998), Acoustic Backscatter Measurements of Estuarine Suspended Cohesive Sediment Concentration Profiles, *Journal of Coastal Research*, *14*(4), 1213-1224.

Herrling, G., and H. D. Niemeyer (2008), Set-up of a morphodynamic model for the Ems-Dollard estuary, *Report of the European Project HARBASINS. Lower Saxony Water Management, Coastal Defence and Nature Conservation Agency, Norden, Germany*.

Hill, D. C., et al. (2003), Derivation of sediment resuspension rates from acoustic backscatter time-series in tidal waters, *Continental Shelf Research*, *23*(1), 19-40.

Hoekstra, P., et al. (2004), Bedform migration and bedload transport on an intertidal shoal, *Continental Shelf Research*, *24*(11), 1249-1269.

Hoitink, A. J. F., and P. Hoekstra (2005), Observations of suspended sediment from ADCP and OBS measurements in a mud-dominated environment, *Coastal Engineering*, *52*(2), 103-118.

Holdaway, G. P., et al. (1999), Comparison between ADCP and transmissometer measurements of suspended sediment concentration, *Continental Shelf Research*, *19*(3), 421-441.

Hovikoski, J., et al. (2008), Ichnology and Sedimentology of a Mud-Dominated Deltaic Coast: Upper Cretaceous Alderson Member (Lea Park Fm), Western Canada, *Journal of Sedimentary Research*, *78*(12), 803-824.

Hsu, T.-J., et al. (2009), High-resolution numerical modeling of wave-supported gravity-driven mudflows, *Journal of Geophysical Research*, *114*, C05014.

Hsu, T. J., et al. (2007), On modeling boundary layer and gravity-driven fluid mud transport, *Journal of Geophysical Research*, *112*(C4), C04011.

Ichaso, A. A., and R. W. Dalrymple (2009), Tide- and wave-generated fluid mud deposits in the Tilje Formation (Jurassic), offshore Norway, *Geology*, *37*(6), 539-542.

Inglis, C. C., and F. H. Allen (1957), The regimen of the Thames Estuary as affected by currents, salinities and river flow, *Proceedings of the Institution of Civil Engineers 7*, 827-868.

Irion, G., et al. (1987), Transport of clay minerals and anthropogenic compounds into the German Bight and the provenance of fine-grained sediments SE of Helgoland, *Journal of the Geological Society*, *144*(1), 153-160.

Jensen, J., et al. (2003), Hydrological changes in tidal estuaries due to natural and anthropogenic effects, paper presented at Proceedings of the 6th International MEDCOAST 2003 Conference, Ravenna, Italy.

Jensen, J., and C. Mudersbach (2006), Recent sea level variation at the North Sea and Baltic Sea coastlines, *Proceedings of International Conference on Coastal Engineering, ICCE, San Diego*.

Jiang, J., and A. J. Mehta (2002), Interfacial instabilities at the lutocline in the Jiaojiang estuary, China, in *Fine Sediment Dynamics in the Marine Environment - Intercoh 2000*, edited by J. C. Winterwerp and C. Kranenburg, pp. 125-137, Elsevier.

Joint, I. R., and A. J. Pomroy (1981), Primary production in a turbid estuary, *Estuarine and Coastal Shelf Science*, *13*, 303-316.

Kim, Y. H., and G. Voulgaris (2003), Estimation of suspended sediment concentration in estuarine environments using acoustic backscatter from an ADCP, *Proceedings of the International Conference on Coastal Sediments*.

Kineke, G. C., et al. (1996), Fluid mud processes on the Amazon Continental Shelf, *Continental Shelf Research*, *16*(5-6), 667-696.

Kirby, R., and W. R. Parker (1977), The physical characteristics and environmental significance fine sediment suspensions in estuaries, *Estuaries, Geophysics and the Environment*, 110-120.

Kirby, R., and W. R. Parker (1983), Distribution and behavior of fine sediment in the Severn Estuary and Inner Bristol Channel, U.K., *Canadian Journal of Fisheries and Aquatic Science*, *40*, 83-95.

Kirby, R. (1988), High Concentration Suspension (Fluid Mud) Layers in Estuaries, in *Physical processes in estuaries*, edited by J. Dronkers and W. Van Leussen, pp. 463-487, Springer, Berlin

Kleinhans, M. G. (2004), Sorting in grain flows at the lee side of dunes, *Earth-Science Reviews*, *65*(1-2), 75-102.

Knaapen, M., et al. (2005), Quantifying bedform migration using multi-beam sonar, *Geo-Marine Letters*, *25*(5), 306-314-314.

Knaapen, M. A. F. (2005), Sandwave migration predictor based on shape information, *Journal of Geophysical Research*, *110*(F4), F04S11.

Kostaschuk, R. (2000), A field study of turbulence and sediment dynamics over subaqueous dunes with flow separation, *Sedimentology*, *47*, 519-531.

Kostaschuk, R., et al. (2005), Measuring flow velocity and sediment transport with an acoustic Doppler current profiler, *Geomorphology*, *68*(1-2), 25-37.

Kranck, K. (1984), Settling behaviour of cohesive sediment, in *Estuarine Cohesive Sediment Dynamics - Intercoh 1984*, edited by A. J. Mehta, pp. 151-169, Springer, Berlin.

Kranenburg, C., and J. C. Winterwerp (1997), Erosion of Fluid Mud Layers. I: Entrainment Model, *Journal of Hydraulic Engineering*, *123*(6), 504-511.

Krebs, M., and H. Weilbeer (2008), Ems-Dollard Estuary, *Die Küste*, *74*.

Lampitt, R. S., et al. (1993), Seasonal and daily variation in the open ocean concentration of marine snow aggregates, *Nature 362*, 737-739.

Lang, G., et al. (1989), Data Interpretation and Numerical Modeling of the Mud and Suspended Sediment Experiment 1985, *Journal of Geophysical Research*, *94*(C10), 14381-14393.

Lee, T. H., and D. M. Hanes (1995), Explicit solution to the acoustic backscatter equation to measure the concentration of uniform, suspended particles, *Journal of Geophysical Research*, *100*(C2), 2649-2657.

Lefebvre, A., et al. (2010), Influence of compound bedforms on hydraulic roughness in a tidal environment, *Physics of Estuaries and Coastal Seas Conference 2010*, 4.

Lewis, D. W., and D. McConchie (1994), *Analytical sedimentology*, 512 pp., Chapman & Hall, New York.

Li Hir, P., et al. (2001), *Application of the continuous modeling concept to simulate high-concentration suspended sediment in a macro-tidal estuary*, in *Coastal and Estuarine Fine Sediment Processes*, edited by W. H. McAnally and A. J. Mehta, pp. 229-247, Elsevier.

Liebetruth, F., and F. P. Eißfeldt (2003), Grundlagen für die Sicherheit und Leichtigkeit des Schiffsverkehrs - Untersuchungen zur nautischen Sohle, *Mitteilungen der Bundesanstalt für Wasserbau*, *87*, 77-82.

Loeser, H. T. (1992), *Sonar engineering handbook*, 217 pp., Peninsula, Los Altos, California.

Lueck, R. G., and Y. Lu (1997), The logarithmic layer in a tidal channel, *Continental Shelf Research*, *17*(14), 1785-1801.

Lunau, M., et al. (2004), A new sampling device for microaggregates in turbid aquatic systems, *Limnology and Oceanography: Methods*, *2*, 387-397.

Lüneburg, H. (1955), Beiträge zur Hydrographie der Wesermündung, Teil IV: zur Verteilung der Sinkstoffe in den Seitenräumen der

Wesermündung, *Veröffentlichungen des Instituts für Meeresforschung in Bremerhaven*, *III*, 228-265.

Lüneburg, H., et al. (1974), Physiographie des Weser-Ästuars (Deutsche Bucht), *Veröffentlichungen des Instituts für Meeresforschung in Bremerhaven*, *15*(3), 195-226.

Lüneburg, H., et al. (1975), Physiographie des Weser-Ästuars (Deutsche Bucht), *Veröffentlichungen des Instituts für Meeresforschung in Bremerhaven*, *15*(3), 195-226.

MacCready, P., and W. R. Geyer (2009), Advances in Estuarine Physics, *Annual Review of Marine Science*, *2*(1), 35-58.

Madson, J. A., and C. K. Sommerfield (2003), Application of side-scan sonar, sub bottom profiling, and echo-sounding techniques to study sediment deposition and erosion in estuaries: results from the lower Delaware River and upper Delaware Bay, paper presented at Proceedings of the US Hydro 2003 Conference, The Hydrographic Society of America (THSOA), Rockville, Maryland, Biloxi, Mississippi, 24-27 March 2003.

Malcherek, A. (1995), Mathematische Modellierung von Strömungen und Stofftransportprozessen in Ästuaren, PhD thesis, 200 pp, Universität Hannover.

Malone, T. C. (1976), Phytoplankton productivity in the apex of the New York Bight: Environmental regulation of productivity/chlorophyll a, in *The middle Atlantic Shelf and New York Bight*, edited by M. G. Gross, pp. 260-272.

Manning, A. J., and K. R. Dyer (2002), A comparison of floc properties observed during neap and spring tidal conditions, in *Fine Sediment Dynamics in the Marine Environment - Intercoh 2000*, edited by J. C. Winterwerp and C. Kranenburg, pp. 233-250, Elsevier.

Manning, A. J., and K. R. Dyer (2007), Mass settling flux of fine sediments in Northern European estuaries: Measurements and predictions, *Marine Geology*, *245*(1-4), 107-122.

Manning, A. J., et al. (2010), A review of sediment dynamics in the Severn Estuary: Influence of flocculation, *Marine Pollution Bulletin*, *61*(1-3), 37-51.

McAnally, W. H., et al. (2007a), Management of Fluid Mud in Estuaries, Bays, and Lakes. I: Present State of Understanding on Character and Behavior, *Journal of Hydraulic Engineering*, *133*(1), 9-22.

McAnally, W. H., et al. (2007b), Management of Fluid Mud in Estuaries, Bays, and Lakes. II: Measurement, Modeling, and Management, *Journal of Hydraulic Engineering*, *133*(1), 23-38.

McLean, S., et al. (2008), Double-averaged velocity profiles over fixed dune shapes, *Acta Geophysica*, *56*(3), 669-697.

McLean, S. R., and D. Smith (1979), Turbulence Measurements in the Boundary Layer Over a Sand Wave Field, *Journal of Geophysical Research*, *84*(C12), 7791-7808.

McLean, S. R., et al. (1999), Spatially averaged flow over a wavy boundary revisited, *Journal of Geophysical Research*, *104*(C7), 15743-15753.

McLean, S. R., et al. (2007), Suspended sediment in the presence of dunes, *River, Coastal and Estuarine Morphodynamics Conference 2007*, 611-618.

Medwin, H. (2005), *Sounds in the Sea - From Ocean Acoustics to Acoustic Oceanography*, University Press, Cambridge.

Mehta, A. J. (1984), Characterization of cohesive sediment properties and transport processes in estuaries, in *Estuarine Cohesive Sediment Dynamics - Intercoh 1984*, edited by A. J. Mehta, pp. 290-325, Springer, Berlin.

Mehta, A. J. (1989), On estuarine cohesive sediment suspension behavior, *Journal of Geophysical Research*, *94*(C10), 14303.

Meischner, D., and J. Rumohr (1974), A light-weight, high-momentum gravity corer for subaqueous sediments, *Senckenbergiana maritima*, *6*(1), 105-117.

Merckelbach, L., and H. Ridderinkhof (2006), Estimating suspended sediment concentration using backscatterance from an acoustic Doppler profiling current meter at a site with strong tidal currents, *Ocean Dynamics*, *56*(3), 153-168.

Mikkelsen, O., and M. Pejrup (2001), The use of a LISST-100 laser particle sizer for in-situ estimates of floc size, density and settling velocity, *Geo-Marine Letters*, *20*(4), 187-195.

Mikkelsen, O. A. (2002), Examples of spatial and temporal variations of some fine-grained suspended particle characteristics in two Danish coastal water bodies, *Oceanologica Acta*, *25*(1), 39-49.

Miles, J. W. (1961), On the stability of heterogeneous shear flows, *Journal of Fluid Mechanics*, *10*(4), 496-508.

Milligan, T. G. (1995), An examination of the settling behaviour of a flocculated suspension, *Netherlands Journal of Sea Research*, *33*(2), 163-171.

Mueller, D. S., and C. R. Wagner (2007), Correcting Acoustic Doppler Current Profiler Discharge Measurements Biased by Sediment Transport, *Journal of Hydraulic Engineering*, *133*(12), 1329-1336.

Müller, H. (1985), Vergleichende Messungen der Sohllage in einem Unterweserquerschnitt innerhalb der Schlickstrecke bei Nordenham, *Die Küste*, *42*, 209-225.

Murdoch, A., and J. M. Azcue (1995), *Manual of aquatic sediment sampling*, 189 pp., CRC, Boca Raton, Florida.

Muste, M., et al. (2004a), Practical aspects of ADCP data use for quantification of mean river flow characteristics; Part II: fixed-vessel measurements, *Flow Measurement and Instrumentation*, *15*(1), 17-28.

Muste, M., et al. (2004b), Practical aspects of ADCP data use for quantification of mean river flow characteristics; Part I: moving-vessel measurements, *Flow Measurement and Instrumentation*, *15*(1), 1-16.

Nasner, H. (1974), Über das Verhalten von Transportkörpern im Tidegebiet, *Mitteilungen des Franzius-Instituts für Wasserbau und Küsteningenieurwesen*, *40*, 1-140.

Nelson, J. M., et al. (1993), Mean Flow and Turbulence Fields Over Two-Dimensional Bed Forms, *Water Resources Research*, *29*(12), 3935-3953.

Nezu, I., and H. Nakagawa (1993), *Turbulence in open-channel flows*, 281 pp., IAHR Monograph.

Nguyen, K. D., et al. (2009), A two-phase numerical model for suspended-sediment transport in estuaries, *Advances in Water Resources*, *32*(8), 1187-1196.

Nichols, M. M., and G. Poor (1976), Sediment transport in a coastal plain estuary, *Journal of the Waterways and Harbors Division*, *93*, 83-95.

Nichols, M. M., and R. B. Biggs (1985), Estuaries, in *Coastal Sedimentary Environments*, edited by P. A. Davis, pp. 77-186, Springer-Verlag, New York.

Nielsen, P. (1992), *Coastal Bottom Boundary Layers and Sediment Transport*, World Scientific Publishing.

Nikora, V., et al. (2007a), Double-Averaging Concept for Rough-Bed Open-Channel and Overland Flows: Applications, *Journal of Hydraulic Engineering*, *133*(8), 884-895>.

Nikora, V., et al. (2007b), Double-Averaging Concept for Rough-Bed Open-Channel and Overland Flows: Theoretical Background, *Journal of Hydraulic Engineering*, *133*(8), 873-883.

Nitsche, F. O., et al. (2004), Process-related classification of acoustic data from the Hudson River Estuary, *Marine Geology*, *209*, 131-145.

Noh, Y., and H. J. S. Fernando (1991), Dispersion of suspended particles in turbulent flow, *Physics of Fluids A: Fluid Dynamics*, *3*(7), 1730-1740.

Paarlberg, A. J., et al. (2007), A parameterization of flow separation over subaqueous dunes, *Water Resources Research*, *43*, 60020-/RIS.

Paarlberg, A. J., et al. (2009), Modeling river dune evolution using a parameterization of flow separation, *Journal of Geophysical Research*, *114*(F1), F01014.

Pennock, J. R., and J. H. Sharp (1986), Phytoplankton production in the Delaware Estuary: Temporal and spatial variability, *Marine Ecology Progress Series*, *34*, 143-155.

Pommepuy, M., et al. (1992), Enteric bacteria survival factors, *Water Science and Technology*, *25*(12), 93-103.

Postma, H., and K. Kalle (1955), Die Entstehung von Trübungszonen im Unterlauf der Flüsse, speziell im Hinblick auf die Verhältnisse in der Unterelbe, *Ocean Dynamics*, *8*(4), 137-144.

Prandle, D. (2004), Sediment trapping, turbidity maxima, and bathymetric stability in macrotidal estuaries, *Journal of Geophysical Research*, *109*(C8), C08001.

Pritchard, D. W. (1954), A study of the salt balance in a coastal plain estuary, *Journal of Marine Research*, *13*(1), 133-144.

Puls, W., et al. (1988), Settling Velocity of Mud Flocs: Results of Field Measurements in the Elbe and the Weser Estuary, in *Physical processes in estuaries*, edited by J. Dronkers and W. Van Leussen, pp. 404-424, Springer, Berlin

RD Instruments (2008), ADCP Coordinate Transformation Formulas and Calculations, 31 pp, RD Instruments, San Diego, California.

Riethmüller, R., et al. (1988), Hydrographic measurements in the turbidity zone of the Weser estuary, in *Physical processes in estuaries*, edited by J. Dronkers and W. Van Leussen, pp. 332-344, Springer, Berlin.

Ross, M. A., and A. J. Mehta (1989), On the mechanics of lutoclines and fluid mud, *Journal of Coastal Research*, *SI5*, 51-61.

Rozen, Y., and S. Belkin (2001), Survival of enteric bacteria in seawater, *FEMS Microbiology Ecology*, *25*, 513-529.

Sanford, L. P., et al. (2001), Reconsidering the physics of the Chesapeake Bay estuarine turbidity maximum, *Estuaries and Coasts*, *24*(5), 655-669.

Sato, T., et al. (2011), Generation of tidal bedding in a circular flume experiment: formation process and preservation potential of mud drapes, *Geo-Marine Letters*, *31*(2), 101-108-108.

Schieber, J., et al. (2007), Accretion of Mudstone Beds from Migrating Floccule Ripples, *Science*, *318*(5857), 1760-1763.

Schoellhamer, D. H., et al. (2000), Influence of salinity, bottom topography, and tides on locations of estuarine turbidity maxima in northern San Francisco Bay, in *Coastal and Estuarine Fine Sediment Processes - Intercoh 1998*, edited by W. H. McAnally and A. J. Mehta, pp. 343-357, Elsevier.

Schrottke, K., et al. (2005), Bed Mobility in the Weser Estuary Turbidity Zone, *Hydro International*, *9*(7), 27-29.

Schrottke, K., and F. Abegg (2006), Measurements of near-bed suspended sediment dynamics in a tidal channel of the German Wadden Sea, *Die Küste*, *69*, 353-367.

Schrottke, K., et al. (2006), Fluid mud dynamics in the Weser estuary turbidity zone tracked by high-resolution side-scan sonar and parametric sub-bottom profiler, *Geo-Marine Letters*, *26*(3), 185-198.

Schubel, J. R., and H. H. Carter (1984), The estuary as a filter for fine-grained suspended sediment,, in *The Estuary as a Filter*, edited by V. S. Kennedy, pp. 81-107, Academic Press, Orlando.

Shanley, K. W., et al. (1992), Tidal influence in Cretaceous fluvial strata from Utah, USA: a key to sequence stratigraphic interpretation, *Sedimentology*, *39*(5), 905-930.

Sheng, Y. P., and C. Villaret (1989), Modeling the Effect of Suspended Sediment Stratification on Bottom Exchange Processes, *Journal of Geophysical Research*, *94*(C10), 14429-14444.

Shi, J. Z., et al. (2006), Bottom fine sediment boundary layer and transport processes at the mouth of the Changjiang Estuary, China, *Journal of Hydrology*, *327*(1-2), 276-288.

Shi, Z., et al. (1996), Vertical suspension profile in the Changjiang Estuary, *Marine Geology*, *130*, 29-37.

Shi, Z., et al. (1997), Acoustic imaging of cohesive sediment resuspension and re-entrainment in the Changjiang Estuary, East China Sea, *Geo-Marine Letters*, *17*(2), 162-168.

Shi, Z. (1998), Acoustic Observations of Fluid Mud and Interfacial Waves, Hangzhou Bay, China, *Journal of Coastal Research*, *14*(4), 1348-1353.

Shi, Z., et al. (1999), Acoustic profiling of fine suspension concentration in the Changjiang estuary, *Estuaries and Coasts*, *22*(3), 648-656.

Siegenthaler, C. (1982), Tidal cross-strata and the sediment transport rate problem: A geologist's approach, *Marine Geology*, *45*(3-4), 227-240.

Simon, M., et al. (2002), Microbial ecology of organic aggregates in aquatic ecosystems, *Aquatic Microbial Ecology*, *175-211*, 175-211.

Simons, D. B., et al. (1965), Unsteady movement of ripples and dunes related to bedload transport, *Proceedings of IAHR Congress, Leningrad, U.S.S.R.*, *3*(29), 1-8.

Simpson, J., et al. (1990), Tidal straining, density currents, and stirring in the control of estuarine stratification, *Estuaries and Coasts*, *13*(2), 125-132.

Simpson, M. R., and R. N. Oltmann (1993), Discharge-measurement system using an acoustic Doppler current profiler with applications to large rivers and estuaries, *US Geological Survey Water-Supply Paper 2395*(32).

Simpson, R. L. (1989), Turbulent Boundary-Layer Separation, *Annual Review of Fluid Mechanics*, *21*(1), 205-232.

Smith, J. D., and S. R. McLean (1977), Spatially Averaged Flow Over a Wavy Surface, *Journal of Geophysical Research*, *82*(12), 1735-1746.

Sorby, H. C. (1908), On the Application of Quantitative Methods to the Study of the Structure and History of Rocks, *Quarterly Journal of the Geological Society*, *64*(1-4), 171-233.

Sottolichio, A., and P. Castaing (1999), A synthesis on seasonal dynamics of highly-concentrated structures in the Gironde estuary, *Comptes Rendus de l'Académie des Sciences - Series IIA - Earth and Planetary Science*, *329*(11), 795-800.

Soulsby, R. (1997), *Dynamics of Marine Sands: A Manual for Practical Applications*, Thomas Telford, London.

Soulsby, R., and R. J. S. W. Whitehouse (1997), Threshold of sediment motion in coastal environments, paper presented at *Pacific Coasts and Ports Conference*, Christchurch, New Zealand.

Soulsby, R. L. (1980), Selecting Record Length and Digitization Rate for Near-Bed Turbulence Measurements, *Journal of Physical Oceanography*, *10*(2), 208-219.

Soulsby, R. L., and J. S. Damgaard (2005), Bedload sediment transport in coastal waters, *Coastal Engineering*, *52*(8), 673-689.

Spingat, F. M. (1997), Analyse der Schwebstoffdynamik in der Trübungszone eines Tideflusses, *Leichtweiss-Instituts für Wasserbau der Technischen Universität Braunschweig, Mitteilung*, *139*.

Stark, N., et al. (2011), Coupled penetrometer, MBES and ADCP assessments of tidal variations in surface sediment layer characteristics along active subaqueous dunes, Danish Wadden Sea, *Geo-Marine Letters*, 1-10.

Steen, D. (2003), Planungen und Eingriffe im Dollartraum nach 1945, *Zwischen Weser und Ems*, *37*, 74-91.

Streif, H., and R. Köster (1978), Zur Geologie der deutschen Nordseeküste, *Die Küste*, *32*, 30-48.

Stull, R. B. (1993), *An introduction to boundary layer meteorology*, 666 pp., Kluwer Academic Publishers, Dordrecht.

Svenson, C., et al. (2009), Tide-driven sediment variations on a large compound dune in the Jade tidal inlet channel, Southeastern North Sea, *Journal of Coastal Research*, *SI56*, 361-365.

Talke, S. A., and H. E. de Swart (2006), Hydrodynamics and Morphology in the Ems/Dollard Estuary: Review of Models, Measurements, Scientific Literature, and the Effects of Changing Conditions, *Report # R06-01, Institute for Marine and Atmospheric Research Utrecht, University of Utrecht, The Netherlands*, 134.

Talke, S. A., et al. (2009), Feedback between residual circulations and sediment distribution in highly turbid estuaries: An analytical model, *Continental Shelf Research*, *29*(1), 119-135.

Tennekes, H., and J. L. Lumley (1972), *A First Course in Turbulence*, MIT Press, Cambridge, MA.

Thorne, P. D., et al. (1991), Measuring suspended sediment concentrations using acoustic backscatter devices, *Marine Geology*, *98*(1), 7-16.

Thorne, P. D., et al. (1993), Analysis of Acoustic Measurements of Suspended Sediments, *Journal of Geophysical Research*, *98*(C1), 899-910.

Thorne, P. D., et al. (1994), Analysis of results obtained from a triple frequency acoustic backscatter system for measuring suspended sediments, paper presented at 6th International Conference on Electronic Engineering in Oceanography, Cambridge.

Thorne, P. D., and D. M. Hanes (2002), A review of acoustic measurement of small-scale sediment processes, *Continental Shelf Research*, *22*(4), 603-632.

Toorman, E. A. (2000), Cohesive sediment transport modeling: European perspective, in *Coastal and Estuarine Fine Sediment Processes - Intercoh 1998*, edited by W. H. McAnally and A. J. Mehta, pp. 1-18, Elsevier.

Topping, D. J., et al. (2007), High-resolution measurements of suspended-sediment concentration and grain size in the Colorado River in Grand Canyon using a multi-frequency acoustic system, paper presented at Proceedings of the Tenth International Symposium on River Sedimentation, Moscow, August 1-4.

Trevethan, M., et al. (2009), High frequency measurements about the water fluid mud boundary in the estuarine zone of the Ems River Germany, *Proceedings of 33rd Biennial IAHR Congress, Vancouver, Canada*, 4167-4174.

Trowbridge, J. H., and G. C. Kineke (1994), Structure and dynamics of fluid muds on the Amazon continental shelf, *Journal of Geophysical Research*, *99*(C1), 865-874.

Trump, C. L., and G. O. Marmorino (1997), Calibrating a Gyrocompass Using ADCP and DGPS Data, *Journal of Atmospheric and Oceanic Technology*, *14*(1), 211-214.

Uittenbogaard, R. E. (1995), The importance of internal waves for mixing in a stratified estuarine tidal flow.

Uncles, R., et al. (2006a), Properties of suspended sediment in the estuarine turbidity maximum of the highly turbid Humber Estuary system, UK, *Ocean Dynamics*, *56*(3), 235-247.

Uncles, R. J., et al. (1992), Observations of fine sediment concentrations and transport in the turbidity maximum region of an estuary, in *Dynamics and exchanges in estuaries and the coastal zone*, edited by D. Prandle, pp. 255-276, American Geophysical Union, Washington, D. C. .

Uncles, R. J. (2002), Estuarine Physical Processes Research: Some Recent Studies and Progress, *Estuarine, Coastal and Shelf Science*, *55*(6), 829-856.

Uncles, R. J., et al. (2006b), Turbidity maximum in the macrotidal, highly turbid Humber Estuary, UK: Flocs, fluid mud, stationary suspensions and tidal bores, *Estuarine, Coastal and Shelf Science*, *67*(1-2), 30-52.

Urick, R. J. (1948), The Absorption of Sound in Suspensions of Irregular Particles, *Journal of the Acoustical Society of America*, *20*(3), 283-289.

Van de Kreeke, J., et al. (1997), Tidal variations in suspended sediment concentration in the Ems estuary: origin and resulting sediment flux, *Journal of Sea Research*, *38*(1-2), 1-16.

Van Den Berg, J. H. (1987), Bedform migration and bed-load transport in some rivers and tidal environments, *Sedimentology*, *34*(4), 681-698.

Van den Berg, J. H., et al. (2007), Diagnostic sedimentary structures of the fluvial-tidal transition zone – Evidence from deposits of the Rhine and Meuse, *Netherlands Journal of Geosciences*, *86*(3), 287-306.

Van der Ham, R., et al. (2001), Turbulent exchange of fine sediments in a tidal channel in the Ems/Dollard estuary. Part I: Turbulence measurements, *Continental Shelf Research*, *21*(15), 1605-1628.

Van der Mark, C. F., et al. (2008), Quantification of variability in bedform geometry, *Journal of Geophysical Research*, *113*(F03020), 11.

Van Dijk, T. A. G. P., et al. (2008), Separating bathymetric data representing multiscale rhythmic bed forms: A geostatistical and spectral method compared, *Journal of Geophysical Research*, *113*(F4), F04017.

Van Leussen, W. (1988), Aggregation of Particles, Settling Velocity of Mud Flocs: A Review, in *Physical processes in estuaries*, edited by J. Dronkers and W. Van Leussen, pp. 347-403, Springer, Berlin

Van Leussen, W., and J. M. Cornelisse (1993), The determination of sizes and settling velocities of estuarine flocs by an underwater video system, *Netherlands Journal of Sea Research*, *31*, 231-241.

Van Leussen, W. (1995), Estuarine macroflocs - their role in fine-grained sediment transport, PhD thesis, 484 pp, University Utrecht, Utrecht, The Netherlands.

Van Rijn, L. C. (1984), Sediment Transport, Part I: Bedload Transport, *Journal of hydraulic engineering*, *110*(10), 1431-1456.

Van Rijn, L. C. (1993), *Principles of sediment transport in rivers, estuaries and coastal seas*, 1200 pp.

Villard, P. V., et al. (2000), Influence of wave groups on SSC patterns over vortex ripples, *Continental Shelf Research*, *20*(17), 2391-2410.

Vincent, C. E. (2007), Measuring suspended sand concentration using acoustic backscatter: a critical look at the errors and uncertainties, *Geological Society, London, Special Publications*, *274*(1), 7-15.

Vinzon, S. B., and A. J. Mehta (2003), Lutoclines in High Concentration Estuaries: Some Observations at the Mouth of the Amazon, *Journal of Coastal Research*, *19*(2), 243-253.

Vinzon, S. B., et al. (2009), Mud deposit formation on the open coast of the larger Patos Lagoon-Cassino Beach system, *Continental Shelf Research*, *29*(3), 572-588.

Visser, M. J. (1980), Neap-spring cycles reflected in Holocene subtidal large-scale bedform deposits: A preliminary note, *Geology*, *8*(11), 543-546.

Watanabe, R., et al. (2000), Modeling of fluid mud flow on an inclined bed, in *Coastal and Estuarine Fine Sediment Processes - Intercoh 1998*, edited by W. H. McAnally and A. J. Mehta, pp. 249-261, Elsevier.

Wellershaus, S. (1981), Turbidity maximum and mud shoaling in the Weser Estuary, *Archiv für Hydrobiologie*, *92*(2), 161-198.

Wells, J. T. (1995), Tide-Dominated Estuaries and Tidal Rivers, in *Geomorphology and Sedimentology of Estuaries*, edited by G. M. E. Perillo, pp. 179-205, Elsevier.

West, J. R., and K. O. K. Oduyemi (1989), Turbulence measurements of suspended solids concentrations in estuaries, *Journal of Hydraulic Engineering*, *115*, 457-474.

Whitehouse, R., et al. (Eds.) (2000), *Dynamics of Estuarine Muds: A Manual for Practical Applications*, 210 pp., Thomas Telford, London.

Wienberg, C. (2003), Korrigiert und ausgebaggert - die Außenweser im Wandel der Zeit, in *Konfliktfeld Küste: ein Lebensraum wird erforscht*, edited by I. Heidbrink, pp. 139-160, Hanse-Studien, Oldenburg.

Wilbers, A. W. E., and W. B. M. ten Brinke (2003), The response of subaqueous dunes to floods in sand and gravel bed reaches of the Dutch Rhine, *Sedimentology*, *50*, 1013-1034.

Wilbers, A. W. E. (2004), The development and hydraulic roughness of subaqueous dunes, PhD thesis, 224 pp, Utrecht University, Utrecht, The Netherlands.

Winterwerp, J. C. (1999), On the dynamics of high-concentrated mud suspensions, PhD thesis, Delft University of Technology, Delft, The Netherlands.

Winterwerp, J. C. (2002), On the flocculation and settling velocity of estuarine mud, *Continental Shelf Research*, *22*(9), 1339-1360.

Winterwerp, J. C., et al. (2002), Dynamics of Concentrated Benthic suspension layers, in *Fine Sediment Dynamics in the Marine Environment - Intercoh 2000*, edited by J. C. Winterwerp and C. Kranenburg, pp. 41-55, Elsevier.

Winterwerp, J. C., and T. van Kessel (2003), Siltation by sediment-induced density currents, *Ocean Dynamics*, *53*(3), 186-196.

Winterwerp, J. C., and W. G. M. Van Kesteren (Eds.) (2004), *Introduction to the physics of cohesive sediment in the marine environment*, 466 pp., Elsevier B.V.

Wolanski, E., et al. (1988), Fluidization of Mud in Estuaries, *Journal of Geophysical Research*, *93*(C3), 2351-2361.

Wolanski, E., et al. (1989), Mixing across a lutocline, *Limnology and Oceanography*, *34*(5), 931–938.

Wolanski, E., et al. (1992a), Settling of ocean-dumped dredged material, Townsville, Australia, *Estuarine, Coastal and Shelf Science*, *35*(5), 473-489.

Wolanski, E., et al. (1992b), The Role of Turbulence in the Settling of Mud Flocs, *Journal of Coastal Research*, *8*(1), 35-46.

Woodruff, J. D., et al. (2001), Seasonal variation of sediment deposition in the Hudson River estuary, *Marine Geology*, *179*(1-2), 105-119.

Wu, J., et al. (2006), Dispersion of disposed dredged slurry in the meso-tidal Changjiang (Yangtze River) Estuary, *Estuarine Coastal and Shelf Science*, *70*, 663-672.

Wunderlich, W., and S. Müller (2003), High-resolution sub-bottom profiling using parametric acoustics, *International Ocean Systems*, *7*(4), 6-11.

Wurpts, R. (2005a), 15 years experience with fluid mud: definition of the nautical bottom with rheological parameters, *Terra et Aqua*, *99*, 22-32.

Wurpts, R. (2005b), Hyperconcentrated flow. Reduzierter Unterhaltungsaufwand bei Berücksichtigung der Fließfähigkeit des Baggergutes, *Hansa International Maritime Journa*, *143*, 75-88.

Zimmerman, J. T. F., and H. Kausch (1996), Microaggregates in the Elbe Estuary: structure and colonization during spring, *Archiv für Hydrobiologie*, *48*, 85-92.